IECO

Volume 5 No 4 Year 2022

■ Volume 5

■ No 4

■ Year 2022

University of Sistan and Baluchestan

Iranian Association of Electrical and Electronics Engineers

International Journal Of

Industrial Electronics Control and Optimization

In This Issue:

Research Articles:

IECO

International Journal Of

Industrial Electronics Control and Optimization

About Journal

The University of Sistan and Baluchestan entered into strategic partnership with Iranian Association of Electrical and Electronic Engineers (IAEEE) to publish the **International Journal of Industrial Electronics Control and Optimization (IECO)**. The IECO is a refereed international journal which presents to the international scientific community important results of work in these fields, whether in the form of modeling simulation, analysis, fundamental research, development, application, design or real-time implementation. The scope of IECO is broad, encompassing all aspects of Industrial Electronics, Control and Optimization.

Note: International Journal of Industrial Electronics, Control and Optimization (IECO) has qualified to **ACADEMIC RESEARCH JOURNAL (ELMI-PAJOHESHI)** status certified by the ministry of Science, Research and Technology of Iran (No. 231566/3/18 dated 1396/10/09), and is published by the University of Sistan and Baluchestan through a formal partnership (No. 952/2/1500 dated 1395/11/04) with Iranian Association of Electrical and electronic Engineers (IAEEE) in order to develop scientific and research cooperation.

Aims and Scope

International Journal of Industrial Electronics, Control and Optimization (IECO) is a Peer reviewed journal of advanced and state-of-the-art in the science and engineering of Industrial Electronics, Control and Optimization. Its Scope encompasses the applications of Industrial Electronics, power systems, control, optimization and computational intelligence for the enhancement of industrial and manufacturing system and processes. The scope of the journal include the following:

I. Industrial Electronics

- *Low and high power converters*
- *Renewable energy*
- *Drive control techniques*
- *Techniques for advanced power semiconductor devices*
- *Power quality and utility applications*
- *Communications*
- *Flexible AC Transmission Systems (FACTS)*
- *Control in power electronics*
- *Electromagnetic and thermal performance of electronic power converters*
- *Motion control, robotics, sensors and actuators*
- *Fault detection and diagnosis*
- *Power systems*
- *Factory automation, communication, and computer networks*

II. Control

- *Adaptive control*
- *Control of process systems*
- *Control theory*
- *Data processing*
- *Design of control systems*
- *Hybrid systems*
- *Identification and observation*
- *Intelligent systems*
- *Model-predictive control*
- *Optimal control*
- *Robust control*
- *Fractional order systems*

III. Optimization

- *Ant Colony*
- *Chaos Theory*
- *Evolutionary Computing*
- *Fuzzy Computing*
- *Hybrid Methods*
- *Immunological Computing*
- *Neuro Computing*

- *Particle Swarm*
- *Probabilistic Computing*
- *Rough Sets*
- *Wavelet*

International Journal Of
Industrial Electronics Control and Optimization
Print ISSN: 3517-2645
Online ISSN: 3568-2645
Homepage: https://ieco.usb.ac.ir/

A New Squirrel Cage Rotor Structure to Improve the Dynamic Performance of the Single-Phase Induction Motor

Hamed Shadfar[1] | Hamid Reza Izadfar[2]

Department of Electrical and Computer Engineering, Semnan University, Semnan, Iran.[1,2]
Corresponding author's email: hrizadfar@semnan.ac.ir

Article Info

Article type:
Research Article

Article history:
Received: 10 July 2022
Revised: 18 Oct 2022
Accepted: 28 Oct 2022
Published online: 21 Nov 2022

Keywords:
Electromagnetic force,
Single- phase induction motor,
Slip ring rotor,
Squirrel cage rotor, Rotor bar

ABSTRACT

Improving the performance of electric machines has been focused on by researchers for many years. Reducing vibration and noise is one of the factors that are effective in improving the performance of electric machines. Electromagnetic forces are produced by the harmonics in the magnetic flux of the air gap, and vibration and electromagnetic noise are produced by the electromagnetic forces exerted on the stator and rotor structures. This paper proposes a new structure of the squirrel cage rotor to improve the distribution of the air gap magnetic flux and reduce the electromagnetic forces and, consequently, the electromagnetic noise in a single-phase induction motor. For this purpose, the rotor bars in the proposed design are located on the rotor in a sinusoidal form. The results show that this rotor structure improves the dynamic behavior and many parameters, such as electromagnetic forces, harmonic distortion of magnetic flux, and torque ripple.

I. Introduction

In general, induction motors are divided into two groups based on rotor structure: squirrel cage motors and slip ring motors (wound rotors). Due to their simple and robust structure, more than 90% of induction motors are squirrel cage rotor types. Single-phase induction motors (SPIM) are the most common type of low-power motors in single-phase systems and are extensively used in domestic and industrial applications [1-2].

With the development and progress of the process of designing and manufacturing electric machines, various technologies of them have been presented for specific purposes. On the other hand, these machines must be able to meet many specific application requirements such as speed, torque, reliability, longevity, low noise and vibration, and maintenance. Therefore, improving the performance of electric machines has always drawn researchers' attention [3-5]. In general, many factors in the process of design, production, and operation of electric machines affect their performance. In [6 - 8], the effect of non-sinusoidal voltage is examined on the steady-state performance of a motor. The results show that harmonic voltages produce non-sinusoidal currents in the stator and rotor, resulting in additional losses and torque ripples. SPIMs have low starting torque. Also, during the transient and steady-state, these motors produce a significant level of torque pulses, which create noise and vibration in the electric machine. In [9], to solve these problems, a pulse width modulation (PWM) inverter has been used to start the motor. In [10-13], by designing the winding and using the pole-change method, reduces the harmonic components of the magnetic flux density air gap. In general, air gap field harmonics play a major role in the performance of electric machines, including the level of electromagnetic forces and the production of noise and vibration in them.

In [14], by injecting a small current into the stator winding, which has a controlled magnitude, frequency, and phase, waves are created that are contrary to the existing harmonics and limit or eliminate them. Also, efforts are made in [15-17] to reduce the field harmonics by using the compensators of the negative current component. In [18-21], the effect of the geometry of the rotor bars and stator slots is investigated on the magnetic field of the air gap and the performance of the squirrel cage induction

DOI: 10.22111/IECO.2022.42485.1431

motor. In [22], to improve the starting characteristic of the motor, it is suggested to use skew slots in the stator core instead of the rotor. Another method to improve the performance of SPIM in a specific speed range is to use an adjustable capacitor. In [23], a chaotic pulse width modulation method is proposed to extend the power spectrum of the induction motor drive system. The results show that in this method, carrier, voltage/current, and acoustic switching noise spectrum are dispersed over a chaotic frequency range with no specific frequency concentration.

In [24], the effect of capacitor changes on motor characteristics including efficiency, electromagnetic torque, torque ripple, power factor, and current in a specific speed range is investigated, and the results confirm the improvement of motor performance. In [A], it deals with the reduction of quantization noise in the direct torque control of an induction motor. In the proposed method, by using a random dither signal that is added to the truncating analog-to-digital converter (ADC) outputs, the average error of the ADC reaches zero, and as a result, the integrator output error is reduced. The proposed quantization method can improve the result of the digital converter. Therefore, this method can reduce the current measurement result. Therefore, torque and flux ripples are reduced. To make electric motors with high reliability and low losses, a high-temperature superconducting induction/synchronous motor (HTS-ISM) is studied in [B]. The torque density and structural dimensions of HTS-ISM are optimized using the collective decision optimization algorithm (CDOA).

The results show an increase in torque of about 51.75% through the optimization process. Also, the particle swarm optimization (PSO) algorithm has been used as a common optimization method to compare the results. The results show that CDOA is more capable than PSO in motor design parameter optimization problems. In [25-27], the effects of the combination of different rotor and stator slots on the electromagnetic force are investigated by the finite element method using theoretical analysis. The results show that the coordination of the slots is very important and significant in the design process of low-noise motors. Another effective method of noise reduction is the use of skew slots in the rotor [28-30]. In [28-29], a new type of skew slot is presented and it is compared with previous types to examine the effectiveness of the proposed method. As mentioned, different goals are considered in different machines depending on the type of application for improving their performance.

This paper presents a new structure of the squirrel cage rotor to improve the distribution of the air gap magnetic flux. In the proposed design, by maintaining the composition and geometry of the stator and rotor slots, as well as the identical distribution of the stator winding, the rotor bars are located on the rotor according to a sinusoidal function. For this purpose, the conventional squirrel cage rotor and the proposed designs are simulated in ANSYS Maxwell 2D software. With the new rotor design, the total harmonic distortion (THD) of the magnetic field of the motor is reduced. As a result, the level of electromagnetic forces is reduced. Besides, some dynamic performances such as torque ripple and speed response are improved. The rest of the paper is organized as follows. Section II presents the stator windings. In Section III, the proposed design of a squirrel cage rotor will be introduced. Section IV presents the simulation results. Finally, the conclusion of the paper is provided in Section V.

II. Distributions of Stator Windings

As was already mentioned, one of the factors affecting the electromagnetic forces in electric machines is the distribution of stator winding. The winding distribution can be concentric or lap. However, since this paper aims to investigate the effect of the position of the squirrel cage rotor bars on SPIM on the electromagnetic forces, the distribution of the winding in both conventional and proposed designs is considered to be similar.

In [13], the effect of different types of the stator winding distribution on electromagnetic forces in a SPIM is considered and a new winding is introduced to reduce electromagnetic forces. This paper considers the stator winding in both conventional and proposed designs to be 4-poles and exactly similar to the winding introduced in [13]. This winding type is a lap. The pitch of the main and auxiliary windings equals 7. The widespread design of the stator winding distribution (main and its auxiliary windings) is shown in Fig. 1.

III. Proposed Design of Squirrel Cage Rotor

The cross-sectional of the conventional and proposed designs of the squirrel cage rotor is shown in Figs. 2 and 3, respectively. In the proposed design the distribution of the centers of rotor bars is located on a sinusoidal function. All other parameters such as dimensions, composition, and geometry of the stator and rotor slots are identical in both motors. Also, the shape and area of the rotor bars are kept constant.

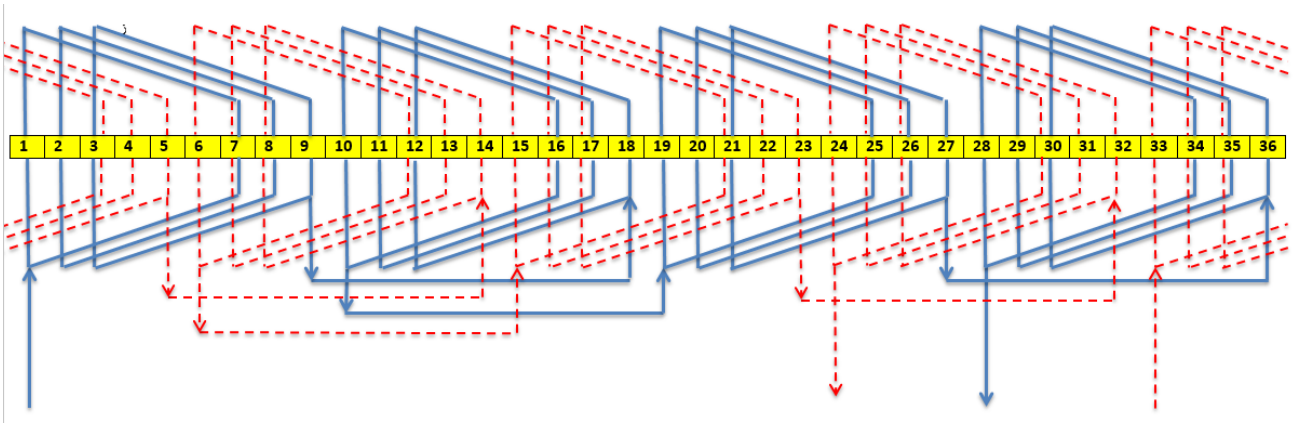

Fig. 1. The widespread design of stator winding: main (solid line) and auxiliary (dashed line) – 4poles [13]

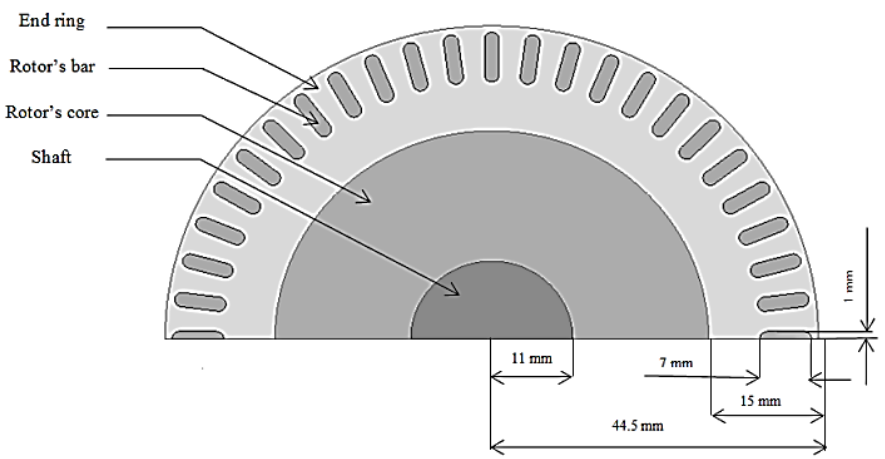

Fig. 2. The cross-sectional of the conventional squirrel-cage rotor

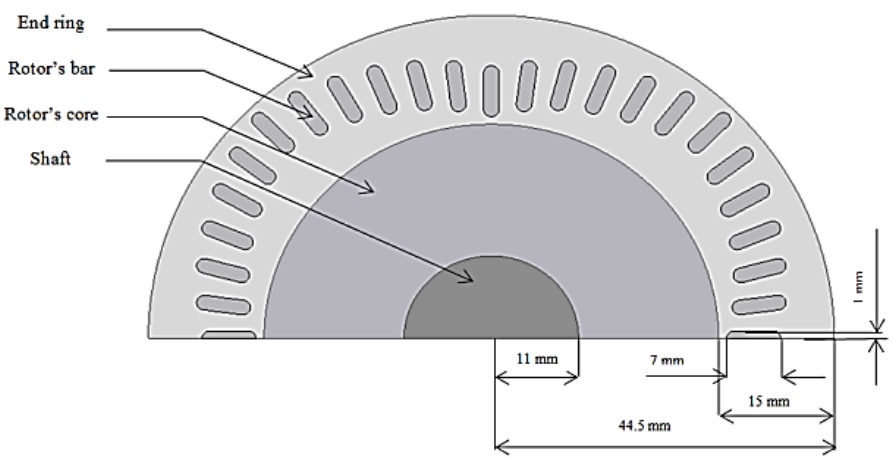

Fig. 3. The cross-sectional of the proposed design of the squirrel cage rotor

IV. Simulation and Results

To evaluate the proposed design and compare it with the conventional design of the squirrel cage rotor, these two designs are simulated in ANSYS Maxwell 2D software. The electrical specifications of the studied single-phase induction motor (run and start capacitor) are presented in Table 1 and its sizing information are according to Table 2. In this comparison, the stator structure and its winding distribution

are the same. Also, the dimensions, geometry, and area of the rotor bars and their core are identical, and the only difference is in the placement of the rotor bars.

TABLE 1
ELECTRICAL SPECIFICATIONS OF THE SINGLE-PHASE INDUCTION MOTOR STUDIED

Parameters	Values
Output power (hp)	0.75
Voltage (V)	220
Phase number	1
Frequency (Hz)	50
Run capacitor (μF)	25
Start capacitor (μF)	160
Pole number	4

TABLE 2
SIZING INFORMATION OF THE SINGLE-PHASE INDUCTION MOTOR STUDIED

Parameters		Values
Stator	Outer diameter (mm)	160.6
	Inner diameter (mm)	89.8
	Length (mm)	66
	Number of slots	36
Air gap(mm)		0.45
Rotor	Outer diameter (mm)	88.9
	Number of bars	48
	Length (mm)	66
	End ring thickness(mm)	5
	End ring height (mm)	15

A. Distribution of Magnetic Field

Figs. 4 and 5 display the magnetic field distribution and flux lines in machines. The curves of the air gap flux density variations in the conventional and proposed designs are shown in Fig. 6. According to these curves, the average variations of flux density amplitude in conventional and proposed designs are 0.43 Tesla and 0.56 Tesla, respectively. Also, the Fast Fourier Transform (FFT) analyses of these waveforms in conventional and proposed models are depicted in Figs. 7 and 8, respectively. Accordingly, the total harmonic distortion (THD) percentages in these designs are 71 and 52, respectively. To investigate the effect of the proposed structure on the air gap field, the effect of the rotor field in the conventional and proposed designs has been independently analyzed. Fig. 9 displays the flux density change curves due to only the rotor field in these designs. According to these curves, the average variations of flux density magnitude in conventional and proposed designs are 0.35 Tesla and 0.41 Tesla, respectively. The FFT of these curves is also shown in Figs. 10 and 11, respectively. Accordingly, the THD percentages in these designs are 83 and 61, respectively. As is seen in these figures, the new placement of rotor bars increases the magnetic field generated by the rotor. As a result, as the magnitude of the air gap magnetic field increases, its distortion decreases.

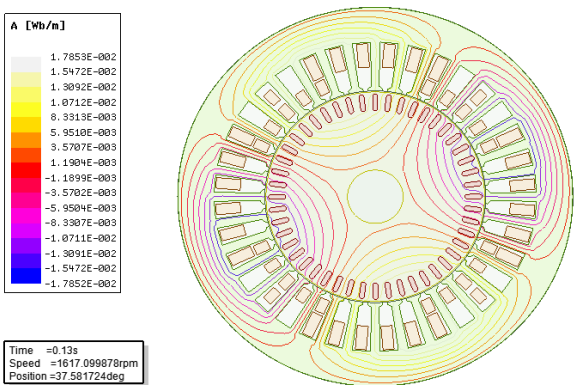

Fig. 4. Magnetic flux distribution in conventional design

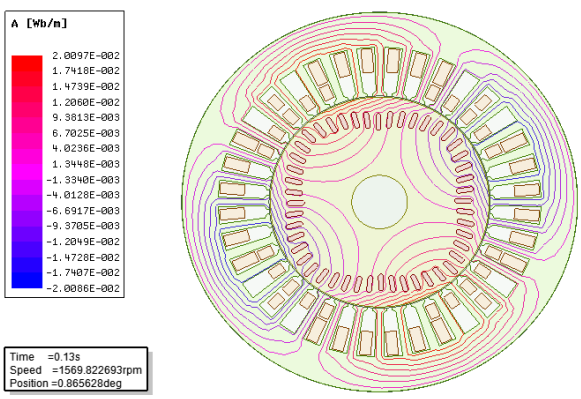

Fig. 5. Magnetic flux distribution and flux lines in proposed design

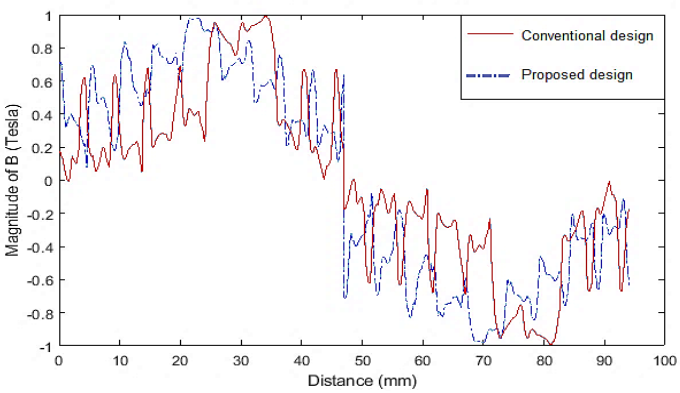

Fig. 6. Air gap flux density curves

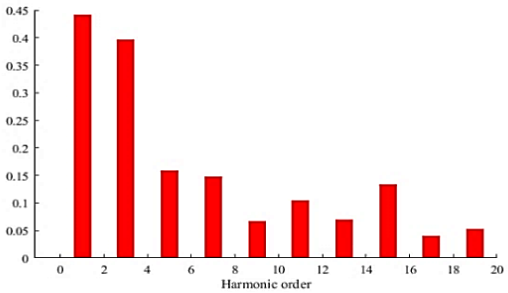

Fig.7. FFT of the air gap flux density in the conventional design

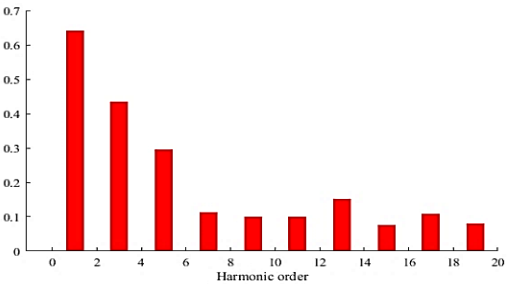

Fig. 8. FFT of the air gap flux density in the proposed design

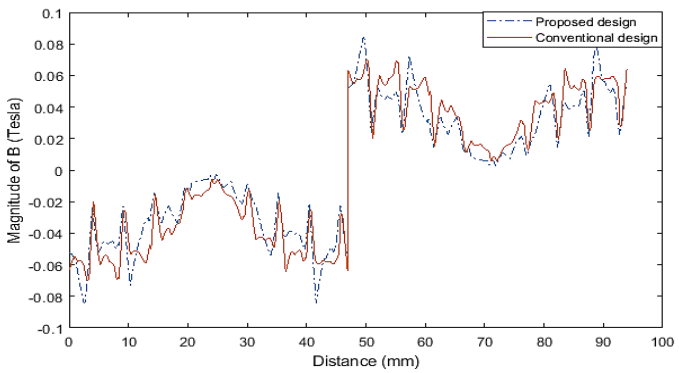

Fig. 9. Rotor field curves

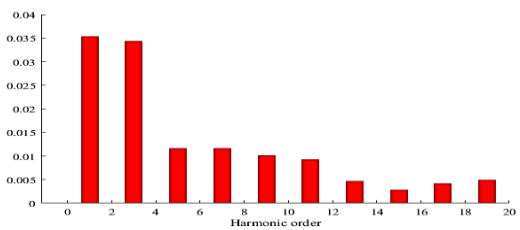

Fig. 10. FFT of the rotor field in the conventional design

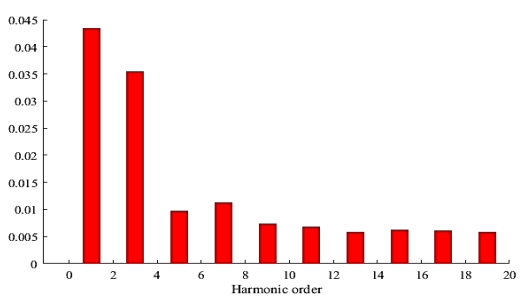

Fig. 11. FFT of the rotor field in the proposed design

B. *Electromagnetic Forces in Induction Motor*

The harmonics in the magnetic flux in the air gap are the main cause of electromagnetic noise and vibration in electric machines. Recently, reducing noise and vibration in electric machines to improve their performance has been highly regarded by researchers. In general, radial and tangential electromagnetic forces are two major sources of electromagnetic vibration. Radial electromagnetic forces are the main source of electromagnetic noise in electric machines.

Today, with the development of the process of designing and manufacturing electric machines, the harmonic components affecting vibration and noise have been reduced greatly. However, various factors caused by internal/external defects of the motor such as power supply, load, stator core structure, rotor, etc. can cause serious problems that affect the normal performance of the motor [33-35].

Electromagnetic pressure (Maxwell pressure) or in other words electromagnetic forces (Maxwell forces) per unit area (*Pm*) can be calculated by Eq. (1).

$$P_m(\theta.t) = \frac{b_r^2(\theta.t) - b_t^2(\theta.t)}{2\mu_0} \quad (1)$$

In Eq. (1), θ is the mechanical angular position in degree, t is time, μ_0 is the magnetic permeability in the air gap, $b_r(\theta.t)$ and $b_t(\theta.t)$ 000.00000000000000000…..are the radials the tangential components of flux density in the air gap, respectively. In general, the radial component is much larger than the tangential component, so in most cases, the tangential component is ignored.

C. *Analysis of The Dynamic Characteristics*

Fig. 12 depicts the curve of the electromagnetic force applied to the rotor and stator cores in the conventional and proposed designs. For example, according to this figure, the mean value of the variation of the electromagnetic force in the conventional and proposed models by a numerical method under loading condition 2 N.m is equal to 4.58 N and 0.59 N, respectively. Also, the curves of speed, main winding current, and torque are shown in Figs. 13, 14, and 15 respectively.

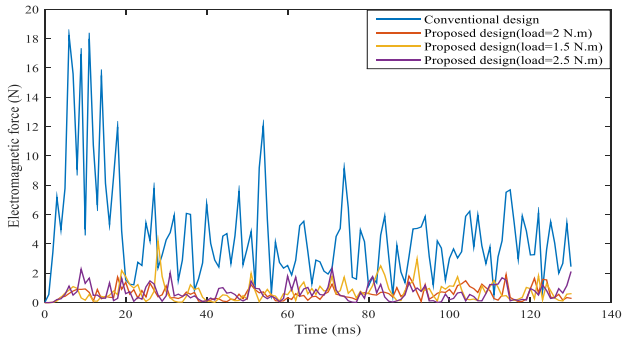

Fig. 12. Electromagnetic force-time curves

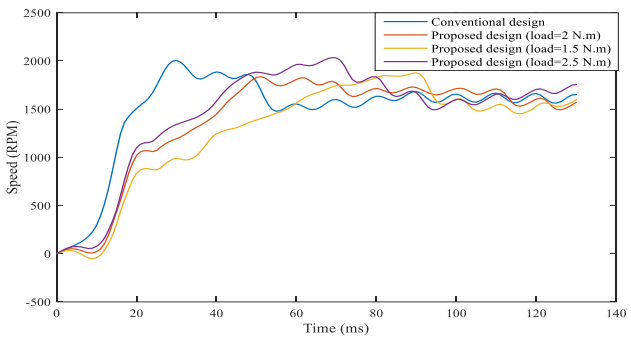

Fig. 13. Speed-time curves

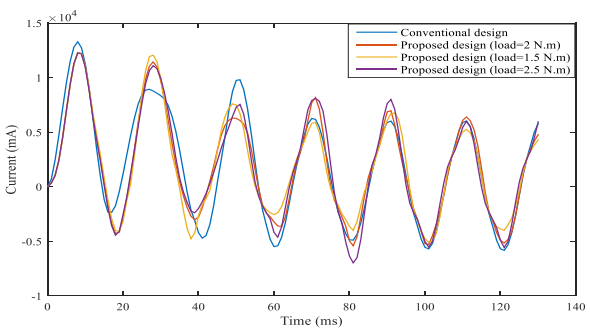

Fig. 14. Main winding current - time curves

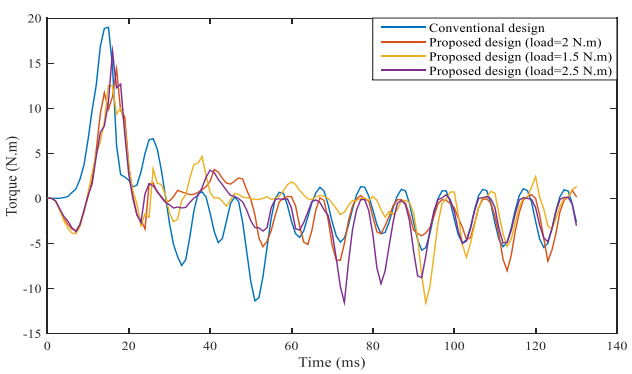

Fig.15. Torque-time curves

Table 3 shows the comparison of losses in two conventional and proposed models under different loading conditions. According to this table, core losses and copper losses under different loading conditions including 100%, 80% and 60% of nominal load have been calculated and compared. The total losses in the proposed design are smaller than the conventional design. This means that the efficiency of the proposed motor has been modified.

TABLE 3
COMPARISON OF LOSSES IN CONVENTIONAL AND PROPOSED DESIGN

Losses / Design	Core loss (W)	Copper loss (W)	Total losses (W)
Conventional (load=1.5 N.m)	12	82	94
Conventional (load=2 N.m)	12	104	114
Conventional (load=2.5 N.m)	12	148	160
Proposed (load=1.5 N.m)	14	64	78
Proposed (load=2 N.m)	14	83	97
Proposed (load=2.5 N.m)	14	120	134

V. Conclusion

In this paper, it was determined that if the position of the rotor bars follows the sinusoidal distribution, the first harmonic component of the air gap magnetic flux will increase and other harmonic components will decrease. Therefore, it can be achieved with less electromagnetic force and noise. Also, the single-phase induction motor will show better behavior in transient operations. The analytical and simulation results by Maxwell software of both simulated models are summarized in Table 4.

TABLE 4
COMPARISON OF PARAMETERS IN CONVENTIONAL AND PROPOSED DESIGN

Motor / Quantity		Conventional design	Proposed design
Stator winding Current (A)	Main	6	5
	Auxiliary	5	4
Winding Resistance (Ω)	Main	3.9	
	Auxiliary	4	
Torque ripple (N.m)		2.50	2.25
The calculated average of Maxwell radial force magnitude by numerical method (N)		4.58	0.59
The calculated average of Maxwell radial force magnitude by analytical method (N)		12.06	2.68
The variations average of flux density amplitude (Tesla)		0.43	0.56
The THD of flux density (%)		71	52
Total copper consumed (gram)		235	

References

[1] Khan, M. A., Khan, F., Rahman, L. U., & Fatima, A. "Analysis and electromagnetic noise suppression of three-phase squirrel cage induction motor", In 2018 International Conference on Computing, Electronic and Electrical Engineering (ICE Cube), pp. 1-5, 2018.

[2] Cho, D. H., & Kim, K. J. "Modelling of electromagnetic excitation forces of small induction motor for vibration and noise analysis", IEE Proceedings-Electric Power Applications, vol. 145, no. 3, pp. 199-205, 1998.

[3] Bendaas, Ismail, and Farid Naceri. "A new method to minimize the chattering phenomenon in sliding mode control based on intelligent control for induction motor drives." Serbian journal of electrical engineering, vol. 10, no. 2, pp. 231-246, 2013.

[4] Nahilia, H., Boudour, M., Cardenas, A., Agbossou, K., & Doumbia, M. L. "Doubly fed induction wind generators model and field orientation vector control design and implementation on FPGA", International Journal of Dynamics and Control, vol. 7, no. 3, pp. 1005-1014, 2019.

[5] Stojić, Đorđe M., and Milić R. Stojić. "Induction motor IFOC based speed-controlled drive with asymptotic disturbance compensation." Serbian Journal of Electrical Engineering, vol. 9, no. 3, pp. 301-314, 2012.

[6] Vamvakari, A., Kandianis, A., Kladas, A., Manias, S., & Tegopoulos, J. "Analysis of supply voltage distortion effects on induction motor operation", IEEE Transactions on Energy Conversion, vol. 16, no. 3, pp. 209-213, 2008.

[7] El Daoudi, S., Lazrak, L., El Ouanjli, N., & Lafkih, M. A. "Improved DTC-SPWM strategy of induction motor by using five-level POD-PWM inverter and MRAS SF estimator", International Journal of Dynamics and Control, vol. 9, no. 2, pp. 448-462, 2021.

[8] Kong, W., Guo, H., Tang, G., & Zhong, Z. "Optimized Non-Sinusoidal Power Supply in High-Power Multiphase Induction Motor Drive Based on Harmonic Parameter Analysis", Journal of Electrical Engineering & Technology, vol. 15, no. 6, pp. 2627-2638, 2020.

[9] Olarinoye, G. A., Yusuf, J., & Jimoh, B. "Improvement of Torque Production in Single-Phase Induction Motors", Nigerian Journal of Technological Development, vol. 14, no. 2, pp. 39-45, 2017.

[10] Nam, H., Jung, S. K., Kang, G. H., Hong, J. P., & Jung, T. U. "Design of pole change single-phase induction motor for household appliances", In 38th IAS Annual Meeting on Conference Record of the Industry Applications Conference, vol. 2, pp. 1126-1133, 2003.

[11] Jung, T. U., Yun, C. H., Cha, H. R., Chae, M. G., & Kim, H. M. "Improved design for driving characteristics in single phase induction motor with concentrated winding", In 2007 IEEE Power Electronics Specialists Conference, pp. 2418-2422, 2007.

[12] Tessarolo, A., Mezzarobba, M., & Contin, A. "A stator winding design with unequally-sized coils for adjusting air-gap space harmonic content of induction machines", In The XIX International Conference on Electrical Machines-ICEM 2010, pp. 1-7, 2010.

[13] Shadfar, H., & Izadfar, H. R. "Improvement of Electromagnetic Forces in a Single-Phase Induction Motor by Providing a New Winding Distribution", Iranian Journal of Electrical and Electronic Engineering, vol. 16, no. 1, pp. 74-84, 2020.

[14] Cassoret, B., Corton, R., Roger, D., & Brudny, J. F. "Magnetic noise reduction of induction machines", IEEE Transactions on power electronics, vol. 18, no. 2, pp. 570-579, 2003.

[15] Sadigh, A. K., & Hagh, M. T. "Elimination of instantaneous backward mmf in single phase induction motors", In 2009 5th IEEE GCC Conference & Exhibition, pp. 1-6, 2009.

[16] Zhong, H., Wang, X., Leng, X., & Wang, D. "A new type single-phase induction motor with negative sequence compensatory winding", In 2007 2nd IEEE Conference on Industrial Electronics and Applications, pp. 82-85, 2007.

[17] Zhong, H., Wang, X., Wang, D., & Qiao, D. "Analysis and design of a new type high-efficiency single-phase induction motor based on negative sequence magnetic field compensation", In 2008 International Conference on Electrical Machines and Systems, pp. 3962-3966, 2008.

[18] Makhetha, E., Muteba, M., & Nicolae, D. V. "Effect of Rotor Bar Shape and Stator Slot Opening on the Performance of Three Phase Squirrel Cage Induction Motors with Broken Rotor Bars", In 2019 Southern African Universities Power Engineering Conference/Robotics and Mechatronics/Pattern Recognition Association of South Africa (SAUPEC/RobMech/PRASA), pp. 463-468, 2019.

[19] Brojboiu, M. A. R. I. A. "Concerning the influence of the rotor bar geometry on the induction motor performances", In 5th International Conference on Telecommunications in Modern Satellite, Cable and Broadcasting Service. TELSIKS 2001. Proceedings of Papers (Cat. No. 01EX517), Vol. 2, pp. 647-650, 2001.
[20] Kim, Y. S. "Effects of rotor bar shape for squirrel cage induction motor in transient state using moving band technique", IEEE transactions on applied Superconductivity, vol. 24, no. 3, pp. 1-4, 2013.
[21] Iqbal, M. A., & Singh, G. "A review on influence of rotor geometry on the performance of single-phase capacitor-run Induction motor", International Journal of Advanced Research in Electrical, Electronics and Instrumentation Engineering, vol. 3, pp. 10216-10224, 2014.
[22] Kim, B. T., Kim, D. K., Kwon, B. I., & Lipo, T. A. "Optimal skew angle for improving of start-up performance of a single-phase line-start permanent magnet motor", In 2008 IEEE Industry Applications Society Annual Meeting, pp. 1-6, 2008.
[23] Kim, J. H., & Jung, Y. G. "Spreading Power Spectrum of an Induction Motor Drive System by Chaotic Pulse Width Modulation Method", Journal of Electrical Engineering & Technology, pp. 1-10, 2021.
[24] Hekmati, P., Yazdanpanah, R., Monfared, J. M., & Mirsalim, M. "Adjustable capacitor for the single-phase IM performance improvement", In The 5th Annual International Power Electronics, Drive Systems and Technologies Conference (PEDSTC 2014), pp. 7-12, 2014.
[25] Taheri, Asghar, and Amir Ghasemian. "Quantization Noise Reduction Using Random Dither in Direct Torque Control of an Induction Motor." International Journal of Industrial Electronics Control and Optimization, vol. 3, no. 4, pp. 439-445, 2020.
[26] Niaz Azari, Milad, Vasiye Lohrasbi, and Seyed Abdolah Mousavi. "Optimum Design of High-Temperature Superconducting Induction/Synchronous Motor to Increase Torque Density Using Collective Decision Optimization Algorithm." International Journal of Industrial Electronics Control and Optimization, vol. 3, no. 2, pp. 137-145, 2020.
[27] Liu, C., Xu, Y., & Feng, J. "Low Electromagnetic Noise Squirrel Cage Motor Analysis and Optimization of Slot Coordination", MECHANICS, vol. 4, no.1100, pp. 1100, 2015.
[28] Kobayashi, T., Tajima, F., Ito, M., & Shibukawa, S. "Effects of slot combination on acoustic noise from induction motors", IEEE Transactions on Magnetics, vol. 33, no.2, pp. 2101-2104, 1997.
[29] Le Besnerais, J., Lanfranchi, V., Hecquet, M., & Brochet, P. "Optimal slot numbers for magnetic noise reduction in variable-speed induction motors", IEEE Transactions on Magnetics, vol. 45, no. 8, pp. 3131-3136, 2009.
[30] Zhu, H., Zhou, G., Chen, J., & Liu, H. "Analysis and study of skewed slot tooth distance on low electromagnetic noise of three-phase induction motor with squirrel cage rotor", In 2012 Sixth International Conference on Electromagnetic Field Problems and Applications, pp. 1-4, 2012.
[31] Wang, C., Bao, X., Xu, S., Zhou, Y., Xu, W., & Chen, Y. "Analysis of vibration and noise for different skewed slot-type squirrel-cage induction motors", IEEE Transactions on Magnetics, vol. 53, no. 11, pp. 1-6, 2017.
[32] Wang, L., Bao, X., Di, C., & Li, J. "Effects of novel skewed rotor in squirrel-cage induction motor on electromagnetic force", IEEE Transactions on magnetics, vol. 51, no. 11, pp. 1-4, 2015.
[33] Hilgert, T. G., Vandevelde, L., & Melkebeek, J. A. "Numerical analysis of the contribution of magnetic forces and magnetostriction to the vibrations in induction machines", IET Science, Measurement & Technology, vol. 1, no. 1, pp. 21-24, 2007.
[34] Hirotsuka, I., Tsuboi, K., & Ishibashi, F. "Effect of slot-combination on electromagnetic vibration of squirrel-cage induction motor under loaded condition", In Proceedings of Power Conversion Conference-PCC'97, vol. 2, pp. 843-848, 1997.
[35] J. F. Gieras, C. Wang, and J. C. Lai, "Noise of polyphase electric motors",Boca Raton, FL: CRC Press, 2005.

Hamed Shadfar received the M.Sc. degree from Semnan University, Semnan, Iran. He is currently working toward the Ph.D. degree in Faculty of Electrical and Computer Engineering, Semnan University, Semnan, Iran. His major research interests include design, fault detection, protection, monitoring and control of electric machines.

H. R. Izadfar is currently an Assistance Professor in the Electrical and Computer Engineering Department of Semnan University. His main research interests are the design and analytical and numerical analysis of electric machines and drives.

International Journal Of
Industrial Electronics Control and Optimization
Print ISSN: 3517-2645
Online ISSN: 3568-2645
Homepage: https://ieco.usb.ac.ir/

Improving Delay In SDNS By Metaheuristic Controller Placement

Maedeh Abedini Bagha[1] | Kambiz Majidzadeh[2] | Mohammad Masdari[3]| Yousef Farhang[4]

Department of Computer Engineering, Urmia Branch, Islamic Azad University, Urmia, Iran.[1,2,3]
Department of Computer Engineering, Khoy Branch, Islamic Azad University, Khoy, Iran.[4]
Corresponding author's email: kambiz.majidzadeh@iau.ac.ir

Article Info

Article type:
Research Article

Article history:
Received: 04 Aug 2022
Revised: 09 Oct 2022
Accepted: 31 Oct 2022
Published online: 21Nov 2022

Keywords:
Controller placement,
Seagull optimization algorithm,
Software-defined network.

ABSTRACT

Software-defined networking is a new network model proposed to solve the complexity of traditional network problems and facilitate dynamic network operation and management. The separation of the control plane from the data plane is the main idea of software-defined networks. Controllers are the operating system of software-defined networks and are responsible for managing the entire network. It is essential to locate controllers appropriately to have a balanced topology while guaranteeing low latency. In this work, a metaheuristic algorithm is used for controller placement. First, the problem is formulated and the network is partitioned by a clustering algorithm. Then, the seagull optimization algorithm is used to determine a suitable place for the controller in each network partition dynamically. Simulations are performed on the standard network topology from the internet topology zoo dataset to evaluate the proposed method. Simulation results reveal that the proposed method performs well in case of delay and load balancing compared with the state-of-the-art optimization algorithms.

I. Introduction

Software-defined networks (SDNs) [1] are a promising new network model proposed to solve the complexity of traditional networks [2] and facilitate the operation and management of dynamic networks [3]. The main idea in SDNs is the separation of the control plane from the data plane [4]. The control function of network components, such as switches in SDNs, is transferred to the control plane and controllers. SDNs are programable networks with many advantages [5], such as simplifying network management, improving network utilization efficiency, and supporting network innovation [6].

Network switches, also known as SDN nodes, are responsible for forwarding data based on the flow table [7], while controllers route network packets through the switches. When an unknown flow arrives at a switch, the switch sends a flow setup request to the controller, and the controller responds to the request by entering the flow in the switch's flow table [8]. Often a large-scale network with a single controller has high latency to perform control actions. In addition, the main obstacle in single controller networks is "single point failure". Also, it handles the entire network traffic, which may not be efficient. Since a single controller is responsible for all control activities in the entire SDN, any network failure will significantly impact network performance [9]. Several controllers have been distributed in the network to overcome these problems. The optimal placement of controllers in networks is a known problem, which is called controller placement problem (CPP). Because controllers play a vital role in increasing network performance, they must be located in optimal locations [10].

An example of the CPP in an SDN is shown in Fig. 1. The control plane consists of two controllers in this sample that can manage the entire network. In an SDN with multiple controllers, the number of controllers is usually determined by network scale and traffic.

The CPP unveils several challenges that must be considered. The optimal place of controllers is one of the CPP challenges as it widely impacts several parameters like delay, reliability, and load balancing [11]. The solutions should consider the controllers' capacities, the load distribution between the controllers, and the delay. Just as delay is the most crucial challenge in all networks [12], it is also crucial in SDN, and

DOI: 10.22111/IECO.2022.42638.1436

the propagation delay between the controllers and the switches must be considered in CPP.

The CPP is difficult due to its NP-hard nature [13]. The conventional formulation for CPP optimizes the objective function by linear programming (LP). But, LP does not run effectively on large networks with many nodes and links. Since real SDNs are often dynamic with variations (e.g., the number of users, topology, device failure, etc.), computation time and resources are constraining factors [11]. Therefore, it is suggested to use metaheuristic techniques to solve it.

Seagull Optimization Algorithm (SOA) [14] is a new population-based bio-inspired algorithm. Some of the advantages of metaheuristic algorithms including SOA are flexibility, deviation-free, simplicity, understandability, and avoidance of local optima [15]. Metaheuristic algorithms focus on exploring the workspace to reduce the stickiness of a local solution. Local solutions are not the right solution to any problem [16]. SOA is flexible enough to solve different problems of different natures. It uses the randomness of variables to solve problems and eliminate computation to extract search space, making it more applicable to existing problems [14].

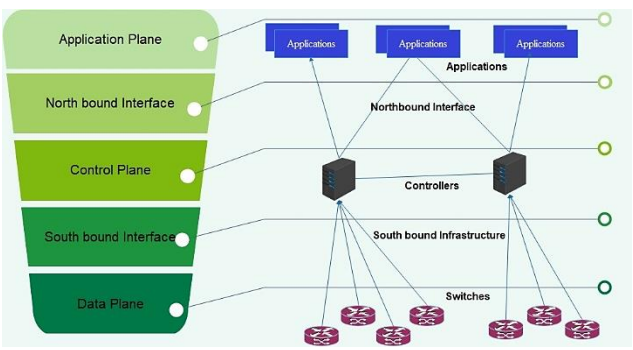

Fig. 1. An example of the CPP in SDN

In this work, we find the appropriate location of the controllers in the network. This research formulates CPP based on the load balancing in controllers, controller-to-switch latency, and inter-controller latencies.

Since CPP is NP-hard and to solve such problems, an optimal solution cannot be obtained in a reasonable time [15], researchers have developed optimization algorithms based on metaheuristics. Metaheuristic techniques are suitable for solving complex problems and are widely used [17]. So, we use SOA to determine the location of the controllers. To the best of the authors' knowledge, this is the first time that SOA is used to solve the CPP. Finally, the proposed method is evaluated using the Internet topology zoo dataset. The main contributions of this research can be summarized as follows:

1. Formulating the CPP as an optimization problem aimed to minimize the delay and improve load balancing
2. Partitioning the network by Fuzzy C-Means (FCM) clustering algorithm
3. Determining appropriate places for controllers by SOA

The rest of the paper is organized as follows. Section 2 presents a literature review of the CPP. Section 3 defines and formulates the CPP. The proposed method, clustering network by FCM, and controller placement by SOA are presented in Section 4. The proposed method is evaluated in Section 5. Finally, Section 6 concludes the paper.

II. Related Works

Separating the data and control planes in the SDN architecture forces operators to design the control plane, so the design of the control plane is a hot topic in SDN. CPP has been studied from various perspectives in previous research, such as network performance [18], [19], [20], [21], deployment scenarios [22], [23], [24] etc., focusing on optimizing network performance. The following is an overview of research associated with CPP.

CPP was first introduced by [18] in 2012. The authors studied CPP to minimize the propagation latency from the switches to the dedicated controller. Their approach included a large class of localization problems corresponding to a K-center problem to minimize the average propagation delay.

Controller load balancing is another critical performance metric on CPP. Dixit et al. [22] proposed a flexible distribution of controllers to maintain the number of controllers by changing the controllers' number according to the SDN traffic. However, these methods improved only one parameter, like propagation delay or load balancing.

Authors in [25] studied a multi-objective genetic algorithm to produce an approximate Pareto optimal frontier on large-scale networks. They considered load imbalance, latency, and reliability of network parameters. Also, they introduced inverted generational distance (IGD) as a performance metric to measure the distance between the estimated Pareto frontier and the optimal Pareto frontier.

In [26], the authors focus on CPP in software-defined vehicular networks (SDVN) and consider the dynamicity of vehicular networks' topology. They proposed a dynamic placement method based on integer linear programming (ILP) that adaptively adjusts the number and location of controllers according to road traffic fluctuations. But, ILP does not run effectively on large networks with many nodes and links.

In [27] and [28], the authors try to solve CPP by partitioning the network. In [27], a hierarchical K-means algorithm is proposed, and in [28], a network partitioning technique with an optimized K-means algorithm is proposed to minimize the delay. Authors in [9] introduce deep Q-network-based dynamic clustering and placement (DDCP) for dynamic clustering of SDN switches and controllers and show that it can significantly improve response time and network resource utilization. However, deep learning requires a large amount of data and computational resources.

In [20] and [21], the authors propose a mathematical model to

improve the delay in the distributed controller plane in SDN. They use two data-ownership models, single-data ownership (SDO) and multiple-data ownership (MDO), which provide consistency and eventual consistency. They show that both the switch-to-controller and the inter-controller latencies affect the response time of controllers in the SDO model. Also, the switch-to-controller latency is the only significant parameter affecting the controllers' response time in the MDO model. They propose two mathematical models to solve CPP that minimize the response time. For this purpose, they comprehensively examine all possible controller placement locations to determine Pareto optimal locations in switch-to-controller and inter-controller latencies. Still, they do not consider the capacity of controllers and load balancing of controllers.

Gao et al. [29] used particle swarm optimization (PSO) to solve CPP while considering the capacity of controllers. Gao et al. [30] presented a variant of the PSO heuristic for CPP while accounting for the load balance of controllers and latency. In [31], a discrete cuckoo search algorithm is applied to CPP. Simulation results show that the discrete cuckoo search algorithm performs well regarding latency and process time. However, it is designed for static environments and does not consider the load balancing of controllers.

In [32], a dynamic optimization algorithm is developed based on the salp swarm optimization algorithm (SSA). It dynamically checks the optimum number of controllers and the optimal assignment of switches to controllers in large-scale SDNs. It aims to improve execution time and reliability but it does not consider controllers' capacity and load balancing.

Schütz and Martins [33] proposed a formal mathematical model to reduce the controllers' propagation delay and load balance. The authors determined the location of the controllers, taking into account the capacity of the controller and the minimum number of controllers, and assigned nodes to the controllers.

Authors in [10] use Pareto integrated tabu search (PITS) algorithm for CPP. They use a graph theory approach to determine the proper number of controllers. The PITS algorithm is proposed to identify the optimal location of controllers and switch assignments. Also, a heuristic approach is proposed to perform switch migration and improve SDN's reliability.

Authors in [34] propose a new controller placement algorithm using Manta-Ray foraging optimization (MRFO) and salp swarm algorithm (SSA), but it only improves the delay parameter. They do not consider inter-controller latency either.

Authors in [35] deal with traffic and energy consumption in SDN. They design an energy-aware routing algorithm formulated as a multi-objective NP-hard for the CPP. A heuristic approach is developed to find optimal routing for traffic between controllers and the controller to switches to improve energy consumption. It can rearrange traffic to meet provisioning criteria by utilizing the capacity-aware design, but the network delay is not considered.

Authors in [24] address CPP and design a subgraph of a tee that can satisfy delay and availability constraints. Also, they consider geodiversity constraints to improve robustness to disaster-based failures. In [36], a DPC optimization algorithm is designed to solve the problem of poor aggregation effect in low-density regions. Also, the SC metric is addressed. The authors improve the BeeDPC algorithm to determine the controllers' position, simplify controller design and reduce average latency in SDN. Simulation results show that the optimized DPC algorithm can reduce the average delay. However, they do not consider the controller capacity.

Authors in [37] propose a hybrid metaheuristic algorithm for CPP. At first, the authors improve the SDN network based on graph theory. Then, the optimal controllers are selected using the firefly optimization algorithm (FA). Finally, multiple controllers are placed using a hybrid metaheuristic algorithm, which includes a harmonic search algorithm and a particle swarm optimization algorithm (HSA-PSO). Among the advantages of this method can be mentioned the improvement of latency, reliability and throughput.

Most existing research on controller placement optimizes the delay by improving switch-to-controller propagation latency, but they usually don't consider the capacity and load of the controllers. This research investigates the problem of delay minimization considering controller-to-controller and switch-to-controller latencies, controllers' capacity, and their load balance.

III. Problem Definition

In this section, the CPP treatment is formulated by the following assumptions.

(a) Each switch is assigned to precisely one controller.
(b) Each controller can respond to requests according to its capacity. Also, the sum of the requests processed by each controller at any moment must be within the processing capacity of the controller.
(c) The switch requests cannot be split to be processed by multiple controllers.
(d) The network load is dynamic and changes over time.
(e) Each controller can only be placed in one of the nodes' coordinates.
(f) No two or more controllers can share the same nodes' coordinates.

We modeled an SDN topology by a graph $G = (V, E)$ where V is the finite set of our switches or nodes and E is the set of links between them. Then, K is the number of controllers that must be placed in SDN and $K \leq |V|$.

A. End-to-End Delay

Eq. (1) shows the SDN total delay from source to destination [38] where $delay_{end\text{-}end}$ is an end-to-end delay, d_{proc} is the

processing delay at each router or controller, and d_{prop} is the propagation on each link. Also, d_{trans} is the total transmission rate of each switch to the controller that shows ds2c and the delay of transmission rate from each controller to another controller, shown by d_{c2c} in Eq. (2).

$$delay_{end\text{-}end} = d_{proc}+d_{trans}+d_{prop} \quad (1)$$

$$d_{trans} = d_{s2c} + d_{c2c} \quad (2)$$

The number of network nodes is denoted by N, and $d_{v,c}$ represents the shortest path from controller $c \in C$ to node $v \in V$. Eq. (3) shows the average propagation delay for a set of controllers C [13].

$$d_{avg}(C) = \frac{1}{N}\sum_{v\in V} \min_{c\in C} d_{v,c} \quad (3)$$

and the worst-case propagation latency for a set of controllers' C[13]:

$$d_{wc}(C) = \max_{v\in V} \min_{c\in C} d_{v,c} \quad (4)$$

B. Inter-Controller Propagation Latency

The average controller-to-controller latencies characterize the average latency between any pair of controllers in the network. The average of inter-controller latencies is calculated by Eq. (5) where $d(c1, c2)$ is the delay of c1 to c2:

$$d_{c2c} = \frac{1}{K.(K-1)} \sum_{c_i,c_j \in C} d(c1, c2) \quad (5)$$

C. Switch to controller propagation latency

We need to calculate the latency of switch-to-controller propagation, too. Eq. 6 shows the average latency of switch-to-controller in SDNs where $A_{s\,c}$ is the assignment of switch s to controller c.

$$d_{s2c} = \frac{1}{|V|}\sum_{s\in S}\sum_{c\in C} d(s,c)\ A_{s,c} \quad (6)$$

D. The Load of Controller

The traffic between SDN switches is unpredictable, and there are no known traffic patterns, but traffic load can be monitored during the runtime. The processing load of controllers often consists of three main parts: a load of rule installation in each controlled switch by c, the computational load of routing new arriving flows from the outside of SDN, and the computational load of routing new arriving flows from other SDN domains. B ($f_{o,\,Si}$) shows the computational load of routing newly arrived flows at switch (S_i) from the outside of SDN with a rate of $f_{o,\,Si}$.

B ($f_{Sj,Si}$) shows the computational load due to routing at the controller of Si for flows arriving at S_i from switch S_j controlled by another SDN controller with a rate of $f_{Sj,\,Si}$.

Calculating SDN controllers' load is critical to performing path computation and depends on the arrival rate of flows through function B. The objective of this study is not the definition of function B [39].

LR in Eq. (7) shows the computational load to rules installation for switch Si at the controller [36].

$$LR = \sum_{Sj\in S} F(f_{Si,sj})/bw_{ij} + F(f_{Si,o}) \quad (7)$$

It expresses the number of flows traversing Si going out of SDN or other switches. Function F maps the flow arrival rate at Si to the computational load at the SDN controller needed for rules installation. bw_{ij} is the bandwidth of link node i to node j. Pm denotes the set of assigned switches. The overall computational load at SDN controller (LT_c) is computed by Eq. (8) [36].

$$LT_c = \sum_{Si\in Pm\ ,Sj\in S} B(f_{0,Si}) + \sum_{Sj\notin Pm\ ,Si\in Pm} B(f_{Sj,Si})/bw_{ji} + \sum_{Si\in Pm\ ,Sj\in Pm} F(f_{Si,Sj})/bw_{ij} + \sum_{Si\in Pm} F(f_{Si,o}) \quad (8)$$

Eq. (9) shows the average load of all controllers in the entire network.

$$LT_{Avg} = \frac{1}{K} \sum_{c\in C} LT_c \quad (9)$$

IV. Proposed Method

The optimal locations of controllers change dynamically as the network load changes. Consequently, we must solve a dynamic optimization problem to find the optimal location of controllers in the network [25]. There are several switches in SDN that controllers must control. But, the problem is how switches are assigned to controllers that can provide the communication locality to decrease delay and increase load balancing at the controller level. For example, if switch No. 3 usually sends data to switch No. 8 to provide the locality of the communication, it is better that switches No. 3 and No. 8 are supported by the same controller. This research aims to find the best arrangement of switches with controllers to localize, reduce inter-controller and switch-to-controller latency, and balance the controllers' load.

The proposed method is based on SOA, which uses the seagull optimizer to find the proper location for the controllers. Firstly, the network is clustered by FCM, and then the optimal controller locations are determined in each cluster by SOA.

In the first step, the network is clustered by FCM [40]. FCM is a clustering method that allows each data point to belong to multiple clusters with varying degrees of membership. Previous research like [27] and [28] used K-means clustering to partition the network, but we use FCM because of its flexibility. This means that if a node is in one cluster in the clustering step, its cluster can be changed in the placement step, which is possible in FCM. To optimize the controller placement, SOA [14] is adopted in the next step.

After FCM clusters the network, the controllers' location in each cluster is determined using SOA. In defining the fitness function of SOA according to the research objectives, switch-to-controller latency, controller-to-controller latency, and controllers' load are considered.

A. Seagull Optimization Algorithm

We use the seagull optimizer to find the optimal place for controllers in each cluster [41]. SOA is a metaheuristic population-based algorithm that simulates seagulls' migration and attacking behaviors. Population-based metaheuristic algorithms share various advantages, including scalability, simplicity, and computational time reduction [32] .Also, population-based algorithms can find the global optimum [14]. SOA is superior to optimizers such as spotted hyena optimizer (SHO) [41], grey wolf optimizer (GWO) [42], particle swarm optimization (PSO) [43], moth-flame optimization (MFO) [44], and genetic algorithm (GA) [45] with better exploration and exploitation, less time complexity and faster execution time.

Seagulls are seabirds that are found all over the planet. Seagulls generally live in groups. They use their intelligence to find and attack their prey. They attract fish by baiting bread crumbs or earthworms. They make rain-like sounds with their feet to draw earthworms hidden beneath to the ground. The most important thing about seagulls is their migratory and aggressive behavior. Migration is defined as the seasonal movement of seabirds from one place to another to find a place with a better climate and more food resources [46].

Seagulls' behavior is illustrated as follows:

- Seagulls migrate in groups. During migration, they maintain their position to avoid colliding with each other.
- Seagulls can move towards the best seagull for survival in the group.
- Seagulls can update their initial positions based on the fittest of the seagull.

These birds often attack when they see migratory birds. They attack with a spiral shape. These behaviors can be formulated so that they can be optimized with the objective function. SOA focuses on two natural behaviors of seagulls: migration and attack.

1) Migration (exploration)

During migration, the algorithm simulates how a group of seagulls moves from one position to another. In this phase, a seagull should satisfy three conditions: 1. collision avoidance, 2. the movement direction, and 3. remaining close to the best seagull.

a) Collision avoidance:

With the help of variable *A*, the new Search Agent (SA) position is calculated, and collisions with neighbors are avoided in migration.

$$\overrightarrow{C_s} = A \times \vec{P}_s(x) \quad (10)$$

where $\overrightarrow{C_s}$ represents the position of the SA that does not collide with another SA, x indicates the current iteration, $\vec{P}s$ represents the current position of the SA, and *A* represents the movement behavior of the SA in a given search space that is calculated by Eq. (11) in the standard version of SOA.

$$A = f_c - (x \times \frac{f_c}{Max_{iteration}}) \quad (11)$$

where x=0, 1, 2, …., Max $_{iteration}$ and *A* is a variable that decreases linearly from f_c to 0, and f_c sets the frequency of using variable *A*.

b) Movement Direction:

The SAs move to the best neighbor while avoiding collisions between neighbors.

$$\overrightarrow{M_s} = B \times (\vec{P}_{bs}(x) - \vec{P}_s(x)) \quad (12)$$

where $\vec{M}s$ represents the positions of SA $\vec{P}s$ towards the best-fit SA $\vec{P}bs$ (i.e., fittest seagull), the variable *B* is deployed to make balancing between exploration and exploitation randomized. Eq. (13) states *B* calculation.

$$B=2\times A^2 \times rd \quad (13)$$

where *rd* is a random number in the range of [0, 1].

c) Remaining Close to the Best Seagull:

Finally, the SA can update its position concerning the best SA.

$$\overrightarrow{D_s} = |\vec{C}_s + \vec{M}_s| \quad (14)$$

The distance between the SA and the best agent is illustrated by $\vec{D}$s.

2) Attacking (Exploitation)

When seagulls attack prey, they perform a spiral movement. This behavior in the x, y, and z planes are defined. The new position of the SA is calculated using Eq. 15 to 18. In these equations, *r* is the radius of each spiral turn, *k* is a random number in the range of 0 to 2π, *u* and *v* are constants to define the spiral shape, and *e* is the base of the natural logarithm.

$$x' = r \times \cos(k) \quad (15)$$

$$y' = r \times \sin(k) \quad (16)$$

$$z' = r \times k \quad (17)$$

$$r = u \times e^{kv} \quad (18)$$

The best solution is stored in $\overrightarrow{P_s}(x)$, and the position of other SAs is updated based on it. In SOA, like most metaheuristic population-based algorithms, a random initial population is first created. SAs update their position according to the best SA in each iteration. *A* decreases linearly from *fc* to *0*. Variable *B* is responsible for the smooth transition between exploration and exploitation [14].

$$\vec{P}_s(x) = (\vec{D}_s \times x' \times y' \times z') + \vec{P}_{bs}(x) \quad (19)$$

The initial population of seagulls is vectors, along with the number of switches. For example, if the initial population is 20 seagulls and the number of switches is ten, the initial size of the matrix will be 20×10. Suppose that the algorithm's input

and the number of controllers for placement are "3". In that case, the initial population should be adjusted so that only three elements to locate the controller in each vector are selected. Element number may be "1" or "0". "1" shows that this place is selected as controller placement, and other places equal "0". So, in the initial population vector, three elements will be equal to "1", and seven elements will be equal to "0". Fig. 2 shows an example of three seagulls.

The basic idea of the SOA in this study is to satisfy the controller plane's load balance, minimize the inter-controller, and switch to controller distances and latency. So, the fitness function is modeled as follows:

$$\text{Min fit}(d_{trans}, LT_{Avg}) \quad (20)$$

where *fit* is a non-linear function of deployed controllers and d_{trans} is the total transmission rate out of each switch to the controller and the delay of transmission rate out of each controller to another controller calculated by Eq. (2). LT_{Avg} is the average load of controllers calculated by Eq. (9). The fitness function aims to minimize these parameters.

Seagull 1	0	0	0	1	0	0	1	0	1	0
Seagull 2	0	0	1	1	1	0	0	0	0	0
Seagull 3	0	0	0	0	0	0	1	0	1	1

Fig.2. An example of three seagulls

V. Performance Evaluation

A simulation environment is performed for the proposed method's performance testing. We compare our proposed method (SOA) with the state-of-the-art metaheuristic algorithms like Cuckoo Search Algorithm (CSA) [31], SSA [32] , and PSO [29] on the Internet topology zoo (ITZ) dataset [47].

Fig. 3 Myren and Cogent network topologies [36]

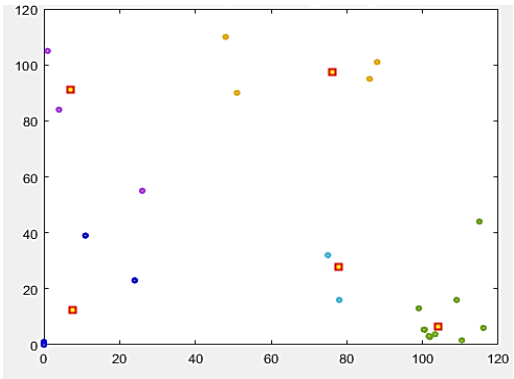

Fig. 4. The controller placement in the Myren topology

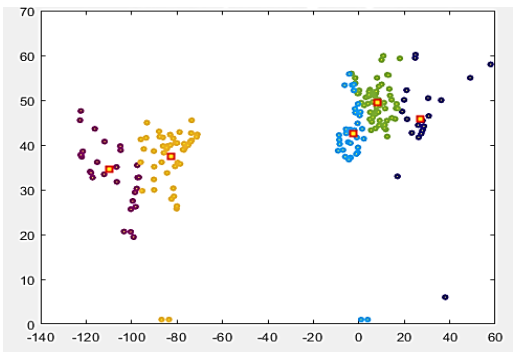

Fig. 5. The controller placement in the Cogent topology

A.Simulation Setup

The proposed method is evaluated using MATLAB 2018b over a machine equipped with an Intel Core i3 processor and 8 GB RAM. As shown in Fig. 3, the Myren and Cogent topologies from the ITZ dataset [47] are selected as small and large network topologies. The detail of these topologies is shown in Table I. Table II shows the simulation parameters. The initial number of populations in algorithms is set to 200, the iteration count is 50, and the algorithms run for ten rounds. Figs. 4 and 5 depict five controllers' placement and node assignment obtained by the proposed method. In these figures, color stars show the switches, and red squares show the controller locations.

TABLE 1.
DETAILS OF THE SOFTWARE-DEFINED NETWORKS

	Network	Type	Geo extent	Geolocation	Layer	No. switch	No. links
1	Myren	REN	Country	Malaysia	IP	36	39
2	Cogent	COM	Country+	USA, Europe	IP	197	212

TABLE 2.
THE SIMULATION PARAMETERS

Parameter/ constants	value
Initial population	200
Run time	10 rounds
Traffic	Random (0,250)
Iteration	50
PSO	$c_1 = 2.0$, $c_2 = 2.0$, w(0.9→0.4)

A. End-to-End Delay

In this section, the end-to-end delay is evaluated based on the number of packages sent. As can be seen in Figs. 6 and 7, the proposed method differs significantly from the other two algorithms in terms of the end-to-end delay. The proposed method, in most cases, has less latency than the other three methods and has made a significant improvement in reducing latency. This is because of considering the controller-to-controller and switch-to-controller latencies in the fitness function and the flexibility of FCM to handle the nodes to select the appropriate cluster.

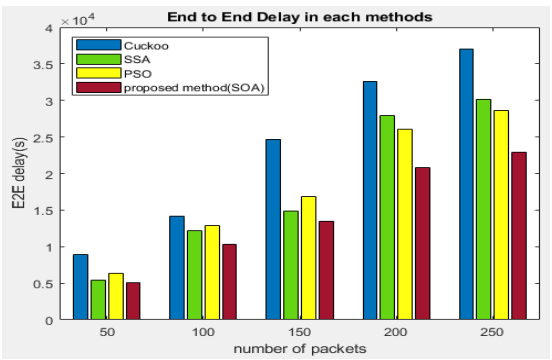

Fig. 6. End-to-end delay in Myren

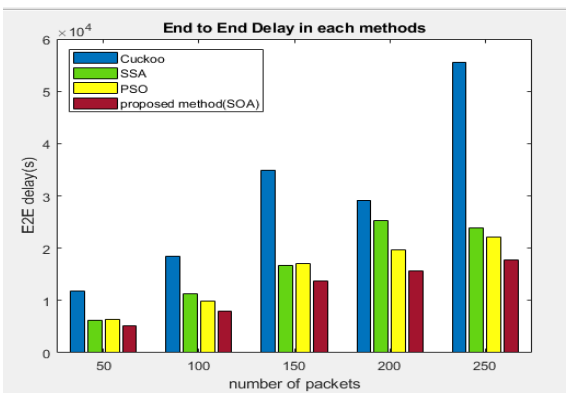

Fig. 7**.** End-to-end delay in Cogent

B. Load Balancing

The controllers' load is evaluated to evaluate the network load balance. For this purpose, the maximum load of the controllers and the total load of the controllers over time are investigated. Figs. (8) and (9) show the maximum load of controllers in Myren and Cogent topologies in 10 rounds, respectively. Figs. (10) and (11) display the summation of controllers load in Myren and Cogent topologies in 10 rounds. Cuckoo and SSA have the highest loads among evaluated methods, but the proposed method has good performance in this parameter, and it has a better load balance and proper load distribution on the controllers than other methods.

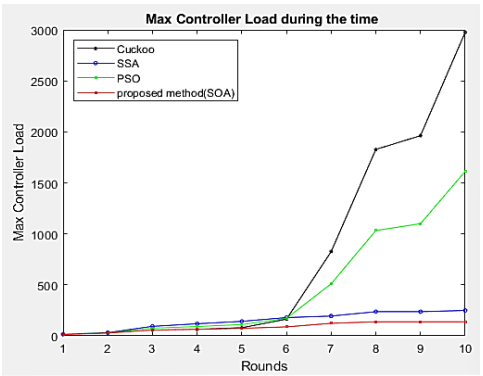

Fig. 8. The maximum controller load in Myren topology

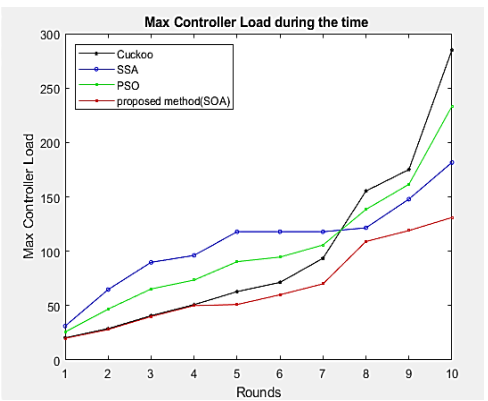

Fig. 9**.** The maximum controller load in Cogent topology

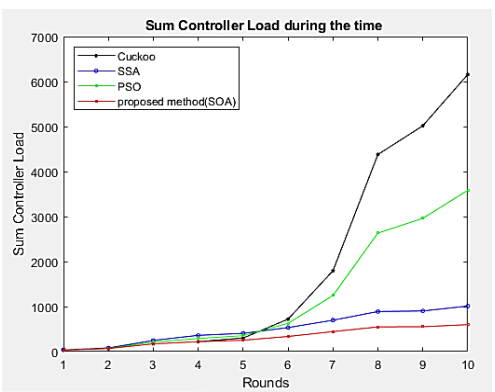

Fig. 10**.** The sum of the controller loads in Myren topology

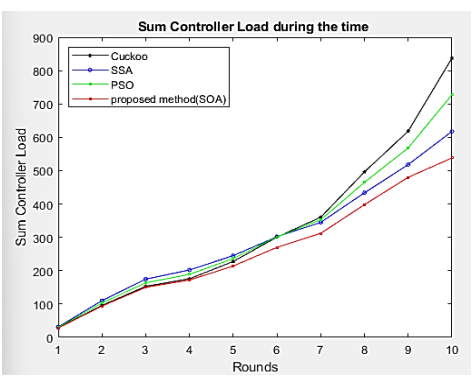

Fig. 11. The sum of the controller loads in Cogent topology

REFERENCES

[1] D. Kreutz, F. Ramos, P. E. Veríssimo, C. E. Rothenberg, S. Azodolmolky, and S. Uhlig, Proc. IEEE., vol. 103, no. 1, 2015.

[2] Masdari, M., Sangar, A. B., & Majidzadeh, K., "A Hybrid Multi-objective Algorithm for Imbalanced Controller Placement in Software-Defined Networks.," Journal of Network and Systems Management, vol. 30, no. 3, pp. 1-54, 2022.

[3] Jafarian, T., Masdari, M., Ghaffari, A., & Majidzadeh, K. , "Security anomaly detection in software-defined networking based on a prediction technique," International Journal of Communication Systems, vol. 33, no. 14, 2020.

[4] Jafarian, T., Masdari, M., Ghaffari, A., & Majidzadeh, K., "SADM-SDNC: security anomaly detection and mitigation in software-defined networking using C-support vector classification," Computing, vol. 103, no. 4, pp. 641-673, 2021.

[5] J. Liu, Z. Jiang, N. Kato, O. Akashi, and A. Takahara, "Reliability evaluation for NFV deployment of future mobile broadband networks," IEEE Wireless Commun., vol. 23, no. 3, pp. 90-96, 2016.

[6] JIE LU , ZHEN ZHANG, TAO HU , PENG YI, AND JULONG LAN, "A Survey of Controller Placement Problem in Software-Defined Networking," IEEE Access, vol. 7, pp. 24290-24307, 2019.

[7] tohid jafarian, Mohammad Masdari, ali ghaffari, kambiz majidzadeh, "A Survey and Classification of the Security Anomaly Detection Mechanisms in Software Defined Networks," Cluster Computing, vol. 24, p. 1235–1253 , 2021.

[8] Yuqi Fan, Lunfei Wang, Xiaohui Yuan, "Controller placements for latency minimization of both primary and backup paths in SDNs," Computer Communications, vol. 163, pp. 35-50, 2020.

[9] Jafarian, T., Masdari, M., Ghaffari, A., & Majidzadeh, K. , "Security anomaly detection in software-defined networking based on a prediction technique. ," International Journal of Communication Systems, vol. 33, no. 14, 2020.

[10] Manoharan, G. Ramya · R., "Enhanced optimal placements of multi-controllers in SDN," Journal of Ambient Intelligence and Humanized Computing, 2020.

[11] EL Hocine Bouzidi, Abdelkader Outtagarts, Rami Langar, Raouf Boutaba, "Dynamic clustering of software defined network switches and controller," Computer Networks, vol. 207, 2022.

[12] Beheshte Sadeghi Sabzevari, Mohammad Haddad Zarif, and Seyed Kamal Hosseini Sani, "Event-Triggered Predictive Networked Control Systems with Network Imperfections and External Disturbance," International Journal of Industrial Electronics, Control and Optimization, vol. 5, no. 1, pp. 11-22, 2022.

[13] B. Heller, R. Sherwood, N. McKeown,, "The controller placement problem,," in Proceedings of the First Workshop on Hot Topics in Software Defined Networks, in: HotSDN '12, ACM, , New York, NY, USA, 2012.

[14] Gaurav Dhiman, Vijay Kumar, "Seagull optimization algorithm: Theory and its applications for large-scale industrial engineering problems," Knowledge-Based Systems, vol. 165, pp. 169-196, 2019.

[15] Hassan Ghaedi; Seyed Reza Kamel Tabbakh Farizani; Reza Gaemi, "A Novel Meta-heuristic Framework for Solving Power Theft Detection Problem: Cheetah Optimization Algorithm," International Journal of Industrial Electronics, Control and Optimization , vol. 5, no. 1, pp. 63-76, 2022.

[16] Muhammad Fahad, Farhan Aadil , Zahoor-ur- Rehman, Salabat Khan , PeerAzmat Shah , Khan Muhammad , Jaime Lloret , Haox, "Grey wolf optimization based clustering algorithm for vehicular ad-hoc networks," Computers and Electrical Engineering, pp. 1-18, 2018.

[17] Saman M. Almufti, Ridwan B. Marqas, Pawan Sh. Othman, Amira Bibo Sallow, "Single-based and Population-based Metaheuristics for Solving NP-hard problems," Iraqi Journal of Science, vol. 62, no. 5, pp. 1710-1720, 2021.

[18] B. Heller, R. Sherwood, N. McKeown,, "The controller placement problem," in in: Proceedings of the First Workshop on Hot Topics in Software Defined Networks, in: HotSDN ', ACM, New York, NY, USA, 2012.

[19] K.S. Sahoo, S. Sahoo , A. Sarkar , B. Sahoo , R. Dash, "On the placement of controllers for designing a wide area software defined networks," in Proc. IEEE Region 10 Conference (TENCON), 2017.

[20] T. Zhang , A. Bianco , P. Giaccone, " The role of inter-controller traffic in sdn controllers placement," in Proc. IEEE Conference on Network Function Virtualization and Software Defined Networks (NFV-SDN), pp. 87–92 , 2016 .

[21] T. Zhang , P. Giaccone , A. Bianco , S.D. Domenico, "The role of the inter-controller consensus in the placement of distributed sdn controllers," Comput. Commun. , vol. 113, no. Supplement C, pp. 1-13, 2017.

[22] A. Dixit, F. Hao, S. Mukherjee, T.V. Lakshman, R.R. Kompella,, "ElastiCon: An Elastic Distributed SDN Controller," IEEE Comp Soc Tech Comm Comp Architecture, pp. 17-24, 2014.

[23] Ze Yang , Kwan L. Yeung, "MinimumWeight Controller Tree Design in SDN," Computer Networks, 2019.

[24] Dorabella Santos; Teresa Gomes; David Tipper, "SDN Controller Placement With Availability Upgrade Under Delay and Geodiversity Constraints," IEEE Transactions on Network and Service Management , pp. 301 - 314, 2021.

[25] V. Ahmadi, M. Khorramizadeh ,, "An adaptive heuristic for multi-objective controller placement in software-defined networks," Comput. Electr. Eng., vol. 66, pp. 204-228, 2018.

[26] Soufian Toufga, Slim Abdellatif , Hamza Tarik Assouane, Philippe Owezarski, Thierry Villemur, "Towards Dynamic Controller Placement in Software Defined Vehicular Networks," Sensor, vol. 20, 2020.

[27] Hailan Kuang; Yiwen Qiu; Ruifang Li; Xinhua Liu, "A Hierarchical K-Means Algorithm for Controller Placement in SDN-Based WAN Architecture," in 2018 10th International Conference on Measuring Technology and Mechatronics Automation (ICMTMA), Changsha,

China, 2018.

[28] Guodong Wang; Yanxiao Zhao; Jun Huang; Qiang Duan; Jun Li, "A K-means-based network partition algorithm for controller placement in software defined network," in 2016 IEEE International Conference on Communications (ICC), Kuala Lumpur, Malaysia, 2016.

[29] C. Gao, H. Wang , F. Zhu , L. Zhai , S. Yi, "A particle swarm optimization algorithm for controller placement problem in software defined network,," Cham, Springer International Publishing, p. 44–54, 2015.

[30] S. Liu, H. Wang , S. Yi , F. Zhu ,, "Ncpso: a solution of the controller placement problem in software defined networks,," in G. Wang, A. Zomaya, G. Martinez K. Li (Eds.), Algorithms and Architectures for Parallel Processing,, Cham, Springer International Publishing, Cham, pp. 213–225, 2015.

[31] X. X. Feixiang Li, "A Discrete Cuckoo Search Algorithm for the Controller Placement Problem in Software Defined Networks 2018 IEEE 9th Annual Information Technology,," in Electronics and Mobile Communication Conference (IEMCON), Vancouver, BC, Canada, 2018.

[32] Abdelhamied A. Ateya , Ammar Muthanna , Anastasia Vybornova , Abeer D. Algarni, "Chaotic salp swarm algorithm for SDN multi-controller networks," Engineering Science and Technology, an International Journal, vol. 22, pp. 1001-1012, 2019.

[33] G. Schütz, J.A. Martins , "A comprehensive approach for optimizing controller placement in Software-Defined Networks," Computer Communications, vol. 159, pp. 198-205, 2020.

[34] Nasrin Firouz, Mohammad Masdari, Amin Babazadeh Sangar, Kambiz Majidzadeh, "A novel controller placement algorithm based on network portioning concept and a hybrid discrete optimization algorithm for multicontroller software-defined networks," Cluster Computing, 2021.

[35] Abeer A. Z. Ibrahim; Fazirulhisyam Hashim; Aduwati Sali; Nor K. Noordin; Saber M. E. Fa, "A Multi-Objective Routing Mechanism for Energy Management Optimization in SDN Multi-Control Architecture," IEEE Access, vol. 10, pp. 20312 - 20327, 2022.

[36] Xin Cui, Xiaohui Gao, Yan Ma, "An Optimized Controller Placement Algorithm in 5G Based on SDN," in 2020 International Wireless Communications and Mobile Computing (IWCMC), Limassol, Cyprus, 2020.

[37] Neamah S. Radam , Sufyan T. Faraj Al-Janabi and Khalid Sh. Jasim, "Multi-Controllers Placement Optimization in SDN by the Hybrid HSA-PSO Algorithm," Computers , vol. 11, no. 7, 2022.

[38] James F. Kurose, Keith W. Ross, in COMPUTER NETWORKING A Top-Down Approach, 8th ed., Pearson, , pp. 35-46, 2021.

[39] Marco Cello; Yang Xu; Anwar Walid; Gordon Wilfong; H. Jonathan Chao; Mario Marchese, "BalCon: A Distributed Elastic SDN Control via Efficient Switch Migration," in IEEE International Conference on Cloud Engineering (IC2E), Vancouver, BC, Canada, 2017 .

[40] J.C. Bezdek, R. Ehrlich, W. Full, "FCM: the fuzzy c-means clustering algorithm," Comput Geosci, vol. 10, no. 2, pp. 191-203, 1984.

[41] Gaurav Dhiman, Vijay Kumar, "Spotted hyena optimizer for solving complex and non-linear constrained engineering problems Harmony Search and Nature Inspired Optimization Algorithms," Springer, pp. 857-867, 2019.

[42] Seyedali Mirjalili, Seyed Mohammad Mirjalili, Andrew Lewis, "Grey wolf optimizer," Adv. Eng. Softw. , vol. 69, pp. 46-61, 2014.

[43] James Kennedy, Russell C. Eberhart,, "Particle swarm optimization," in Proceedings of IEEE International Conference on Neural Networks, pp. 1942–1948., 1995.

[44] Seyedali Mirjalili, "Moth-flame optimization algorithm: A novel natureinspired heuristic paradigm," Knowl.-Based Syst. , vol. 89, p. 228–249, 2015.

[45] Eric Bonabeau, Marco Dorigo, Guy Theraulaz, , "Swarm Intelligence: From Natural to Artificial Systems," in Oxford University Press, Inc., New York, NY, USA, , 1999.

[46] Choi, C. and J.-J. Lee, "Chaotic local search algorithm," Artificial Life and Robotics, vol. 2, no. 1, pp. 41-47, 1998.

[47] "Internet Topology Zoo," the University of Adelaide, [Online]. Available: http://www.topology-zoo.org/index.html. [Accessed 5 March 2022].

Maedeh Abedini Bagha received the B.Sc. degree in computer engineering software from Islamic Azad University, Zahedan, Iran, in 2007 and M.Sc. degree in computer engineering software from the Science and Research Branch of Islamic Azad University, Tabriz, Iran, in 2013. She is currently a Ph.D. candidate in computer software at the Islamic Azad University, Urmia Branch. Her research interests are in Distributed Systems, Optimization, and Metaheuristic algorithms.

Kambiz majidzadeh was born in Urmia, Iran, in 1980. He received the B.Sc. degree in software engineering from the Islamic Azad University of Khoy, Khoy, Iran, in 2002, and the M.Sc. degree in computer networking and the Ph.D. degree in information technology from Baku State University (BSU), Baku, Azerbayijan in 2005 and 2009, respectively. His research interests are very large-scale integration design and computer networking.

Mohammad Masdari received his B.Tech. degree in Computer Software Engineering from Islamic Azad University, Qazvin Branch, Iran, in 2001, and M.Tech degree in Computer Software Engineering from Islamic Azad University, South Tehran Branch, Tehran, Iran, in 2003. He received his Ph.D. degree in Computer Software Engineering from Islamic Azad University, Science and Research Branch, Tehran, Iran, in 2014. Since 2003, he worked as a faculty member of Islamic Azad University, Urmia Branch, Iran. Presently he is an Assistant Professor in the Department of Computer Engineering of Islamic Azad University, Urmia Branch, Iran. His research interests include Distributed Systems and Network Security.

Yousef Farhang was born Khoy, Iran, in 1978. He received the B.S. degree in software engineering in 2001 from Islamic Azad University, Khoy, Iran, and his M.S. degree in software engineering in 2005 from Islamic Azad University, Arak, Iran. He received the Ph.D. degree in computer science in 2016 in Universiti Teknologi Malaysia (UTM). He was with Islamic Azad University, Khoy branch, as a researcher and lecturer from 2003 to now. His research interests include data mining, clustering algorithm, image clustering and machine learning algorithms.

International Journal Of
Industrial Electronics Control and Optimization
Print ISSN: 3517-2645
Online ISSN: 3568-2645
Homepage: https://ieco.usb.ac.ir/

An Improved Linear Switched Reluctance Motor for Elevator Application

Allahverdi Azadrou[1] | Siamak Masoudi[2] | Shahla Gharaati[3]

Department of Electrical Engineering, Islamic Azad University, Salmas Branch, Salmas, Iran. [1]
Department of Electrical Engineering, Islamic Azad University, Abhar Branch, Abhar, Iran. [2]
Administration of education, Salmas, Iran. [3]
Corresponding author's email: Masoudi.elec@gmail.com

Article Info

Article type:
Research Article
Article history:
Received: 05 July 2022
Revised: 04 Oct 2022
Accepted: 15 Oct 2022
Published online: 21 Nov 2022
Keywords:
Linear motor,
Motor Design,
Switched reluctance motor

ABSTRACT

This work deals with minimizing fluctuations of propulsion force and improving the motion quality in a linear switched reluctance motor. In order to minimize the jerks in the moving part of the motor, a new profile is used to generate an appropriate reference speed profile. Then, a simple fuzzy logic system which is able to overcome the uncertainties problem in nonlinear systems is designed and applied to the motor. The fuzzy control system can regulate the motor performance so that it tracks the reference speed with minimum error and fluctuation. The system is designed and its efficiency is shown through simulation and experimental tests in different performance situations. The obtained results confirm that the proposed strategy outperforms other conventional methods.

I. Introduction

Linear electrical motors are efficient and useful instruments in industrial applications with direct motion. Using these motors, rotary to linear motion mechanical converters are eliminated resulting in a simpler, cheaper, and more robust system. Linear switched reluctance motors (LSRMs) have several advantages that distinguish them from other types of electrical motors [1]. LSRMs have only one set of coils on the stator or translator, while the other side has no winding or PM. This feature is especially important in applications that involve a long movement path such as electric trains and elevators in tall buildings. Different LSRMs have been presented which can be used in various applications [1] and [2]. The standard design of LSRMs is done based on the design of corresponding rotary motors [1]. Review of different topologies of linear switched reluctance motor has been done in [3]. Reference [4] reviewed different topologies of LSRMs suitable for vertical motion applications, and finally a structure was selected which has been used in later studies [5] – [9]. The structure selected in the mentioned articles is a good choice for elevator application, though it needs massive iron to be placed for the entire movement path in tall buildings. In [10], a linear switched reluctance motor with additional permanent magnets has been examined in a railway system. The motor tempuratur studies has been done in [11]. The presented motor can create high force dencity, but PMs increase the total cost significantly. Use of more teeth at poles has a good effect on LSRM performance and the propulsion force quality. Two of these structures have been presented in [12] and [13]. The LSRM studied in [13] consisted of a modular toothed linear hybrid reluctance motor with permanent magnets in tranbslator slots. Details of the motor has been explained in [14]. All mentioned single-sided topologies in [10] – [14] were efficient in horizontal movement, but they were not good candidates in vertical motion applications such as elevator systems. Iron loss analysis and flux characteristics of a LSRM have been discussed in [15] and [16]. End-effects of a LSRM were explored in [17] based on mathematical and finite element analysis. A double-sided segmental stator LSRM with a high force density was presented in [18] which can be an appropriate choice for railway applications. A modular-stator LSRM with an active translator was presented in [19], which would produce a good average force though requiring

DOI: 10.22111/IECO.2022.42777.1437

extensive iron to be placed along the entire path in elevator application. In [20], a double-sided yokeless multi-tooth LSRM was proposed consisting of PMs in translator poles. It show a very good performance in terms of force ripple and cogging force. Analysis, design, and optimization of toroidally wound mover LSRM with segmental stator were done in [21] and [22]. A double-sided linear switched reluctance motor with two translators in a common stator was used in elevator application in [23] where the presented system indicated high average force with low ripple. In [24], seeker optimization algorithm was employed to achieve the least force ripple with maximum average force. Influence of design parameters and dimensions in the optimization of LSRM under thermal and weight constraints was discussed in [25]. In order to have a price electromagnetic model of a switched reluctance motor, it is very useful to analyze the flux, inductance, and force characteristics. These were done for two different LSRMs in [26] and [27]. In [28], the magnetic equivalent circuit of the LSRM was utilized to examine the performance of LSRM under asymmetric air-gap. This work presents the design and optimization of a double-sided linear switched reluctance motor with segmented stator and yokeless translator. In order to widen the positive force region, non-uniform air-gap has been designed and optimized. The proposed LSRM offers the advantages of the high force to mass ratio and low total cost. The influence of non-uniform air-gap dimension on the inductance and force characteristics of the motor is investigated and optimized via non-dominated sorting genetic algorithm to offer the maximum average force with minimum ripple. Finite element analysis of the proposed system has been done, and the results have been compared with a conventional LSRM.

II. Selected Structure Of LSRM

A. Elevator application

Fig. 1 displays the schematic view of the proposed LSRM. The motor has a twin opposing segmented stator with a yokeless translator as a motion guide in the path. The stator has eight concentric windings wound around the yoke of phases that are separated mechanically together. The LSRM shown in Fig. 1 has some advantages making it a good candidate for elevator application. In this motor, two phases are fed simultaneously, thus a high-power density is produced. The stator is made segmental and there is almost no mutual inductance between the phases. Hence, in addition to reducing the weight of the moving part, the losses are also reduced. Further, the translator has no yoke, which is very important economically in tall buildings and occupies less space.

B. The main idea

In the elevator application, the force produced by phases is always upward. In ascending motion, this force acts as a propulsion power while in descending motion it prevents the moving part from falling. According to (1), the phase force has a direct relationship with derivative of the inductance. In a conventional structure, a phase inductance is symmetrical in a pole pitch. In an elevator, the phase force generated in the inductance increasing zone ($dL/dx > 0$) is used for both ascent and descent. In this work, by changing the pole shape and the air-gap, the inductance curve becomes asymmetric whereby the inductance ascent side is greater than the other side's. This has two major advantages:

- Positive force is generated in a wider area, so the average force increases.
- Air-gap changes continuously, which is effective in the force ripple reduction.

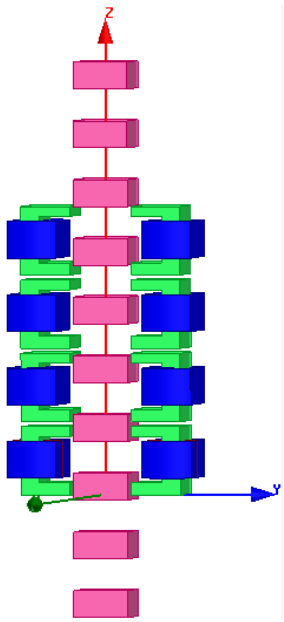

Fig. 1. 3-D FEA model of the proposed LSRM.

The proposed structure and the phase inductance curve are shown in Fig. 2. In a conventional structure, the phase inductance grows and then remains constant in its maximum value, while in the proposed structure, the inductance has a small constant zone with a large positive slope region.

C. Propulsion Force Generation

In the LSRM, the generated phase force in Z-axis direction can be written as [21]:

$$f_z = \frac{1}{2} i^2 \frac{dL}{dz} \quad (1)$$

where, L is the phase inductance and i represents the phase winding current. The average force from unaligned position z_2 to aligned position z_1 is written as:

$$f_{av} = \frac{\int_{z_1}^{z_2} f_z dz}{z_2 - z_1} = \frac{W'_{z=z_1} - W'_{z=z_2}}{dz} = \frac{W'_t}{z_2 - z_1} \quad (2)$$

where, W'_z and W'_t denote the co-energy at position z and total co-energy from aligned to unaligned position, respectively. Neglecting the energy in the core, we can write the co-energy at the aligned position as:

$$W'_{z_1} = \oint_V \frac{B_g^2}{2\mu_0} dV = \oint_V \frac{(\mu_0 H_g)^2}{2\mu_0} dV =$$
$$\int_0^L \int_0^g \int_0^{w_{sp}} B_g^2(x,y,z)dxdydz = \frac{\mu_0 H_g^2}{2} g L w_{sp}. 2\beta_s\gamma \quad (3)$$

where, β_s denotes the ratio of stator pole width to stator pitch, while γ indicates the ratio of translator pole width to stator pole width. In this work, d is assumed to be equal or larger than the stator pole width. This causes the overlap of the poles at aligned position to be approximately same as the conventional structure. Thus, the magnetic resistance at the aligned position will remain almost unchanged.

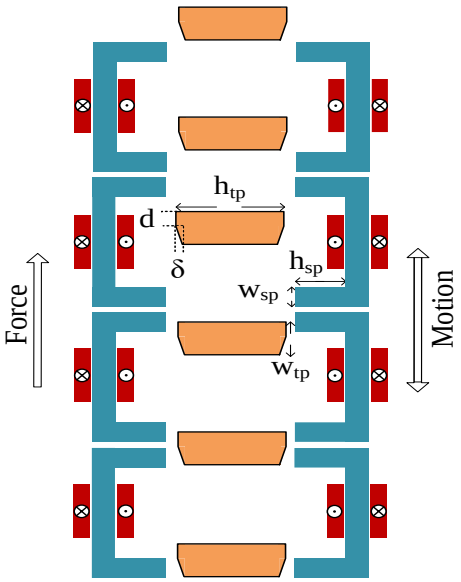

a

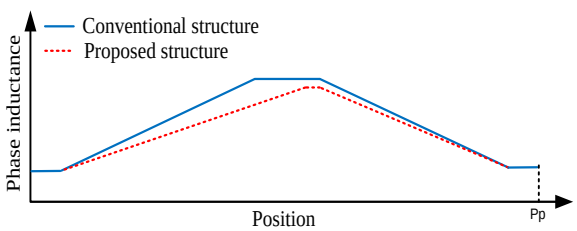

b

Fig. 2. (a) 2-D model of the proposed LSRM with non-uniform air-gap, (b) Ideal inductance curves.

D. Propulsion Structural Reforms

In order to improve the structure of the LSRM for elevator application, translator poles in Fig. 3-a were changed to a new shape as Fig. 3-b. The results indicated that this change is effective in enhancing the average force and reducing the ripple of force. A new problem is that, in the new structure there is a negative force agree with the earth's gravity in the unaligned position which is due to the asymmetry of the rotor poles. To solve this problem, a pole-shoe was added to the up side of the stator poles as Fig. 3-c. Inductance and force profiles for a phase are depicted in Fig. 4 for three structures. These profiles have been curved based on finite element analysis and the optimized dimensions.

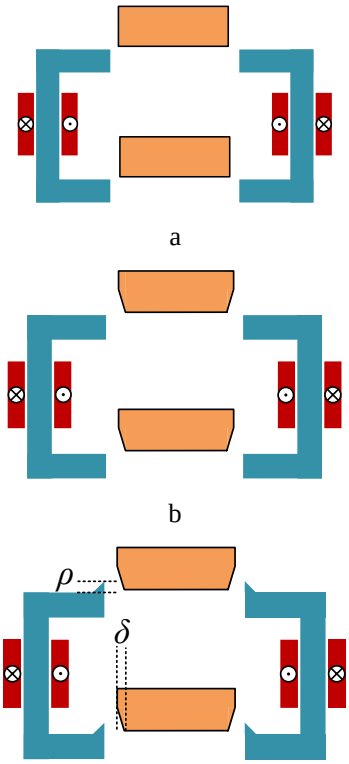

a

b

c

Fig. 3. (a) initial structure- Type 1, (b) translator pole change- Type 2, (c) proposed structure- Type 3.

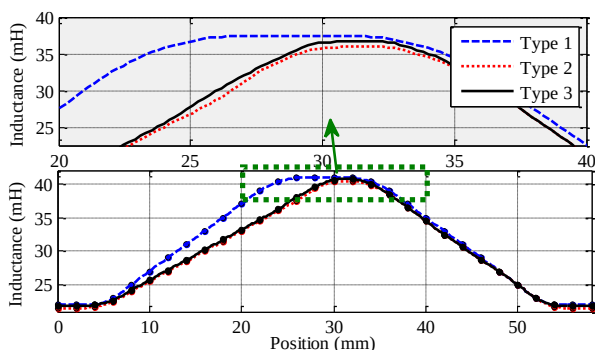

a

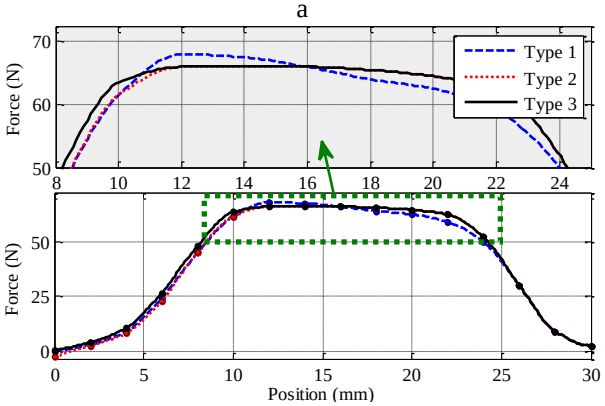

b

Fig. 4. (a) Inductance profile, (b) Phase force profile.

III. Optimization Of The Structure

A. Multi-Objective Optimization Problem

Multi-objective optimization problem (MOOP) deals with a *K*-dimensional decision space of objective function $\underline{U}(\underline{X}) = \{U_1(\underline{X}), U_2(\underline{X}), \dots, U_q(\underline{X})\}$ based on decision vectors $\underline{X}$. This method includes a set of non-dominated solutions instead of a single optimal method. Minimization of the objective functions leads to a minimum MOOP.

$$Minimize\ \ \underline{U}(\underline{X}) = \{U_1(\underline{X}), U_2(\underline{X}), \dots, U_q(\underline{X})\} \qquad (4)$$

where $\underline{X} = [\underline{X}_1, \underline{X}_2, \dots, \underline{X}_K] \in R^K$ denotes a state in the *K*-dimensional decision space (R^k), and $\underline{U} = [U_1, U_2, \dots, U_q] \in \Omega^q$ is the objective space with q minimization objectives. In this work, the average force, propulsion force ripple, and total mass of the motor have been selected as objective functions [24].

B. Objective Functions

Determining an appropriate objective function is the first step in an optimization problem. Linear switched reluctance motors have inherently high force ripple which limits their applications in various industries. Initially, dimensions of the LSRM should be optimized so that it generates a high average force (F_{av}) with minimal ripple (*RF*) which is defined as ratio of the ripple to the average force in percent. Also, the total mass of the motor (*M*) is another important factor. Accordingly, three objective functions can be determined as follows:

$$u_1(\underline{x}) = \frac{1}{F_{av}} \qquad (5)$$

$$u_2(\underline{x}) = RF \qquad (6)$$

$$u_3(\underline{x}) = M \qquad (7)$$

where, *x* denotes a vector including all dimension variables that may be adjusted to optimize the objective functions. Given some structural limitations, the parameters denoted in Fig. 2-a have been considered as optimization dimensions. The air-gap is considered constant 2 mm in the work. Hence, the adjustable parameters vector can be written as:

$$\underline{x} = (w_{sp}, w_{tp}, h_{sp}, h_{tp}, \delta, d, \rho) \qquad (8)$$

C. Multi-Objective Optimization

Dimensions of the LSRM denoted as x vector are changed and functions (5) – (7) are calculated at each step. The process continues until the function (9) reaches its minimum value.

$$f = min\ \{u_1, u_2, u_3\} \qquad (9)$$

In this work, the non-dominated sorting genetic algorithm (NSGA II) presented in [29] has been employed to solve the optimization problem. In this algorithm, the objective functions are calculated and the initial populations are sorted based on non-domination into each front. In the second step, crossover and mutation are performed. Identification of non-dominated individuals from the first front population occurs in the third step which is the ranking step. The non-dominated set of solutions creates the first front solution whose individuals dominate the second front individuals. Thus, the front continues and all the fronts are determined. In each font, the sort values are described by individuals with specified crowding distance. By knowing the sort values and crowding distance, all of the first solutions or individuals are selected based on competition selection. The offspring population is developed from crossover and mutation operators. The best K individuals are chosen and the populations including the current population and offspring populations are ranked based on non-domination. The process continues until the stopping conditions are met. In the proposed optimization algorithm, population size, crossover probability, mutation probability, and maximum gen are 25.4, 0.8, 0.01, and 100 respectively, while the process has 100 independent runs.

IV. Simulation Results

The LSRM displaced in Fig. 3 – c was optimized through the genetic algorithm mentioned in the previous section. Some parameters which are constant are reported in TABLE 1.

TABLE 1
CONSTANT PARAMETERS OF THE LSRM

Parameter	value
air-gap length	2 mm
turns in each coil	240 turns
rated voltage	150 v
rated current	12 A
friction coefficient	25 N/m/s
phase resistance	2.8 Ω

For better and more accurate conclusions, both Type 1 and Type 3 LSRMs were optimized whereby the values indicated in TABLE 2 were obtained.

TABLE 2
OPTIMIZED PARAMETERS OF THE LSRM

Parameter	Initial	Optimized Type 1	Optimized Type 3
w_{sp}	14 mm	15 mm	15.5 mm
w_{tp}	28 mm	34 mm	33 mm
h_{sp}	30 mm	32 mm	31 mm
h_{tp}	36 mm	34 mm	30 mm
d	14 mm	---	15 mm
δ	4 mm	---	3 mm
ρ	3 mm	---	3.5 mm

Finite element analysis of three types LSRMs was performed through Maxwell 16. In the analysis, the stator is moved by 1-mm steps along a pole pitch, where the phase force as well as inductance is recorded at each point. The data obtained have been plotted in Fig. 4 using the curve fitting algorithm. The results in three aligned, mid-aligned, and un-aligned positions for three structures are presented in Fig. 5.

Fig. 6 compares the average force and the ripple of the propulsion force at nominal current. It can be observed that the proposed structure has a higher average value. In order to achieve a complete comparison, the average force and the ripple for different phase currents are indicated in TABLE III. In the table, Fav denotes the average force and RF indicates the ration ripple to the average force in percent. It can be seen that the proposed structure has fewer force ripples due to the gradual reduction of the air-gap length. Further, the average force in the proposed structure is higher which is due to the wider phase force.

TABLE 3
OPTIMIZED PARAMETERS OF THE LSRM

Phase current		**3 A**	**6 A**	**9 A**	**12 A**
Type 1	$F_{av}(N)$	22	48	94	152
	RF (%)	5.2	6.5	7.1	7.2
Type 2	$F_{av}(N)$	28	53	99	159
	RF (%)	4.6	5.8	6.3	6.3
Type 3	$F_{av}(N)$	31	56	104	163
	RF (%)	3.4	3.6	4.1	4.1

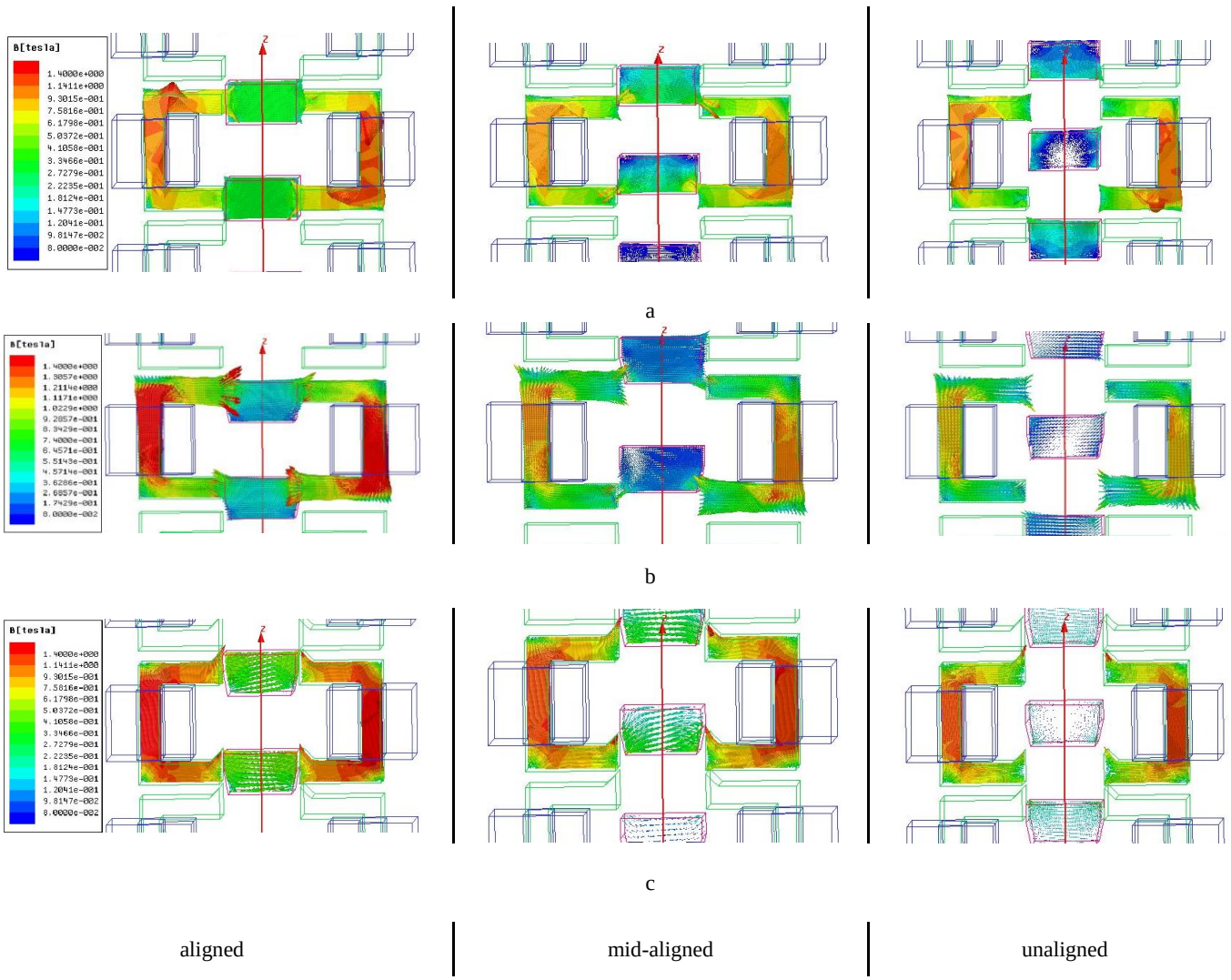

Fig. 5. Finite element analysis of three structures, (a) Type 1, (b) Type 2, (c) Type 3

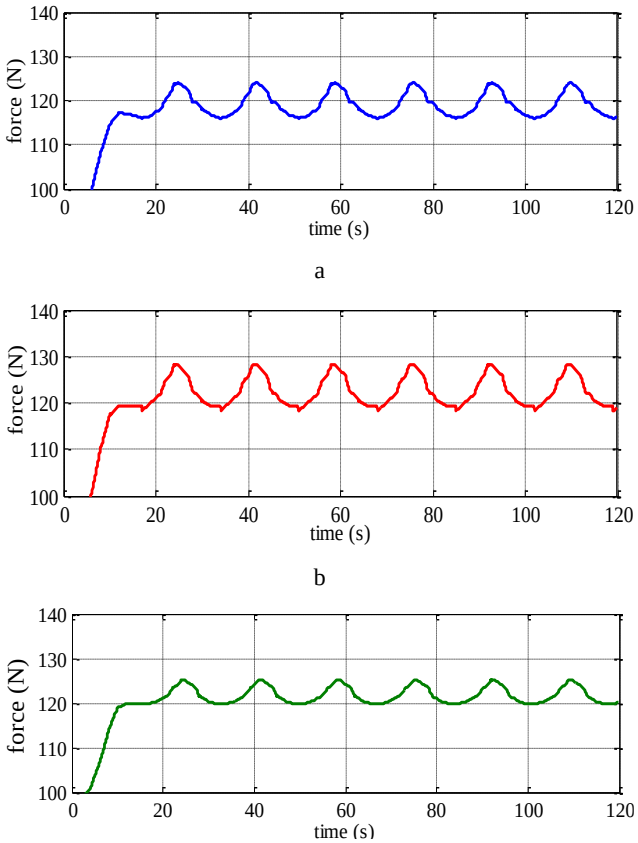

Fig. 6. Propulsion force at i=10 A, (a) Type 1, (b) Type 2, (c) Type 3.

V. Experimental results

To demonstrate the performance of the proposed structure, both type 1 and type 3 structures with the dimensions expressed in Tables I and II were constructed and compared experimentally. Both the stator and translator cores are made of silicon steel sheets. All poles need careful installation because of the poles of the stator and translator are separated individually due to no back iron. Thus, poles of both stator and translator are mounted on aluminum frames with a fixed distance of 2 mm as the initial air gap. A spacer is installed to ensure the constant distance. The structures of the LSRM are shown in Fig. 7. Propulsion force and inductance of the LSRMs are measured after locking the moving part using a plate and connectors at the desired position and energizing one phase winding with a constant DC current through a PWM power converter. A load cell sensor has been used to record the propulsion force data at a steady state current. For the inductance measurement, the angle between input voltage and current is determined from an oscilloscope. Results obtained from the mentioned experimental tests (EXP) are shown in Fig. 80 compared with the finite element analysis (FEA). Results indicate that the practical results are relatively close to the finite element analysis results. This confirms the performance of the proposed structure of the LSRM for the elevator application as a unidirectional motion industry.

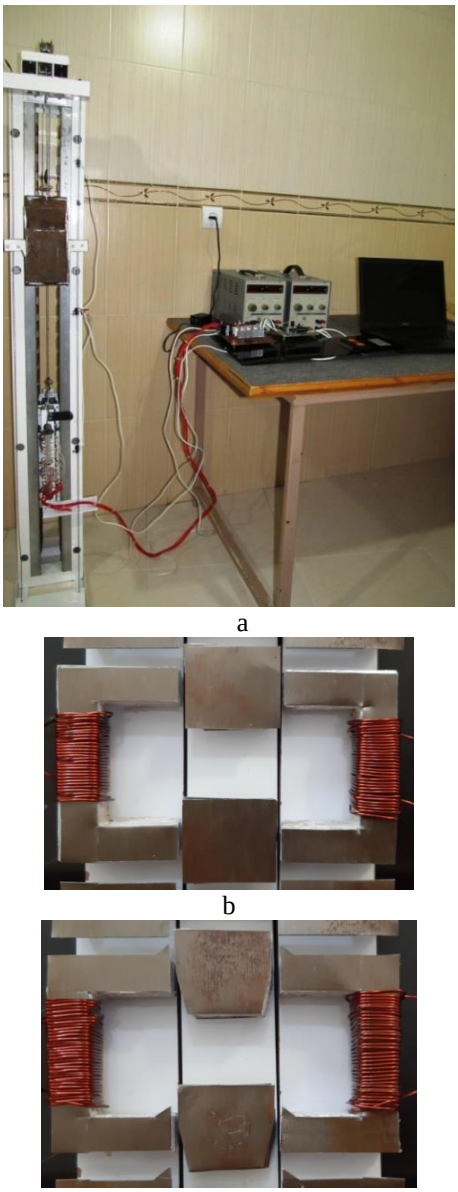

Fig. 7.(a) Prototype system, (b) Poles for Type 1, (c) Poles for Type 3.

VI. Conclusions

This work demonstrated the design and optimization of a linear switched reluctance motor for the elevator application. The propulsion force in the proposed structure was always upward corresponding to the working characteristics of an elevator. The translator was without yoke, making the system light and suitable economically, while the stator included separate poles leading to minor core losses. The translator was designed with a non-uniform air-gap length to generate wider positive force region and thus higher average force. Finite element analysis of the proposed structure along with a conventional one was performed and compared. A prototype system with two type 1 and type 3 pole structures was constructed and practical tests were performed. The obtained results were very close to the finite element analysis results confirming the robustness of the proposed structure.

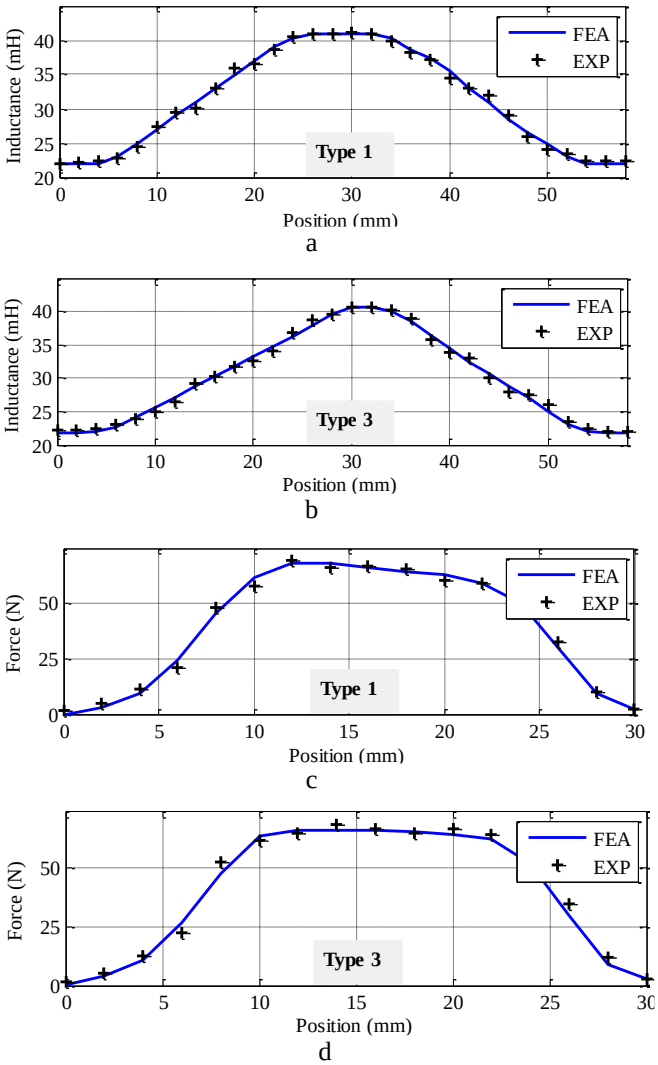

Fig. 8. Comparison of the experimental results and finite element results, (a) Inductance, Type 1, (b) Inductance Type 3, (c) Phase force Type 1, (d) Phase force Type 3.

REFERENCES

[1] Krishnan, R., 'Switched reluctance motor drives: modeling, simulation, analysis, and applications', CRC Press, Boca Raton, 2001.

[2] N. Prasad, S. Jain, S. Gupa, "FEM based analysis and design of linear switched reluctance motor topologies for high speed transit application," 2021 2nd International Conference on Electrical Power and Energy Systems (ICEPES), Bhopal, India, 2021.

[3] N. Prasad, S. Jain, S. Gupa, "Review of linear switched reluctance motor designs for linear propulsion applications", CES Transactions on Electrical Machines and Systems, vol. 6, no. 2, pp. 179-187, 2022.

[4] H. S. Lim, R. Krishnan, "Ropleless elevator with linear switched reluctance motor drive actuation systems", IEEE Trans. Ind. Electron., vol. 54, no. 4, pp. 2209-2217, 2007.

[5] H. S. Lim, R. Krishnan, N. S. Lobo. "Design and control of a linear propulsion system for an elevator using linear switched reluctance motor drives," IEEE Trans. Ind. Electron. vol 55, no. 2, pp. 534-542. Jan 2008.

[6] S. Masoudi, M. R. Feyzi, M. B. B. Sharifian. "Force ripple and jerk minimization in double sided linear switched reluctance motor used in elevator application," IET Elec. Pow. Appl. vol. 10, no. 6, pp. 508-516. Jun 2016.

[7] S. Masoudi, M. R. Soltanpour, H. Abdollahi. "Adaptive fuzzy control method for a linear switched reluctance motor," IET Elec. Pow. Appl. vol. 12, no. 9, pp. 1328-1336, Nov 2018.

[8] A. Azadrou, S. Masoudi, R. Ghanizadeh, P. Alemi. "New adaptive fuzzy sliding mode scheme for speed control of linear switched reluctance motor," IET Elec. Pow. Appl. vol. 13, no. 8, pp. 1141-1149, 2019.

[9] A. Azadrou, S. Masoudi, R. Ghanizadeh, P. Alemi. "Improving Quality of Movement in a Linear Switched Reluctance Motor Using a Fuzzy Logic System," International journal of industrial Electronics, Control and Optimization, vol. 3, no. 4, pp. 459-468, 2020.

[10] R. Cao, E. Su, M. Lu, "Comparative study of permanent magnet assisted linear switched reluctance motor and linear flux switching permanent magnet motor for railway transportation," IEEE Transaction on Applied Superconductivity, vol. 30, no. 4, 2020.

[11] M. Lu, R. Cao, "Comparative investigation of high temperature superconducting linear switched flux-reluctance motor and high temperature superconducting linear switched reluctance motor for urban railway transit," IEEE Transaction on Applied Superconductivity, vol. 31, no. 5, 2021.

[12] H. J. Liang, S. D. Huang, G. Z. Cao, T. Liang, "Design and analysis of a large-thrust and small-deformation double-sided linear switched reluctance motor," 5th International Electrical and Energy Conference (CIEEC), Nangjing, Chaina, 2022.

[13] M .Vatani, A. Ghaffarpour, M. A. J. Kondelaji, M. Mirsalim, "Study of a toothed linear hybrid reluctance motor with permanent magnets in translator slots," IEEE Trans. On Transportation Electrification, vol. 8, no. 3, pp. 3554-3567, 2022.

[14] M. Vatani, M. Mirsalim, "The modular and crooked-tooth translator linear switched reluctance motor with a high-thrust per weight," IEEE Trans. On Transportation Electrification, vol. 7, no. 3, pp. 3554-3567, 2021.

[15] H. Chen, W. Yan, K. Wang, "Iron loss analysis of double-sided linear switched reluctance launcher," IEEE Transactions on Plasma Science, vol. 47, no. 5, pp. 2323-2330, 2019.

[16] H. Chen, W. Yan, K. Wang, "Electromagnetic analysis of flux characteristics of double-sided switched reluctance linear machine," IEEE Transactions on Applied Superconductivity, vol. 26, no. 4, 2016.

[17] Z. Zhang, N. C. Cheung, K. W. E. Cheng, X. D. Xue, J. K. Lin, "Longitudinal and transversal end-effect analysis of linear switched reluctance motor," IEEE Transaction on Magnetics, vol. 47, no. 10, pp. 3979-3983, 2011.

[18] D. Wang, X. Wang, X. F. Du, "Design and comparison of a high force density dual side linear switched reluctance motor for long rail propulsion application with low cost," IEEE Transaction on Magnetics, vol. 53, no. 6, 2017.

[19] M. Vatani, M. Mirsalim, "Comprehensive research on a modular-stator linear switched reluctance motor with a toroidally wound mover for elevator applications," 10th International Power Electronics, Drive Systems and

Technologies Conference (PEDSTC), Shiraz, Iran, Feb. 2019.
[20] Y. Shen, Q. Lu, H. Li, J. Cai, X. Huang, Y. Fang, "Analysis of a novel double-sided yokeless multi-tooth linear switched-flux PM motor," IEEE Trans. On Ind. Elec., vol. 65, no. 2, pp. 1837-1845, 2018.
[21] D. Wang, X. Du, D. Zhang, X. Wang, "Design, optimization, and prototyping of segmental-type linear switched – reluctance motor with a toroidally wound mover for vertical propulsion application," IEEE Trans. On Ind. Elec., vol. 65, no. 2, pp. 1865-1874, 2018.
[22] J. F. Pan, L. Qui, J. Zhu, B. Zhang, "Optimal positioning coordination for multiple linear switched reluctance machines," IEEE Transaction on Magnetics, vol. 53, no. 11, 2009.
[23] S. Masoudi, H. Mehrjerdi, A. Ghorbani, "New elevator system constructed by multi-translator linear switched reluctance motor with enhanced motion quality," IET Electric Power Application, vol. 14, no. 9, pp. 1692-1701, 2020.
[24] M. R. Soltanpour, H. Abdollahi, S. Masoudi, "Optimisation of double-sided linear switched reluctance motor for mass and force ripple minimisation," IET Science, measurement and technology, vol. 13, no. 4, pp. 509-517, 2019.
[25] J. G. Amoros, P. Andrada, B. Blangue, M. M. Genesca, "Influence of design parameters in the optimization of linear switched reluctance motor under thermal constraints," IEEE Transaction on Ind. Elec., vol. 65, no. 2, pp. 1875-1883, 2018.
[26] H. Chen, X. Liu, W. Yan, "Three-dimentional magnetic equivalent circuit research of double-sided switched reluctance linear machine," IEEE Trans. On Applied Superconductivity, vol. 30, no. 4, 2020.
[27] W. Zaafrane, M. Dursun, "Double sided linear switched reluctance motor analysis and modeling including end-effect," 5th International Conference on Electrical and Electronic Engineering (ICEEE), Istanbul, Turkey, 2018.
[28] H. Chen, W. Yan, "Flux characteristics analysis of double-sided switched reluctance linear machine under asymmetric air gap," IEEE Trans. On Ind. Elec., vol. 65, no. 12, pp. 9843-9852, 2018.
[29] K. Deb, A. Pratap, S. Agarwal, "A fast and elitist multi-objective genetic algorithm: NSGA-II," IEEE Trans. on Evolutionary Computation, vo;. 6, no. 2, pp. 182-197, 2002.
[30] K. S. Ha; S. G. Oh, B. MacCleery, and R. Krishnan, "An automated reconfigurable FPGA-based magnetic characterization of switched reluctance machines," in Proc. of the IEEE International Symposium on Industrial Electronics, vol. 2, pp. 839 – 844, 2005.

Allahverdi Azadrou was born in Salmas, Iran, in 1983. He received his B.S. degree in electrical engineering from Islamic Azad University, Abhar Branch, Abhar, Iran, and M.S. degree from Dezful Branch, Dezful, Iran. He is a member of science in Islamic Azad University, Salmas Branch, Iran since 2012. Currently he is Ph.D student in Islamic Azad University, Urmia Branch, Urmia, Iran.

Siamak Masoudi was born in Miyaneh, Iran. He received his B.S. degree in power engineering from Tarbiat Moallem Tabriz University, Tabriz, Iran, in 2006, and his M.S. and Ph.D. degrees in Electrical Machines and Drives from University of Tabriz, Tabriz, Iran, in 2009 and 2016, respectively. From 2010, he is a member of science in Islamic Azad University, Abhar Branch, Zanjan, Iran. His current research interests include Electrical machines design and control and linear motors/generators.

Shahla Gharaati was born in Salmas, Iran, in 1986. He received his B.S. and M.S. degrees in electrical engineering Islamic Azad University, Urmia Branch, Urmia, Iran in 2009, and 2013, respectively. She works in administration of education in Salams, Iran.

International Journal Of
Industrial Electronics Control and Optimization
Print ISSN: 3517-2645
Online ISSN: 3568-2645
Homepage: https://ieco.usb.ac.ir/

Reliability-based Probabilistic Wind Power Planning Considering Correlation of Load and Wind

Morteza Jadidoleslam[1] | Morteza Ghaseminezhad[2]

Department of Electrical Engineering, Sirjan University of Technology, Sirjan, Iran.[1,2,]
Corresponding author's email: jadidoleslam@sirjantech.ac.ir

Article Info

Article type:
Research Article

Article history:
Received: 06 Feb 2022
Revised: 11 Sep 2022
Accepted: 15 Sep 2022
Published online: 21 Nov 2022

Keywords:
Power system reliability
Shuffled frog leaping algorithm
Uncertainty modeling
Wind power planning

ABSTRACT

Wind power has been considered a future alternative to fossil energy resources. However, due to its stochastic nature, the integration of wind power plants (WPPs) into power systems poses some reliability problems such as a mismatch between load profile and efficient wind power generation. This issue can be alleviated by considering the correlation between hourly load and wind speed variations in the planning phase. To this end, a reliability-based wind power planning procedure is proposed and formulated as a stochastic programming problem. The objective function is the minimization of total costs, including capital investment, operating and maintenance, and customer energy not served costs. A new hybrid method that combines features of the load-duration curve and the K-means clustering algorithm is proposed to model the uncertainty of the input data. A shuffled frog-leaping algorithm is used to solve the proposed model. The simulation results indicate that the amount of adaptation between hours with high loads and those with high wind speeds markedly affects the selection of wind sites as optimal locations for WPP installation. Considering this issue can also improve power system reliability in the presence of WPPs.

NOMENCLATURE

$C_{inv}^{\max}$	Budget for investment in wind capacity
$X_{k,s}$	Capacity of the WTG type *k* at wind site *s*
CRF_k	Capital recovery factor of the *k*th WTG type
V_{ci} /V_{co}	Cut-in/cut-out speed of WTG
dr	Discount rate
L_k	Economic life of the *k*th WTG
$EENS_d$	Expected energy not served in block *d*
$\gamma_{d,l}$	Final operating scenario related to cluster *l* in block *d*
$IEAR$	Interrupted energy assessment rate
$IL_{d,l}$	Interrupted load in cluster *l* and block *d*
C_k^{inv}	Investment cost of the *k*th WTG type
$p_{d,l,i}^{D}$	Load value of the *i*th member in cluster *l* and block *d*
$X_s^{\min}$ / $X_s^{\max}$	Minimum/maximum capacity of wind farm *s*
$N_{d,l}^{HD}$	Number of demand hours of cluster *l* in block *d*
Nh_d	Number of hours in load block *d*
$N_{d,l,s}^{HW}$	Number of wind speed hours at site *s* in cluster *l* and block *d*
$C_k^{O\&M}$	Operating costs of the *k*th WTG type
V_r / P_r	Rated speed/power of WTG
Ω_b	Set of load blocks
Ω_S	Set of wind sites
Ω_K	Set of WTG types
Ω_d	Set of clusters in load block *d*
Ω_{ld}	Set of load data in cluster *l* and block *d*
Ω_{sld}	Set of wind speed data at site *s* in cluster *l* and block *d*
X_T^{wind}	Total installation wind capacity
$WS_{d,l,s,j}$	Wind speed value at site *s* for member *j* of cluster *l* in block *d*
$p_{d,l,s}^{w}$	Wind power at site s for cluster *l* in block *d*
$W_{d,l}$	Weight of cluster *l* in load block *d*
$WS_{d,l}$	Wind speed of cluster *l* in block *d*

DOI: 10.22111/IECO.2022.41721.1416

I. Introduction

The share of renewable resources in the generation sector of many countries is rapidly increasing. Wind power has attracted more attention among different renewable resources because of its specifications, such as very low operating and maintenance costs and the lack of environmental pollution [1, 2]. Due to the random nature of wind speed, the amount of generated wind power is uncertain. In a wind turbine generator (WTG), design parameters, including the turbine rated, cut-in, and cut-out speeds, and the rated capacity are involved in the output power at a specific wind site. Moreover, each WTG has its specific economic and reliability parameters. Hence, identifying the optimal type, number, and location of WTGs is essential to achieving the maximum economic and reliability benefits in wind power planning studies.

On the other hand, there is uncertainty in the forecasted electric demand which affects power system reliability and changes the planning decisions. The reliability of the power system is a key issue in planning studies, especially in the presence of variable resources, such as wind power. In recent years, different papers have analyzed the reliability of power systems in the presence of WPPs using different techniques. For example, in [3], an analytical multi-state model is presented for the adequacy assessments of the generating system incorporating wind power. A procedure is presented in [4] based on the Markov process to model wind farms for reliability evaluation purposes. For a long-term assessment of wind power, an analytical approach is introduced in [5] and used to assess the performance of a hybrid renewable power system. A method to assess the reliability indices is proposed in [6] from the viewpoint of reactive power management for a power system including wind power. A framework for optimal selection of wind turbines is presented in [7], considering the capacity factor of WTG and the EENS reliability index. The proposed method helps compare the performance of wind turbines, but the uncertainties associated with the input data are not considered.

Many papers have analyzed the generation capacity investment problem. In most of them, the problem is solved for conventional generation sources [8, 9]. Nevertheless, because of the uncertain character of wind speed, the WPPs need different models from the conventional plants. In [10], considering both long- and short-term uncertainties of wind power, a two-stage generation expansion planning model is developed, and an ARMA model is adopted to deal with the uncertainties. In [11], the impact of wind energy penetration on the capacity investment and incentives of individual wind power investors is analyzed in the power market. A risk-constrained multi-stage stochastic programming model is proposed in [12] to make optimal decisions for investment in wind capacity.

Some studies have investigated the optimal design of hybrid energy systems including WPPs. In [13], a framework is presented for the optimal design of a grid-connected wind/photovoltaic/storage energy system, and reliability is considered as constraint. For optimal sizing of the components of a hybrid wind/photovoltaic/battery system, an ant lion optimization method is proposed in [14]. The objective function is the minimization of the system's total cost. An approach based on the tunicate swarm optimization method is introduced in [15] to design a wind/photovoltaic/fuel cell hybrid system considering reliability and cost. In these studies, the advantages of hybrid energy systems have been exploited to supply the load, but the effect of uncertainty and the correlation of input data has not been considered in the results.

The commonly used method to deal with uncertainties is stochastic programming [2, 12, 16, 17]. In this approach, which is also used here, uncertainty is represented via scenarios utilizing the input data. A significant aspect of scenario modeling in wind power planning studies is the consideration of the statistical correlation between electric load and wind power generation. Low values of electricity demand usually occur during the night when wind speed (wind power generation) is relatively higher [18]. Hence, considering load and wind as independent phenomena may result in non-optimal investment decisions.

In this paper, regarding the uncertainties and correlation between the input data, such as electric load and wind power, a new method is proposed to represent scenarios in the planning procedure. A stochastic-based programming model is presented for wind power capacity planning, considering the costs and reliability of the electric power system. The proposed model is a combinatorial constrained and nonlinear optimization problem that is properly solved by the shuffled frog leaping algorithm. To demonstrate the performance and effectiveness of the proposed approach, it is implemented in two modified power systems, and several case studies are presented. The main contributions of this paper are as follows:

- Proposing a new hybrid method for scenario modeling that combines features of the load-duration curve and the K-means clustering algorithm in a probabilistic planning framework of WPPs
- Considering and assessing the impact of the correlation between input data on the results of wind power planning from a reliability point of view in the power system.

II. Probabilistic WPP Modeling

A. Uncertainty characterization and scenario modeling

Electric load and wind power generation are not statistically independent values in an electric power system. Low values of electricity demand usually correspond to high wind power generation [18]. Therefore, the uncertainty of both parameters should be jointly investigated. For modeling purposes, hourly historical data can be used for load and wind speeds at different wind sites in one or several years in the studied power system. It is assumed that the historical data are sufficiently scaled to

DOI: 10.22111/IECO.2022.41721.1416

take demand growth into account. Each piece of historical data is a set of values, including the electric load and wind speeds at different wind sites, representing an operating scenario. Considering all scenarios (e.g., 8760 for one year) in solving the problem may result in intractability in a realistic power system. Therefore, a proper method should be adopted for reducing the primary data into a tractable data set.

To model the uncertainties of the electric load and wind speed data, a novel hybrid method is presented that combines features of the load-duration curve (LDC) and the K-means clustering algorithm. The main advantage of the proposed method is achieving scenarios that have maximum concordance with the input data while the correlation between them is maintained.

A flowchart of the proposed method for scenario modeling is depicted in Fig. 1. Evidently, the method is initialized with load and wind speed data input. To create initial scenarios, both load and wind speed data in the same time slot are jointly placed in a group to form an operating scenario. Then, the LDC is formed by sorting the load data in descending order. By so doing, the corresponding wind speed data that are in the same group are also moved, and the temporal correlation between them is maintained. Afterward, the load duration curve is divided into N_{LB} load blocks (LBs), and the number of clusters in each LB (N_{Cl}) is also determined.

In the next step, the K-means clustering algorithm starts by determining the number of iterations. The K-means method is an iterative algorithm that attempts to categorize a dataset into K subgroups (clusters) based on similarity [19]. As shown in Fig. 1, the K-Means method operates as follows:

1) Initialize centroids by randomly selecting K data points as the centers of clusters.
2) Calculate distances between data points and all the centroids.
3) Assign each data point to the closest cluster (centroid).
4) Update centroids by taking the average of all data points that belong to each cluster.
5) Repeat Steps 2 to 4 until the centroids no longer change, or the maximum number of iterations is reached.

After the end of the K-means algorithm, to form the final operating scenarios, the values of wind speeds and load related to each cluster are obtained using (1) and (2), respectively.

$$WS_{d,l,s} = \frac{\sum_{j\in\Omega sld} WS_{d,l,s,j}}{N^{HW}_{d,l,s}}; \forall d, \forall l, \forall s \quad (1)$$

$$P^{D}_{d,l} = \frac{\sum_{i\in\Omega_{ld}} p^{D}_{d,l,i}}{N^{HD}_{d,l}}; \forall d, \forall l \quad (2)$$

Moreover, the weight of each final cluster is calculated using the following equation:

$$W_{d,l} = \frac{N^{HD}_{d,l}}{\sum_{l\in\Omega_d} N^{HD}_{d,l}} = \frac{N^{HW}_{d,l,s}}{\sum_{l\in\Omega_d} N^{HW}_{d,l,s}}; \forall d, \forall l \quad (3)$$

Finally, the output of this method is a reduced set of operating scenarios.

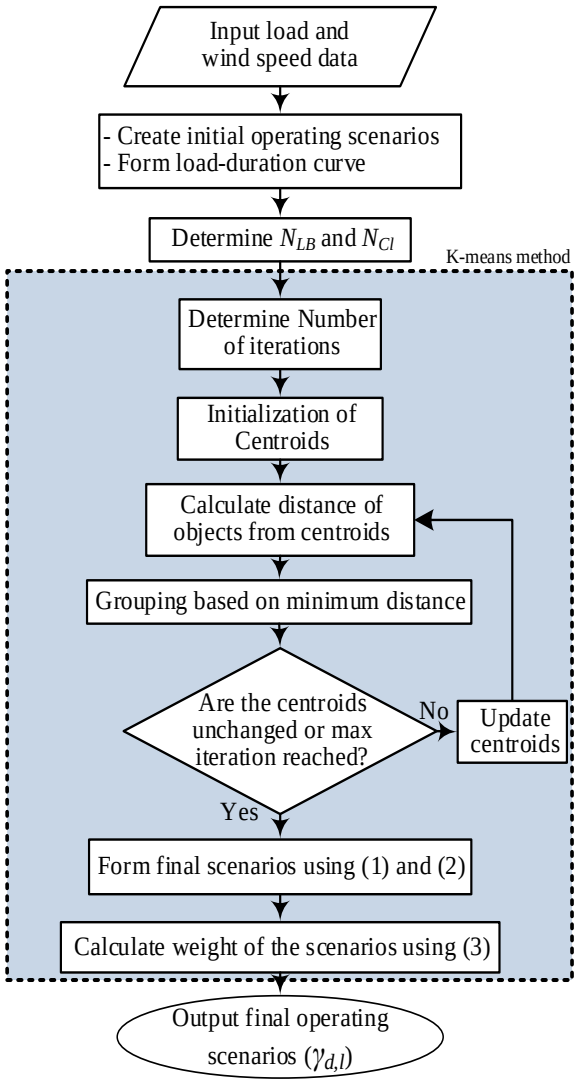

Fig. 1. Flowchart of the proposed method for scenario modelling

Each final scenario contains values of the load, wind speeds at different wind sites, and the occurrence probability that can be expressed as (4).

$$\gamma_{d,l} = \left[P^{D}_{d,l}; WS_{d,l,s}, \forall s; W_{d,l} \right]; \forall d, \forall l. \quad (4)$$

B. WPP modeling for reliability evaluation

In addition to an appropriate representation of uncertain input data, two factors should be taken into account for modeling a WPP which directly affect the WTG output. The first one is the relationship between the wind speed and the output power of the WTG, which can be specified using the WTG design parameters, including the rated capacity and the turbine cut-in, cut-out, and rated speeds. The second factor is the unavailability of the WTG, expressed by the WTG forced outage rate (FOR).

Considering the nonlinear relationship between the wind speed and output power of a WTG, the output power curve of a wind turbine can be represented as follows [3, 20].

$$P_{d,l,s}^{WTG}=\begin{cases}P_r(\alpha+\beta\times WS_{d,l,s}+\lambda\times WS_{d,l,s}^2), & V_{ci}\le WS_{d,l,s}\le V_r\\ P_r, & V_r\le WS_{d,l,s}\le V_{co}\\ 0, & \text{otherwise}\end{cases};\forall d,\forall l,\forall s. \quad (5)$$

Constants α, β, and λ are calculated using the following equations:

$$\alpha=\frac{1}{(V_{ci}-V_r)^2}\left[V_{ci}(V_{ci}+V_r)-4(V_{ci}.V_r)\left(\frac{V_{ci}+V_r}{2V_r}\right)^3\right] \quad (6)$$

$$\beta=\frac{1}{(V_{ci}-V_r)^2}\left[4(V_{ci}+V_r)\left(\frac{V_{ci}+V_r}{2V_r}\right)^3-(3V_{ci}+V_r)\right] \quad (7)$$

$$\lambda=\frac{1}{(V_{ci}-V_r)^2}\left[2-4\left(\frac{V_{ci}+V_r}{2V_r}\right)^3\right]. \quad (8)$$

After determining the output power generated by a WTG, the next step is the identification of the WPP model. An analytical method is adopted to build a WPP model that incorporates the FOR of WTG units [3]. In this method, a WPP is divided into two basic parts: wind conditions and WTG units. If WPP comprises identical WTG units with zero FOR, the WPP model will be the same as a single WTG unit. However, if the FOR of WTG units is not zero, wind conditions and the WTG units form a series system (Fig. 2). Therefore, the WPP model can be obtained by combining the capacity outage probability table (COPT) of the WTG units and the wind conditions [3]. To create the COPT of a WTG unit (WTG-COPT), the following procedure is followed:

1) The output states of the WTG are defined as segments of the rated power.
2) The total number of times that an output power falls within one of the output states is determined.
3) The probability of each state is calculated by dividing the total number of occurrences for each output state by the total number of data points.

After forming the WTG-COPT, the multi-state model of a WPP, including multiple WTG units, is created using the following steps.

1) The WTG units with specified rated power and FOR are combined to create a COPT using the conventional COPT algorithm [21].

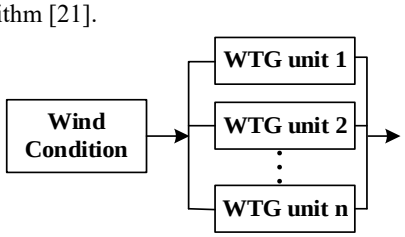

Fig. 2. WPP Model including multiple WTG units.

2) The wind condition model is represented by the WTG-COPT.
3) The wind condition and the COPT of Step 1 are combined to create the multi-state WPP-COPT.

To evaluate the reliability of the generation system, the generation model and load model should be convolved to create the risk model [21]. The generation model (GEN-COPT) is formed using the WPP-COPTs of different WPPs (Table 1) [21]. The first column shows the outage capacity level (O_i) in MW. Thus, the available capacity of the generation system will be the installed capacity minus the outage capacity, which is shown in the second column. In this table, the third column indicates the probability of the generation outage O_i which is calculated using the FOR of the generating units. The load model is described as the LDC displayed in Fig. 3. Based on this figure, for the generation outage of O_i, the load is lost for the period of t_i. Consequently, the loss of load expectation (LOLE) can be calculated as

$$LOLE=\sum_{i=1}^{N}p_i\times t_i. \quad (9)$$

The area under the LDC indicates the energy demand. Hence, the unserved energy due to the generation outage of O_i is E_i, and the expected energy not served (EENS) can be calculated as

$$EENS=\sum_{i=1}^{N}p_i\times E_i. \quad (10)$$

In (9) and (10), N is the number of states of GEN-COPT and p_i is the probability of the generation outage O_i.

III. Problem Formulation

The goal of a power system planner is to identify the optimal wind power investment plans that minimize total costs. Consequently, the objective function of the proposed model is the minimization of total costs, including capital investment, operating and maintenance, and customer energy not served costs. Since the WTGs may have different lifetimes, the annual equivalent cost approach is adopted to evaluate different plans. The proposed wind power planning model is formulated as follows.

TABLE 1
EXAMPLE OF CAPACITY OUTAGE PROBABILITY TABLE.

Capacity outage (MW)	Available capacity (MW)	State probability
O_1	Installed capacity - O_1	p_1
O_2	Installed capacity - O_2	p_2
⋮	⋮	⋮
O_i	Installed capacity - O_i	p_i
⋮	⋮	⋮
O_N	Installed capacity - O_N	p_N

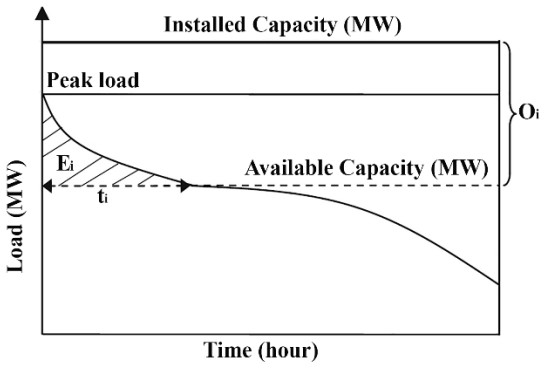

Fig. 3. Load duration curve for reliability evaluation [22].

$$\underset{X_{k,s},\forall l,d}{\text{Minimize}} \quad \sum_{s\in\Omega_S}\sum_{k\in\Omega_K} CRF_k \times C_k^{inv} \times X_{k,s} + \sum_{s\in\Omega_S}\sum_{k\in\Omega_K} C_k^{O\&M} \times X_{k,s} + \sum_{d\in\Omega_b} IEAR \times EENS_d \tag{11}$$

subject to:

$$EENS_d = \sum_{l\in\Omega_d} Nh_d \times W_{d,l} \times IL_{d,l}\,;\forall d \tag{12}$$

$$X_s^{\min} \le \sum_{k\in\Omega_K} X_{k,s} \le X_s^{\max}\ ;\forall s \tag{13}$$

$$\sum_{s\in\Omega_S}\sum_{k\in\Omega_K} X_{k,s} = X_T^{wind}. \tag{14}$$

In (11), CRF_k is the capital recovery factor used to calculate the annual equivalent investment cost and is expressed as follows [22]:

$$CRF_k = \frac{dr\times(1+dr)^{L_k}}{(1+dr)^{L_k}-1}. \tag{15}$$

The objective function of (11) consists of three parts. The first one is related to the capital investment cost of newly installed WPPs. It includes the costs of the turbine, turbine erection, foundations, roads, and grid connections. The second part is the operating and maintenance cost of all WPPs. This cost is calculated annually within the lifetime of a WPP. Finally, the third part is the customer energy not served cost. Reliability and cost models are required to estimate this cost for a power system. Reliability can be assessed by the expected energy not served (EENS) index, using the analytical approach described in Section II. The commonly used cost model to estimate customer energy not served cost is the composite customer damage functions [23]. These functions can estimate a cost factor in ($/MWh), known as the interrupted energy assessment rate (IEAR). Therefore, the cost of energy not served can be calculated using the IEAR factor and EENS index.

In the proposed model, Constraint (12) represents the equation for calculating the EENS reliability index in demand block *d*. Constraint (13) imposes the limitation of the total wind power installation capacity at a wind site. Wind power capacity, which can be installed at a wind site, is generally limited by factors such as the limitation of a geographical area and wind power availability. Constraint (14) indicates the total targeted wind power capacity that must be constructed in a power system. It is either determined by the future energy plans or forced by the accepted renewable portfolio standard (RPS) mandates. In some cases, Constraint (14) can be replaced by the investment budget constraint as follows:

$$\sum_{s\in\Omega_S}\sum_{k\in\Omega_K} X_{k,s} \le C_{inv}^{\max}. \tag{16}$$

IV. Solution Approach Using the Shuffled Frog Leaping Algorithm

The shuffled frog leaping algorithm (SFLA) is a population-based meta-heuristic optimization method presented in 2003 by Eusuff and Lansey [24]. SFLA is inspired by the evolution of food-seeking frogs. It has a local search ability which makes it a powerful and efficient algorithm. SFLA has been used to solve various problems in power system studies and has shown good efficiency and performance in solving nonlinear and complex optimization problems [2, 9, 25].

In the first step, to start the algorithm, an initial population of '*N*' hypothetical frogs is created in the search space. Then, each member of the population is evaluated based on its location (Z_n) using the objective function of the problem, and the population of frogs is sorted in descending order according to their fitness values.

The next step is called local search, which commences by dividing the frogs into a pre-determined number of groups (m). Each group is called a memeplex, and the number of frogs in each one is equal to N/m. In the local search procedure, using the frog leaping rule (Equations 17 and 18), the location of the worst frog (Z_w) changes regarding the best frog (Z_b). This jump is limited by the CP^{max} value.

$$Z_w^{new} = Z_w + CP \tag{17}$$

$$CP = a\times(Z_b - Z_w),\ \|CP\| < CP^{\max} \tag{18}$$

In (17), a is a random number between 0 and 1. If this jump leads to a better position, it will replace the worst frog; otherwise, by substituting the best frog with the global best frog (Z_g), the leaping rule will apply again. After this, if no improvement is achieved, the worst frog will be replaced by a new randomly generated one. The position of the frogs improves by continuing the evolutionary process in the memeplexes for a specified number of iterations.

In the final step, by using the so-called shuffling process, all the frogs are combined and sorted again. The local search and shuffling processes continue until the convergence criterion is met. A flowchart of the implementation of the proposed SFLA method is depicted in Fig. 4. More information and details can be obtained from [24].

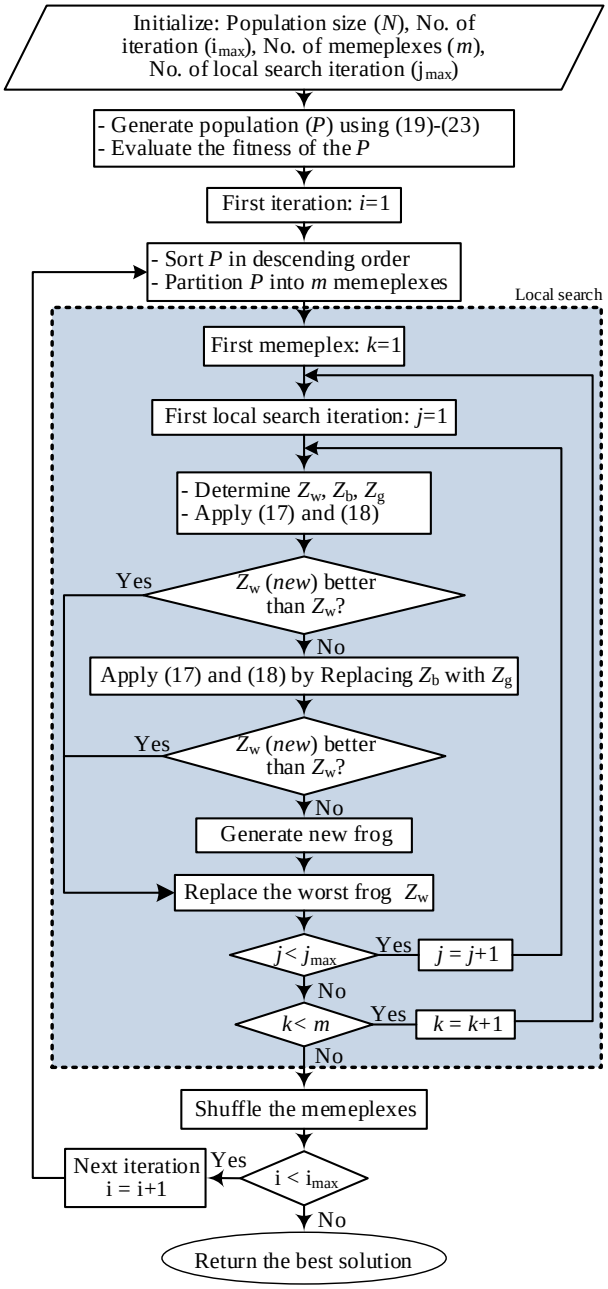

Fig. 4. Flowchart of the SFLA method

It is relatively difficult to apply equality constraints in the SFLA method. An adjustment technique is adopted here to meet Constraints (13) and (14) as follows:

1) Allocate the minimum wind power capacity (X_s^{min}) to each wind site ($s=1,2,...,ns$), and calculate the remaining capacity (X_T^R) using (19).

$$X_T^R = X_T^{wind} - \sum_{s\in\Omega_s} X_s^{\min} \tag{19}$$

2) Using the X_T^R, the allocated capacity at the sth wind site (X_s^A) is determined as follows:

$$X_s^A = X_s^{\min} + \text{rand}\left[\max\left(0, X_s^R - \sum_{m=s+1}^{n_s}(X_m^{\max} - X_m^{\min})\right), \left(X_s^{\max} - X_s^{\min}\right)\right] \tag{20}$$

where X_S^R is the remaining capacity after capacity allocation to the $(s-1)$th wind site and calculated using (21).

$$X_s^R = X_T^R - \sum_{m=1}^{s-1} X_m^A. \tag{21}$$

If X_s^A is greater than X_S^R, then $X_s^A = X_S^R$ and the allocated capacity at the remaining wind sites ($s+1,...,ns$) will be X_s^{min}.

For the last wind site ($s=ns$), the allocated capacity is given by

$$X_{n_s}^A = X_s^{\min} + (X_T^R - \sum_{s\in\Omega_s\setminus\{n_s\}} X_s^A). \tag{22}$$

Note that the order of wind sites for capacity allocation is randomly chosen. Thus, all wind sites will have the same chance for capacity allocation in the optimization process.

3) Calculate the number of the kth-type WTG units at wind site s using (23).

$$N_{s,k} = \left[\frac{X_s^A}{X_{k,s}}\right] \tag{23}$$

where [ ] is an integer truncation function.

When using the integer truncation function, the total capacity allocated to all wind sites might become less than X_T^{wind}. Hence, to meet Constraint (14) as accurately as possible, the number of the WTG with the lowest rated capacity is adjusted.

V. Numerical Results

To illustrate the performance and effectiveness of the proposed approach, results of different cases based on the RBTS [26] and IEEE-RTS [27] test systems are provided here.

A. Data and parameters

Suppose that four wind sites are considered to develop WPPs in the test systems. The wind speed data are from wind sites at Borujen, Moghar, Moorche-Khort, and Varzane in Isfahan Province, Iran [28]. The mean wind speeds of these sites are 13.5, 15.9, 16.9, and 17.1, respectively. The load data of the RTS [27] are used in the studies. To perform wind power planning, 12 WTG types with different design and operating parameters are considered (Table 2). The FOR and lifetimes of all WTG units are assumed to be 4% and 25 years, respectively. A discount rate of 8% is assumed in the studies. An average IEAR factor of 6.3 K$/MWh is assumed to calculate the energy not served cost [23].

The proper selection of parameters for optimization algorithms has a significant effect on convergence speed and the results obtained. In this paper, the parameters of the employed algorithms (SFLA, PSO, and GA) are selected experimentally by performing several experiments. For this purpose, the SFLA has been run many times using different

parameter values. Following that, the appropriate parameters of the algorithm have been selected. To make a fair comparison between all employed algorithms, the parameters of the PSO and GA, such as the initial population and the number of iterations, have been selected proportionally. The selected parameters of the SFLA for both test systems are presented in Table 3.

B. Number of scenarios selected

In the proposed hybrid method for data modeling, the number of final scenarios is determined using the product of the number of LBs (N_{LB}) and the number of clusters in each LB (N_{Cl}). By increasing N_{LB} and N_{Cl}, both modeling accuracy and computational volume increase. To select the proper number of N_{LB} and N_{Cl}, a trade-off must be made between accuracy and computational volume.

To represent load data appropriately, the width of the LBs (in terms of hour span) varies according to the variations (slope) in the LDC curve. For example, since the peak load can greatly affect planning decisions, for the first LB representing the peak load, the width is considered narrower.

Since the number of scenarios affects the accuracy of LOLE index calculation, to find an appropriate number of scenarios, the LOLE is calculated for different numbers of scenarios. For this purpose, the IEEE-RTS test system is considered, and it is assumed that WPPs can be installed at four wind sites with various capacities. The results are depicted in Fig. 5. Evidently, the LOLE is relatively constant after 48 scenarios for all wind power capacities. The results indicate that modeling the operating conditions using 48 scenarios is adequate for generation system reliability assessment and planning studies. These scenario data are provided in Table 4.

TABLE 2
CANDIDATE WTG UNIT PARAMETERS

Type	Rated capacity (MW)	Capital cost (k$/MW)	O&M costs ($/MW-yr)	Rated speed (km/h)	Cut-in speed (km/h)	Cut-out speed (km/h)
W1	0.5	1350	36	40	10	80
W2	0.5	1350	36	45	10	70
W3	1	1250	35	40	12	80
W4	2	1120	30	30	12	55
W5	1	1220	33	33	13	60
W6	1	1250	32	40	14	90
W7	2	1100	35	33	15	50
W8	2	1100	30.5	33	15	60
W9	1	1200	32	37	15	70
W10	1	1250	32	48	18	70
W11	2	1100	30	45	18	70
W12	2	1100	30	35	18	75

TABLE 3
SFLA PARAMETERS

Parameters	RBTS	IEEE-RTS
No. of memeplexes (m)	4	6
CP^{max}	Inf.	Inf.
Population size (N)	40	60
No. of iterations	60	100
Local search iterations	10	10

TABLE 4
LOAD AND WIND SPEED SCENARIOS

#	block	Hours	Load (pu)	Wind speed (pu)			
				Borujen	Moghar	Moorche-khort	Varzane
1	1	81	0.885	0.156	0.268	0.160	0.347
2		66	0.886	0.296	0.095	0.305	0.199
3		61	0.884	0.273	0.126	0.562	0.232
4		55	0.871	0.333	0.335	0.211	0.14
5		85	0.891	0.281	0.135	0.274	0.461
6		52	0.878	0.170	0.130	0.159	0.095
7	2	153	0.812	0.233	0.201	0.479	0.131
8		175	0.812	0.291	0.160	0.373	0.449
9		88	0.817	0.506	0.504	0.519	0.119
10		223	0.803	0.108	0.197	0.147	0.106
11		194	0.818	0.396	0.171	0.196	0.134
12		167	0.822	0.157	0.262	0.169	0.400
13	3	139	0.745	0.389	0.449	0.222	0.138
14		135	0.735	0.327	0.123	0.560	0.244
15		189	0.737	0.155	0.187	0.283	0.454
16		175	0.739	0.184	0.219	0.337	0.129
17		291	0.743	0.078	0.16	0.132	0.129
18		171	0.737	0.45	0.164	0.214	0.123
19	4	185	0.666	0.473	0.215	0.198	0.114
20		372	0.664	0.070	0.208	0.145	0.109
21		270	0.667	0.199	0.101	0.263	0.151
22		215	0.667	0.312	0.146	0.565	0.174
23		202	0.674	0.259	0.391	0.332	0.205
24		256	0.669	0.161	0.199	0.251	0.437
25	5	179	0.608	0.232	0.419	0.239	0.179
26		204	0.602	0.211	0.183	0.549	0.164
27		308	0.600	0.076	0.207	0.118	0.108
28		323	0.593	0.092	0.115	0.251	0.153
29		261	0.591	0.112	0.198	0.214	0.413
30		225	0.608	0.415	0.135	0.225	0.138
31	6	217	0.508	0.381	0.175	0.323	0.214
32		331	0.516	0.086	0.145	0.241	0.347
33		373	0.509	0.083	0.115	0.191	0.112
34		101	0.513	0.255	0.554	0.336	0.143
35		283	0.510	0.078	0.301	0.156	0.171
36		195	0.518	0.101	0.177	0.512	0.184
37	7	234	0.447	0.067	0.116	0.29	0.107
38		185	0.45	0.08	0.141	0.143	0.157
39		177	0.446	0.077	0.35	0.179	0.185
40		116	0.452	0.394	0.131	0.207	0.134
41		97	0.441	0.097	0.153	0.558	0.202
42		191	0.442	0.087	0.169	0.243	0.394
43	8	125	0.375	0.075	0.136	0.324	0.305
44		69	0.384	0.073	0.176	0.526	0.172
45		65	0.384	0.481	0.215	0.240	0.202
46		109	0.386	0.074	0.182	0.188	0.425
47		215	0.377	0.061	0.090	0.251	0.08
48		177	0.389	0.073	0.226	0.181	0.156

C. RBTS case study

The RBTS is a 6-bus test system composed of 11 conventional power plants and five load points. The system peak load and the installed capacity are 185 MW and 240 MW, respectively. Two potential wind sites with the wind regimes of Borujen and Moghar are considered to add WPPs to the RBTS. Three case studies are assumed to demonstrate the performance and effectiveness of the proposed approach. In Case 1, as the base case, the total limitation of wind power capacity is 40 MW. The maximum and minimum capacity constraints at every wind site are 40 and 10 MW, respectively.

Case 2 is similar to Case 1, except that the objective function is replaced by the consumer energy not served cost. In Case 3, the peak load is increased from 185 MW in Case 1 to 200 MW.

The best value of the objective function for Case 1, obtained by the SFLA, is provided in Table 5. For comparison and verification, particle swarm optimization (PSO) and genetic algorithm (GA) are also applied to solve the problem, and the results are listed in this table. The SFLA has found a better solution with a lower cost than the others. The optimal solution is provided in Table 6. Table 7 also shows the values of different components of the objective function and reliability indices for the optimal solution.

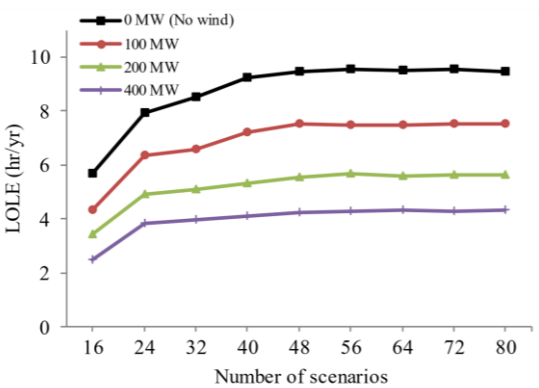

Fig. 5. LOLE values in IEEE-RTS for different numbers of scenarios.

TABLE 5
BEST RESULT VALUES FOR DIFFERENT ALGORITHMS IN RBTS

Case study	Cost (K$)		
	SFLA	PSO	GA
case 1	5362.82	5364.16	5365.53
case 2	27.45	27.45	30.096
case 3	5515.28	5521.38	5525.88

TABLE 6
OPTIMAL SOLUTIONS OF RBTS IN DIFFERENT CASES

Case study	WTG type (No. of WTGs)	
	Borujen	Moghar
case 1	W12 (11)	W12 (9)
case 2	W4 (11)	W4 (9)
case 3	W8 (15)	W12 (5)

The convergence characteristics of the SFLA, PSO, and GA methods are depicted in Fig. 6. The SFLA has superior performance and converges to a better solution faster than the other algorithms. For a better comparison between the algorithms, the SFLA, PSO, and GA are applied 20 times to solve the problem in Case 1, and the results are graphically depicted in Fig. 7. This figure presents the best, average, and worst values obtained by these methods. The results of the SFLA are better than the others, which proves its superiority in terms of success rate and solution quality.

TABLE 7
COMPONENTS OF THE OBJECTIVE FUNCTION FOR OPTIMAL SOLUTION OF RBTS

Case	Total cost (K$)	Annual Investment cost (K$/yr)	O&M cost (K$/yr)	Energy not Served cost (K$/yr)	LOLE (hr/yr)	EENS (MWh/yr)
1	5362.82	4121.87	1200	40.95	0.810	6.480
2	5424.26	4196.81	1200	27.45	0.467	4.343
3	5515.28	4121.87	1215	178.42	3.198	28.23

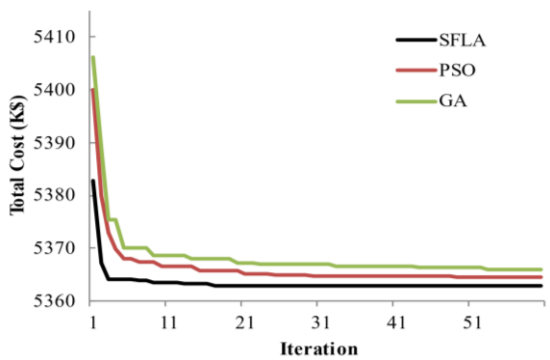

Fig. 6. Convergence characteristics of algorithms in case 1 of RBTS.

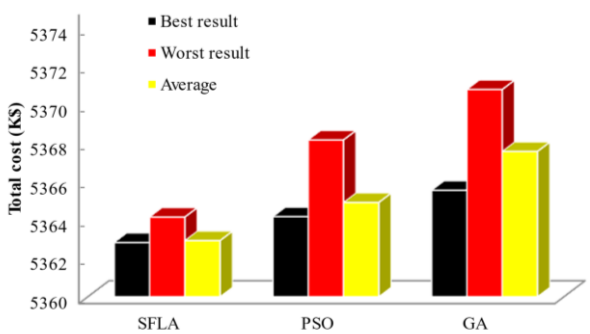

Fig. 7. Best, worst, and average values of algorithms in case 1 of RBTS.

The best values of the objective function in Case 2, obtained by different algorithms, are illustrated in Table 5. In this case, both SFLA and PSO reached the optimal solution, which is provided in Table 6. A comparison of the results for Cases 1 and 2 shows that the optimal plans for these cases significantly differ due to their different objective functions. In case 2, as shown in Table 7, the reliability of the generation system is better than in Case 1. However, the total cost in Case 1 is lower

than in Case 2. The results demonstrate the suitability of the proposed approach in searching for different objectives.

Case 3 was introduced to express the effectiveness of the proposed approach in different cases. The results of this case, obtained using various algorithms, are listed in Table 5. The optimal solution obtained by SFLA is better than the other algorithms. This solution is shown in Table 6. In Case 3, the types of the installed WTG units are W8 and W12, whereas in Cases 1 and 2, they are W12 and W4, respectively. The results of this case (Table 7) show that when the peak load of the system is increased, the reliability cost becomes more important in the total cost.

D. IEEE-RTS case study

To express the ability of the proposed approach for solving the problem in a larger-scale power system, it is applied to the RTS system. The RTS is a 24-bus system with 32 conventional generating units. The system peak load and the total generation capacity are 2850 MW and 3450 MW, respectively. All four wind sites are considered to add WPPs to the RTS. Two case studies are examined here. In Case 1, the total WPP capacity limitation is 500 MW. The maximum and minimum capacity constraints at every wind site are 200 and 20 MW, respectively. In Case 2, the customer energy not served cost is considered as the objective function instead of the original one.

The best values of the objective function in both cases, obtained via the SFLA, PSO, and GA methods, are given in Table 8. The results of the SFLA are superior to the others in both case studies. The optimal solutions for these cases are shown in Table 9. Various components of the objective function for these cases are also depicted in Table 10. Because of the different objective functions used in the model, there is a considerable difference between optimal plans and reliability indices. In Case 2, the WTG types for all four wind sites are type W4, whereas in Case 1, they are W4, W8, and W12.

TABLE 8
BEST OBJECTIVE FUNCTION VALUES FOR DIFFERENT ALGORITHMS IN RTS

Case study	Cost (K$)		
	SFLA	PSO	GA
case 1	69592.86	69625.14	69648.76
case 2	2218.11	2241.29	2258.26

TABLE 9
OPTIMAL SOLUTIONS OF RTS IN DIFFERENT CASES

Case	WTG type (No. of WTGs)			
	Borujen	Moghar	Moorche-khort	Varzane
1	W4 (81)	W12 (10)	W12 (59)	W8 (100)
2	W4 (87)	W4 (10)	W4 (53)	W4 (100)

Fig. 8 displays the convergence characteristics for the different optimization algorithms. The SFLA converges to a better solution with a high convergence speed. Results of Case 1, obtained from 20 independent runs using different algorithms, are illustrated in Fig. 9. The best, average, and worst results of the SFLA are better than those of other algorithms. In RTS, the performance of SFLA is more evident where the number of decision variables is increased compared to the RBTS system.

TABLE 10
COMPONENTS OF THE OBJECTIVE FUNCTION FOR OPTIMAL SOLUTIONS OF RTS

Case	Total cost (K$)	Annual Investment Cost (K$/yr)	O&M cost (K$/yr)	Energy not served cost (K$/yr)	LOLE (hr/yr)	EENS (MWh /yr)
1	69592.86	51826.84	15100	2666.01	3.80	423.18
2	69678.22	52460.11	15000	2218.11	3.25	352.08

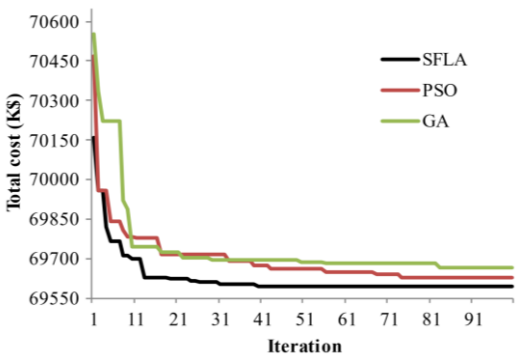

Fig. 8. Convergence characteristics of algorithms in case 1 of RTS.

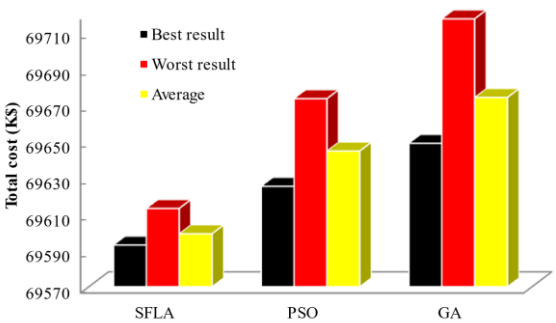

Fig. 9. Best, worst, and average values of algorithms in case 1 of RTS.

E. Considering the correlation between input data

To demonstrate the impact of considering the correlation between input data on the optimal planning schemes, the installed capacity of WPPs for RBTS and RTS is depicted in Figs. 10 and 11, respectively. Based on Fig. 10, although the average wind speed in Borujen is lower than Moghar, more capacity of WPP is installed in the Borujen wind site. This is due to the greater adaptation between hours with high electricity demand and high wind speed in Borujen compared with Moghar. Similar results can be observed in Fig. 11, where

the results of RTS are shown. Because of the suitable adaptation between the load and wind speed in Borujen, the installed capacity is more than Moghar and Moorche-Khort which have a higher average wind speed than Borujen. These results demonstrate the importance of considering the correlation between the input data in wind power planning studies.

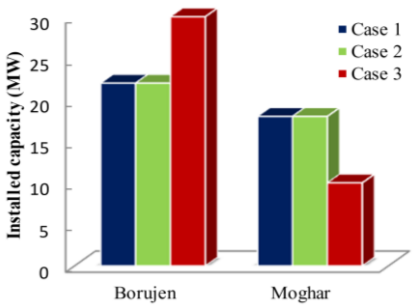

Fig. 10. Installed capacity of WPPs in RBTS system.

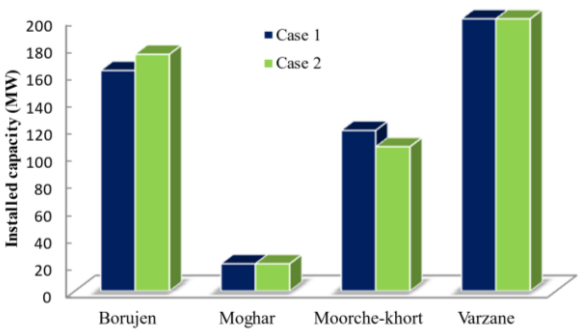

Fig. 11. Installed capacity of WPPs in RTS system.

F. Sensitivity analysis

Herein, the effect of wind speed variations on the planning results is analyzed. To this end, wind power planning is carried out while neglecting wind power uncertainty in the RBTS test system (Case I). The results are compared with the results of considering wind power uncertainty (Case II). In both cases, the peak load is 185 MW, and the objective function is energy not served cost. It is assumed that the wind speed at the wind sites varies from -10% to +10% of the original values. The LOLE reliability index for both cases is depicted in Fig. 12. Case II is more robust than Case I. Especially when the wind speed is reduced, there is a significant increase in the LOLE index in Case I and, consequently, the cost of unsupplied energy. Furthermore, with increasing the wind speed, there is a slight improvement in the LOLE index for this case. Accordingly, the proposed approach for wind power planning considering the uncertainties is more flexible and robust, which can help the planner reduce the costs and system risks.

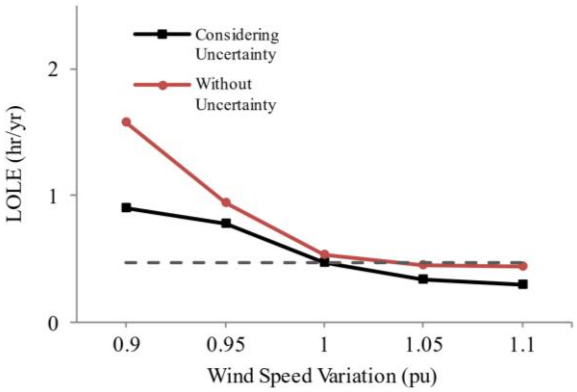

Fig. 12. LOLE index versus wind speed variations.

VI. Conclusion

This paper presents an approach for identifying optimal wind power investment plans, considering the uncertainty and correlation of electric load and wind power. The SFLA method is successfully applied to solving the proposed model. Based on the results of different case studies, the following conclusions can be drawn: 1) Statistical correlations between electric load and wind speeds significantly affect the optimal WPP investment plans. Thus, considering load and wind speeds as independent phenomena may result in non-optimal decisions. 2) A high average wind speed at a specific wind site is not sufficient for the better reliability performance of a WPP. The amount of adaptation between hours with high electricity demand and those with high wind speed also plays a key role in this regard. 3) When reliability receives more attention, the impact of the adaptation between wind and load speeds on the results becomes more salient. 4) Future works should include the development of a model considering the reactive power and transmission lines in the planning procedure.

References

[1] E. Jafari, "Coordinated Operation of Wind Farms, Cascaded Hydro, Photo-voltaic, and Pump-storage Considering WT-ANN-ICA Hybrid Prediction Method," *International Journal of Industrial Electronics, Control and Optimization,* vol. 4, no. 1, pp. 127-139, 2021.

[2] M. Jadidoleslam, A. Ebrahimi, and M. A. Latify, "Probabilistic transmission expansion planning to maximize the integration of wind power," *Renewable Energy,* vol. 114, pp. 866-878, 2017.

[3] R. Billinton and Y. Gao, "Multistate Wind Energy Conversion System Models for Adequacy Assessment of Generating Systems Incorporating Wind Energy," *IEEE T Energy Conver,* vol. 23, pp. 163-170, 2008.

[4] M. Haji-Bashi and A. Ebrahimi, "Markovian Approach Applied to Reliability Modeling of a Wind Farm," *Turk J Electr Eng Co,* vol. 22, pp. 287-301, 2014.

[5] S. Eryilmaz, İ. Bulanık, and Y. Devrim, "Reliability based modeling of hybrid solar/wind power system for long term performance assessment," *Reliability Engineering & System Safety,* vol. 209, pp. 1074-78, 2021.

[6] A. Heshmati and H. R. Najafi, "Wind farm incorporation in

reliability assessment of power systems from the viewpoint of reactive power management," *Journal of Energy Management and Technology,* vol. 4, no. 4, pp. 57-67, 2020.
[7] S. Eryilmaz and J. Navarro, "A decision theoretic framework for reliability-based optimal wind turbine selection," *Reliability Engineering & System Safety,* vol. 221, p. 108291, 2022.
[8] S. Rebennack, "Generation Expansion Planning under Uncertainty with Emissions Quotas," *Electr Pow Syst Res* vol. 114, pp. 78-85, 2014.
[9] M. Jadidoleslam and A. Ebrahimi, "Reliability Constrained Generation Expansion Planning by a Modified Shuffled Frog Leaping Algorithm," *Electr Pow Energy Syst,* vol. 64, pp. 743-751, 2015.
[10] O. H. Abdalla, L. Smieee, M. A. A. Adma, and A. S. Ahmed, "Two-stage robust generation expansion planning considering long- and short-term uncertainties of high share wind energy," *Electric Power Systems Research,* vol. 189, p. 106618, 2020.
[11] S. Mokhtari and K. K. Yen, "Impact of large-scale wind power penetration on incentive of individual investors, a supply function equilibrium approach," *Electric Power Systems Research,* vol. 194, p. 107014, 2021.
[12] L. Baringo and A. J. Conejo, "Risk-constrained multi-stage wind power investment," *IEEE Trans Power Syst,* vol. 28, pp. 401-411, 2013.
[13] A. Naderipour *et al.*, "Optimal design of hybrid grid-connected photovoltaic/wind/battery sustainable energy system improving reliability, cost and emission," *Energy,* vol. 257, p. 124679, 2022 2022.
[14] S. M. H. Baygi and J. Farzaneh, "Application of Artificial intelligence techniques for optimum design of hybrid grid-independent PV/WT/battery power system," *International Journal of Industrial Electronics, Control and Optimization,* vol. 3, no. 3, pp. 275-290, 2020.
[15] R. Krishnakumar and C. S. Ravichandran, "Reliability and Cost Minimization of Renewable Power System with Tunicate Swarm Optimization Approach Based on the Design of PV/Wind/FC System," *Renewable Energy Focus,* vol. 42, pp. 266-276, 2022.
[16] T. Cai, M. Dong, H. Liu, and S. Nojavan, "Integration of hydrogen storage system and wind generation in power systems under demand response program: A novel p-robust stochastic programming," *International Journal of Hydrogen Energy,* vol. 47, no. 1, pp. 443-458, 2022.
[17] R. Li, S. Guo, Y. Yang, and D. Liu, "Optimal sizing of wind/ concentrated solar plant/ electric heater hybrid renewable energy system based on two-stage stochastic programming," *Energy,* vol. 209, p. 118472, 2020.
[18] S. Wharton and J. K. Lundquist, "Atmospheric Stability Affects Wind Turbine Power Collection," *Environ Res Lett,* vol. 7, pp. 1-9, 2012.
[19] R. Xu and D. Wunsch, "Survey of Clustering Algorithms," *IEEE Trans Neural Net,* vol. 16, pp. 645-678, 2005.
[20] R. Billinton and A. A. Chowdhury, "Incorporation of wind energy conversion systems in conventional generating capacity adequacy assessment," *IEE Proc. C* vol. 139, pp. 47-56, 1992.
[21] R. Billinton and R. N. Allan, *Reliability Evaluation of Power Systems*, 2nd ed. Plenum, 1996.
[22] H. Seifi and M. S. Sepasian, *Electric Power System Planning: Issues, Algorithms and Solutions*. Springer 2011.
[23] R. Billinton and W. Wangdee, "Predicting Bulk Electricity System Reliability Performance Indices Using Sequential Monte Carlo Simulation," *IEEE T Power Deliver,* vol. 21, pp. 909-917, 2006.
[24] M. M. Eusuff and K. Lansey, "Optimization of Water Distribution Network Design Using the Frog Leaping Algorithm," *J Water Res Planning Manage,* vol. 129, pp. 21-25, 2003.
[25] M. Wang, Q. Zhang, H. Chen, A. A. Heidari, M. Mafarja, and H. Turabieh, "Evaluation of constraint in photovoltaic cells using ensemble multi-strategy shuffled frog leading algorithms," *Energy Conversion and Management,* vol. 244, p. 114484, 2021.
[26] R. Billinton *et al.*, "A Reliability Test System for Educational Purposes-Basic Data," *IEEE Power Engineering Review,* vol. 9, pp. 67-68, 1989.
[27] Reliability Test System Task Force, "The IEEE reliability Test System-1996," *IEEE Trans Power Syst,* vol. 14, pp. 1010-1020, 1999.
[28] Renewable Energy Organization of Iran. (2016). *Wind Energy Office Data.* Available: http://www.suna.org

Morteza Jadidoleslam received the B.Sc. degree from the Shahid Bahonar University of Kerman, Kerman, Iran, in 2008, the M.Sc. degree from the Isfahan University of Technology, Isfahan, Iran, in 2011, and the Ph.D. degree from Isfahan University of Technology, Isfahan, Iran, in 2017, all in electrical engineering. He is currently an Assistant Professor in the Department of Electrical Engineering, Sirjan University of Technology, Sirjan, Iran. His research interests are power system planning and operation, renewable energy, and micro grids.

Morteza Ghaseminezhad was born in Bardsir, Iran, in 1985. He received the B.Sc. degree from Electrical Engineering Department of Shahid Bahonar University, Kerman, Iran, in 2007 and the M.Sc. and Ph.D. Degree in electrical engineering from Shahed University, Tehran, Iran, in 2010, and 2017, respectively. At the present, he is the assistant professor of electrical engineering department in Sirjan University of Technology. His especial fields of interest include transient in power systems, power quality and electrical machines.

IECO

This page intentionally left blank.

International Journal Of
Industrial Electronics Control and Optimization
Print ISSN: 3517-2645
Online ISSN: 3568-2645
Homepage: https://ieco.usb.ac.ir/

Design of optimal sliding mode control based on linear matrix inequality for fractional time-varying delay systems

Mohammad Ghamgosar[1] | Seyed Mehdi Mirhosseini-Alizamini[2]| Mahmood Dadkhah[3]

Academic Center for Education, Cultural and Research (ACCECR), Rasht, Iran[1]
Department of Mathematics, Payame Noor University (PNU), Tehran, Iran[2,3]
Corresponding author's email: m_mirhosseini@pnu.ac.ir

Article Info

Article type:
Research Article

Article history:
Received: 20 April 2022
Revised: 18 Sep 2022
Accepted: 19 Sep 2022
Published online: 25 Nov 2022

Keywords:
Delay systems,
Integral sliding mode,
Linear quadratic regulator,
Fractional order systems,
Optimal sliding mode.

ABSTRACT

This paper considers an optimal sliding mode control based on the cost control guaranteed approach using the linear quadratic regulator method to stabilize delay fractional under involved disturbance. We propose an approach to an open research problem in the design of an LMI-based sliding mode controller in which there are some constraints such as optimizing system performance. The sliding mode technique is well-known as an effective tool for calculating the transient response of the system and achieving robust system performance. LQR classic techniques are less effective for studying an optimal fractional system in the presence of disturbance due to nonlinearity, so we use the optimal sliding mode approach control law designed for the nominal system and, then, combined it with a fractional sliding mode controller. By using the Razumikhin theorem for the stability of fractional order systems with delay and linear matrix inequality, conditions on asymptotically stabilization were obtained. The presented controller stabilizes the nominal system and guarantees an adequate level of system performance. The sliding mode controller presented in the article, in addition to eliminating the effect of disturbance in the system, is independent of the delay A numerical example was provided to illustrate the effectiveness of the main results.

I. Introduction

The linear quadratic regulator (LQR) method is a major problem in optimal control [1,2,3]. From an engineering point of view, it is desirable to design control systems that are only asymptotically stable, but can also ensure an appropriate level of system performance. As the cornerstone of modern control theory, the optimal control technique has a major limitation because it usually requires an accurate mathematical model of the system. Therefore, a precise definition of the system is required to determine the optimal controller. If the system is subject to any uncertainty due to parameter changes or external disturbances during the process, including input and output interference, sensor noise and actuator noise, the optimal controller will most likely not work properly [4]. However, all the physical systems are affected by uncertainty and deviate from the desired value [5]. Such uncertain conditions may even lead to system instability. Therefore, an optimal controller must be robust to ensure attenuated performance in the event of uncertainty. In the field of robust control, sliding mode control has become widely popular as a successful control strategy for nonlinear systems [6,7,8 ,9,10,11]. In the early 1970, sliding mode control gained considerable attention, due to the simplicity and inherent strength of uncertainties [12,13]. Sliding mode controllers consist of a discontinuous control input that directs the controlled system to a specified sliding surface. When the system is on the sliding surface, it is protected from uncertainty. In [14], a linear fractional system with delayed input was studied. The sliding surface used was a fractional sliding surface. In [15], the LQR problem was studied for a class of nonlinear and non-fractional systems in the presence of perturbation. The fractional sliding mode was

DOI: 10.22111/IECO.2022.42132.1423

employed to eliminate the perturbation effect. Lyapunov theorem was adopted for the stability of the system. In this study, the delay effect was not considered. Given that LQR plays a key role in the design of optimal control [16,17] and is widely used in engine control, chemical process control , aircraft flight control, etc., research on the design of sliding mode controllers using the LQR strategy for nonlinear systems is still an important research topic [18,19]. Usually, the most conservative scenario is designed for the worst-case scenario where system uncertainties and external disturbances predominate. In such cases, stability is the main concern that needs serious attention. However, during nominal system operation, stability is not the only concern of controller design, criteria such as minimizing control input gain and faster convergence to the point of equilibrium also merit attention in the nominal system process stage. On the other hand, near the point of equilibrium, when uncertainties become the main factor, the sliding mode controller is ideally suited as the controller. To ensure this dual purpose, the optimal control strategy is integrated with the sliding mode controller to achieve optimal sliding mode control (OSMC) [8]. Research on optimal sliding mode control is ongoing. In the optimal sliding mode method, optimal control is designed for a nominal system such that it is stable has optimal performance and is then combined with a sliding mode controller. For this, we find an upper bound for the LQR cost function that ensures its performance. The plan of the switching surface can guarantee asymptotic stability and desired performance. In recent years, different results have been derived for nonlinear fractional-order systems [4,11,20,21]. The combination of optimal control with SMC-based methods preserves the main benefits of this technique. Tanks to its, simplicity and inherent robustness towards the matched uncertainty, it also provides greater precision and optimal performance. The tool that has been considered in recent research is linear matrix inequality (LMI). Using an LMI and based on several variables called decision variables, the negative definite of a certain matrix can be determined [22]. In [19], an optimal sliding mode controller was presented for non-fractional and uncertain systems by using an integral sliding surface. In [5], an optimal second-order sliding mode control method was utilized to stabilize non- fractional and nonlinear systems affected by uncertainties. In [23], a second-order sliding mode control was proposed for finite-time bounded and nonlinear fractional-order systems without delay. Given the existing work, slight attention has been paid to the problem of sliding mode design for nonlinear and fractional systems. The design of the LMI-based sliding mode controller, in which there are some constraints such as optimizing system performance, is still an open research problem. In his paper, we solve this problem for the asymptotic stability of a class of delayed nonlinear systems in the presence of perturbations. We design a delay-independent sliding mode controller to ensure system stability and optimization. This paper uses a cost control guaranteed approach which provides a high limit on the system performance index and ensures that the system performance reduction due to uncertainties is less than this limit. Based on this idea, many significant results are presented for nonlinear systems with an integer order. Fractional order systems have special features compared to non-fractional order systems, so analyzing the stability of fractional order systems is more complex and difficult than integer order systems. In particular, it is difficult to solve the control problem using the cost control guaranteed method for fractional order systems [23,24]. Section 2 is devoted to the necessary preliminaries of LMI and fractional calculus including Razumikhin stability for fractional order systems with delay. The problem statement is given in Section 3. In Section 4, we present an optimal state feedback control law for nominal system. In Segment 5, we plan a delay independent and optimal SMC technique, and a condition based on a linear matrix inequality and prove the stability of the system. In Section 6, the numerical example is simulated to demonstrate the reasonableness of our theory. Finally, we conclude the paper in Section 6.

II. FUNDAMENTAL CONCEPTS

Notations ${}_{t_0}^{C}D_t^{\alpha}z(t)$ and ${}_{t_0}I_t^{\alpha}z(t)$ denote fractional operators, the Caputo derivative, and the Riemann-Liouville integral of function z(t), respectively.

Lemma 1. [25]. For differentiable function $z(t)$, the following relation between ${}_0^{C}D_t^{\alpha}z(t)$ and ${}_0I_t^{\alpha}z(t)$ holds:

$${}_0I_t^{\alpha}({}_0^{C}D_t^{\alpha}z(t)) = z(t) - z(0), \qquad 0 < \alpha < 1.$$

Lemma 2. [26]. Let $z(t) \in \mathbb{R}^n$ be a vector of differentiable function, the following inequality holds:

$$\frac{1}{2}D^{\alpha}\left(z^T(t)Pz(t)\right) \le z^T(t)\Theta D^{\alpha}z(t), \qquad \forall\alpha \in (0,1).$$

where $\Theta \in \mathbb{R}^{n\times n}$ and $\Theta = \Theta^{\mathrm{T}} > 0$.

Lemma 3.. [27]. For constant matrices $\Theta_1, \Theta_2, \Theta_3$ where Θ_1 and Θ_2 are symmetric, and $\Theta_2 > 0$, then $\Theta_1 + {\Theta_3}^T{\Theta_2}^{-1}\Theta_3 < 0$, if and only if :

$$\begin{bmatrix}\Theta_1 & {\Theta_3}^T\\ \Theta_3 & -\Theta_2\end{bmatrix} < 0.$$

Lemma 4. [6]. For any matrix Θ_1 and Θ_2 with compatible dimensions, and for $\delta > 0$, and vectors $z, x \in \mathbb{R}^n$ we have

$$2z^T\Theta_1\Theta_2 x \le \delta\ z^T{\Theta_1}^T\Theta_1 z + \delta^{-1}x^T{\Theta_2}^T\Theta_2 x.$$

Theorem 1. [28]. For the delay fractional system as follows:

${}_{to}^{C}D\ {}_{t}^{\alpha}z(t) = f(t, z_\theta)$.

where $z(t) \in \mathbb{R}^n$, $z_\theta(t) = z(t+\theta), -h \le \theta \le 0$, suppose that $v_1, v_2, v_3 : \mathbb{R}^+ \to \mathbb{R}^+$ are scalar, continuous and non-decreasing functions, and $v_1(0) = v_2(0) = v_3(0) = 0$, $v_2(.)$ is strictly increasing, if there exists a continuous function $V : \mathbb{R}^+ \times \mathbb{R}^n \to \mathbb{R}^+$ such that:

(i) $v_1(\|z\|) \le V(t,z) \le v_2(\|z\|)$,

(ii) $D\ {}_{t}^{\alpha}V\big(t, z(t)\big) \le -v_3(\|z\|)$, $0 < \alpha \le 1$, provided

$V\big(t+\theta, z(t+\theta)\big) \le V\big(t, z(t)\big), \quad \theta \in [-\tau, 0]$

for $q > 1$, $-h \le \theta \le 0$, and $t \ge 0$, then system (1) is uniformly stable.

III. PROBLEM STATEMENT

Consider the fractional system with state time-delay described by:

$$ {}_{t_0}^{C}D_t^{\alpha} z(t) = A_0 z(t) + A_{\ d}\ z(t-h) + Bu(t) + \omega\big(t, z(t)\big), \quad t \ge t_0. \qquad (2)$$

$$ z(t) = \Psi(t), \qquad t_0 - h \le t \le t_0. $$

where $0 < \alpha < 1$, and $z(t) \in \mathbb{R}^n$, and $u(t) \in \mathbb{R}^m$, are the state and control vectors, respectively, and $A_0, A_{\ d}$, B are constant matrices with appropriate dimensions. Moreover, the vector $\omega : \mathbb{R}^n \to \mathbb{R}^n$, represents the system nonlinearity and any model uncertainties in the system including external disturbances, which is Lipschitz:

$$ \exists \lambda > 0, \qquad \|\omega(z(t)\| \le \lambda \|z(t)\|, \forall z(t) \in \mathbb{R}^n. \qquad (3)$$

$\Psi(t) \in C([t_0 - h, t_0], \mathbb{R}^n)$ is the continuous initial state function; and h > 0 is the constant time-delay of the system. In this paper, the control law is designed based on the sliding surface technique to stabilize the time-delay system (2) in the face of external disturbance. The task is to design an asymptotically stabilizing control law that also minimizes the following cost functional:

$$ J = {}_0 I_t^{\alpha}\big(z^T(t)Qz(t) + u^T(t)Ru(t)\big)dt, \qquad (4)$$

where $Q \in \mathbb{R}^{n\times n}$, and $R \in \mathbb{R}^1$ are positive definite weighing matrices, respectively and integral I is the Riemann-Liouville fractional integral.

Assumption 1. The cost functional is minimized such that the following relation holds for the LQR cost function [25]:

$$ J = {}_0 I_t^{\alpha}(z^T(t)Qz(t) + u^T(t)Ru(t))dt < \tilde{J}, \tilde{J} \in \mathbb{R} \qquad (5)$$

(1)

IV. OPTIMAL CONTROLLER DESIGN

In the following, we design two control laws. First, an optimal control law u_1 is designed for the nominal system such that the nominal system be stable and Eq. (5) holds for LQR cost function. Then, u_1 combines with a switching control law u_2 to reduce external disturbances. Neglecting the nonlinearity term, the nominal system with the delay of (2) becomes

$$ {}_{t_0}^{C}D_t^{\alpha} z(t) = A_0 z(t) + A_{\ d}\ z(t-h) + Bu_1(t), \qquad (6)$$

The cost functional that should be minimized should hold to Eq. (5). In this section, we find an optimal state control $u_1 = Kz(t)$ introduced using the stability criteria in theorem (1) for system (6).

Theorem 2. The state feedback control law $u_1 = kz(t)$, stabilizes the nominal system defined in (6) by minimizing the performance index (5) if there is a symmetric positive definite matrix P, a matrix Y and two positive constants δ1 and δ2, such that the following LMIs holds:

$$ \begin{bmatrix} M & I \\ I & -\delta_1 I \end{bmatrix} < 0, $$

$$ \delta_1 \|A_d\|^2 P < \delta_2 I, \qquad (8)$$

where

$M = A_0P + PA_0^T + BY + Y^TB^T + PQP + Y^TRY + \delta_2 P$, and $K = YP^{-1}$.

Proof. We can consider the following Lyapunov function:

$$ V(t) = z^T(t)P^{-1}z(t). $$

It can be easily observed that $V(t) = z^T(t)P^{-1}z(t)$ is bounded by $v_1(t) = \lambda_{min}(P^{-1})\|z\|^2$ and $v_2(t) = \lambda_{max}(P^{-1})\|z\|^2$. Therefore, the first condition of theorem (1) is satisfied. Now, according to theorem (1), we consider the second condition of the Razumikhin stability theorem. To this end we consider the closed-loop system as follows:

$$ {}_{t_0}^{C}D_t^{\alpha} z(t) = A_0 z(t) + A_{\ d}\ z(t-h) + Bu(t) = (A_0 + Bk)z(t) + A_{\ d}\ z(t-h). \qquad (9)$$

According to lemma (2), we have

$$ D^{\alpha}V(t) \le 2z^TP^{-1}D^{\alpha}z(t) \le 2z^TP^{-1}[(A_0 + BK)z(t) + (A_{\ d})\ z(t-h) \le 2z^TP^{-1}(A_0 + BK)z(t) 2z^TP^{-1}\ (A_{\ d})\ z(t-h). $$

Considering the above relation as a sum of two terms, we have for the first term:

$$ 2z^TP^{-1}(A_0 + BK)z = z^T[P^{-1}A_0 + A_0^TP^{-1} + P^{-1}BK + K^TB^TP^{-1}]z. \qquad (10)$$

and for the second term, according to lemma (4):

$$2z^T P^{-1}\ A_d\ z(t-\tau) \le \delta_1 z^T(t-h)A_\tau^T A_\tau\ z(t-h) + \delta_1^{-1} z^T P^{-1} P^{-1} z. \quad (11)$$

By combining these two relations and considering Eq. (3), it is straightforward to see that:

$$D^\alpha V(t) \le z^T[P^{-1}A_0 + A_0^T P^{-1} + P^{-1}BK + K^T B^T P^{-1} + \delta_1^{-1}P^{-1}P^{-1} + Q + K^T RK]z + \delta_2 z^T(t-h)P^{-1}z(t-h) - z^T[Q + K^T RK]z.$$

Now, if the following assumption holds

$$V\big(t+s, z(t+s)\big) = z^T(t+s)P^{-1}z(t+s) < q^* z^T P^{-1} z; \qquad s \in [-h, 0],$$

where $q^* = 1+\delta, \delta > 0$, then by substituting $s = -h$, and from (4.3), $\delta_1 \|A_d\|^2 P < \delta_2 I$, we have

$$D^\alpha V(t) \le z^T[P^{-1}A_0 + A_0^T P^{-1} + P^{-1}BK + K^T B^T P^{-1} + \delta_1^{-1}P^{-1}P^{-1} + Q + K^T RK]z + q^*\delta_2 z^T P^{-1} z - z^T[Q + K^T RK]z.$$

Because $q^* = \delta + 1$ by $\delta \to 0$, and also P and Q are positive definite matrices, so

$$D^\alpha V(t) \le z^T M_2 z - z^T[Q + K^T RK]z \le z^T M_2 z.$$

where

$$M_2 = P^{-1}A_0 + A_0^T P^{-1} + P^{-1}BK + K^T B^T P^{-1} + \delta_1^{-1}P^{-1}P^{-1} + Q + K^T RK + \delta_2 P^{-1}.$$

Now, pre and post multiplying both sides of M_2 by P and let $K = YP^{-1}$ we have:

$$M_1 = A_0 P + PA_0^T + BY + Y^T B^T + \delta_1^{-1} I + PQP + Y^T RY + \delta_2 P.$$

we have $M_2 < 0$ if $M_1 < 0$. From the Schur complement lemma, $M_1 < 0$ is equal to

$$\begin{bmatrix} M & I \\ I & -\delta_1 I \end{bmatrix} < 0,$$

where $M = A_0 P + PA_0^T + BY + Y^T B^T + PQP + Y^T RY + \delta_2 P$.

Thus, according to theorem (1), the closed- loop system (9) is stable. Finally, we have

$V(t) = z^T(x)P^{-1}z(t) > 0$, also:

$$\lambda_{min}(P^{-1})\|z(0)\|^2 \le V(t) \le \lambda_{max}(P^{-1})\|z(0)\|^2$$

Moreover, $D^\alpha V(t) < 0$, Q and R are positive definite matrices, so by using lemma (1):

$$D^\alpha V(t) + z^T[Q + K^T RK]z \le 0$$

$${}_0 I_t^\alpha z^T[Q + K^T RK]z < - {}_0 I_t^\alpha\big(D^\alpha V(t)\big) = V(0) - V(t) < \lambda_{max}(P^{-1})\|z(0)\|^2.$$

Thus, we have $\tilde{J} = \lambda_{max}(P^{-1})\|z(0)\|^2$ which completes the proof.

V. SLIDING MODE CONTROLLER DESIGN

Here, finding the parameters of a sliding mode controller guarantee that the directions of the SMC system guided to the a presupposed sliding surface in a constrained moment and the closed-loop system is asymptotically stable subject to the influences of external disturbances. To do this, we plan an integral-type sliding surface for the system. From theorem (2), the optimal controller is equal to $u_1 = Kz(t)$, so the control law for system (2) can be defined as $u = u_1 + u_2$, where u_2 is a switching control law. Here, u is the optimal sliding mode control law. Consequently, we have:

$${}_{t_0}^{C} D_t^\alpha z(t) = A_0 z(t) + A_d\ z(t-h) + Bu(t) + \omega\big(t, z(t)\big). \quad (12)$$

To combine the optimal controller with a sliding mode controller, an integral sliding surface $\Lambda(t)$is designed as

$$\Lambda(t) = CI^{1-\alpha}z(t) - \int_{t_0}^{t} C(A_0 + BK)z(\xi)d\xi \quad (13)$$

where $\Lambda(t) \in \mathbb{R}^m$ is the sliding surface, $K \in \mathbb{R}^{m\times n}$ of the gain matrix and $G \in \mathbb{R}^{m\times n}$ is also a constant matrix that must be designed in such a way that $GB \in \mathbb{R}^{m\times m}$ is non-singular. Integral I is the Riemann-Liouville fractional integral. Matrix K is designed using theorem (2). Now, we proceed to design a second-order SMC such that the reachability of the specified sliding surface $\Lambda(t)$ and $\dot{\Lambda}(t) = 0$. is ensured. Consider system (12) involving time delay, the control law u ensures the convergence of the state variables to the sliding surface inside a limited time T^*. The following theorem will prove the reachability law.

Theorem 3. Consider the time-delay system (12) with the sliding surface in (13). The following control law guarantees that all trajectories of the sliding surface reach it in the finite time:

$$u(t) = u_1(t) + u_2(t) = Kz(t) - (CB)^{-1}\rho\big(z(t)\big)sign\big(\Lambda(t)\big), \quad (14)$$

where $sign(.)$ is the sign function, and the switching gain $\rho(z(t))$ is given by:

$$\rho\big(z(t)\big) = \beta + (\|GA_d\| + \|G\|\lambda)sup\|z(t)\|, \quad (15)$$

with $\beta > 0$.

Proof. After derivating from (12), we have

$$\dot{\Lambda}(t) = GD^{\alpha}z(t) - G[(A_0 + BK)z(t)].$$

Using (11), one has

$$\begin{aligned}\dot{\Lambda}(t) &= G(A_0 z(t) + (A_d)z(t-h) \\ &+ Bu(t) + \omega(z(t)) \\ &- (G[(A_0 + BK)z(t)] \\ &= GA_d z(t-h) + GBu(t) + G\omega\big(z(t)\big) - CBKz(t).\end{aligned}$$

from (13) and the above relation one can see that

$$\dot{\Lambda}(t) = GA_d z(t-h) - \rho sign\big(\Lambda(t)\big) + G\omega\big(z(t)\big). \quad (16)$$

The following Lyapunov function is considered:

$$V(t) = 0.5\Lambda(t)\Lambda^T(t).$$

According to Eq. (14), the time derivative of Eq. (16) is obtained as:

$$\begin{aligned}\dot{V}(t) = \Lambda(t)\dot{\Lambda}(t) &= \Lambda(t)(GA_d z(t-h) - \rho\ sign\big(\Lambda(t)\big) \\ &+ G\omega(t, z(t)) \\ &\le \|GA_d z(t-\tau)\|\|\Lambda(t)\| \\ &- \rho\|\Lambda(t)\| + \|G\omega\|\|\Lambda(t)\| \\ &\le (\|GA_d z(t-h)\| + \|G\omega\|)\|\Lambda(t)\| \\ &- \rho\|\Lambda(t)\|. \quad (18)\end{aligned}$$

We also have:

$$\|z(t-\tau)\| < sup\|z(t)\|, \quad (19)$$

Substituting Eq. (19) in Eq. (18), yields

$$\begin{aligned}\dot{V}(t) &\le (\|GA_d z(t-\tau)\| + \|G\omega\|)\|\Lambda(t)\| - \rho\|\Lambda(t)\| \\ &\le (\|GA_d\| \\ &+ \|G\|\lambda)sup\|z(t)\|\|\Lambda(t)\| - \rho\|\Lambda(t)\| \\ &= (\|GA_\tau\| + \|G\|\lambda)sup\|z(t)\| \\ &- \rho)\|\Lambda(t)\| \\ &= -(-\|GA_d\| - \|G\|\lambda)sup\|z(t)\| \\ &+ \rho)\|\Lambda(t)\|.\end{aligned}$$

Thus, the control law in Eq. (14) satisfies the following condition in the presence of external disturbance, where $\rho = \beta + (\|GA_d\| + \|G\|\lambda)sup\|z(t)\|$ and $\beta > 0$:

$$\dot{V}(t) = -\beta\|\Lambda(t)\| \le 0. \quad (20)$$

Therefore, the reaching law is established. Using (20), it can be shown that the trajectories of the sliding surface reach it in a finite time T^*, where:

$$t_0 < \mathrm{T}^* \le \beta^{-1}\sqrt{2V(t_0)} + t_0.$$

In fact, from (15), we have $\dot{V}(t) \le -\beta\sqrt{V(t)}$. By integrating from this inequality, the time occurrence of the reaching phase is calculated in this way:

$$\frac{\dot{V}(t)}{\sqrt{2V(t)}} \le -\beta \rightarrow \int_{t_0}^{t} \frac{\dot{V}(\xi)}{\sqrt{2V(\xi)}}d\xi \le \int_{t_0}^{t} -\beta\ d\xi,$$

By integrating, we have:

$$\int_{t_0}^{t} \frac{\dot{V}(\xi)}{\sqrt{2V(\xi)}}d\xi = \sqrt{2V(t)} - \sqrt{2V(t_0)} \le -\beta(t - t_0)$$

Now, when $\Lambda(t) = 0$, we have $V(t) = 0$, then

$$-\beta^{-1}\sqrt{2V(t_0)} - t_0 \le -T^* \rightarrow \mathrm{T}^* \le \beta^{-1}\sqrt{2V(t_0)} + t_0.$$

This completes the proof.

By substituting u(t) from (14) in (2), the equation of the closed loop system can be derived as follows

$$\begin{aligned}{}_{t_0}^{C}D_t^{\alpha}z(t) &= A_0 z(t) + A_d z(t-h) + \omega\big(t, z(t)\big) \\ &- B(CB)^{-1}\rho(z(t))sign(\Lambda(t)). \quad (17)\end{aligned}$$

According to theorem (3), state variables reach the sliding surface in finite time, so the sliding surface for $t > T^*$, we have $\Lambda(t)=0$. As a result, the closed loop system in the sliding mode is as follows:

$$\begin{aligned}D^{\alpha}z(t) &= (A_0 + BK)z(t) + A_d z(t-h) \\ &+ w\big(t, z(t)\big). \quad (21)\end{aligned}$$

Here, we present a lemma to find the necessary conditions for the parameters of theorem (2) so that the choice of matrices K and P can ensure the asymptotic stability of the closed-loop system on the sliding surface. In the following lemma, we show that for the stability of the closed-loop system (21), in addition to (8), a linear matrix inequality must also hold.

Lemma 5. In system (2), matrix $K = YP^{-1}$, closed loop systems (18) is asymptotically stable if there is a positive number δ_3, such that the following LMI holds:

$$\begin{bmatrix} \mathrm{N}_1 & \lambda\mathrm{P} & I \\ \lambda P & -\delta_3 I & 0 \\ I & 0 & -\delta_1 I \end{bmatrix} < 0, \quad (22)$$

where $N_1 = A_0 P + PA_0^T + BY + Y^T B^T + \delta_2 P + \delta_3 I$.

Proof. The following Lyapunov function is considered, where P is the same as P in theorem (2):

$$V(t) = z^T(t)P^{-1}z(t).$$

To satisfy the first condition of theorem (1), we have $v_1(t) = \lambda_{min}(P^{-1})\|z\|^2$ and $v_2(t) = \lambda_{max}(P^{-1})\|z\|^2$. Considering Eq. (23) and lemma (2), the time derivative of Eq. (22) is obtained as:

$$\begin{aligned}D^{\alpha}V(t) &\le 2z^T P^{-1}D^{\alpha}z(t) \\ &\le 2z^T P^{-1}\big[(A_0 + BK)z(t) + (A_d)\,z(t-h) \\ &+ \omega\big(t, z(t)\big)\big] \\ &+ 2z^T P^{-1}\omega\big(t, z(t)\big). \quad (24)\end{aligned}$$

By considering the above relation as a sum of three terms,

and Eq. (3) and lemma (4), we have for the last term:

$$2z^T P^{-1}\omega \leq \delta_3 z^T P^{-1}P^{-1}z + \delta_3^{-1}\lambda^2 z^T z. \quad (25)$$

By substituting (24) in (23), and using (10) and (11), we have:

$$D^\alpha V(t) \leq z^T \left[P^{-1}A_0 + A_0^T P^{-1} + P^{-1}BK + K^T B^T P^{-1} + \delta_1^{-1} P^{-1}P^{-1} + \delta_3 P^{-1}P^{-1} + \delta_3^{-1}\lambda^2 I\right] z + \delta_1 z^T(t-h)A_d^T A_d\, z(t-h).$$

As for LMI (8) and for $q^* = \delta + 1 > 1$, the assumption $V\big(t+s, z(t+s)\big) < q^* V(t, z(t))$ for $s \in [-h, 0]$ implies:

$$D^\alpha V(t) \leq z^T[A_0P + PA_0^T + BY + Y^T B^T + \delta_1^{-1} I + \delta_2 P + \delta_3 I + \delta_3^{-1}\lambda^2 PP]z.$$

Therefore, according to the Schur complement lemma $D^\alpha V(t) < 0$, if

$$\begin{bmatrix} N_1 & \lambda P & I \\ \lambda P & -\delta_3 I & 0 \\ I & 0 & -\delta_1 I \end{bmatrix} < 0,$$

where, $N_1 = A_0P + PA_0^T + BY + Y^T B^T + \delta_2 P + \delta_3 I$. Thus, whenever $V\big(t+s, z(t+s)\big) < q^* V(t, z(t))$ is satisfied, condition $D^\alpha V(t) < 0$ is also satisfied, by using the stability criteria in theorem (1), the closed-loop system (21) is stable.

Finally, the following procedure is suggested for the design of the optimal sliding mode controller:

(I) Solve **LMI (7)** and Find matrix **K**

(II) Use **K** to design sliding mode surface $\boldsymbol{\Lambda(t)}$

(III) Compute switching control $\mathbf{u_{sw}}$

(IV) Compute equivalent control $\mathbf{u_{eq}}$

(V) Compute $\mathbf{u} = \mathbf{u_{sw}} + \mathbf{u_{eq}}$

(VI) Check the satisfaction of the **LMI (22).** If this **LMI** is satisfied, **u** is **optimal sliding mode controller** for delayed fractional order system with disturbances,

VI. SIMULATION RESULTS

In this section, we provide a numerical example to demonstrate the effectiveness of our methods. The numerical simulation is created utilizing Ninteger and Yalmip toolbox in MATLAB software.

Example. Consider the nonlinear time-delay system (2) with $\alpha = 0.7$ and the following system characteristics:

$$\boldsymbol{D^\alpha z} = \begin{bmatrix} -9 & 5 & -8 \\ -4 & -3 & 5 \\ -4 & 9 & 0 \end{bmatrix} z(t) + \begin{bmatrix} 0.4 & -1.2 & 1.9 \\ 0.2 & -0.9 & 0.1 \\ -0.1 & -0.5 & 2.7 \end{bmatrix} z(t-h) + \begin{pmatrix} 4 \\ -1 \\ 12 \end{pmatrix} u(t) + \begin{pmatrix} 0.8\sin(z_1^2(t)) \\ 0.8\sin(z_2^2(t)) \\ 0.8\sin(z_3^2(t)) \end{pmatrix}.$$

Subject to:

$$J = {}_0 I_t^\alpha \big(z^T(t)Qz(t) + u^T(t)Ru(t)\big)dt.$$

where $Q = \begin{bmatrix} 1 & 0 & 0 \\ 0 & 0.5 & 0 \\ 0 & 0 & 0.9 \end{bmatrix}$, $R = 1$. Function $\omega(t, z(t))$ is Lipschitz, and $\lambda = 0.8$. This system is unstable for u = 0 as shown in Fig. 1. In this example, we choose h = 1, 3 and 5. By applying theorem (2) and lemma (5), the LMIs conditions hold if:

$$P = \begin{bmatrix} 9.3016 & -0.3530 & 6.2433 \\ -0.3530 & 0.8247 & -1.3964 \\ 6.2433 & -1.3964 & 7.3454 \end{bmatrix},$$

$$Y = [-4, 1, -12].$$

and $\delta_1 = 4.4250$, $\delta_2 = 17.7142$, and $\delta_3 = 0.4482$.

Then the controller gain matrix can be obtained as $K = YP^{-1} = [2.9474, -6.6859, -5.4098]$. Now, by using theorem (2), we have $\tilde{J} = \lambda_{max}(P^{-1})\|z(0)\|^2 = 14.7427\|z(0)\|^2$. Matrix G is chosen $G = [-0.1, 0.1, -0.1]$. By (12), the sliding surface function can be computed by movable parameters, $\beta = 1$. According to the conditions of theorem (3) we have GB is non-singular and $\beta > 0$. By applying the control law in theorem (3), we find that the condition of the theorem is satisfied. Figs. 2-4 display the trajectories of the states of the closed-loop system with optimal SMC controller law (13). Fig. 5 presents the simulation results of the feedback control law and Fig. 6 depicts the simulation results of the sliding function. Therefore, we show that the system is stable. These figures demonstrate the efficiency of our method for selecting controller gain matrix K to guarantee robustness against perturbations and minimize the LQR cost function. This indicates that the sliding mode controller, independent of the delay, stabilizes the system. To prevent the control signals from chattering, we replace $sign\big(\Lambda(t)\big)$ with $\Lambda(t) = \frac{\Lambda(t)}{\|\Lambda(t)\| + 0.04}$.

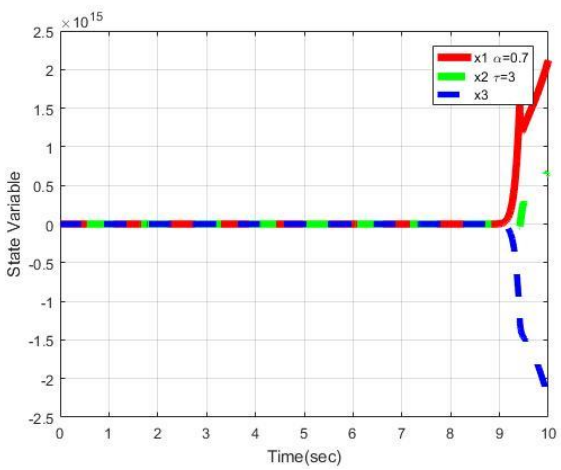

Fig. 1: Trajectories of the open-loop system with h = 1.

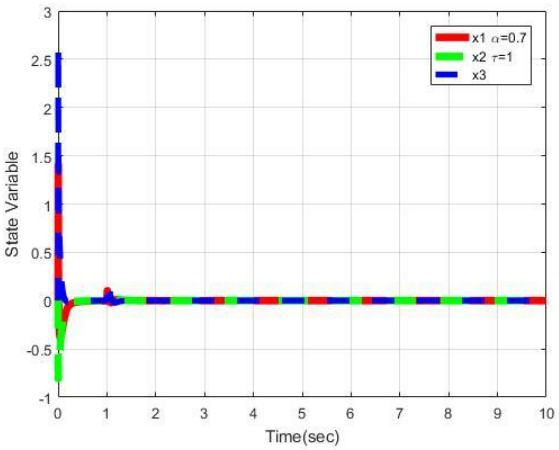

Fig. 2: Trajectories of the closed-loop system with h = 1.

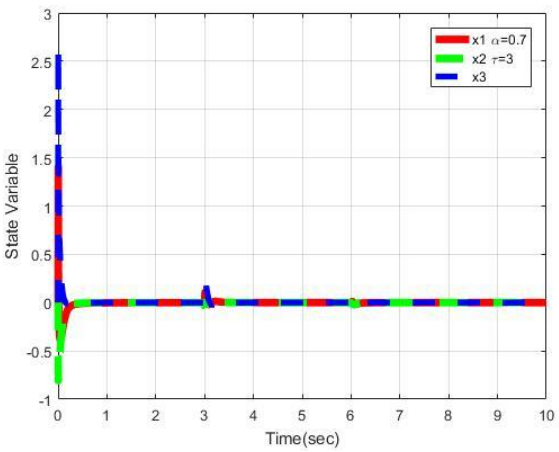

Fig. 3: Trajectories of the closed-loop system of the system with h = 3.

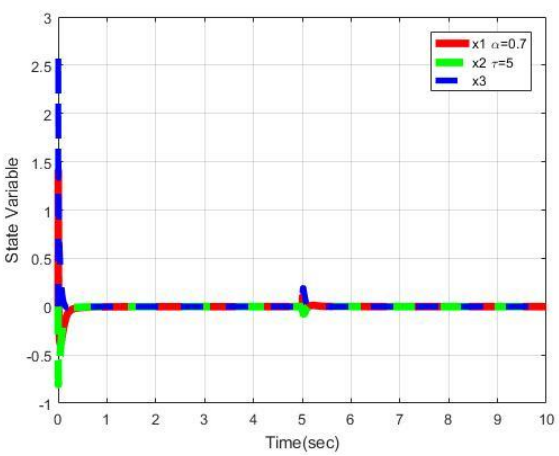

Fig. 4: Trajectories of the closed-loop system with h = 5.

Fig. 5: Feedback control law h = 3.

Fig. 6: Sliding Manifold with h = 5.

VII. Conclusions

In this paper, we studied the problem of asymptotically stabilization of a class of uncertain nonlinear fractional-order time-varying delayed systems subject to nonlinear disturbance on the basis of an LMI- based SMC with LQR cost function. We proposed new sufficient conditions expressed using LMI based on the Razumikhin approach. The performance of the main results was demonstrated using an example showing that the results of combining LQR with SMC could guarantee better efficiency of the optimal control system. We will apply the results obtained in this paper to the problem of robust FTB of fractional nonlinear time-varying delay systems using LQR-based SMC in our future work.

REFERENCES

[1] M. Imani, U.M. Braga, and S. Xiao, " Finite-horizon LQR controller for partially observed Boolean dynamical systems," Automatica, Vol. 95, pp. 172–179, 2018.

[2] S. M. Mirhosseini-Alizamani, "Solving linear optimal control problems of the time-delayed systems by Adomian decomposition method," Iranian Journal of Numerical Analysis of Optimization, Vol.9, No. 2, , pp. 165-185,2019.

[3] S. M. Mirhosseini-Alizamani, S. Effati and A. Heydari, "An iterative method for suboptimal control of a class of nonlinear time-delayed systems," Systems and Control Letters, Vol. 82, pp. 40-50, 2015.

[4] R. Sakthivel , B. Kaviarasan , P.Selvaraj and H.R. Karimi , "EID based sliding mode investment policy design for fuzzy stochastic jump financial systems," Nonlinear Analysis: Hybrid Systems, pp. 100–108, 2018.

[5] M. Li, J. Wang, "Finite time stability of fractional delay differential equations," Applied Mathematics Letters, Vol. 64, pp. 170-176, 2017.

[6] Y. Han , Y. Kao, C. Gao, J. Zhao and C.Wang , "H∞ sliding mode control of discrete switched systems with time-varying delays," ISA Trans, pp. 12–19, 2019.

[7] S. Haghighatnia , H.T. Shandiz, and A. Alfi, " Conformable Fractional Order Sliding Mode Control for a Class of Fractional Order Chaotic Systems," International Journal of Industrial Electronics, Control and Optimization, Vol. 2, pp. 177-188, 2019.

[8] Y.H Lan , L.L . Wang and C.X. Chen , "Optimal Sliding Mode Robust Control for Fractional-Order Systems with Application to Permanent Magnet Synchronous Motor Tracking Control," J Optim Theory Appl, Vol. 174, pp. 197–209, 2017.

[9] R. Sedaghati , M.R. Shakarami,, " A New Sliding Mode-Based Power Sharing Control Method for Multiple Energy Sources in the Microgrid under Different Conditions," International Journal of Industrial Electronics, Control and Optimization, Vol. 2, pp. 25-38, 2019

[10] S.S. Shamsabad Farahani , S. Fakhimi Derakhshan,, " LMI-based Congestion Control Algorithms for a Delayed Network," International Journal of Industrial Electronics, Control and Optimization, Vol. 2, pp. 91-98, 2019.

[11] Y. B. Shtessel, I. A. Shkolnikov and M. D. J. Brown, "An asymptotic second order smooth sliding mode control," Asian Journal of Control, Vol. 5, pp. 498–504, 2003.

[12] M. Li, J. Wang, "Finite time stability of fractional delay differential equations," Applied Mathematics Letters, Vol. 64, pp. 170-176, 2017.

[13] J. Li, X. Guo, C. Chen and Q. Su, "Robust fault diagnosis for switched systems based on sliding mode observer," Applied Mathematics and Computation, Vol. 341, pp. 193–203, 2019.

[14] A. Si-Ammour, S. Djennoune, and M. Bettayeb, "A sliding mode control for linear fractional systems with input and state delays," Commun Nonlinear Sci Numer Simulat, Vol. 14, pp. 2310–2318, 2009.

[15] H. Zhang, L. Cao and S. Tang, " Fractional-order sliding mode control for a class of uncertain nonlinear systems based on LQR," International Journal of Advanced Robotic Systems, Vol. 14 , pp. 367-377, 2017.

[16] M. H. Heydari, M. Razzaghi, " Extended Chebyshev cardinal wavelets for nonlinear fractional delay optimal control problems," International Journal of Systems Science , , Vol. 53, 2022.

[17] M.H. Heydari, M.Razzaghi,, " A numerical approach for a class of nonlinear optimal control problems with piecewise fractional derivative," Chaos, Solitons & Fractals, Vol. 152, 2021.

[18] K. Mathiyalagan, G. Sangeetha, "Finite-time stabilization of nonlinear time delay systems using LQR based sliding mode control," control, Journal of the Franklin Institute, Vol. 356, No. 7, pp. 3948-3964, 2019.

[19] S.D. Mulje, R.M. Nagarale, "LQR Technique based Second Order Sliding Mode Control for Linear Uncertain Systems," International Journal of Computer Applications , Vol. 137, pp. 8887–975, 2016.

[20] D. T. Hong, N. H. Sau, "Output feedback finite-time dissipative control for uncertain nonlinear fractional-order systems," Asian Journal of Control, pp. 1–10, 2021.

[21] M. V. Thuan, N. H. Sau, N. T. T. Huyen, "Finite-time H∞ control of uncertain fractional-order neural Networks," Computational and Applied Mathematics, Vol. 59, pp. 39-59, 2020

[22] B. B. He, H. C. Zhou, C. H. Kou and Y. Chen, "Stabilization of uncertain fractional order system with time varying delay using BMI approach," Asian Journal of Control, Vol. 53, 2019.

[23] K. Mathiyalagan, G. Sangeetha, "Second-order sliding mode control for nonlinear fractional-order systems," Applied Mathematics and Computation, Vol. 383, 2020.

[24] V. Phat, P. Niamsup and M. V. Thuan, " New Criteria for Guaranteed Cost Control of Nonlinear Fractional-Order Delay Systems: a Razumikhin Approach, " Vietnam J.Mah, Vol. 47, pp. 403–415 ,2019.

[25] A.A. Kilbas , H.M. Srivastava and Trujillo J.J., "Theory and Application of Fractional Differential Equations," Elsevier, New York, 2006

[26] M.A. Duarte-Mermoud , N. Aguila-Camacho , J.A. Gallegos and R. Castro-Linares, "Using general quadratic Lyapunov functions to prove Lyapunov uniform stability for fractional order systems," Communications in Nonlinear Science and Numerical Simulation, pp. 650–659, 2015.

[27] L. Chen, R. Wu, Y. Cheng and Y. Chen, "Delay dependent and order dependent stability and stabilization of fractional order linear systems with time varying delay," IEEE Transactions on Circuits and Systems II: Express Briefs, 2019.

[28] S. Liu, W. Jiang and X. Zhou, " Lyapunov stability analysis

of fractional nonlinear systems," Applied Mathematics Letters, Vol. 51, pp. 13-19, 2015.

[29] H. Shen , F. Li , J. Cao J., Z.G. Wu and G. Lu , "Fuzzy-model-based output feedback reliable control for network-based semi-Markov jump nonlinear systems subject to redundant channels," IEEE Transactions on Cybernetics, 2019.

[30] D. Sierociuk, B.M. Vinagre, "Infinite Horizon State-feedback LQR Controller for Fractional Systems," 49th IEEE Conference on Decision and Controls, pp. 15-17, 2010.

[31] M. Thuan, D. C. Huong, "New Results on Stabilization of Fractional-Order Nonlinear Systems via an LMI Approach," Asian Journal of Control, Vol. 20, No. 4, pp.1541-1550, 2018.

[32] C. Yin, Y. Chen and S. Zhong, "LMI based design of a sliding mode controller for a class of uncertain fractional order nonlinear systems," American Control Conference (ACC), pp. 6526-6531, 2013.

Mohammad Ghamgosar received his B.S. degree in Pure Mathematics from Gulian University, Rasht in 2000, his M.S. degree in Mathematics from Iranian University of Scince and Technology(IUST), Tehran in 2002, and his Ph.D. in Applied Mathematics (Control & Optimization) from PNU, Tehran in 2022 He joined the ACCECR as an researcher . His current research interests include Time delay systems, optimal control, fractional optimal control problems.

Seyed Mehdi Mirhosseini-Alizamini received his B.S. degree in Applied Mathematics from Damghan University, Damghan in 2004, his M.S. degree in Applied Mathematics (Control & Optimization) from Isfahan University of Technology, Isfahan in 2006, and his Ph.D. in Applied Mathematics (Control & Optimization) from PNU, Tehran in 2015 under the supervision of Professor Sohrab Effati at the Ferdowsi University of Mashhad, Mashhad, Iran. Currently he is an Assistant Professor at Department of Mathematics of Payame Noor University, Iran. His research interests are Time delay systems, optimal control, fractional optimal control problems and numerical methods.

Mahmood Dadkhah received his B.S. degree in Applied Mathematics from Tabriz University, Tabriz in 2001, his M.S. degree in Applied Mathematics from Sistan and Baluchestan University in 2004, and his Ph.D. in Applied Mathematics (Control & Optimization) from PNU, Tehran in 2016 under the supervision of Professor Mohammad Hadi Farahi at the University of Ferdowsi, Mashhad, Iran. He joined the Department of Mathematics at the University of Payame Noor in 2008 as a Lecturer and was promoted to Assistant Professor in 2016. His current research interests include optimal control, delay optimal control problems, differential equations and numerical methods

IECO

This page intentionally left blank.

International Journal Of
Industrial Electronics Control and Optimization
Print ISSN: 3517-2645
Online ISSN: 3568-2645
Homepage: https://ieco.usb.ac.ir/

A Novel Control to Improve Dynamic Stability of Power Systems Including DFIG and SSSC

Saeed Abazari[1]| Zabihollah Faramarzi[2]
Faculty of Engineering, Shahrekord University, Shahrekord, Iran[1,2]
Corresponding author's email: saeedabazari@yahoo.com

Article Info

Article type:
Research Article

Article history:
Received: 11 Aug 2022
Revised : 01 Nov 2022
Accepted: 15 Nov 2022
Published online: 30 Nov 2022

Keywords
DSC,
DFIG,
Dynamic Stability,
SSSC.

ABSTRACT

This study is concerned with the design of multi-input Dynamic Surface Control (DSC) to dynamic stability improvement of power systems which include both Doubly Feed Induction Generator (DFIG) and Static Synchronous Series Compensator (SSSC). The presented control method has a multi-input feature which acts on synchronous generators. To improve dynamic stability, the control law is developed by applying a suitable Lyapunov function. The coefficients of the proposed controller are determined by use of metaheuristic optimization algorithms. This optimal control law leads to a significantly improved performance in comparison with linear control. A particular low-pass filter is also introduced and applied to cancel the effects of additional undesired terms in the design method, leading to a simplified control form compared to the other available approaches in the literature. Implementing an adaptive parameter estimation scheme will result in the robustness of the proposed method. The effectiveness of the presented approach is investigated on a standard 39-Bus power system which includes DFIG and SSSC.

I. Introduction

In today's world, there is a tremendous attention to implement new sources of energy. Of particular importance, the renewable energy resources such as wind energy are at the main center of research and practical efforts. Due to the fact that the wind velocity varies with time, the DFIGs are introduced to extract maximum electrical power from wind-turbines [1, 2].

Considering load demands growth, it is quite desirable to transmit higher level of electrical power through the existing electrical transmission networks. On the other hand, dealing with the issues such as dynamic stability, insulations components, and thermal capacity of the current electrical networks all together limits the maximum possible level of electric power transmission. Moreover, the safety, technical difficulties and high cost of constructing new electrical transmission lines, reduce the possibility of expanding new transmission lines. Hence, implementing Flexible AC Transmission Systems (FACTS) to increase the capacity of the existing power networks has been rapidly attracted researcher's attentions. Among FACTS devices, SSSC is one of the sophisticated and favorable in increasing the capacity of the transmission line [3-5]. In the SSSC structure, passive elements are not employed. High level of switching mode in SSSC results in injection and absorption of active electrical power with low cost and high speed [6].

Dynamic stability of power system is one of important aspects of power system operation, which usually occurs after unwanted disturbances. In power systems equipped with SSSC and DFIG elements, dynamic stability could be further improved [7, 8]. Traditionally, Power System Stabilizers (PSS) have been used to stimulate synchronous generators. The application of PSSs to improve dynamic stability is widely studied and investigated in the recent decades. However, due to their weak local performance and occurring of problems such as Sub-Synchronous Resonance (SSR), applying PSSs is very limited. Most of the PSS design methods are based on the assumption of considering a local linear model of the power network and small signal analysis. In some recent papers, Linear Matrix Inequalities (LMIs) technique is applied to suitably place

DOI: 10.22111/IECO.2022.41721.1416

the eigenvalues of the assumed local linear models in certain points in order to improve the dynamic stability. However, due to the high intrinsic nonlinearity nature of the power networks, the mentioned approach does not guarantee the robustness of dynamic stability against parameter variations, [9, 10].

Beside the complexity in the nonlinear methods design, compared to the previous approaches applying nonlinear methods leads to robust and high-quality results. These nonlinear methods reduce sensitivity of the overall system to variations in the parameters [11, 12]. In [13], nonlinear back-stepping approach to stimulate the synchronous generators was developed to improve dynamic stability. However, DFIG and SSSC components was not implemented. A fuzzy DSC scheme was applied in the design method of [14]. However, the proposed method is limited to vary the synchronous generators stimulation field circuit. In [15-16], DFIG and SSSC components was separately employed to stimulate synchronous generators. In the current study, to improve the dynamic stability, utilizing both DFIG and SSSC devices together with nonlinear adaptive multi-input DSC method is proposed. The effects of control signals on each other and on the performance of the power system are also considered. Moreover, the parameters of the designed control law are optimized by use of intelligent algorithms in order to improve the stability. A low-pass filter is introduced in the design scheme to cancel the undesired terms in control law and to prevent large variations in control signals. Also, implementing the adaptive law for unknown parameters leads to the robustness against parameters variations.

In this paper, firstly the assumed models for DFIG and SSSC are introduced. Then, based on a third-order model for synchronous generators, a generic model for the overall power network is offered. Finally, an adaptive multi-input DSC control law is developed. The results of implementing the proposed approach are verified by performing time domain simulations implemented on the 10-machine New England test system which also includes DFIG and SSSC. The results are compared with two linear and nonlinear approaches in the literature.

TABLE 1
SI BASE UNITS

SYMBOL	VARIABLE NAME
δ_i	Rotor angle of ith generator
ω_i	Rotor speed of ith generator
$\acute{E}_{qi}$	Internal voltage of ith generator in q-axes
$\acute{E}_i$	Internal voltage of ith generator
I_{di}	Stator current of ith generator in d-axis
I_{qi}	Stator current of ith generator in q-axis
u_{fi}	Excitation voltage of ith generator
M_i	Moment of inertia of ith generator
P_{mi}	Mechanical input power of ith generator
u_d	Signal control of DFIG
TABLE 1 CONTINUED	
δ_{0i}	Rotor angle of ith generator in steady state
ω_{0i}	Rotor speed of i ith generator in steady state
V_i	Amplitude of Generator terminal voltage ith
Θ_i	Phase of Generator terminal voltage ith
$\acute{T}_{d0i}$	Constant time generator excitation coil ith
x_{di}	d-axis reactance generator steady state ith
$\acute{x}_{di}$	d-axis reactance generator transient state ith
x_{qi}	q-axis reactance generator steady state ith
X_i	EQUIVALENT REACTANCE OF DFIG IN STEADY STATE
$\acute{X}_i$	EQUIVALENT REACTANCE OF DFIG IN TRANSIENT STATE

II. Power System Modeling

A. DFIG Modelling

Figure 1. depicts the multi-machine power system including DFIG. The DFIG consists of Rotor Side Converter (RSC) and Grid Side Converter (GSC). Since the RSC plays the main role in stability improvements, the presented model is based on controlling this converter inputs. In the literature, this model is known as the synchronous generator model for DFIG. In this model, it is assumed that the stator resistance is zero. Hence, the following equations will represent the DFIG dynamic, see [17]:

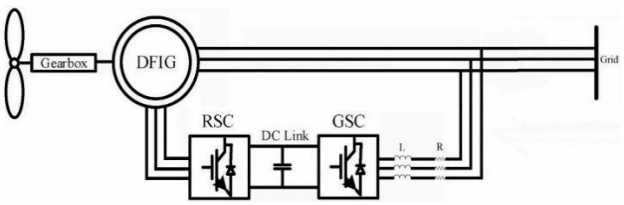

Fig 1. DFIG Connected to a Multi-Machine Network [1]

$$\dot{\delta}_i = \frac{1}{\acute{E}_{qi}T_{0i}}(-T_{0i}(\omega_i - \omega_0\ )\acute{E}_{qi} - \frac{X_i-\acute{X}_i}{\acute{E}_{qi}T_{0i}}\ V_i sin(\delta_i - \theta_i) + T_{0i}\omega_0(u_{d1i}cos(\delta_i) + u_{d2i}sin(\delta_i))]$$

$$\dot{\omega}_i = \frac{\omega_0}{2H_i}[P_{mi}\frac{\omega_s}{\omega_i} - B_{ij}\acute{E}_{qi}V_i \sin(\delta_i - \theta_i)]$$

$$\dot{\acute{E}}_i = \frac{1}{T_{0i}}(-\frac{X_i}{\acute{X}_i}\acute{E}_{qi} + \frac{X_i-\acute{X}_i}{\acute{X}_i}\ V_i cos(\delta_i - \theta_i) + T_{0i}\omega_0(u_{d1i}sin(\delta_i) + u_{d2i}cos(\delta_i))]\ )$$

(1)

where, V_i و θ_i are the amplitude and phase angle of the connected bus voltage, respectively. B_{ij} is the susceptance of admittance matrix between the DFIG and the connected buses. $\acute{E}_i$ represents the internal voltage of ith generator. V_{ri} و Φ_{ri} are respectively, the amplitude and the phase angle of the applied voltage to the DFIG rotor in polar coordinates. Finally, u_{d1i} and u_{d2i} are DFIG control inputs, which lead to the improvements in dynamic stability [17,18].

B. SSSC Model

The series converter is the applied model for SSSC. This converter injects active-power to the series link which leads to the dynamic stability improvement of connected buses voltages. According to the Fig.2, it is assumed that SSSC is placed between the ith and jth buses [19,20].

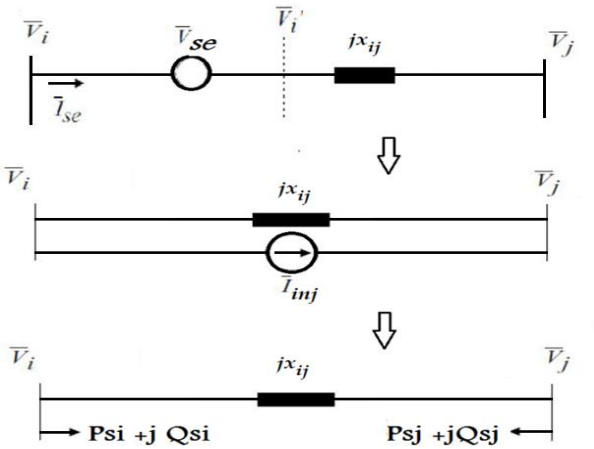

Fig. 2. a. SSSC between bus I and bus j b. equivalent circuit of SSSC c. Alternative equivalent injection model of SSSC in power system

It is possible to model the SSSC performance with a series voltage source. This series voltage, V_{se}, is controlled by the following equations:

$$\begin{cases} \bar{I}_{inj} = -jB_{ij}V_{se} \\ v_{se} = V_{se}e^{j\Phi_{se}} \\ B_{ij} = \frac{1}{x_{sij}} \end{cases} \quad (2)$$

In the presented analysis method, the SSSC is replaced by its equivalent injection model in the considered power system. The resulted configuration is depicted in Fig. 2.c. In this figure, the injected power are P_{si}، P_{sj} ، $Q_{si}$and Q_{sj} for ith and jth buses [21]:

$$\begin{aligned} P_{si} &= -B_{ij}V_{se}V_i \sin(\theta_i - \Phi_{se}) \\ Q_{si} &= B_{ij}V_{se}V_i \cos(\theta_i - \Phi_{se}) \\ P_{sj} &= B_{ij}V_{se}V_j \sin(\theta_j - \Phi_{se}) \\ Q_{sj} &= -B_{ij}V_{se}V_j \cos(\theta_j - \Phi_{se}) \end{aligned} \quad (3)$$

In this study, it is assumed that SSSC is only able to generate and consume reactive power. Therefore, its total active power generation and consumption must be zero. Since the series resistance of the of transmission lines, in which the SSSC is took places, is negligible, the SSSC voltage can be represented by the following equations:

$$\Phi_{se} = tan^{-1}\left(\frac{V_j \sin(\theta_j) - V_i \sin(\theta_i)}{V_j \cos(\theta_j) - V_i \cos(\theta_i)}\right) \quad (4)$$

C. *TOTAL POWER SYSTEM MODEL INCLUDING SYNCHRONOUS GENERATORS, DFIG, AND SSSC*

Fig.3 shows the general schematic of a power system network which includes Synchronous Generators, DFIG, and SSSC. This network consists of n1 synchronous generators, one DFIG and one SSSC. It is assumed that the mechanical input power of synchronous generators is constant. The stator's resistances are also assumed to be negligible. The total power in ith bus is modeled by $Y_i = G_i - jB_i$.

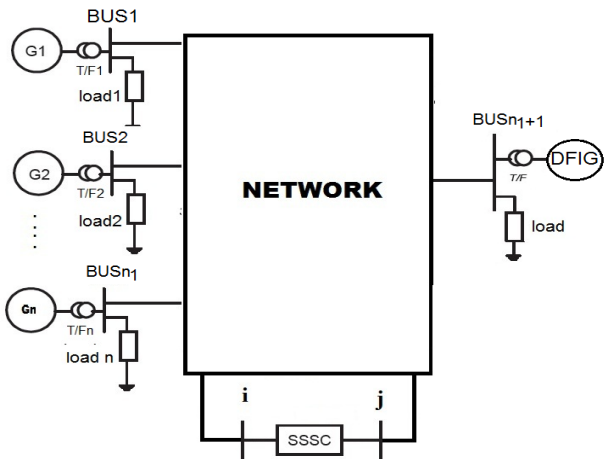

Fig.3. The Assumed Overall Power System Network

The considered model for each synchronous generator is a third-degree-equation which is described in (5). In (5), u_{fi} is the control input of the generators, see [22]:

$$\begin{aligned} \dot{\delta}_i &= \omega_i - \omega_0 \\ \dot{\omega}_i &= \frac{1}{M_i}[P_{mi} - \acute{E}_{qi}I_{qi}] \\ \dot{\acute{E}}_{qi} &= \frac{1}{\acute{T}_{d0i}}\left(u_{fi} - \acute{E}_{qi} - (x_{di} - \acute{x}_{di})I_{di}\right) \end{aligned} \quad (5)$$

The combination of the algebraic power balance equations of all connected buses to the synchronous generators with DFIG equations, in addition to the injected power of SSSC models will result in the following equations of the whole power system network model:

$$\begin{aligned} \dot{\delta}_i &= \omega_i - \omega_{0i} \\ \dot{\omega}_i &= \frac{1}{M_i}[P_{mi} - \acute{E}_{qi}I_{qi}] \\ \dot{\acute{E}}_{qi} &= \frac{1}{\acute{T}_{d0i}}(u_{fdi} - \acute{E}_{qi} - (x_{di} - \acute{x}_{di})I_{di}) \end{aligned} \quad (6)$$

$$\begin{aligned} \dot{\delta}_i &= \frac{1}{\acute{E}_i T_{0i}}\left[-T_{0i}(\omega_i - \omega_0\ )\acute{E}_i - \frac{X_i - \acute{X}_\iota}{\acute{E}_{qi}T_{0i}}V_i \sin(\delta_i - \theta_i)\right) \\ &\quad + T_{0i}\omega_0(u_{d1i}cos(\delta_i) + u_{d2i}sin(\delta_i))] \\ \dot{\omega}_i &= \frac{\omega_0}{2H_i}[P_{mi}\frac{\omega_s}{\omega_i} - B_i\acute{E}_iV_i\sin(\delta_i - \theta_i) \\ \dot{\acute{E}}_i &= \frac{1}{T_{0i}}[-\frac{X_i}{\acute{X}_\iota}\acute{E}_i + \frac{X_i - \acute{X}_\iota}{\acute{X}_\iota}\ V_i cos(\delta_i - \theta_i) \\ &\quad + T_{0i}\omega_0(u_{d1i}sin(\delta_i) + u_{d2i}cos(\delta_i))] \end{aligned} \quad (7)$$

$$\begin{cases} \dot{V}_i = \sum_{j=1}^{N} c_{ij}H_j + \sum_{j=1}^{N} d_{ij}u_{fj} + \sum_{j=1}^{N} k_{ij}\,r \\ \dot{\Phi}_i = \sum_{j=1}^{N} c_{i+n+2,j}H_j + \sum_{j=1}^{N} d_{i+n+2,j}u_{fj} + \sum_{j=1}^{N} k_{i+n+2,j}\,r \end{cases}$$

In above, (6) is the assumed dynamic model for synchronous generators, (7) is for the DFIG part and (8) describes the buses voltages of SSSC. N is the number of all the connected buses to the synchronous generators, DFIG and the connected buses to the SSSC. $B_{ij}'s$ are the elements of the reduced order admittance matrix of the power system network, where:

$$\begin{cases} \dot{\delta} = [\dot{\delta}_1 \; .. \dot{\delta}_{n1} \quad \dot{\delta}_d]^T \\ \dot{U}_s = \begin{bmatrix} \dot{u}_{s1} \\ \dot{u}_{s2} \end{bmatrix} = \begin{bmatrix} r_1 \\ r_2 \end{bmatrix} = r \\ \dot{E}_q = \left[\dot{E}_{q1} \; .. \dot{E}_{qn1} \quad \dot{E}\right]^T \\ \dot{v} = [\dot{V}_1 \; .. \dot{V}_{n+2} \quad \dot{\theta}_1 .. \quad \dot{\theta}_{n+2}]^T \\ h_i = \frac{1}{T_{0i}}(-\acute{E}_{qi} - (X - \acute{X})I_{di}) \\ H = [h_1 \; .. \quad h_{n1}]^T \end{cases} \tag{9}$$

It should be noticed that r_1 and r_2 are related to each other, therefore, only one control input will be considered for SSSC. U_f is:

$$U_f = [\;\; u_{f1} \quad \cdots u_{fn1} \quad u_{d1} \;\;]^T \tag{10}$$

$$\begin{cases} \dot{X}_1 = X_2 \\ \dot{X}_2 = M_{inv}[P_m - X_3] \\ \dot{X}_3 = F_T + U \; + \; \Gamma\varphi \end{cases} \tag{11}$$

WHERE:

$$U = G_T U_f + Lr \tag{12}$$

$$\begin{cases} X_1 = [x_{11} \quad x_{12} \quad .. \quad x_{1n}]^T \\ X_2 = [x_{21} \quad x_{22} \quad .. \quad x_{2n}]^T \\ X_3 = [x_{31} \quad x_{32} \quad .. \quad x_{3n}]^T \\ X_{3s} = [x_{3d1} \quad x_{3d2} \quad .. \quad x_{3dn}]^T \\ \varphi = [x_{d1} - \acute{x}_{d1} \quad x_{d2} - \acute{x}_{d2} \quad .... \quad x_{dn} - \acute{x}_{dn}]^T \\ \Gamma = \begin{bmatrix} \Gamma_1(X_1, X_2, X_3) & \cdots & 0 \\ \vdots & \ddots & \vdots \\ 0 & \cdots & \Gamma_n(X_1, X_2, X_3) \end{bmatrix} \end{cases} \tag{13}$$

WHERE IN (13), $x_{1i} = \delta_i - \delta_i^*$, $x_{2i} = \omega_i - \omega_i^*$ AND

$$x_{3i} = \begin{cases} \frac{\acute{E}_{qi}V_i sin(\delta_i - \theta_i)}{\acute{x}_{di}} + \frac{{V_i}^2 sin2(\delta_i - \theta_i)}{2x_{qi}\acute{x}_{di}}(\acute{x}_{di} - x_{qi}) & 1 \leq i \leq n1 \\ \frac{\acute{E}_i V_i \sin(\delta_i - \theta_i)}{\acute{x}_{di}} & n1+1 \leq i \leq n \end{cases}$$

AND

$$\Gamma_i = \begin{cases} \frac{-(\acute{E}_{qi} - V_i \cos(\delta_i - \theta_i))}{\acute{x}_{di}T_{0i}} & 1 \leq i \leq n1 \\ \frac{V_i}{\acute{X}_i T_{0i}}(\cos(\delta_i - \theta_i) + \frac{\sin(\delta_i - \theta_i)\cos(\delta_i)}{\sin(\delta_i)}) & n1+1 \leq i \leq n \end{cases} \tag{8}$$

Here, n is the total number of the generators including synchronous and DFIG ones. Since it is assumed that only one DFIG is in the considered power system, n1, the number of synchronous generators, equals n-1.

III. Design of Nonlinear Adaptive Multi-Input DSC Control Law

In this section, based on the described model for power system network developed in Section 2, together with DSC method and adding an adaptive scheme for estimating uncertain parameters, a multi-input control law will be designed. In this framework, the following equations are formulated [23]:

$$\begin{cases} Z_1 = X_1 \\ Z_2 X_2 \; - X_{2d} \\ Z_3 = X_3 - X_{3d} \end{cases} \tag{14}$$

Based on the DSC method, the function x_{2d} is determined in such a way that x_1 stabilizes and x_{3d} stabilizes x_2.

where:

$$Z_1 = [z_{11} \quad z_{12} \quad .. \quad z_{1n}]^T,\; Z_2 = [z_{21} \quad z_{22} \quad .. \quad z_{2n}]^T \tag{15}$$

We then have:

$$\begin{cases} \dot{Z}_1 = X_2 \\ \dot{Z}_2 = M_{inv}[P_m - X_3] - \dot{X}_{d2} \\ \dot{Z}_3 = F_T + U \; + \; \Gamma\varphi - \dot{X}_{d3} \end{cases} \tag{16}$$

$$\begin{cases} \tau_2\dot{X}_{2d} + X_{2d} = \bar{X}_2 \\ \tau_3\dot{X}_{3d} + X_{3d} = \bar{X}_3 \end{cases} \tag{17}$$

Now, in the following steps, a suitable Lyapunov function is defined which leads to the design of final control law [24, 25]:

Step #1:

$$V_{z1} = \frac{1}{2}{Z_1}^T Z_1 \tag{18}$$

$$\dot{V}_{z1} = {Z_1}^T(Z_2 + X_{2d} - \bar{X}_2 + \bar{X}_2) \rightarrow \bar{X}_2 = -K_D Z_1 \tag{19}$$

$$\dot{V}_{z1} = -{Z_1}^T K_D Z_1 - {Z_1}^T(\bar{X}_2 - X_{2d}) + {Z_1}^T Z_2$$

Step #2:

$$V_{z2} = V_{z1} + \frac{1}{2}{Z_2}^T Z_2 \tag{20}$$

$$\begin{aligned} \dot{V}_{z2} &= -{Z_1}^T K_D Z_1 - {Z_1}^T(\bar{X}_2 - X_{2d}) + {Z_1}^T Z_2 \\ &+ {Z_2}^T(M_{inv}[P_m - X_3] - \dot{X}_{2\mathrm{d}}) \\ &= -{Z_1}^T K_D Z_1 - {Z_1}^T(\bar{X}_2 - X_{2d}) + {Z_2}^T(Z_1 \\ &+ M_{inv}[P_m - Z_3 - X_{3d} + \bar{X}_3 - \bar{X}_3] - \dot{X}_{2\mathrm{d}}) \\ &= -{Z_1}^T K_D Z_1 - {Z_1}^T(\bar{X}_2 - X_{2d}) \; + {Z_2}^T(Z_1 \\ &\qquad + M_{inv}[P_m - \bar{X}_3] - \dot{X}_{2\mathrm{d}}) \\ &- {Z_2}^T M_{inv} Z_3 - {Z_2}^T M_{inv}(\bar{X}_3 - X_{3d}) \end{aligned} \tag{21}$$

It is assumed that:

$$Z_1 + M_{inv}[P_m - \bar{X}_3] - \dot{X}_{2\mathrm{d}} = -K_T Z_2 \quad (22)$$

which in equations (19) and (22) K_D and K_T are arbitrary positive definite matrices.

$$\rightarrow \bar{X}_3 = {M_{inv}}^{-1}(K_T Z_2 + M_{inv} P_m + Z_1 - \dot{X}_{2\mathrm{d}}) \quad (23)$$

Considering Equation (19) we have:

$$\dot{V}_{z2} = -{Z_1}^T K_D Z_1 - {Z_1}^T(\bar{X}_2 - X_{2d}) \ - {Z_2}^T K_T Z_2 - {Z_2}^T M_{inv}(\bar{X}_3 - X_{3d}) - {Z_2}^T M_{inv} Z_3$$

Step #3:

$$V_{z3} = V_{z2} + \frac{1}{2}{Z_3}^T Z_3 + \frac{1}{2}\tilde{\varphi}^T \gamma \tilde{\varphi} \quad (24)$$

$$\dot{V}_{z3} = \dot{V}_{z2} + {Z_3}^T \dot{Z}_3 + \gamma^{-1}\tilde{\varphi}^T \tilde{\varphi}$$

$$\dot{V}_{z3} = \dot{V}_{z2} + {Z_3}^T(F_T + U \ + \ \Gamma\varphi - \dot{X}_{3\mathrm{d}}) + \tilde{\varphi}^T \gamma \dot{\tilde{\varphi}} \ )$$

$$\dot{V}_{z3} = -{Z_1}^T K_D Z_1 - {Z_1}^T(\bar{X}_2 - X_{2d}) \ - {Z_2}^T K_T Z_2 - {Z_2}^T M_{inv}(\bar{X}_3 - X_{3d}) - {Z_2}^T M_{inv} Z_3 + {Z_3}^T(F_T + U \ + \ \Gamma\varphi - \dot{X}_{3\mathrm{d}}) + \tilde{\varphi}^T \gamma \dot{\tilde{\varphi}} \ )$$

$$\dot{V}_{z3} = -{Z_1}^T K_D Z_1 - {Z_1}^T(\bar{X}_2 - X_{2d}) \ - {Z_2}^T K_T Z_2 - {Z_2}^T M_{inv}(\bar{X}_3 - X_{3d}) + {Z_3}^T(F_T + U \ + \ \Gamma\varphi - \dot{X}_{3\mathrm{d}} - M_{inv} Z_2) + \dot{\tilde{\varphi}}^T \gamma \tilde{\varphi}$$

$$\dot{V}_{z3} = -{Z_1}^T K_D Z_1 - {Z_1}^T(\bar{X}_2 - X_{2d}) \ - {Z_2}^T K_T Z_2 - {Z_2}^T M_{inv}(\bar{X}_3 - X_{3d}) + {Z_3}^T(F_T + U \ + \ \Gamma\varphi - \dot{X}_{3\mathrm{d}} - M_{inv} Z_2) + \dot{\tilde{\varphi}}^T \gamma \tilde{\varphi} \quad (25)$$

It should be noted that $\tilde{\varphi} = \varphi - \hat{\varphi}$:

$$\dot{V}_{z3} = -{Z_1}^T K_D Z_1 - {Z_1}^T(\bar{X}_2 - X_{2d}) \ - {Z_2}^T K_T Z_2 - {Z_2}^T M_{inv}(\bar{X}_3 - X_{3d}) + {Z_3}^T(F_T + U \ + \ \Gamma\hat{\varphi} - \dot{X}_{3\mathrm{d}} - M_{inv} \ Z_2) + ({Z_3}^T \Gamma + \dot{\hat{\varphi}}^T \gamma) \quad (26)$$

Since, φ is constant, then $\dot{\varphi} = 0$, hence, $\dot{\tilde{\varphi}} = -\dot{\hat{\varphi}}$. In order to make a negative value for the derivative of Lyapunov function, the following relations should be applied:

$$\begin{cases} (F_T + U \ + \ \Gamma\hat{\varphi} - \dot{X}_{3\mathrm{d}} - M_{inv} \ Z_2) = -K_s Z_3 & (27-a) \\ ({Z_3}^T \Gamma - \dot{\hat{\varphi}}^T \gamma) = 0 & (27-b) \end{cases}$$

Where K_s is positive definite matrix, The following relation is obtained:

$$U \ = -K_s Z_3 - F_T - \ \Gamma\hat{\varphi} + \dot{X}_{3d} \ + M_{inv} \ Z_2 \quad (28)$$

$$({Z_3}^T \Gamma - \dot{\hat{\varphi}}^T \gamma) = 0 \rightarrow \dot{\hat{\varphi}} = {\gamma^{-1}}^T \Gamma Z_3 \quad (29)$$

If the backstepping method is applied, the control input will be obtained from (26).

$$U = -K_s Z_3 - F_T - \ \Gamma\hat{\varphi} + M_{inv} \ Z_2 + {M_{inv}}^{-1}(K_T(M_{inv}[P_m - X_3] - \dot{X}_{2\mathrm{d}}) + M_{inv}\dot{P}_m + Z_2 + X_{2d} - \dot{X}_{2\mathrm{d}} \quad (30)$$

It should be mentioned that the number of terms in (28) is fewer than those ones in (30).

According to (28) for the control input, the derivative of Lyapunov function will be:

$$\dot{V}_{z3} = -{Z_1}^T K_D Z_1 - {Z_2}^T K_T Z_2 - {Z_3}^T K_s Z_3 - {Z_1}^T(\bar{X}_2 - X_{2d}) \ - {Z_2}^T M_{inv}(\bar{X}_3 - X_{3d}) \quad (31)$$

The complete proof is described in Appendix A.There are a number of controller coefficients in (28). In order to design these coefficients, a PSO algorithm will be applied. PSO algorithm in comparison with most of the other intelligent methods is formulated in simple manner. It is a memory-based algorithm and has a higher convergence rate [26].

The cost function considered for optimization by PSO method is selected as follows:

$$J = \sum_{j=1}^{n}(\delta_i - \delta_{i0})^2 + \tau \sum_{j=1}^{n}(\omega_i - \omega_{i0})^2 \quad (32)$$

In relation (32), τ is a weight coefficient that can be determined experimentally.

The designed control system block is shown in Fig. 4. In this control diagram, first the output states of the main plant are sampled and then entered into the parameter estimator and adaptive backstepping controller with the DSC filter. In this block, the appropriate estimation of the uncertain parameters of the system is produced and sent back to the main controller. In the DSC adaptive backstepping controller block, the DSC filter provides the derivative value of the desired values in the design of the backstepping controller without the calculation needed for direct derivation and sends it back to the backstep controller. Finally, the appropriate input control signals to improve the dynamic stability of the power generation system are generated and fed into the DFI

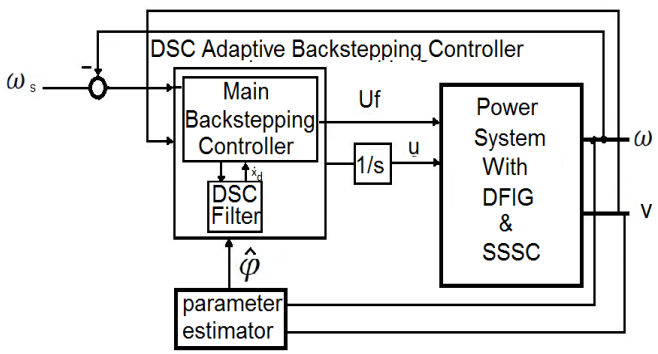

Fig 4. Control diagram and Power System Including DFIG and SSSC Applying Multi-Input Adaptive DSC

A. *The proposed Algorithm for Dynamic Stability Improvement of Power System Including DFIG and SSSC*

Fig. 5 describes the proposed control algorithm for the stability improvements of the power system which includes synchronous generators, DFIG and SSSC.

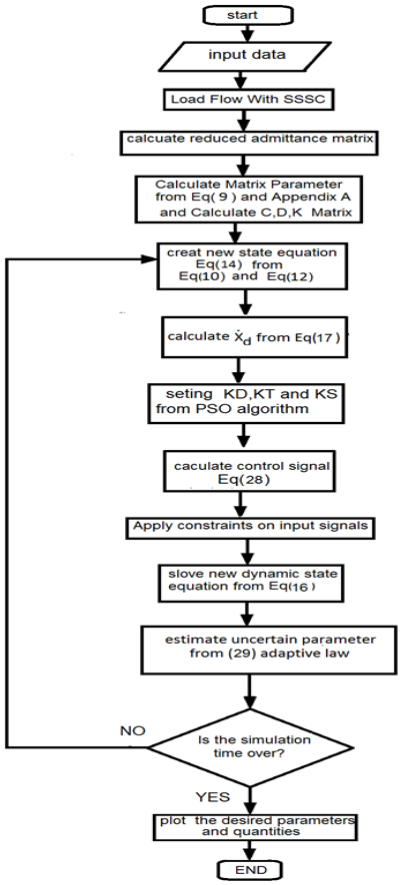

Fig 5. Flowchart Simulation of the Power System Including DFIG and SSSC with Applying Multi-Input Adaptive DSC

IV. Simulation Results

In order to investigate the effectiveness of the proposed control law, a stability analysis in different scenarios is considered for the 10-machine New England test system. This power system is depicted in Fig.6. It includes 10 synchronous machines, one DFIG in Bus 19, and one SSSC component between Bus 6 and Bus 7. The initial data for this system is developed in [27].

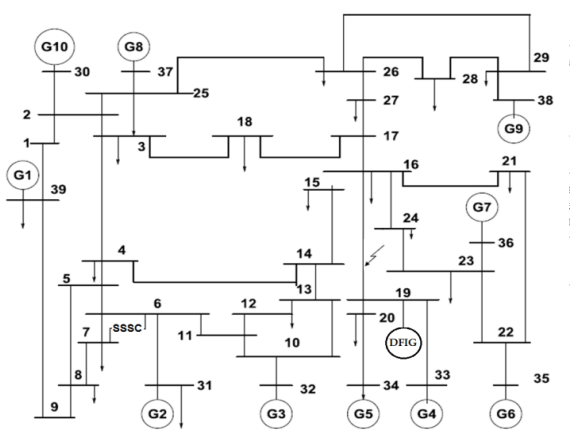

Fig 6. The NEW ENGLAND standard 39-bus power system includes a wind generator equipped with DFIG

In this case-study, a 3-phase short-circuit fault in the vicinity of generator 4 is occurred and lasted for 100 milliseconds. Fig.7 shows the variations in the speed of the G4 and DFIG under the condition in which no control input is employed. It is clear that the power system is dynamically unstable. Now, by applying the proposed control law, the deviations of internal angle and speed of G4 and DFIG are depicted in Fig. 8 and Fig.9. As it can be seen from these figures, the angle and the speed of the rotor reach to their stable condition in about 2 seconds after clearing the fault. Fig.10 shows the behavior of internal angles and angular velocities of the generators of this power system. For a better investigation of the power system damping, the phase diagram for G4 and the DFIG is depicted in Fig.11. It can be seen that the system tends toward its stable condition very fast. Fig.12 show the control input signal for all the machines, DFIG, and SSSC. This figure shows that the amplitudes of all the signals are limited and they reach to their initial values. In Fig.13, the estimation of the unknown parameters of the power system is depicted. It shows that the estimation error tends to zero, and estimation values reach to their references.

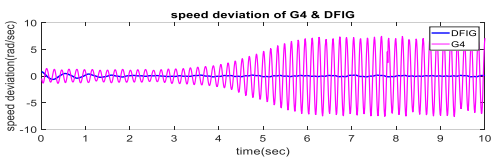

Fig 7. Speed deviation G4 and DFIG while is not control on system

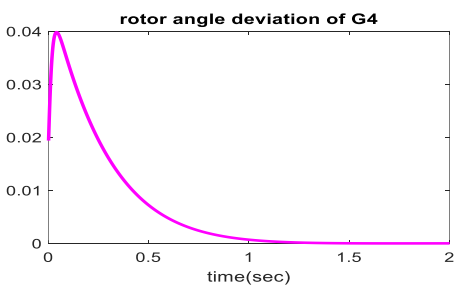

(a)

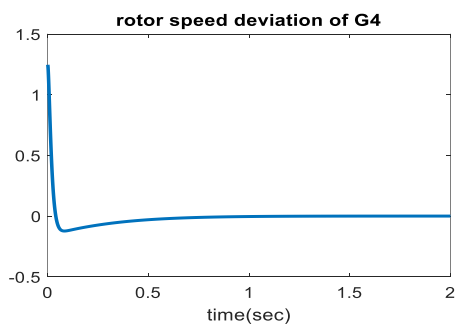

(b)

Fig 8. (a)rotor angle deviation for G4, (b)Speed deviation for G4 after fixing the short circuit error

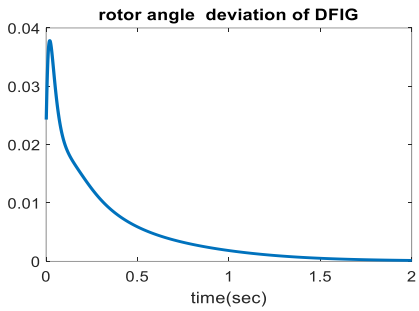

(a)

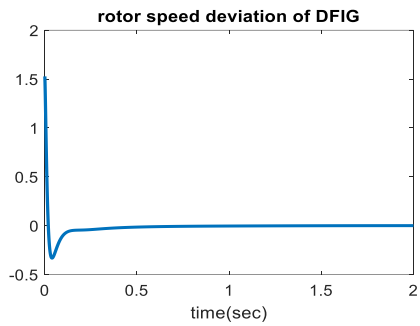

(b)

Fig 9. (a)rotor angle deviation for DFIG, (b)Speed deviation for DFIG after fixing the short circuit

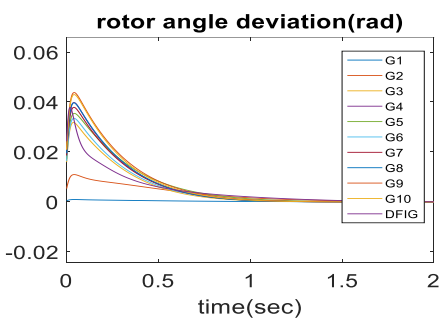

(a)

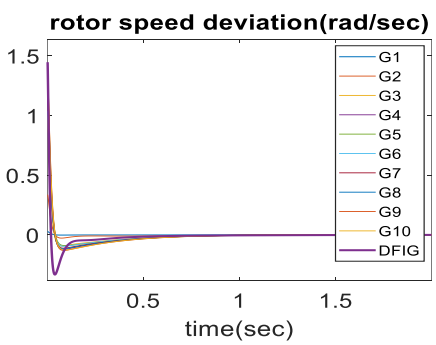

(b)

Fig 10. rotor angle deviation of the generators rotor after fixing the short circuit error in bus39 Rotor Speed deviation of all generators after the short circuit fault in bus 39

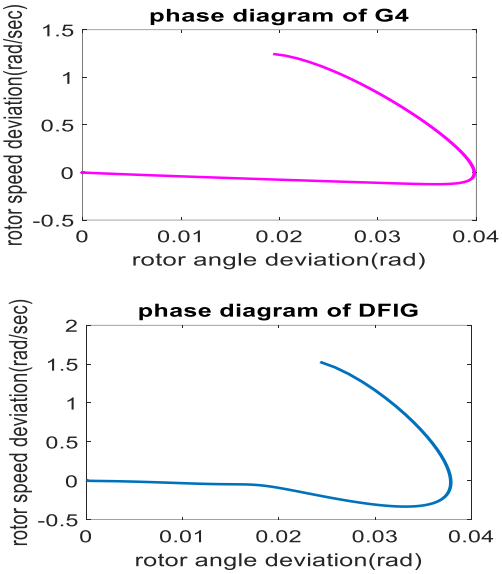

Fig.11. phase diagram of wind turbine based DFIG and G4

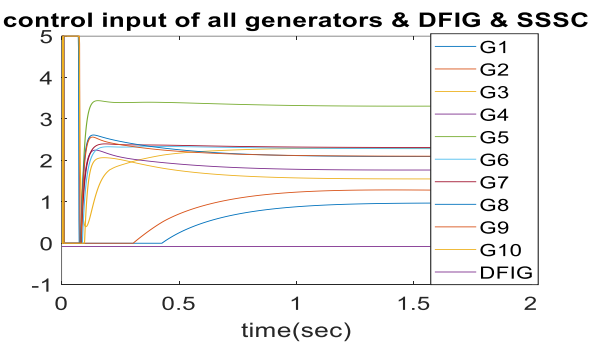

Fig 12. control signals of G4 and DFIG, SSSC by Multi input dynamic surface control

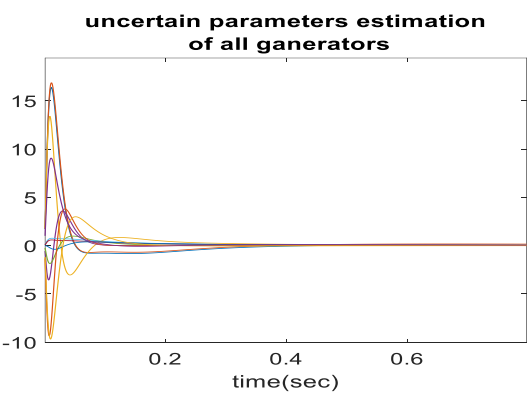

Fig 13. estimation of uncertain parameter for all generators and DFIG

It should be mentioned that the input mechanical power to the generators may vary with time. This condition more frequently happens in Wind-Turbines. Therefore, in order to make a more comprehensive scenario, it is assumed that the mechanical input power to the DFIG suddenly change about 10% and then reach to its initial value. In Fig.14 the variation

in angle and speed of DFIG rotor is depicted. It shows that the controller acts in a correct manner and make the signal amplitude to reach to its stable condition in a short period of time.

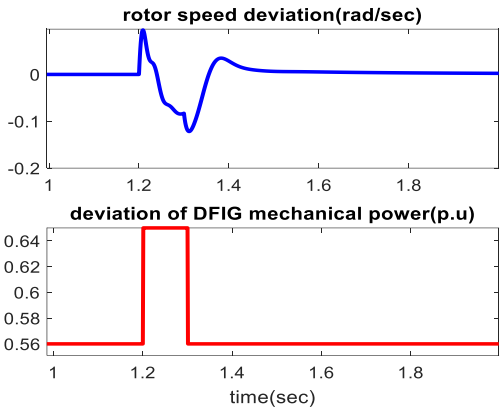

Fig 14. speed deviation of synchronous generator and DFIG against changing point of fault occurrence to near G7

In the Fig.15 to compare the performance of the controller adesigned by the DSC method, the results obtained with the backtracking method are compared. It can be seen that the DSC controller has a better performance for the speed and internal angle diagrams of the generator In addition, this filter softens the response and In Fig.16, for the input signal of G4, a comparison is made between the applied backstepping control approach and the proposed control scheme. It is observed that by use of the proposed control law, the trajectories reach to its stable condition in a faster way with lower overshoot value with respect to controller signal obtained from applying backstepping method. In addition, this filter softens the response as shown in the figure and makes us without the need for derivation.

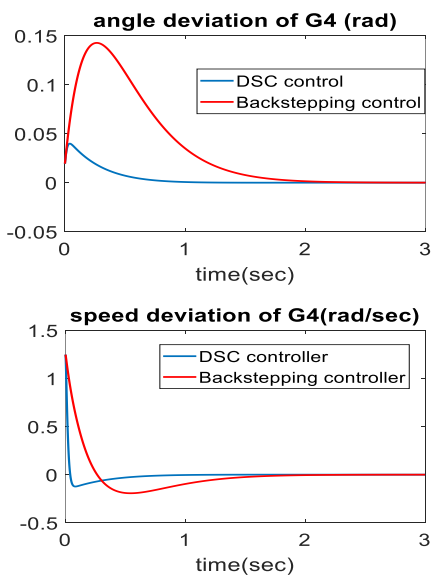

Fig.15.comparing rotor angle and speed deviation G4 in back stepping and DSC methods after the short circuit fault in bus 39

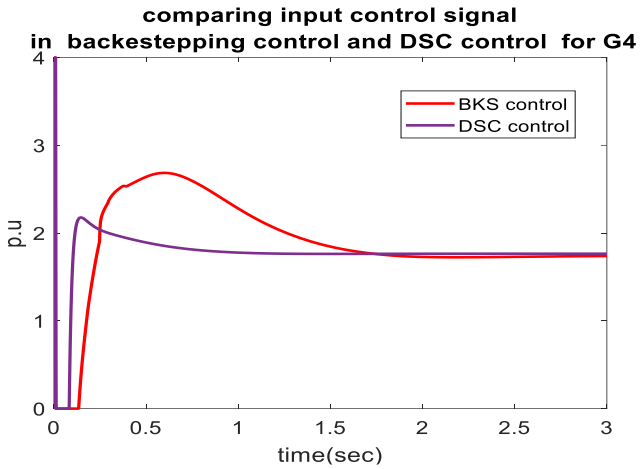

Fig 16. comparing control input signal for G4 in back stepping and DSC methods

In order to further examine the performance of the proposed control law with the other important controller design methods, a comparison is made in Table 2. It is obtained from the information in this table that the proposed method has a superior performance with respect to the linear scheme of [13]. In Table 3, the proposed control law is compared with the nonlinear method offered in [9]. The results show that the proposed control law has a better performance with respect to the results obtained from [9].

TABLE 2
COMPARISON OF CONTROL CRITERIA BETWEEN ADAPTIVE MULTI-INPUT DYNAMIC SURFACE CONTROL AND OPTIMIZED LINEAR CONTROL METHOD IN [13]

	Proposed control in this article			Optimized Linear Control Design in [13]		
G4	Rise time (Sec.)	settling time (Sec.)	Over shoot (p.u.)	Rise time (Sec.)	settling time (Sec.)	Over shoot (p.u.)
Speed dev	0.08	0.7	0.1	0.2	4.5	0.15
Rotor ang	1.50	2.0	2.29˚	0.15	4.0	25˚
Ctrl signal	0.15	1.1	2.1	-	-	-

TABLE 3
COMPARISON OF CONTROL CRITERIA BETWEEN ADAPTIVE MULTI- INPUT DYNAMIC SURFACE CONTROL WITH BACKSTEPPING CONTROL METHOD IN [9]

	Proposed control in this article			Nonlinear Control design in [9]		
G3	Rise time (Sec.)	settling time (Sec.)	Over shoot (p.u.)	Rise time (Sec.)	settling time (Sec.)	O shoot (p.u.)
Speed dev	0.05	0.9	0.12	0.5	5.0	0.5
Rotor angle	1.10	1.8	1.5˚	0.1	5.0	13˚
Ctrl signal	0.08	1.0	1.8	0.4	7.5	3.2

V. Conclusions

In this study, a multi-input adaptive DSC control law is developed to improve dynamic stability of the power system including DFIG and SSSC. The simulation results show the superiority of the proposed control law in improvement the dynamic stability with respect to backstepping method (Table 3) and linear methods (Table 2). For instance, according to Table 3, the overshoot is improved by 50% and the settling time is improved by 20% with respect to the recent reported results of applying backstepping scheme. The performance of the designed control law with respect to the unknown parameter variation and also rapid change in mechanical input of DFIG shows the robustness properties of the proposed control law. In other word, the control signal also has a smooth form with respect to the corresponding signals from backstepping controllers developed in the recent literature.

REFERENCES

[1] S. Muller, M.Deicke & R I K W, “doubly-fed induction generator systems for wind turbines”, IEEE Industry Applications Magazine, June 2002.

[2] H.S.Koa,G.G. Yoonb, N.H. Kyunga,W.Pyo Hongc, “Modeling and control of DFIG-based variable-speed wind-turbine”,Electric Power Systems Research 78, pp:1841–1849, 2008.

[3] N. G. Hingorani and L. Gyugyi, “Understanding FACTS, Concepts and Technology of Flexible AC Transmission Systems,” IEEE Press, 2000.

[4] B. K. Dubey, N.K. Singh,” Multi machine power system stability enhancement with UPFC using linear quadratic regulator techniques”, International Journal of Advanced Research in Engineering and Technology, Vol.11, Issue 4, pp. 219-229, April 2020.

[5] Y. Chi, Y. Xu,” Multi-objective robust tuning of STATCOM controller parameters for stability enhancemnt of stochastic wind-penetrated power systems”, IET Generation, Transmission & Distribution, Sep 2020.

[6] A. Movahedia, A.Halvaei Niasara, G. Gharehpetianb, " Designing SSSC, TCSC, and STATCOM controllers using AVURPSO, GSA, and GA for transient stability improvement of a multi-machine power and GA for transient stability improvement of a multi-machine power system with PV and wind farms system with PV and wind farms, " Elsevier, Electrical Power and Energy Systems, Vol. 106 , pp. 455–466, 2019.

[7] M. A. Mahmud, “An alternative LQR-based excitation controller design for power systems to enhance small-signal stability,” International Journal of Electrical Power & Energy Systems ,Vol. 63, pp. 1–7, Dec 2014.

[8] W. Du, X. Chen, H, Wang, “Parameter tuning of the PLL to consider the effect on power system small-signal angular stability,” IET Renewable. Power Generation., Vol. 12, No. 1, pp. 1-8, 2018.

[9] T. K. Roy, M. A. Mahmud, Amanullah M. T. Oo,” Robust Adaptive Back stepping Excitation Controller Design for Higher-Order Models of Synchronous Generators in Multi machine Power Systems”, Transactions on Power Systems, IEEE, 2018.

[10] Y. Liu, Q. H. Wu, H. Kang, X. Zhou, “Switching Power System Stabilizer and Its Coordination for Enhancement of Multi-machine Power System Stability,” CSEE journal of power and energy systems, Vol. 2, No. 2, June 2016.

[11] M. A. Mahmud, M. J. Hossain, H. R. Pota, and A. M. T. Oo,” Robust Partial Feedback Linearizing Excitation Controller Design for Multimachine Power Systems”, 0885-8950 (c) 2015 IEEE.

[12] T. Parida, S. Dhar,N. Nayak, “A finite time adaptive back-stepping sliding mode control for instantaneous active-reactive power dynamics based DFIG-wind generation towards improved grid stability ”, Wind Energy published by John Wiley & Sons Ltd, 2020 .

[13] M.Maleki, S.Abazari,” Dynamic Stability Improvement of Power System With Simulation and Coordinated Control of DFIG and UPFC using LMI”, International Journal of Industrial Electronics,Control and optimization,vol.4,NO.3,pp.341-353,July.2021.

[14] G. Zhu, L. Nie, M.Zhou ,X.Zhang, L.I. Sun,CH.Zhang, ”Adaptive Fuzzy Dynamic Surface Control for Multi-Machine Power System Based on Composite Learning Method and”, IEEE Access, September 18, 2020.

[15] A. Saleem Mir and N. Senroy, “DFIG damping controller design using robust CKF based adaptive dynamic programming”,IEEE Transactions on Sustainable Energy, 2018.

[16] F.A.L.Jowder,’’Influence of mode of operation of the SSSC on the small disturbance and transient stability of a radial power system,’’ IEEE Transactions on Power Systems, vol.20, Issue. 2, May 2005.

[17] K. Elkington, V.Knazkins, M. Ghandhari, "On the stability of power systems containing doubly fed induction generator-based generation, " Elsevier, Electric Power Systems Research, vol. 78,No. 9 , pp. 1477–1484, September 2008.

[18] S.Ghaedi, S.Abazari, and G.Arab-Markadeh, ”Novel nonlinear control of DFIG and UPFC for transient stability increment of power system”. IET Generation, Transmission & Distribution, Vol.16, No.19, pp.3799-3813, 2022.

[19] P. R. Sahu, P. K. Hota, S. Panda, " Power system stability enhancement by fractional order multi input SSSC based

controller employing whale optimization algorithm ," Science Direct**,** Journal of Electrical Systems and Information Technology , Vol. 5, No 3, pp. 326-336 , December 2018.

[20] M. Noroozian, M.Ghandehari, "Improving Power System Dynamics By Series-Connected FACTS Device,". IEEE Transactions on Power Delivery, Vol. 12, No. 4, October 1997.

[21] Z.Faramarzi, S.Abazari, S.Hoghoughi and N.R.Abjadi "Dynamic stability improvement of power system with DFIG using multi-input backstepping control" Electrical Engineering, pp.1-17, 2022.

[22] P. Kundur, "Power System Stability and Control," New York, NY, USA: McGraw-Hill, 1994.

[23] G. Zhu, L. Nie, M.Zhou ,X.Zhang, L.I. Sun,CH.Zhang ,'' Adaptive Dynamic Surface Control for Servo System Driven by Twin Motors With Unknown Actuator Failures,'' IEEE Access August 23, 2019.

[24] H. K.Khalil, "Nonlinear systems", Upper Saddle River, NJ: Prentice Hall, 2002.

[25] E.Slotine, W.Li, "Applied Nonlinear Control ", Published by Prentice Hall, 1991.

[26] J.Ma, D.Zhao, Y.Shen and A.G.Phadke," Research on Positioning Method of Low Frequency Oscillating Source in DFIG-Integrated System with Virtual Inertia Control", IEEE Transactions on Sustainable Energy, IEEE, 2019.

[27] O. Moradi, S. Abazari, N.Mahdi "Robust Sliding Mode-based UPQC for Transient Conditions in Weak Islanded Networks", International Journal of Industrial Electronics, Control and Optimization, Vol.4,pp.267-276,2021.

Appendix A:

Proof:

It can be shown that:

$\tau_2\dot{X}_{2d} + X_{2d} = \bar{X}_2$,

$\tau_3\dot{X}_{3d} + X_{3d} = \bar{X}_3$

Define the following variables:

$$\begin{cases} Y_1 = X_{2d}\text{-}\bar{X}_2 \\ Y_2 = X_{3d}\text{-}\bar{X}_3 \end{cases} \quad (a.1)$$

According to a.1One can obtain:

$$\dot{Y}_1 = -\frac{Y_1}{\tau_2}\text{-}\dot{\bar{X}}_2 = -\frac{Y_1}{\tau_2} + L_1$$

$$\dot{Y}_2 = -\frac{Y_2}{\tau_3}\text{-}\dot{\bar{X}}_2 = -\frac{Y_2}{\tau_3} + L_2$$

Where-$\dot{\bar{X}}_2 = L_2$ *and* -$\dot{\bar{X}}_3 = L_3$. $|L_i|$ has a maximum value L_{iM} on a compact region. Therefore, $|L_i| \le L_{iM}$. Based on the Young inequality, the following inequalities can be written:

$$Y_i^T\dot{Y}_i = -\frac{Y_i^T Y_i}{\tau_{i+1}} + Y_i^T L_i \le -\frac{Y_i^T Y_i}{\tau_{i+1}} + |Y_i^T||L_i| \le -\frac{Y_i^T Y_i}{\tau_{i+1}} + \frac{1}{2T}L_{iM}^2 Y_i^T Y_i + \frac{T}{2} \quad (a.2)$$

T is a positive definite diagonal matrix, Now a Lyapunov function is defined as (a.3):

$$V_{zn} = V_{z3} + Y_1^T Y_1 + Y_2^T Y_2 \quad (a.3)$$

Let consider equation (a.3), the derivative of the Lyapunov function and replace $\dot{V}_{z3}$ from(31) can be written as:

$$\dot{V}_{zn} = -Z_1^T K_D Z_1 - Z_2^T K_T Z_2 - Z_3^T K_s Z_3 + Z_1^T Y_1 + Z_2^T M_{inv} Y_2 + Y_1^T\dot{Y}_1 + Y_2^T\dot{Y}_2 \quad (a.4)$$

Now by using (a.2) in (a.4) results in:

$$\dot{V}_{z3} \le -Z_1^T K_D Z_1 - Z_2^T K_T Z_2 - Z_3^T K_s Z_3 + Z_1^T Y_1 + Z_2^T M_{inv} Y_2 - \frac{Y_1^T Y_1}{\tau_2} + \frac{1}{2T}L_{1M}^2 Y_1^T Y_1 + \frac{T}{2} - \frac{Y_2^T Y_2}{\tau_3} + \frac{1}{2T}L_{2M}^2 Y_2^T Y_2 + \frac{T}{2}$$

On the other hand, based on Young inequality,

$$Z_1^T Y_1 \le \frac{Z_1^T Z_1}{2} + \frac{Y_1^T Y_1}{2},\ Z_2^T M_{inv} Y_2 \le \frac{Z_2^T Z_2}{2} + \frac{Y_2^T M_{inv}^2 Y_2}{2}$$

(a.5)

Considering (a.5) and (a.4),

$$\dot{V}_{z3} \le -Z_1^T K_D Z_1 - Z_2^T K_T Z_2 - Z_3^T K_s Z_3 + \frac{Z_1^T Z_1}{2} + \frac{Y_1^T Y_1}{2} + \frac{Z_2^T Z_2}{2} + \frac{Y_2^T M_{inv}^2 Y_2}{2} - \frac{Y_1^T Y_1}{T_2} + \frac{1}{2T}L_{1M}^2 Y_1^T Y_1 + \frac{T}{2} - \frac{Y_2^T Y_2}{T_3} + \frac{1}{2T}L_{2M}^2 Y_2^T Y_2 + \frac{T}{2}$$

$$\dot{V}_{z3} \le -Z_1^T(K_D - \frac{I}{2})Z_1 - Z_2^T(K_T - \frac{I}{2})Z_2 - Z_3^T(K_s)Z_3 - Y_1^T(-\frac{I}{2} + \frac{I}{T_2} - \frac{1}{2T}L_{1M}^2)Y_1 - Y_2^T(-\frac{M_{inv}^2}{2} + \frac{I}{T_3} - \frac{1}{2T}L_{2M}^2)Y_2 + T$$

$$a = \min\left\{K_D - \frac{I}{2}, K_T - \frac{I}{2}, K_s, -\frac{I}{2} + \frac{I}{\tau_2} - \frac{1}{2T}L_{1M}^2, -\frac{M_{inv}^2}{2} + \frac{I}{\tau_3} - \frac{1}{2T}L_{2M}^2\right\}$$

$b = \{T\}$

$\dot{V}_{z3} \le -aV_{z3} + b$

$V_{z3}(t) \le (V_{z3}(t_0) - \frac{b}{a})e^{-a(t-t_0)} + \frac{b}{a} \le V_{z3}(t_0) + \frac{b}{a}, \forall t \ge t_0$

From this inequality one can conclude that by suitable choosing of coefficients, the Lyapunov function and therefore the magnitude of errors, could be made smaller and smaller as desired.

Saeed Abazari Received his BS degree in electrical engineering from Esfahan in 1989 , the MSc degree from Ferdowsi university ,Mashad,Iran In 1992, and the PhD degree from Sharif university,Thehran,Iran in 2002.Currently in electrical engineering Department at the university of Sharekolrd,Shahrekord of Iran.His research interests are electrical power distribution system, smart grid, and protection.

Zabihollah Faramarzi Received his BS degree in electrical engineering from Amirkabir university,Tehran,Iran in 2006 , the MSc degree from Esfahan university , Iran In 2013, and the PhD degree from Shahrekord university,Iran in 2021.His research interests are power system stability with renewable energy and FACTS, nonlinear control in power system, and nonlinear control in power electronic.

International Journal Of
Industrial Electronics Control and Optimization
Print ISSN: 3517-2645
Online ISSN: 3568-2645
Homepage: https://ieco.usb.ac.ir/

Sliding Mode Control Design for a Class of Nonlinear Fractional Systems with Application to Glucose-Insulin Systems

Forough Roshanravan [1], Aghileh Heydari [2]

Department of Applied Mathematics, Payame Noor University, Tehran, Iran [1,2]

Corresponding author's email: a_heidari@pnu.ac.ir

Article Info

Article type:
Research Article

Article history:
Received: 27 April 2022
Revised: 10 October 2022
Accepted:17 October 2022
Publish on line: 21 Dec 2022

Keywords:
Glucose-insulin system,
Lu system,
Nonlinear
Fractional systems,
Sliding mode control.

ABSTRACT

Nonlinear fractional systems in the presence of uncertainties and external disturbances are important issues these days and fractional calculus has been evolved to improve the efficiency of controllers. In real world applications, uncertainties and external disturbances can affect the performance of systems. Dealing with these issues is one of the important problems. Sliding mode control is an effective nonlinear robust control method. In this paper, we introduce a method for study and evaluating stability of a class of nonlinear fractional system in the presence of uncertainty and external disturbances by using a robust adaptive fractional sliding mode controller with a new fractional sliding surface. Since in real life, the upper bound of uncertainties and external disturbances are unknown, we use an adaptive law to approximate it. We perform stabilizing analysis of the designed fractional controller using Lyapunuv's theorem. Then, we obtain finite time convergence of system states to the fractional sliding surface. Finally, we illustrate the accuracy of our proposed method on two examples. The fractional models of the glucose-insulin system and the Lu system were considered and simulation confirm analytical results. Besides rapid convergence to the equilibrium point is another advantage of the method.

I. Introduction

Many mathematical theories have been evolved and extended over time. One instance of such theories is integer order calculus, which has been extended using the notion of fractional derivative. The major advantage of fractional calculus is that it is nonlocal. In fact, when we calculate ordinary derivative at a specific point, the resulting value depends only on that point and its around. This property is known as locality. But fractional derivatives are obtained by integrating a wide range of values and depends on the state of the system in the past. It might be difficult to use classical differential equations for the modelling and analysis of systems with memory effects. Nevertheless, that fractional derivatives are non-local allows them to cover memory effects. As a tool, fractional calculus has been evolved to improve the efficiency of control loops in two primary ways, namely, to improve the quality of modelling and to enhance the efficiency of controllers. This tool has been beneficial to the finding of more accurate models for processes by providing a wider context for dynamic models.It is obvious that finding a more accurate model of a process allows us to design more suitable controllers for the handling of that process [1]. Besides, since traditional controllers are special cases of fractional controllers, the use of fractional controllers can improve the efficiency of control systems designed. [2, 3]

The first application of fractional calculus to the modelling of physical phenomena dates back to the 1930s [4]. Since then, this tool has been used in numerous fields of sciences. For example, in physics [5,6], in medical and biological sciences [7, 8], in economics [9] and so on [10,12]. As a special instance of nonlinear fractional order models, the fractional order model of glucose-insulin systems has been investigated by some researchers in recent years. In [13], the existence and uniqueness of fractional order derivatives for glucose-insulin regulation were proved using the fixed-point theorem and an iterative scheme. Also, a fuzzy fractional order predictive control system was proposed in [14] to stabilize the glucose level regulation. In [15] the effect of the incommensurate

DOI: 10.22111/IECO.2022.42485.1417

fractional order derivatives on a glucose-insulin regulatory model is studied. In [16] for blood glucose level control, a Reinforcement Learning method and its combination with sliding mode controllers is used to determine the injection dosage. Stability analysis of fractional systems is more complicated than that of integer order systems. Considering the structure of the response of linear time invariant fractional systems, the stability of the equilibrium point in these systems has been discussed [17]. However, in contrast to linear systems, the stability analysis of nonlinear fractional systems (NFS) runs slowly. Around two decades ago, the problem of structural stability of these systems was studied for the first time, considering the Riemann Liouville derivative and the use of Taylor's polynomial expansion. Furthermore, the concept of Lyapunov stability was introduced in [18], using Gronwall's lemma and Schwarz's inequality. On the other hand, in some references, the method of linearization has been used. However, a unique and specific basis theory has not been obtained yet.

In real world applications, model uncertainties and external disturbances can affect the performance of system. Dealing with these issues is one of the design problems of controllers. Sliding mode control (SMC) is an effective nonlinear robust control method. In recent decades, it has been widely used and has proved successful due to its good features such as high accuracy, ease of implementation and resistance to external disturbances and parametric uncertainties. [19]

This approach received attention after Utkin's work and was extended to control issues [20]. There are two main steps in the design of a sliding mode controller, namely, creating a suitable sliding surface that represents the desired dynamics (the sliding phase) and adjusting the control law in such a way that a sliding condition is achieved (the reaching phase). Sliding mode control (SMC) for integer order systems was used for a long time until its application to fractional systems began [21,23]. In [22], the control of a fractional system with input delay time and state was investigated using the SMC method. In [24], the synchronization of the uncertain, fractional Duffing Holmes system was investigated through the SMC method. In [25], the SMC method was used to stabilize a system of invariant, fractional order with linear time. Fractional chaotic systems were investigated under SMC [26, 27]. Several improved SMC methods based on neural networks [28], Riccati's approach [29], LMI [30] and the adaptive technique [31] have been proposed.

In [32], a fuzzy adaptive controller was designed with a fractional calculus approach and sliding mode. In [33], an adaptive step back output feedback controller was proposed for a group of nonlinear fractional systems. The authors of [34] presented an adaptive sliding mode control for nonlinear systems with uncertainty. In [35], a high order sliding mode observer, combined with an adaptive fraction order sliding mode control, was proposed for diabetic patients. A fractional sliding mode control method was proposed in [36] for a group of nonlinear systems that were subject to uncertainty. The paper [37] examined the design of an adaptive sliding mode controller for fractional linear systems that were exposed to uncertainty and nonlinear disturbances. The authors of [38] assessed the application of a fractional control method based on a sliding mode used to track and stabilize a group of nonlinear fractional systems subject to uncertainty and drew upon a second order sliding mode approach in combination with a PI based design for the single input mode.

A sliding mode control law was proposed in [39], based on a new backstepping technique for nonlinear fractional systems subject to mismatched disturbances. In [40], a fractional sliding mode control was designed to use the particle swarm optimization (PSO) algorithm for a specific class of nonlinear fractional systems. The paper [41] studied the sliding mode control of output feedback for nonlinear fractional systems and proposed a necessary and sufficient condition for the existence of a sliding surface in the LMI form. The authors of [42] used a sliding mode control for a group of fractional systems with matched and mismatched disturbances and offered a fractional disturbance observer to approximate both matched and mismatched disturbances. In addition, the sliding surface was constructed based on the oberver's output. Based on the LMI method, [43] proposed a sliding mode control method for a group of fractional systems in which the upper bound of the known uncertainty was given. In [44], the stabilization problem was investigated by adaptive sliding mode control for a group of uncertain, nonlinear fractional Hopfield neural networks. In [45] a conformable fractional order sliding mode control method is studied for a class of fractional order chaotic systems in the presence of uncertainties and disturbances and stability analysis of the controller is derived by Lyapunov method with conformable fractional order operators.

The authors of [46] presented a second order, LQR- based sliding mode controller for a group of nonlinear fractional systems. A sliding mode active disturbance rejection control was proposed in [47] for nonlinear fractional systems with uncertainty and unknown disturbances. In [48], the asymptotic stability of a group of nonlinear fractional systems with bounded inputs, in the presence of uncertainty and external disturbances, was studied by adaptive constrained sliding mode control. By using sliding mode controllers, the stabilization of chaotic dynamic systems of nonlinear, fractional order was investigated in [49]. Building on the composite learning sliding mode control to control fractional nonlinear systems with actuator faults, [50] introduced a fractional integral sliding surface. Recently, in [51] a new adaptive fuzzy fractional order fast terminal sliding mode control method used for a class of nonlinear systems in the presence of uncertainties and external disturbances.

In the last two or three years, the use of sliding mode control in combination with fractional order calculations or in order to stabilize fractional order systems has attracted the attention of many researchers [52]. Fractional order sliding mode control law has been recently used for stabilizing different systems such as image encryption [53], Power Grids [54], cryptography [55], complex systems [56] and so on.

Despite its significance among advanced control methods resulting from high resistance to uncertainties and high ability to control indeterminate conditions, sliding mode control has a major drawback; the chattering phenomenon. The chattering

phenomenon can lead to unwanted fluctuations in the control system and derail the behavior of the system from what is desirable [57, 58]. There are some ways to prevent chattering. One of the most common methods is to use a fuzzy algorithm to obtain the amplitude of a narrow boundary layer around the sliding surface. Nonetheless, this is a slow process [59]. Another method is to apply high order sliding mode control, what prevents chattering without reducing accuracy. However, in addition to the difficulty of implementation, this method has the problem of chattering when high order sliding dynamics increase the relative degree of the system [60]. The continuous ap proximation method is more useful for the reduction of chattering than the other methods mentioned here. This method designs the control signal discontinuity by substituting a continuous function and creating a narrow boundary layer around the sliding surface; no report has been published concerning this method as yet [61].

Although many studies have been conducted in the field of control of nonlinear fractional systems in the presence of uncertainties and disturbances, most of them have some drawbacks, to the best of our knowledge, that we now briefly describe. First, the studies do not solve the problem of stabilizing for the general form of nonlinear, affine fractional systems. Also, in most cases, the upper bound of uncertainties and external disturbances is considered to be known. This is in contrast to what happens in real applications, where the limits of model uncertainties and external disturbances are unknown in practical systems. This issue has been addressed and discussed in our present research by designing a new robust adaptive fractional sliding mode controller (RAFSMC) which is proposed in next Section.

The contribution and innovations of this paper can then be summarized as follows:

- Considering a more general form of nonlinear fractional order systems as affine nonlinear systems.
- Designing a new robust-adaptive fractional order sliding mode controller by proposing a new fractional order sliding surface.
- Stabilizing the system in the presence of both model uncertainties and external disturbances; where the upper band of uncertainties and disturbances is unknown.
- Estimating the upper bound of uncertainties by designing stable adaptive rules.
- Solving the problem of glucose level regulation by considering the nonlinear fractional order model of Glucose-insulin Systems as applications to the proposed methodology.

This paper is organized as follows. In Section 2, the problem is formulated and the model of nonlinear, fractional affine systems in the presence of model uncertainties and disturbances is presented. The robust adaptive fractional sliding mode controller is designed in Section 3. In Section 4, simulation results are given to confirm the analytical results. Finally, the conclusion closes the paper in Section 5.

II. Formulation of the problem

A. Model of the system

The system under consideration is a class of nonlinear, affine fractional systems that can describe a comprehensive range of dynamic systems:

$$\begin{aligned} {}_0^C D_t^\alpha x(t) &= f(x) + g(x)u(t), \\ x(0) &= x_0. \end{aligned} \tag{1}$$

Here, $f: \mathbb{R}^n \longrightarrow \mathbb{R}^n$ is an arbitrary nonlinear function, piecewise continuous and local Lipschitz with Lipschitz constant in the area enclosing the origin. Also, $x(t) \in \mathbb{R}^n$ denotes pseudo-state, $g: \mathbb{R}^n \to \mathbb{R}^{n\times m}$ is an arbitrary nonlinear function and $u(t) \in \mathbb{R}^m$ is the input of the system. It is assumed that $0 < \alpha < 1$ and ${}_0^C D_t^\alpha$ denotes the Caputo derivative operator, which is defined by

$${}_0^C D_t^\alpha x(t) = \frac{1}{(\Gamma(\lceil\alpha\rceil - \alpha)} \int_0^t \frac{x^{(\lceil\alpha\rceil)}(\tau)}{(t-\tau)^{\alpha-\lceil\alpha\rceil+1}} d\tau \tag{2}$$

where $\Gamma(.)$ denotes the Gamma function and $\lceil\alpha\rceil$ is the least integer that is greater than or equal to α [62].

B. A system with model uncertainty and external disturbance

Considering the external disturbances and model uncertainties, the nonlinear fractional system in (1) can be expressed as

$${}_0^C D_t^\alpha x(t) = \big(f(x(t)) + \delta f(x(t))\big) + g(x(t))u(t) + d(t) \tag{3}$$

where $d(t) \in \mathbb{R}^n$ denotes the external, bounded and unknown disturbance and $\delta f(x)$ shows additive model uncertainties. By aggregating the uncertainties and disturbances, the model of the system can be written as

$${}_0^C D_t^\alpha x(t) = f(x(t)) + g(x(t))u(t) + E(x(t)), \tag{4}$$

where $E(x(t)) = \delta f(x(t)) + d(t)$. Now, consider the following assumption.

This format is actually the general form of fractional order nonlinear affine systems which are exposed to perturbations and many systems in practice can be written in this format. Robotic systems, biological systems, all the linear systems, chemical processes, etc. can be written in this affine form. As you can see, two of these real systems are mentioned in the simulation section, including the glucose-insulin system and the chaotic Lu system.

Assumption 2.1 Assume that the amount of external disturbances and uncertainties is bounded as

$$\| E(x(t)) \| \leq \gamma, \tag{5}$$

where $\gamma \in \mathbb{R}^+$ indicates the upper bound of model uncertainties and external disturbances and is considered to be unknown. The aim of this paper is to design a sliding mode control law for the NFS exposed to model uncertainties and external disturbances in (4), in such a way that in spite of Assumption 2.1 the system becomes asymptomatically stable. In addition, an adaptive law is also designed to estimate the upper bound of model uncertainties in (5). Asymptotic stability is defined as follows

Definition 2.2 ([64]). The constant vector x_{eq} is an

equilibrium point of the fractional system ${}_0D_t^{\alpha}x(t) = f(x(t))$ if and only if

$$f(x_{eq}) = 0$$

We assume, without loss of generality, that the equilibrium point is equal to 0 , that is, $x_{eq} = 0$.

Definition 2.3 ((Stability of NFS) [64]). Suppose that $x_{eq} = 0$ is equilibrium point of ${}_0D_t^{\alpha}x(t) = f(x(t))$. The system is said to be stable if for any initial condition $x(0) \in R^{n\times 1}$, there exists $\delta > 0$ such that any solution $x(t)$ of ${}_0D_t^{\alpha}x(t) = f(x(t))$ satisfies $\| x(t) \| < \delta$, for all $t > 0$. Furthermore, the fractional system is said to be asymptotically stable if the system is stable and $\| x(t) \| \to 0$ as $t \to \infty$.

In the next section, we design a sliding mode stabilizing controller for the NFS in (3).

III. RAFSMC design

SMC is a robust, nonlinear Lyapunov-based control method. The sliding mode design approach consists of two steps. The first involves the design of a switching function $s = 0$, such that the sliding motion satisfies the design specifications. The second one concerns the selection of a control law which will enforce the system to converge to the sliding surface (the sliding mode).

A. Defining the fractional sliding surface

Considering the input affine NFS in (4), the m dimensional, fractional sliding surface can be defined by

$$S(t) = Q\int_0^t {}_0^cD_\tau^{\alpha}x(\tau)d\tau - Q\int_0^t (f(x(\tau)) + L(x(\tau)))d\tau \quad (6)$$

where $S(t) = [s_1, s_2, \dots, s_m] \in \mathbb{R}^{m\times 1}$ is the sliding surface vector, $Q \in \mathbb{R}^{m\times n}$ and $L(x) \in \mathbb{R}^{n\times 1}$ are the control parameters that should satisfy the following assumption.

Assumption 3.1 We assume that the vector $L(x) \in \mathbb{R}^{n\times 1}$ and the matrix $Q \in \mathbb{R}^{m\times n}$ are chosen in such a way that they satisfy the following conditions.

1. $Qg(x) \neq 0$.
2. $Qg(x) \in \mathbb{R}^{m\times m}$ is nonsingular.
3. The NFS ${}_0^cD_t^{\alpha}x(t) = f(x(t)) + L(x(t))$ is asymptotically stable.

We considered the sliding mode such that, firstly, when is 0 , the desired characteristics and provided and, secondly, the system's dynamics would appear by deriving from it.

In the SMC design, the switching surface and its derivative should meet the conditions $s(t) = 0$ and $\dot{s}(t) = 0$, then based on (6) we have

$$Q{}_0^cD_t^{\alpha}x(t) - Q(f(x(t)) + L(x(t))) = 0, \quad (7)$$

where by assuming $Q \neq 0$ we find that

$${}_0^cD_t^{\alpha}x(t) = f(x(t)) + L(x(t))$$

Consequently, according to Assumption 3.1, the fractional equation in (7) implies that the closed-loop system is asymptotically stable, meaning that $x(t) \to 0$, when $t \to \infty$.

B. Selection of the reaching law

To satisfy the sliding mode condition, consider the reaching law

$$\dot{s} = -\mu s - \rho\, \mathrm{sign}(s), \quad (8)$$

where $\mu, \rho \in \mathbb{R}^+$,

and $\mathrm{sgn}(s) = [\mathrm{sgn}(s_1), \mathrm{sgn}(s_2), \dots, \mathrm{sgn}(s_m)]^T \in \mathbb{R}^m$ denotes the sign function vector [9].

Lemma 3.2 ([63]). By adopting the reaching law as in (8), the system reaches the switching surface at the finite time T^* given by

$$T^* = \frac{1}{\mu}\ln\left(\frac{\rho + \mu \max\limits_{i=1,\dots,m} |s_i(0)|}{\rho}\right). \quad (9)$$

C. Controller design

In this subsection, we use the fractional sliding surface in (6) and consider the reaching law in (8) to design a new stabilizing, RAFSMC for the system introduced in (4) which is robust against model uncertainties and external disturbances. Besides, in this controller, the unknown upper bound of model uncertainties and disturbances is obtained via a stable adaptive law.

In the following, we present a theorem that describes the basics and fundamentals of RAFSMC design.

Theorem 3.3 Consider the NFS exposed to model uncertainties and external disturbances described in (3). By applying the control law

$$u(t) = (Qg(x))^{-1}(QL(x) - \mu s - \rho\hat{\gamma}\mathrm{sgn}(s)), \quad (10)$$

in which the estimation of upper bound $\hat{\gamma}$ is obtained from the adaptive law

$$\dot{\hat{\gamma}}(t) = k_1\rho s^T \mathrm{sgn}(s), \quad (11)$$

where $k_1 > 0$ is the adaptive law gain and the sliding surface is defined as in (6), along with Assumptions 2.1,3.1 we find that the closed-loop system (4) is asymptotically stable if the constant, scalar values μ and ρ are chosen such that $\mu > 0$ and $\rho > \| Q \|$.

Proof. Differentiating the sliding surface defined in (6) and substituting the NFS in (3) we obtain

$$\begin{aligned}\dot{s}(t) = {} & QD^{\alpha}x(t) - Q(f(x(t)) + L(x(t)) \\ = {} & Q(f(x(t)) + \delta f(x(t)) + g(x(t))u(t) + d(t)) \\ & -Q(f(x(t)) + L(x(t)) \\ = {} & Q(g(x(t))u(t) + E(x(t)) - QL(x(t)). \end{aligned} \quad (12)$$

Now, consider the Lyapunov candidate function

$$V(t) = \frac{1}{2}s^Ts + \frac{1}{2k_1}\tilde{\gamma}^2, \quad (13)$$

where $k_1 > 0$ and $\tilde{\gamma} = \hat{\gamma} - \gamma$ stands for the upper bound estimation error. Then, differentiating (13) with respect to time and substituting from (12) result in

$$\begin{aligned}\dot{V}(t) = {} & s^T\dot{s} + \frac{1}{k_1}\tilde{\gamma}\dot{\tilde{\gamma}} \\ = {} & s^T(Q(g(x(t))u(t) + E(x(t)) - QL(x(t)))) \\ & + \frac{1}{k_1}\tilde{\gamma}\dot{\tilde{\gamma}}. \end{aligned} \quad (14)$$

Now, applying the RAFSMC in (10) to (14) yields

$$\dot{V}(t) = s^T(QL(x(t)) - \mu s - \rho\hat{\gamma}sgn(s) + QE(x(t)) - QL(x(t)) + \frac{1}{k_1}(\hat{\gamma} - \gamma)\dot{\hat{\gamma}} \quad (15)$$

where removing the similar terms and noticing $\dot{\tilde{\gamma}} = \dot{\hat{\gamma}}$ we obtain

$$\dot{V}(t) = s^T\left(-\mu s - \rho\hat{\gamma}sgn(s) + QE(x(t)) + \frac{1}{k_1}(\hat{\gamma} - \gamma)\dot{\hat{\gamma}}\right. . \quad (16)$$

Now, considering the definition of $\| s \|$ as $s^T sgn(s)$, $s^T s = \| s \|^2$ and applying the adaptive law from (11) we find that

$$\dot{V}(t) = -\mu \| s \|^2 - \rho\hat{\gamma} \| s \| + s^T QE(x(t)) \quad (17)$$

$$+\rho(\hat{\gamma} - \gamma) \| s \| = -\mu \| s \|^2 + s^T QE(x(t)) - \rho\gamma \| s \|. \quad (18)$$

The upper bound of $\dot{V}(t)$ in (18) can be computed as

$$\dot{V}(t) \le -\mu \| s \|^2 + \| s \| \| Q \| \| E(x(t)) \| - \rho\gamma \| s \| \quad (19)$$

So, considering the inequality (5) in Assumption 1 we can write

$$\dot{V}(t) \le -\mu \| s \|^2 + \| s \| \| Q \| \gamma - \rho\gamma \| s \| = -\mu \| s \|^2 + (\| Q \| - \rho)\gamma \| S \quad (20)$$

As a result, by selecting $\mu > 0$ and $(\| Q \| - \rho) < 0$ (or $\rho > \| Q \|$), we find that the upper bound of the derivative of the Lyapunov function is negative semi-definite. Now, by defining $\tilde{w}(t) = \mu \| s \|^2 + \| Q \| - \rho)\gamma \| s \|$ and integrating the both sides of (20), we deduce that $V(0) \ge V(t) + \int_0^t \tilde{w}(\lambda)d\lambda$. From this inequality we conclude that $\infty > V(0) \ge \lim_{t\to\infty} \int_0^t \tilde{w}(\lambda)d\lambda$. Hence, according to the Barbalat lemma [65], $\tilde{w}(t)$ and thus $s(t)$, converges to 0 when $t \to \infty$ and $\tilde{\gamma}$ remains bounded. So, according to the definition of the sliding surface in (6) and the stable equation in (7) and by the convergence of s to 0, the NFS in (3) is asymptotically stable and the psudostate $x(t)$ of the system will asymptotically converge to 0.

It is worth to mention that the RAFSMC controller proposed in this paper, is designed based on Lyapunov theory and none of the controllers designed using this method are unique, because the Lyapunov theory proposes only sufficient and not necessary condition for stability. Therefore, this controller is not necessarily unique, meaning that there may be thousands of other controllers with different structures that may asymptotically stabilize the system.

In this paper, in order to reduce the chattering similar to what is suggested in [63,66], we use a continuous function instead of the sign function. To this end, we approximate the sign function in (10) and (11) by the function

$$\rho\, sgn(s) \cong \frac{\rho^2 s}{\rho \| s \| + \sigma(t)}, \quad (21)$$

where $\sigma(t) > 0$ is a positive, bounded function such that $\int_0^\infty \sigma(t)dt < \infty$. For example,

$$\sigma(t) = \frac{1}{1+t^n}, \quad n \ge 2. \quad (22)$$

IV. Simulation Results

We show the effectiveness of our proposed method by two examples.

Example 4.1. Consider the model that described by the Caputo fractional differential equations [67]

$$\begin{cases} {}_0^C D_t^\alpha x_1(t) = -p_1[x_1(t) - G_b] - x_1(t)x_2(t) + d(t) \\ {}_0^C D_t^\alpha x_2(t) = -p_2 x_2(t) + p_3[x_3(t) - I_b], \quad 1 < \alpha < 1 \\ {}_0^C D_t^\alpha x_3(t) = -n[x_3(t) - I_b] + u(t), \end{cases}$$

$$y = Cx(t) \quad x(0) = [380, 0.0001, 310]^T \quad (23)$$

which $x_1(t)$ represent the temporal dynamics of the blood glucose concentration at time t, $x_2(t)$ the auxiliary function representing insulin-excitable tissue glucose uptake activity, proportional to insulin concentration in a 'distant' compartment and $x_3(t)$ the blood insulin concentration at time t.

$u(t)$ defines the insulin injection rate and replaces the normal insulin regulation of the body, which acts as the control variable. Since the normal insulin regulatory system does not exist in the body of diabetic patients, this glucose absorption is considered as a disturbance for the system dynamics and $d(t)$ shows the rate at which glucose is absorbed by the blood from the intestine, following food intake. The glucose concentration in blood is considered as the output $y(t)$, where

$$y(t) = [1 \quad 0 \quad 0]x(t) \quad (24)$$

For convenience we use the following replacement,

$$\begin{cases} x_1(t) := x_1(t) - G_b \\ x_2(t) := x_2(t) \\ x_3(t) := x_3(t) - I_b \end{cases} \quad (25)$$

Then system (23) will be as follows:

$$\begin{cases} {}_0^C D_t^C x_1(t) = -p_1 x_1(t) - x_1(t)x_2(t) + d(t) \\ {}_0^C D_t^\alpha x_2(t) = -p_2 x_2(t) + p_3 x_3(t) \\ {}_0^C D_t^\alpha x_3(t) = -n x_3(t) + u(t) \end{cases} \quad (26)$$

TABLE 1
PARAMETERS AND DESCRIPTIONS IN (EX. 4.1)

Parameter	DESCRIPTION	Value
p_1	The insulin-independent constant rate of glucose uptake in muscles and liver	$0.001(1/min)$
p_2	Therate for decrease in tissue glucose uptake ability	$0.23(1/min)$
p_3	The insulin-dependent increase in glucose uptake ability in tissue per unit of insulin concentration above the basal level	$6.3 \times 10^{-4}((\mu U/ml)^{-1}min^{-2})$
G_b	The basal value of glucose concentration in plasma	$80(mg/dl)$
I_b	The basal value of insulin concentration in plasma	$10(\mu U/ml)$
n	The first order decay rate for insulin in blood	$0.16(1/min)$

Now, the nonlinear fractional order glucose-insulin model (26) with the parameter values of a diabetic patient can be rewritten as [67]

$$
\begin{aligned}
&{}_{0}^{C}D_{t}^{\alpha}x(t) = f(x) + g(x)u(t) + Dd(t), 0 < \alpha < 1\\
&y(t) = Cx(t),
\end{aligned}
\tag{27}
$$

where

$$
\begin{aligned}
&f(x) = Ax + [-x_1(t)x_2(t), 0, 0]^T\\
&A = \begin{bmatrix} -p_1 & 0 & 0 \\ 0 & -p_2 & p_3 \\ 0 & 0 & -n \end{bmatrix}\\
&g(x) = [0,0,1]^T\\
&D = [1,0,0]^T\\
&C = [1 \quad 0 \quad 0].
\end{aligned}
$$

We calculate the equilibrium point of the system (23) according to Definition 2.2 It will be obtained $[G_b, 0, I_b]$. The model uncertainties and external disturbances are considered as follows.

$$
\begin{aligned}
&\delta f(x(t)) = 0.1 \begin{bmatrix} -p_1 & 0 & 0 \\ 0 & -p_2 & p_3 \\ 0 & 0 & -n \end{bmatrix} \begin{bmatrix} x_1(t) \\ x_2(t) \\ x_3(t) \end{bmatrix},\\
&d(t) = [0.1 \text{ rand}, 0, 0]^T.
\end{aligned}
\tag{28}
$$

where rand is a random value between 0 and 1 . Using Theorem 3.3 and Assumption 3.1, the parameters of the RAFSMC and the adaptive law, respectively in (10) and (11), can be selected as follows.

$$
\begin{aligned}
&L(x(t)) = \begin{bmatrix} x_1(t)x_2(t) - 5x_1(t) \\ -p_3x_3(t) - 4x_2(t) \\ -3x_3(t) \end{bmatrix}\\
&Q = [0 \quad 0 \quad 1]\\
&\mu = 40, \rho = 3, k_1 = 4.
\end{aligned}
\tag{29}
$$

The initial value for the adaptive law are assumed as

$$\gamma(0) = 2$$

in order to eliminate the chattering, by using (21) and (22), the sign function of the RAFSMC (12) is approximated by the function

$$\rho\,\mathrm{sgn}(s) \cong \frac{\rho^2 s}{\rho \parallel s \parallel + \sigma(t)}, \quad \sigma(t) = \frac{1}{1+t^2}. \tag{30}$$

The result of simulating the behavior of system without controller is shown in Fig 1.

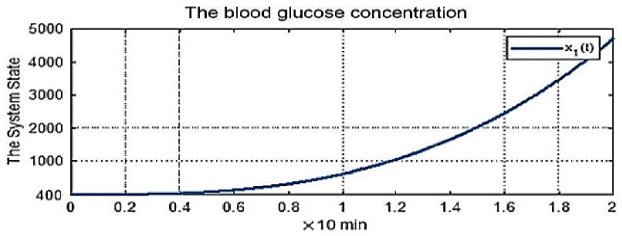

Fig. 1. The state response of the glucose concentration in system without controller (Ex. 4.1)

As it can be seen, the blood glucose concentration rises significantly in a system without a controller. Applying the RAFSMC as in (10)-(11) to the glucose-insulin system in (23), the simulation results shown in Fig 2-7 are obtained.

As it is evident from this Fig 2 the blood glucose concentration converges to the $G_b = 80\text{mg/dl}$ during about 20 minutes which shows asymptotic stability of the system in convergence to its equilibrium point in the presence of random external disturbance and uncertainty in the nonlinear model of Glucose-Insulinn system.

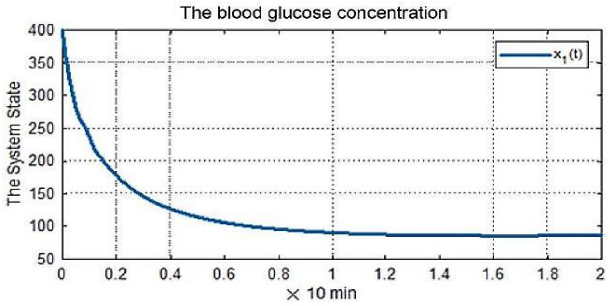

Fig. 2. The state response of the glucose concentration with controller (Ex. 4.1)

Fig 3 and Fig 4 show the trajectories x_2, x_3 that reach the equilibrium point. The insulin concentration as input controller in Fig 5 remained bounded and converges to a bounded value after stabilizing the system.

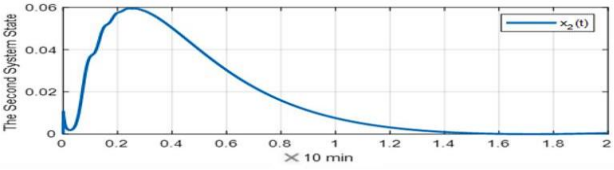

Fig. 3. The state response of the insulin-excitable tissue glucose (Ex. 4.1)

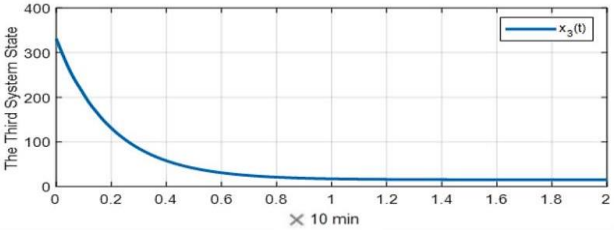

Fig. 4. The state response of the blood insulin concentration (Ex. 4.1)

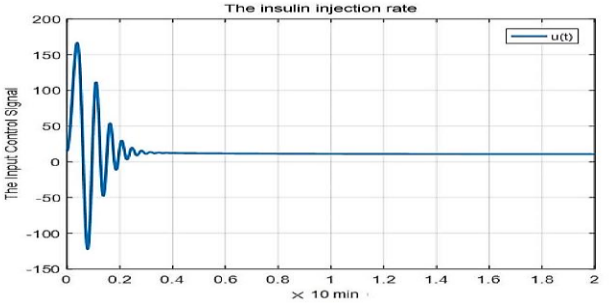

Fig. 5. The insulin concertration as input controller (Ex. 4.1)

In Fig 6, adaptive parameter is shown. These parameter is consistent with what was demonstrated in the stability of Theorem 8 and converge to a constant value. Finally, the sliding surface of the system is indicated in Fig 7. The sliding surface converges to 0 in a finite time.

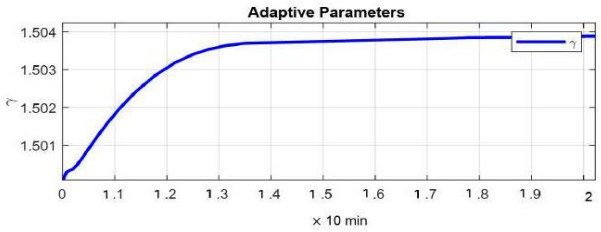

Fig. 6. Estimated adaptive parameter (Ex. 4.1)

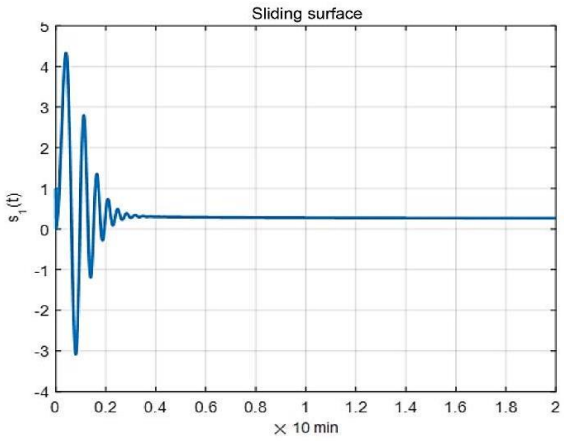

Fig. 7. The sliding surface of the glucose-insulin system (Ex. 4.1)

As a further explanation, it should be noted that Fig 2 to 4 are state variables in the glucose-insulin model. As we can see, glucose concentration, insulinexcitable tissue glucose and blood insulin concentration respectively converge to their equilibrium values. Apart from being achieved in a reasonable time, which is less than 10 minutes for the patient, this convergence has neutralized the effect of uncertainties and disturbances by applying the control law. Fig 6 and 7 are respectively the adaptive parameter and sliding surface. According to the stability proof, we expect that the adaptive parameter converges to zero in a finite constant value and the sliding surface also converges to a finite time while not having chattering. Fig 6 and 7 easily confirm these both facts.

Example 4.2. Consider the Lu fractional system. Given external disturbances and modelling uncertainties, the nonlinear fractional system model is selected from [49].

$$\begin{cases} {}^{C}D^{\alpha}x_1(t) = 36(x_2(t) - x_1(t)) + \delta f_1(t, x(t)) + d_1(t) + u_1(t), \\ {}^{C}D^{\alpha}x_2(t) = 20(x_2(t) - x_1(t)x_3(t) + \delta f_2(t, x(t)) + d_2(t) + u_2 \\ {}^{C}D^{\alpha}x_3(t) = x_1(t)x_2(t) - 3x_3(t) + \delta f_3(t, x(t)) + d_3(t) + u_3(t) \end{cases} \quad (31)$$

$$X(t_0) = [10, -5, 5]^T$$

where the values of uncertainty and disturbance are given by

$$\begin{cases} \delta f_1(t, x(t)) + d_1(t) = 0.2\cos(3t)x_1(t) + 0.15\sin(2t) \\ \delta f_2(t, x(t)) + d_2(t) = 0.25\sin(4t)x_2(t) + 0.2\sin(3t)i \\ \delta f_3\big(t, x(t)\big) + d_3(t) = 0.3\sin(2t)\, x_3(t) + 0.25\cos(4t) \end{cases} \quad (32)$$

This model is widely used in the electrical industry and power distribution systems.

Simulation of the behavior of the system without controller

For $\alpha = 0.98$, the result of simulating the behavior of the system without controller is shown in Fig 8.

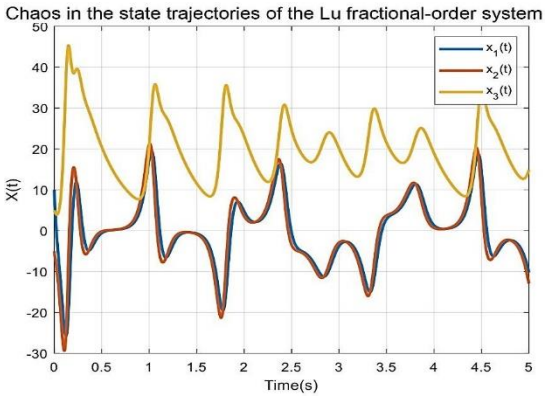

Fig. 8. Behavior of the Lu system without controller (Ex. 4.2).

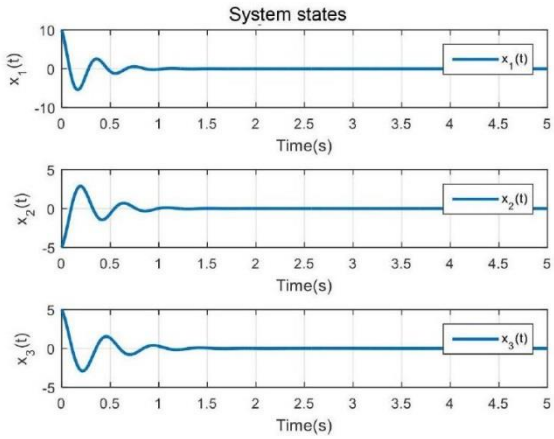

Fig. 9. System states after applying proposed controller (Ex. 4.2)

Simulation of system with controller

Using the method presented in this paper, the closed loop system is simulated in the presence of modelling uncertainties and external disturbances.Select the controller parameters to satisfy the Assumption 3.1 and Theorem 3.3, as follows.

$$L(x(t)) = \begin{bmatrix} -36x_2(t) + 30x_1(t) \\ x_1(t)x_3(t) - 25x_2(t) \\ -x_1(t)x_2(t) - x_3(t) \end{bmatrix}, \quad Q = \begin{bmatrix} 1 & 0 & 0 \\ 0 & 1 & 0 \\ 0 & 0 & 1 \end{bmatrix}. \quad (33)$$

In addition, the control gains and adaptive laws are selected as follows.

$$\mu = 40 \ , \ \rho = 2 \ , \ k_1 = 4. \quad (34)$$

To reduce the chattering, the sign function is approximated by

$$\rho sgn(s) \cong \frac{\rho^2 s}{\rho\|s\|+\sigma(t)} \ , \ \sigma(t) = \frac{1}{1+t^2}. \quad (35)$$

Considering the initial adaptive law as

$$\gamma(0) = 2, \quad (36)$$

the simulation results of the RAFSMC are shown in the Fig 9, 10, 11, 12 .

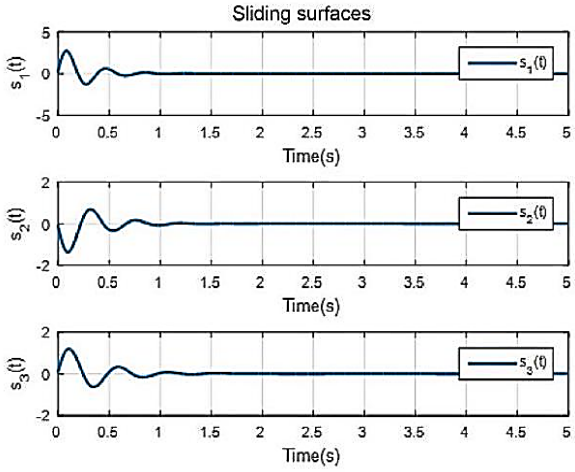

Fig. 10. Sliding surfaces converge to 0 by applying the control law (Ex. 4.2)

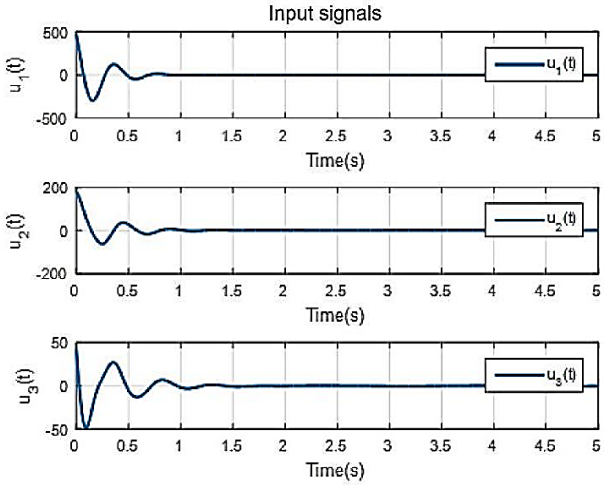

Fig. 11. Proposed RAFSMC (Ex. 4.2)

The stability of system by using the control input is shown in Fig 9, where the system states converge to 0 . Fig 10 shows the convergence of the sliding surface to zero and the control signal is shown in Fig 11. The adaptive parameter tends to a limited value in Fig 12.

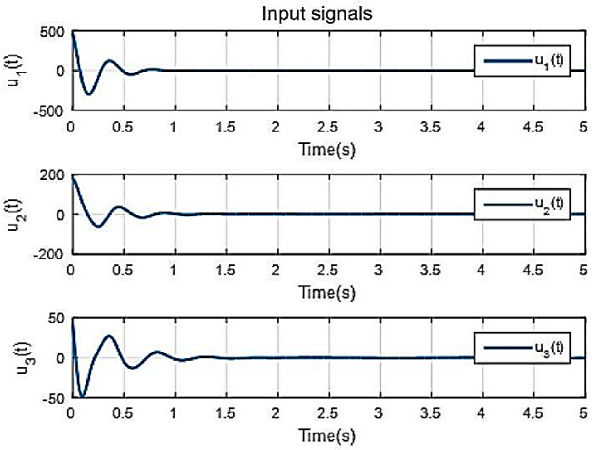

Fig. 12. Estimated adaptive parameter (Ex. 4.2)

We note that in [49], the following assumption is considered for uncertaintties and disturbances.

$$|\delta f_i(x,t)| + |d_i(t)| \le \rho_i < \infty; \ \ i = 1,2,\dots,n. \quad (37)$$

Finally, the control law designed in the article is as follows.

$$u_i(t) = -(f_i(t,x_i(t)) + k_i|x_i(t)|^{\eta}\tanh(x_i(t)) + \rho_i + \gamma_i S_i(t) + \lambda_i|S_i(t)|^{\delta}\tanh(S_i(t)). \quad (38)$$

The outcome is that the parameter ρ_i is used in the control law. That is, the upper bound of the sum of uncertainties and disturbances in this article is assumed to be known and the designer must be aware of and include this upper bound in the control law. However, the method presented in our article does not have such a limitation.

Briefly, we know, the assumption of an unknown upper bound for uncertainties and disturbances is more realistic in practical applications. In this article, according to Equation (3), we consider a nonlinear affine fractional order system exposed to uncertainties and external disturbances with unknown upper bound. A new robust adaptive fractional sliding mode controller was designed to stabilize this system. The proposed controller provides the features and general advantage of sliding mode controllers, such as high accuracy of sliding mode part, simplicity of implementation, and resistance to external disturbances and parametric uncertainties, also we used the advantage of adaptive controller for approximating that upper bound.

The stability of the proposed controller was proved in Theorem 3.3. At the end, for checking the effectiveness of the method, in Example 4.1, we showed that the state variables converge to the equilibrium point faster and in a shorter period compared with the controller used for the stability of the same system in reference [67].

Also, in Example 4.2, the designed controller in reference [49], (with known upper bound of uncertainties and disturbances) was compared with our proposed controller (with unknown upper bound), which is a significant strength and can lead to a more effective solution in real applications.

V. Conclusion

In this paper, stability of a class of NFSs in the presence of uncertainty and external disturbance was considered. To solve the problem, a RAFSMC with a new fractional sliding surface was designed. Since in real life, the upper bound of uncertainties and external disturbances are unknown, we use an adaptive law to approximate it, however in most articles the upper bound is considered to be known. Finally, to evaluate the efficiency of the proposed method, the fractional models of the glucose-insulin system and the Lu system were considered and simulation confirm analytical results. Also rapid convergence to the equilibrium point is another benefit of the method .Extending this work to situations in which the Fractional order nonlinear system is subject to delay (especially in the case of biological systems such as glucose-insulin which are subject to real delay), the design of an adaptive sliding mode control law where the control input is saturated due to the limited range of the input Control in practice, generalizing the method for incommensurate fractional order systems or variable order fractional nonlinear problems and finally, optimization of controller coefficients with methods based on computational intelligence or meta-heuristic algorithms are topics for further work.

REFERENCES

[1] A. Ouannas, I. M. Batiha, et al, "Synchroniza- tion of the Glycolysis Reaction-Diffusion Model via Linear Control Law, MDPI, Entropy", Spe- cial Issue on Advanced Numerical Methods for Differential Equations, Vol. 23, No. 11, pp. 1516, 2021.

[2] M. H. Heydari, M. Razzaghi, "Extended Cheby- shev cardinal wavelets for nonlinear fractional delay optimal control problems", International Journal of System Science, pp. 1048-1067, 2022.

[3] S. M. Kenneth, and R. Bertram, An Introduction to the Fractional Calculus and Fractional Differ- ential Equations, Wiley-Interscience Publication, US, 1993.

[4] F. Mainardi, "An historical perspective on frac- tional calculus in linear viscoelasticity," Frac- tional Calculus and Applied Analysis, Vol. 15, pp. 712-717,2012.

[5] F. Mainardi, Fractional Calculus and Waves in Linear Viscoelasticity: An Introduction to Math- ematical Models, London: Imperial College Press, 2010.

[6] J. Kang, Z. H. Zhu and W. Wang, et al., "Frac- tional order sliding mode control for tethered satellite deployment with disturbances ", Adv. Space Res., Vol. 59, pp. 263-273, 2017.

[7] R. L. Magin, "Fractional Calculus models of Com- plex dynamics in biological tissues," Computers and Mathematics with Applications , Vol. 59, pp. 1586-1593, 2010.

[8] Y. Yan and C. Kou, "Stability analysis for a fractional differential model of HIV infection of CD4+ T cells with time delay ", Math.comput. simul, Vol. 82, No. 9, pp. 1572-1585, 2012.

[9] Zh. Wang, X. Huang and H. Shen, "Control of an uncertain fractional order economic system via adaptive sliding mode ", Neurocomputing, Vol. 83, pp. 83-88, 2012.

[10] M. H. Heydari, M. Razzaghi, "A new class of orthonormal basis functions: application for frac- tional optimal control problems", International Journal of System Science,pp. 240-252, 2022.

[11] M. H. Heydari, M. Razzaghi, Z. Avazzadeh, "Or- thonormal piecewise Bernoulli functions: Appli- cation for optimal control problems generated using fractional integro-differential equations", Journal of Vibration and Control, 2022.

[12] M. H. Heydari, M. Razzaghi, "A numerical ap- proach for a class of nonlinear optimal control problems with piecewise fractional derivative", Chaos, Solitons and Fractals, Vol. 152, 2021.

[13] M. U. Saeem, M. Farmand, A. Ahmad, E.U. Haque, and M.O. Ahmad, "A Caputo Fabrizio fractional order model for control of glucose in insulin therapies for diabetes", Ain Shams Engi- neering Journal, Vol. 11, No. 4, pp. 1309-1316, 2020.

[14] A. Mohammadzadeh and Tufan Kumbasar, "A new fractional order general type-2 fuzzy predic- tive control system and its application for glucose level regulation", Applied Soft Computing, Vol. 91, 2020.

[15] N. Debbouche, A. O. Almatroud, A. Ouan- nas and I. M. Batiha, "Chaos and coexist- ing attractors in glucose-insulin regulatory sys- tem with incommensurate fractional-order deriva- tives", Chaos, Solitons & Fractals, Vol. 143, pp. 110575, 2021.

[16] A. Noori, M. A. Sadrnia and M. B. Naghibi- Sistani, "Fault Tolerant control of Blood Glucose concentration using Reinforcement Learning", International Journal of Industrial Electronics, Control and Optimization, Vol. 3, No. 3, pp. 353-364, 2020.

[17] A. E. Matouk, "Stability Conditions, hyperchaos and Control in a novel fractional order hyper- chaotic system ", Physics Letters Am Jun, Vol. 373, No. 25, pp. 2166-2173, 2009.

[18] B. Bonilla, M. Rivero, L. Rodriguez-Germa and J.J. Trujillo, "Fractional differential equations as alternative models to nonlinear differential equa- tions ", Applied Mathematics and Computation , Vol. 187, No. 1, pp. 79-88 , 2007.

[19] A. Pisano and E. Usai, "Sliding mode Control. A Survey with applications in math ", Mathematicy and Computers in Simulation, Vol. 81, No. 5, pp. 954-979, 2011.

[20] V.I. Utkin, Sliding Modes in Control and opti- mization, New York: Springer-Verlag, 1992.

[21] Mo. Efe and CA. Kasnakoglu, "Fractional adap- tation law for sliding mode Control ", Interna- tional Journal of Adaptive Control and Signal Processing, Vol. 22 , pp. 968-986, 2008.

[22] A. Si-Ammour, S. Djennoune and M. A. Bet- tayeb, "A sliding mode Control for linear frac- tional Systems with input and State delays ", Communications in Nonlinear Science and Nu- merical Simulation, Vol. 14, No. 5, pp. 2310-2318, 2009.

[23] Mo. Efe, Fractional order Sliding mode Con- troller design for fractional order dynamic sys- tems. In New Trends in. Nanotechnology and Fractional Calculus Applications, Guvene ZB, Baleanu D, Tenreiro Machado JA. Springer Ver- lag: Dordrect; 463-470, 2010.

[24] S. H. Hossinnian, R. Ghaderi, A. Ranjber,M. Mahmoudian and S. Momani, "Sliding mode Synchronization of an uncertain fractional order chaotic system ", comput. Math. Appl. , Vol. 59, pp. 1637-1643, 2010.

[25] S. Balochian, A. K. Sedigh and A. Zare, "Vari- able Structur Control of linear time invariant fractional order systems using afinite number of state feedback law ", Commun. Nonlinear SCi. Number. Simulat. , Vol. 16 , pp. 1433-1442, 2011.

[26] M. S. Tavazoei and M. Haeri, "Synchronization of chaotic fractional order –Systems Via active sliding mode controller ", Phys., Vol. 387, pp. 57- 70, 2008.

[27] C. Yin, S. Dadras, S.M. Zhong and Y. Q. Chen, "Control of a novel Class of fractional- order Con- trol approach ", Appl. Mathe. Model , Vol. 37, pp. 2469-2483, 2013.

[28] SW. Wang, Yu. DW and Yu. DL, "Compen- sation for

unmatched uncertainty with adaptive RBF network ", Int J Eng sci., Vol. 3, No. 6 , pp. 801- 804, 2011 .

[29] K. S. Kim and Y. Park, "Designing robust slid- ing hyper planes for parametric uncertain systems , a riccati approach ", Automatica, Vol. 36, No. 7, pp. 1041-1048, 2000.

[30] HC. Han, "Lmi-based sliding Surface design for integral Sliding mode Control of mismatched un- certain systems ", IEEE Trans Autom Control , Vol. 52, No. 4 , pp. 736-42, 2007.

[31] VI. Utkin and AS. Poznyak, "Adaptive Sliding mode Control ", Lecture Notes in Control and Information Sciences , pp. 21-53, 2013.

[32] M. O. Efe, "Fractional fuzzy adaptive sliding- mode control of a 2-DoF direct-drive robot arm ", IEEE Transactions on systems, Man, and cy- bernetics, Vol. 38, No. 6, pp. 1561-1570, 2008.

[33] Y. Wei, PW. Tse, Z. Yao and Y. Wang, "Adaptive backstepping output feedback control for a class of nonlinear fractional order systems ", Non- linear Dyn, Vol. 86, No. 12 , pp. 1-10, 2016.

[34] H. Li, J. Wang and HK. Lam, "Adaptive sliding mode control for interval type-2 fuzzy systems ", IEEE Transactions on systems, Man and cyber- netics: systems , Vol. 46, No. 12 , pp. 1-10 ,2016.

[35] H. Delavari, H. Heydarinejad and D. Baleanu, "Adaptive fractional blood glucose regulator based on high-order sliding mode observer ", IET systems Biology , Vol. 13, No. 2 , pp. 43-54, 2019.

[36] D. Zhang, L. Cao and S. Tang, "Fractional or- der Sliding mode control for a class of uncertain nonlinear systems based on LQR ", International Journal of Advanced Robotic systems , Vol. 14, No. 2, pp. 1-15, 2017.

[37] L. Chen, R. Wu, Y. He and Y. Chai, "Adaptive sliding mode control for fractional order uncer- tain linear systems with nonlinear disturbances ", Nonlinear Dyn, Vol. 80 , pp. 51-58, 2015.

[38] B. Jakovljevic, A. Pisano, M. R. Rapaic and E. Usai, "On the sliding-mode control of fractional- order nonlinear uncertain dynamics", Interna- tional Journal of Robust and Nonlinear Control, Vol. 26, No. 4, 2015.

[39] T. Takamatsu and H. ohmori, "Sliding mode controller design based on backstepping technique for fractional order system ", SICE Journal of control, Measurment and system Integration, Vol. 9, No. 4, pp. 151-157, 2016

[40] A. Djari, T. Bouden and A. Boulkroune, "De- sign of Fractional order sliding mode controller (FSMC) for a class of fraction order Nonlinear commensurate systems using a Particle swarm op- timization (PSO) Algorithm ", CEAI, Vol. 16 , No. 3 , pp . 46-55, 2014.

[41] T. Zhan, X. Liu and Sh. Ma, "A new singular system approach to output feedback sliding mode control for fractional order nonlinear systems ", Journal of the Franklin Institute, Vol. 355, No. 14, pp. 6746-6762, 2018.

[42] Sh. Shi, J. Li and Y. Fang, "Fractional- disturbance-observer-based sliding mode control for fractional order system with matched and mis- matched disturbances ", International Journal of control, Automation and systems, Vol. 17, No. 5, pp. 1184-1190, 2019.

[43] Y. Chun, Y. Chen and S. M. Zhong, "LMI based design of a sliding mode controller for a class of uncertain fractional order nonlinear systems ", Proc. of American control conference, pp. 6511- 6516, 2013.

[44] B. Meng, Zh. Cheng and Zh. Wang, "Adaptive sliding mode control for a class of uncertain non- linear fractional order Hopfield neural networks ", AIP advances , Vol. 9, 2019.

[45] S. Haghighatnia, H. Toosian Shandiz and A. Alfi, "Conformable Fractional Order Sliding Mode Control for a class of fractional order chaotic systems", International Journal of Indus- trial Electronics, Control and Optimization, Vol. 2, No.3, pp. 177-188, 2019.

[46] K. Mathiyalagan and G. Sangeetha, "Second- order sliding mode control for nonlinear fractional systems ", Applied Mathematics and Computa- tion , Vol. 383, 2020.

[47] N. Djeghali, M. Bettayeb and S. Djennoune, "Sliding mode active disturbance rejection con- trol for uncertain nonlinear fractional order sys- tems ", European Journal of control , Vol. 57, pp. 54-67, 2021.

[48] T. V. Moghaddam, S. K. Yadavar Nikravesh and M. A. Khosravi, "Adaptive constrained sliding mode control of uncertain nonlinear fractional or- der input affine systems ", Journal of vibration and control, pp. 1-13, 2019.

[49] A. R. Haghighi and R. Ziaratban, "A non- integar sliding mode controller to stabilize frac- tional order nonlinear systems ", Advances in Dif- ference Equations, 2020.

[50] He. Liu, Ho. Wang, J. Cao, A. Alsaedi and T. Hayat, "Composite learning adaptive slid- ing mode control of fractional order nonlinear systems with actuator faults ", Journal of the Franklin Institute , Vol. 365, pp. 9580-9599, 2019.

[51] A. Noori, M. A. Sadrnia and M. B. Naghibi- Sistani, "Fault Tolerant control of Blood Glu- cose concentration using Reinforcement Learn- ing", International Journal of Industrial Electron- ics, Control and Optimization, Vol. 3, No. 3, pp. 353-364, 2020.

[52] Y. Chen, Ch. Tang and M. Roohi, "Design of a model-free adaptive sliding mode control to syn- chronize chaotic fractional-order systems with in- put saturation: An application in secure commu- nications", Journal of the Franklin Institute, Vol. 358, No. 16, pp. 8109-8137, 2021.

[53] M. Taheri, C. Zhang, Z. R. Berardehi, et al. "No- chatter model-free sliding mode control for syn- chronization of chaotic fractional-order systems with application in image encryption", Multimed Tools Appl, Vol. 81, pp. 24167-24197, 2022.

[54] Z. Esfahani, M. Roohi, M. Gheisarnejad, et al, "Optimal Non-Integer Sliding Mode Control for Frequency Regulation in Stand-Alone Mod- ern Power Grids", MDPI, Applied Sciences, Spe- cial Issue on Microgrids, Vol. 9, No.16, pp. 3411, 2019.

[55] M. Roohi, C. Zhang Y. Chen, "Adaptive model- free synchronization of different fractional-order neural networks with an application in cryptog- raphy", Nonlinear Dynamics, Vol. 100, pp. 3979- 4001, 2020.

[56] M. Roohi, M. H. Khooban, Z. Esfahani, et al, "A switching sliding mode control technique for chaos suppression of fractional-order complex systems", Transactions of the Institute of Measurement and Control, Vol. 41, No. 10, pp. 2932-2946, 2019.

[57] I. Boiko, L. Fridman, A. Pisano and E. Usai, "Analysis of Chattering in Systems with Second order sliding modes ", IEEE Trans Autom. Con- trol , Vol. 52, No. 11, pp. 2085-2102, 2007.

[58] R. Ziaratban, A.R. Haghighi and P. Reihani, "Design of a no-chatter fractional sliding mode control approach for stabilization of non-integer chaotic systems ", lnt. J. lnd math. Vol. 12, No. 3, pp. 215-223, 2020.

[59] M. R. Soltanpour and M. tt. Khooban, "A parti- cle swarm optimization approach for fuzzy sliding mode control for tracking the robot manipulator ", Nonlinear Dyn. , Vol. 74, No. 1, pp. 467-478, 2013.

[60] G. Bartolini, A, Pisano and E. Usai, Second order sliding mode control of container cranes , Automatica , Vol. 38, No. 10, pp. 1383-1790,2002.

[61] M. S. Asl and M. Javidi, "An improved PC scheme for nonlinear fractional differential equa- tions: error and stability analysis ", Comput. Appl.Math. , Vol. 324, pp.

101-117,2017.

[62] I. Podlubny, Fractional differential equations: an introduction to fractional derivatives, frac-tional differential equations, to methods of their solution and some of methods of their application , London: Academic press, 1999.

[63] M. N Soorki and M. S Tavazoei, “Adaptive ro- bust Control of fractional swarm systems in the presence of model uncertain ties and external dis- turbances ”, IET Control Theory Applications, Vol. 12, No. 7, pp. 961-969, (2018).

[64] CP. Li and FR. Zhang, “A survey on the sta- bility of fractional differential equations ”, The European Physical Journal Special Topics, Vol. 193, No. 1 , pp. 27-47, 2011.

[65] V. M. Popov, Hyperstability of control system, Springer-Verlag, Berlin, 1973.

[66] R. K. Munje, M. R. Roda and B. E. Kushare, “Speed control of DC Motor Using PI and SMC ”, Proceedings of IPEC IEEE conference, Singa- pore, Vol. 2, pp. 649-656, 2010.

[67] I. N. Doye, H. Voos, M. Darouach and J. G. Schneider, “Static output Feedback H∞ control for a Fractional-order Glucose-insulin system ”, International Journal of control, Automation, and systems, Vol. 13, No. 4, pp. 1-10, 2015.

Aghileh Heydari was born in 1972. She received her B.S. degree in Applied Mathematics in 1994 from Sharif University, Tehran, Iran and M.S. degree in Applied Mathematics (Optimal Control) in 1997 from Ferdowsi University of Mashhad (FUM), Iran. She wrote her dissertation under supervision of Prof. Ali Vahidian Kamyad. She received her PhD degree under supervision of Prof. Ali Vahidian Kamyad at FUM in March, 2002. She is currently a professor of athematics at Payame Noor University (PNU), Iran. PNU has numerous branches throughout Iran. Her research interests include Optimization, Optimal Control, Fuzzy Optimal Control Problems, Biomathematics, Modelling & optimal control of infectious diseases.

Forough Roshanravan was born in 1985. She received her B.S. degree in Applied Mathematics in 2008 from Ferdowsi University of Mashhad (FUM), Iran and M.S. degree in Applied Mathematics (Numerical Analysis) in 2012 from Ferdowsi University of Mashhad (FUM), Iran. Since 2014, she has been teaching at Birjand University of Technology, Iran as a lecturer. Currently, she is working towards her Ph.D. degree at Payame Noor University (PNU), Iran. Her research interests include nonlinear control theory, robust control, adaptive control, nonlinear fractional order systems and Biomathematics.

IECO

This page intentionally left blank.

International Journal Of
Industrial Electronics Control and Optimization
Print ISSN: 3517-2645
Online ISSN: 3568-2645
Homepage: https://ieco.usb.ac.ir/

A New Multi-Input DC/DC Converter with Coupled and Switched Inductor Applicable for Renewable Energy Sources

Gholamreza Mohebalizadeh[1]| Hasan Alipour[2]| Leila Mohammadian[3]| Mehran Sabahi[4]
Department of Electrical Engineering, Shabestar Branch, Islamic Azad University, Shabestar, Iran.[1,2,3]
Department of Electrical and Computer Engineering, University of Tabriz, Tabriz, Iran.[4]
Corresponding author's email: hasan.alipour2006@gmail.com

Article Info

Article type:
Research Article

Article history:
Received: 22 April 2022
Revised: 29 Sep. 2022
Accepted: 15 Nov. 2022
Published online: 21 Dec. 2022

Keywords:
Coupled Inductor (CI),
Energy Storage System (ESS),
Multi-Port Converter (MPC),
Renewable Energy Sources
Switched Inductor (SI),

ABSTRACT

To overcome the low output voltage of Renewable Energy Sources (RESs) such as photovoltaic arrays (PVAs) and fuel cells, a new multi-input DC/DC converter is presented in this paper. This converter is based on a combination of modified quadratic buck-boost converters, Switched Inductors (SIs), and Voltage Multiplier Modules (VMMs). The high voltage gain can be achieved by adjusting the duty cycle and turn ratio of the coupled inductor of VMM. This structure inherits all the advantages of the SEPIC converter and using a bidirectional input port (in which an Energy Storage System (ESS) can be connected) and several unidirectional input ports. The load power can be flexibly divided among various power sources. Due to the buck-boost characteristics of the presented converter, it is suitable to charge-discharge the ESS. A Coupled Inductor (CI) is used to couple energy from input to the output equipped with the VMM. Moreover, the use of SI reduces the rise time and ripple of the input current. The stability of the proposed converter against momentary changes of VPV and Ro is the main advantage of this converter. Moreover, considering a secondary ESS as Vi instead of PV allows the converter to be active 24 hours a day. In this converter, the use of two ESSs guarantees the supply of the required output power. In addition, two bidirectional input ports prepare the ESSs charging and discharging capabilities. To verify the analysis and feasibilities of the proposed converter, simulation results are presented

I. Introduction

Increasing demands for energy, air pollution, and depletion of fossil fuels have drawn researcher's attention to renewable energy sources (RESs), such as solar and wind energies. Depending on geographical areas, the power attained from RESs is variable. Therefore, an energy storage system (ESS), as an auxiliary power supply in a multi-input converter (MIC), is required to supply load necessities. The obtained output voltage is relatively low in RESs, such as photovoltaic arrays (PVAs). Therefore, high step-up DC/DC converters (HSUDCs) are widely required to overcome this defect for stepping up DC voltage and supplying inverters and DC loads [1-2]. A family of integrated modules of HSUDCs is reviewed in [3]. In single port converters, each RES requires a separate converter, which needs a different control system. Therefore, this enhances the system's complexity. In multi-port converters (MPCs), different RESs and ESSs are integrated as inputs with one output in a single topology with a simple controller [4]. MPCs can be classified into isolated and non-isolated topologies. Using isolated topologies provides a high gain by using high-turn ratio but with low efficiency and heavy weight [5]. Interleaved and non-interleaved converters are proposed in [6-7] and [8], respectively. In [9-12], a voltage multiplier module (VMM) is added to the converter. In [13-14] the voltage-clamped module (VCM) is added to the converter. Coupled inductors (CIs) and MICs are used in all HSUDCs explored in the following reviews, but ESS besides RES has

DOI: 10.22111/IECO.2022.41721.1416

not been considered. In [15-16], VMM and VCM are not considered. A soft-switched three-port converter is presented in [17-18]. There is no auxiliary power supply besides PVA to enhance the converter's ability for supplying a permanent power for output in both presented converters. In [19], because of using multiple CIs and multi-switches in the converter, the efficiency is low. In [20], the high voltage and current stress are the main defects of the converter because the two CIs are directly cascaded. In [21], a two-input DC/DC boost converter based on a coupled inductor and VMM is proposed. The ESS besides RES has not been considered and this is the main defect of this work. In [22], a comparison is made between generalized predictive control and linear controllers in a multi-input DC-DC boost converter, it does not consider ESS besides. Due to the fixed consideration of two inputs in this converter, the PV cannot be used as an input for this converter, which is the main defect of this converter. In [23] a non-isolated single-ended primary-inductor converter (SEPIC)-based multi-input DC/DC converter is presented. This converter inherits step-up/down capability and cannot acts as an HSUDC.

This paper presents a new SEPIC-based multi-input step-up voltage and current converter. The application of switched inductor (SI) instead of input inductance is a good substitute in the proposed converter. Therefore, this substitution minimizes the rise time and input current's ripples. Moreover, this converter has been functionally promoted by applying CI instead of inductor L_2, and adding two VMMs to its output. Therefore, this converter acts as a step-up voltage and current simultaneously, by applying CI with a low turn ratio and two VMMs. Moreover, the stability of the proposed converter against momentary changes of V_{PV} and R_o is the main advantage of the proposed converter. One or more unidirectional port (s) beside one bidirectional port (as a secondary ESS) are considered in this converter as input power sources. Considering a secondary ESS as V_i instead of PV allows the converter to be active 24 hours a day, which is the other important advantage of this converter. This makes the converter to be supplied by various types of RESs.

This paper consists of eight sections. The proposed structure of the converter is presented in Section 2. The proposed converter's functional modes are explained in Section 3. Section 4, explores the converter's power dissipation. Section 5, discusses the proposed converter's dynamic behavior. Section 6, presents a comparison between the proposed converter and other works. The simulation results and power management analysis are presented in the PSCAD environment in Section 7. The last section is devoted to concluding points.

II. Proposed Converter's Structure

Fig. 1 depicts a step-up multi-input SEPIC based on CI, two VMMs, and SI as the proposed converter. The PVA and S_1 are considered the main input and switch of this converter, respectively. The input inductor's structure is a SI based which consists of elements D_1, D_2, D_3, L_{i1}, and L_{i2}. This structure minimizes the input current rise time and ripples. Firstly, the main switch S_1 is turned on, and two inductors L_{i1} and L_{i2} make a parallel structure.

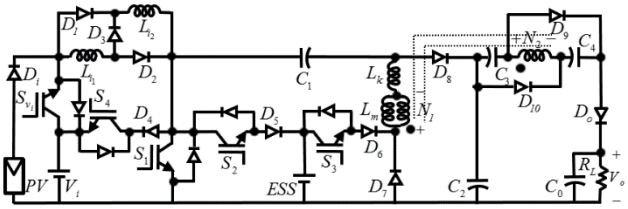

Fig.1. A schematic diagram of the proposed converter

This minimizes the input current's rise time. Secondly, the main switch S_1 is turned off, and two inductors L_{i1} and L_{i2} make a series structure. This minimizes the ripples of the input current after reaching the reference level. The main ESS besides PV is considered for supplying the output power. Switch S_2 and S_3 are applied for charging and discharging the main ESS, respectively. V_i as a secondary ESS is considered for supplying the converter's input power in place of PV at night. Switches S_{vi} and S_4 are applied for discharging and charging V_i, respectively. Magnetic inductor L_m is the output inductor as CI in this converter. In order to raise the load current, the turn ratio is determined low. Moreover, the lesser the CI's turn-ratio determination, the lighter the transformer, the lower the magnetic leakage, and the higher the output current will be attained. By this means, high efficiency can be achieved. Two VMMs are considered to quadruple the secondary voltage of the transformer.

III. Proposed Converter's Functional modes

The demanded output power is assumed constant in this paper. Therefore, three operational modes can be considered by making a comparison between this value and PVA's power. In the first mode, both powers have the same values. This mode is the simplest mode of operation. In this mode, the main switch S_1 is activated. In the second mode, PVA's power is smaller than the output power. This mode consists of two sub-modes, and S_1 and S_3 are triggered. Firstly, only S_1 is activated for reaching the output power to the maximum level attained from PVA. Secondly, S_1 and S_3 are triggered for sending ESS's power to the output for preparing the demanded power. In the 3rd mode, PVA's power is greater than the output demanded power. This mode consists of two sub-modes. Firstly, S_1 is activated so that the output power reaches its desired level. Secondly, the extra power for PVA is transferred through S_2 toward ESS for charging. In the

third state of this mode, the extra power of PVA is transferred through D_4 and S_4 after the time ESS is fully charged to charge the V_i battery. Therefore, V_i can be replaced with V_{pv} by turning on the switch S_{Vi} at night. The other RESs can be added to the input as a replacement of PVA. Therefore, this property makes the converter's input to be expandable. Those aforementioned properties besides the presence of CI, VMMs, and SI produce a converter with a low-ripple and rise-time of input current and step-up voltage/current properties. The following section presents functional modes in detail.

A. *The output demanded power is supplied only by PVA (P_{pv}=P_{out})*

In this mode, PVA can solely supply the output demanded power, and S_1 is the only switch that is triggered. Figs. 2 and 3 depict two states and time characteristics diagrams, respectively.

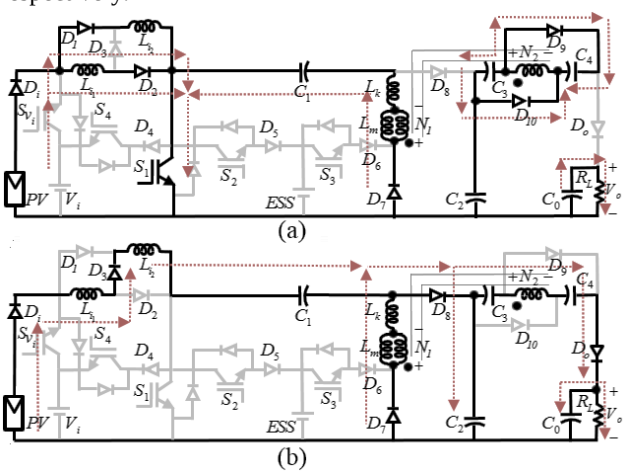

Fig.2. States in the 1st mode; (a): 1st state, S_1 is ON; (b): 2nd state, S_1 is OFF

In accordance with two states (a) and (b) in Fig. 2, (1) and (2) can be derived, respectively. S_1 regulates the inductor current I_{Li}, i.e., the PV's power. Fig. 2 depicts two states as follows.

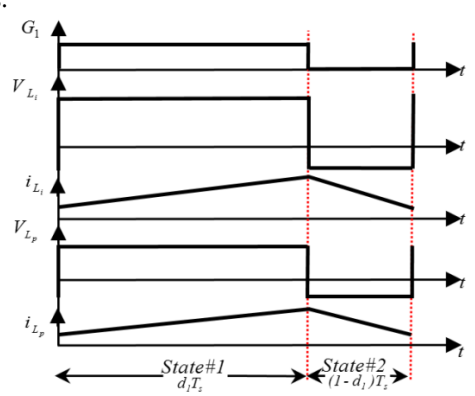

Fig.3. Time characteristic diagrams in the 1st mode

Hint 1:

As Fig. 2 shows, whenever S_1 is turned on, the input inductor L_i is made by a parallel combination of two input inductors L_{i1} and L_{i2}. Therefore, the rise-time of input current goes to a low limit. Whenever S_1 is turned off, L_i is made by a series combination of two input inductors L_{i1} and L_{i2}. Therefore, the input inductor L_i is increased and acts as a high-quality filter for decreasing input current ripples.

a. *Switching state1 ($0<t<d_1T_s$)*

Fig. 2-(a) shows the current flow in this state. S_1 is turned on, and inductors L_i and L_m are magnetized. Capacitors C_3 and C_4 are charged by the secondary voltage of transformer V_{N2}. V_o is supplied by V_{Co}, and capacitor C_1 is charged by primary voltage V_{N1}. Therefore, (1) can be derived in this state as follows:

$$\begin{aligned} &V_{L_i} = V_{pv};\\ &V_{L_m} = V_p = KV_1 = KV_{C_1};\\ &V_{C_3} = V_{C_4} = KNV_{C_1}; \end{aligned} \quad (1)$$

where V_P, K, N, and V_1 are primary voltage, magnetizing coefficient, transformer's turn-ratio, and effective voltage drop in transformer's primary on the 1st state, respectively.

b. *Switching state2 (d1Ts <t<Ts)*

Fig. 2-(b) shows the current flow. S_1 is turned off, and capacitors C_2 and C_o are charged by the primary and secondary transformers' currents, respectively. Therefore, (2) can be derived in this state.

$$\begin{aligned} &V_{L_i} = V_{pv} - V_{C_1} - V_{C_2};\\ &V_{L_m} = V_p = KV_2 = -KV_{C_2};\\ &V_{C_3} = V_{C_4} = \frac{V_o - (1+KN)V_{C_2}}{2}; \end{aligned} \quad (2)$$

where V_2 is the effective voltage drop in the primary on the 2nd state. By applying the volt-second balance equations, (3) and (4) can be deduced as follows:

$$d_1V_{pv} + (1-d_1)(V_{pv} - V_{C_1} - V_{C_2}) = 0;$$

$$V_{pv} - (V_{C_1} + V_{C_2})(1-d_1) = 0 \Rightarrow V_{C_1} + V_{C_2} = \frac{1}{1-d_1}V_{pv} \quad (3)$$

$$d_1V_{C_1} - (1-d_1)V_{C_2} = 0 \Rightarrow V_{C_2} = \frac{d_1}{1-d_1}V_{pv}; V_{C_1} = V_{pv}$$

$$2d_1KNV_{C_1} + (1-d_1)\left[V_o - (1+KN)V_{C_2}\right] = 0;$$

$$\Rightarrow V_o = \frac{d_1(1+KN)}{1-d_1}V_{pv} \quad (4)$$

B. *The PV's power is smaller than demanded power (P_{pv}< P_{out})*

In this mode, PVA cannot solely supply the output power, and S_1 is triggered so that the output reaches the maximum amount of power that can be supplied by PVA. After this time, S_1 and S_3 are triggered to send ESS's power to output

for the power to reach its reference level. This mode can be considered in two sub-modes $d_3>d_1$ and $d_3<d_1$ as follows where d_3, d_1, S_3, and S_1 are duty cycles, respectively.

I. $d_3>d_1$ in ESS discharging mode

Figs. 4 and 5 depict three states of operation and time characteristics diagrams, respectively.

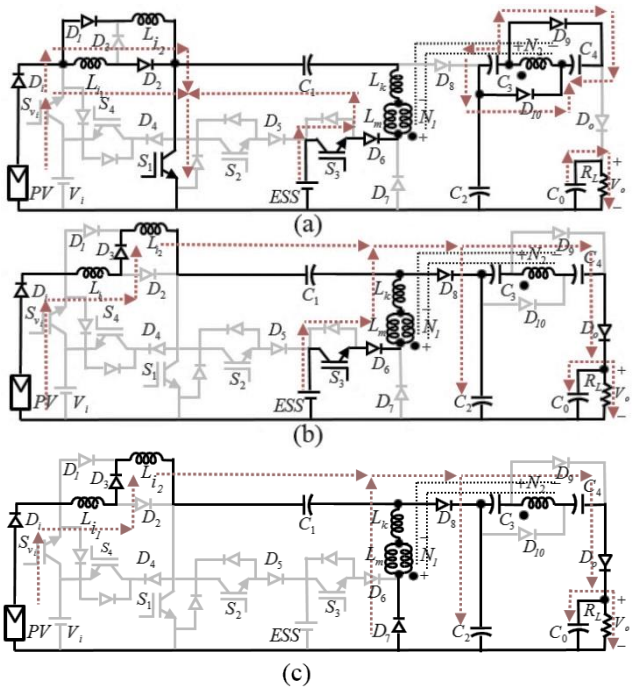

Fig.4. A schematic diagram of the proposed converter in $d_3>d_1$ ESS discharging sub-mode in 2nd mode ($P_{out}> P_{pv}$); (a): 1st state, S_1 and S_3 are ON; (b): 2nd state, S_1 is OFF, but S_3 is still ON; (c): 3rd state, S_1 and S_3 are OFF.

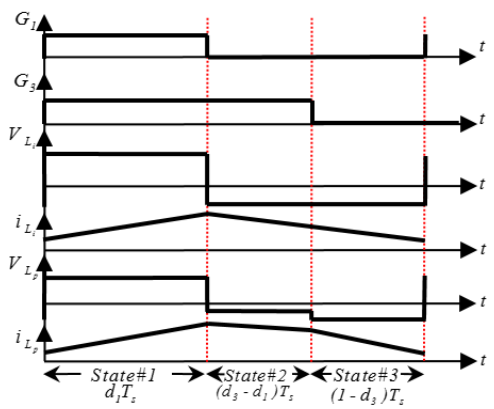

Fig.5. Time characteristic diagrams in $d_3>d_1$ ESS discharging sub-mode in the 2nd mode ($P_{out}> P_{pv}$)

S_1 regulates I_{Li} i.e. PV's power. The discharging rate of ESS is controlled by S_3.

In this sub-mode, three states can be considered as follows:

a. Switching state1 ($0<t<d_1Ts$)

Fig. 4-(a) shows the current flow in this state. S_1 and S_3 are turned on, and inductors L_i and L_m are magnetized. Capacitors C_3 and C_4 are charged by the secondary voltage V_{N2}.V_O is supplied by V_{Co}, and the capacitor C_1 is charged by the primary voltage V_{N1}. Therefore, (5) can be derived.

$$\begin{aligned} V_{L_i} &= V_{pv}\,; \\ V_{L_m} &= V_p = KV_1 = K(V_{ESS} + V_{C_1}) \\ V_{C_3} &= V_{C_4} = KN(V_{ESS} + V_{C_1})\,; \end{aligned} \tag{5}$$

b. Switching state2 ($d_1T_s <t<d_3Ts$)

S_1 is turned off, but S_3 is still turned on. Fig. 4-(b) shows the current flow, and capacitors C_2 and C_o are charged by primary and secondary transformer's currents, respectively. Therefore, (6) can be derived.

$$\begin{aligned} V_{L_i} &= V_{pv} - V_{C_1} - V_{C_2}\,; \\ V_{L_m} &= V_p = KV_2 = K(V_{ESS} - V_{C_2})\,; \\ V_{C_3} &= V_{C_4} = \frac{V_O - (1+KN)V_{C_2} + KNV_{ESS}}{2}\,; \end{aligned} \tag{6}$$

Fig. 4-(c) depicts the current flow. S_3 is turned off, and this state and the 2nd state of the previous mode are quite similar. Therefore, (2) can be used in this state. By applying the volt-second balance to (5), (6), and (2) respectively, (7) and (8) can be deduced as follows:

$$\begin{aligned} & d_1V_{pv} + (1-d_1)(V_{pv} - V_{C_1} - V_{C_2}) = 0\,; \\ & V_{C_1} + V_{C_2} = \frac{1}{1-d_1}V_{pv}\,; \\ & d_1(V_{ESS} + V_{C_1}) + (d_3 - d_1)(V_{ESS} - V_{C_2}) - (1-d_3)V_{C_2} = 0\,; \end{aligned} \tag{7}$$

$$d_1(V_{C_1} + V_{C_2}) = V_{C_2} - d_3V_{ESS} \Rightarrow V_{C_1} + V_{C_2} = \frac{V_{C_2} - d_3V_{ESS}}{d_1}\,; \tag{8}$$

$$V_{C_2} = \frac{d_1}{1-d_1}V_{pv} + d_3V_{ESS}\,; V_{C_1} = V_{pv} - d_3V_{ESS}\,;$$

Thus, the output voltage can be attained as (9)

$$2d_1KN(V_{ESS} + V_{C_1}) + (d_3 - d_1)\left[V_O - (1+KN)V_{C_2} + KNV_{ESS}\right] - (1-d_3)(V_O - (1+KN)V_{C_2}) = 0\,;$$

$$V_O = \frac{1}{1-d_1}\left\{d_1(1-KN)V_{pv} + \left[d_3(1-d_1) - KNd_1(1-d_3)\right]V_{ESS}\right\}\,;$$

(9) In case $d_3=d_1$, (9) can be simplified as follows:

$$V_O = \frac{d_1(1-KN)}{1-d_1}\left[V_{pv} + (1-d_1)V_{ESS}\right]; \qquad (d_3=d_1)$$

II. $d_3<d_1$ in ESS discharging mode

This sub-mode is just like the previous sub-mode, but the

only difference is that $d_3<d_1$. Figs. 6 and 7 depict three states of operation and time characteristics diagrams, respectively. In this sub-mode, three states exist as follows:

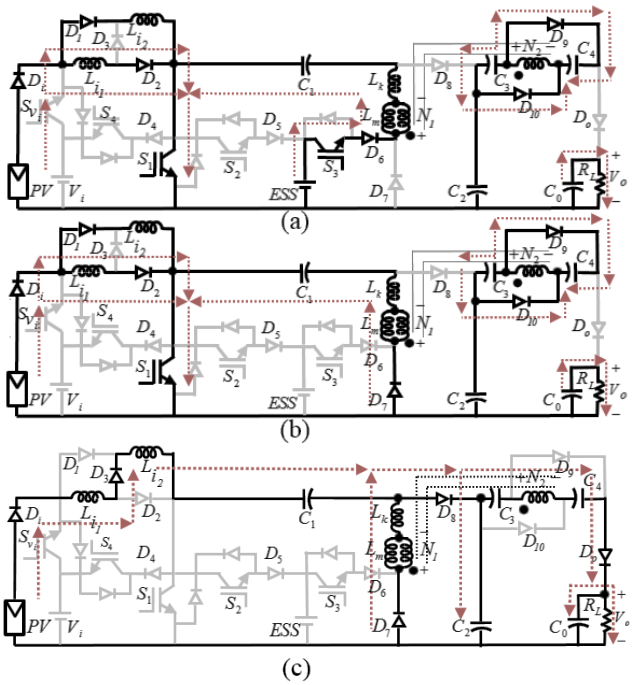

Fig.6. A schematic diagram of the proposed converter in $d_3<d_1$ ESS discharging sub-mode in the 2nd mode ($P_{out}> P_{pv}$); (a): the 1st state, S_1 and S_3 are ON; (b): the 2nd state, S_3 is OFF, but S_1 is still ON; (c): the 3rd state, S_1 and S_3 are OFF.

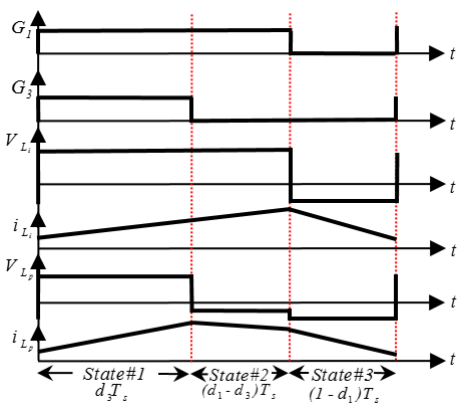

Fig.7. Time characteristic diagrams in $d_3<d_1$ ESS discharging sub-mode in the 2nd mode ($P_{out}> P_{pv}$)

a. Switching state1 ($0<t<d_3T_s$)

Fig. 6-(a) depicts the current flow. S_1 and S_3 are turned on, and this state and the 1st state of the previous sub-mode are quite similar. Therefore, (5) can be used.

b. Switching state2 ($d_3T_s <t<d_1T_s$)

Fig. 6-(b) depicts the current flow. S_3 is turned off, but S_1 is still on. This state and the 1st state of the previous mode are quite similar. Therefore, (1) can be used.

c. Switching state3 ($d_1Ts <t<T_s$)

Fig. 6-(c) depicts the current flow. S_1 is turned off, and this state and the 2nd state of the previous mode are quite similar. Therefore, (2) can be used. By applying the volt-second balance to (5), (1), and (2) respectively, (10) and (11) can be deduced as follows:

$$d_1V_{pv} + (1-d_1)(V_{pv} - V_{C_1} - V_{C_2}) = 0;$$
$$V_{C_1} + V_{C_2} = \frac{1}{1-d_1}V_{pv}; \quad (10)$$

$$d_3(V_{ESS} + V_{C_1}) + (d_1 - d_3)V_{C_1} - (1-d_1)V_{C_2} = 0;$$
$$V_{C_2} = \frac{d_1}{1-d_1}V_{pv} + d_3V_{ESS}; V_{C_1} = V_{pv} - d_3V_{ESS}; \quad (11)$$

Therefore, the output voltage can be attained as (12)

$$2d_3KN(V_{ESS} + V_{C_1}) + 2(d_1 - d_3)KNV_{C_1} + (1-d_1)\left[V_o - (1+KN)V_{C_2}\right] = 0;$$
$$\Rightarrow V_o = \frac{1-KN}{1-d_1}\left[d_1V_{pv} + d_3(1-d_1)V_{ESS}\right]; \quad (12)$$

In the case $d_3=d_1$, (12) can be simplified as follows:

$$V_o = d_1\frac{d_1(1-KN)}{1-d_1}\left[V_{pv} + (1-d_1)V_{ESS}\right]; \quad (d_3=d_1)$$

Hint 2:

From the case $d_3=d_1$ both in (9) and (12), it is clear that by considering a constant amount for d_1 in both case at this point, the output voltages will have equal amounts. As assumed previously, V_o is constant that makes a constant demanded power. Moreover, in conditions which V_{pv} is low, ESS has an important role in supplying the demanded power; Therefore, (12) is applicable for this condition, and (9) can be used whenever V_{pv} is considerably high and it can supply the main amount of the demanded power.

C. The PV's power is greater than demanded power in ESS charging mode.

In this mode, the excess power can be used to charge ESS. This mode can be considered in two sub-modes $P_{pv}>P_{out}$ and $P_{pv}<P_{out}$ as follows

I. $P_{pv}> P_{out}$ in ESS charging mode.

Figs 8 and 9 depict three states of operation and time characteristics diagrams, respectively.

a. Switching state1 ($0<t<d_1T_s$)

Fig. 8-(a) depicts the current flow. S_1 is turned on, and this state and the 1st state of the 1st mode are quite similar. Therefore, (1) can be used in this state

.

b. Switching state2 (d1Ts <t<(d1+d2)Ts)

S_1 is turned off and S_2 is turned on. Fig. 8-(b) shows the current flow. The two inductors L_i and L_P (L_m) are demagnetized and their currents flow to ESS for charging.

The power transmission occurs through the transformer, and capacitors C_3 and C_4 are charged by V_{N2}. V_o is supplied by V_{Co}. C_1 is charged by I_{Lm}. (13) can be derived.

$$V_{L_i} = V_{pv} - V_{ESS};$$
$$V_{L_m} = V_p = KV_2 = K(V_{C_1} - V_{ESS});$$
$$V_{C_3} = V_{C_4} = KN(V_{C_1} - V_{ESS}); \quad (13)$$

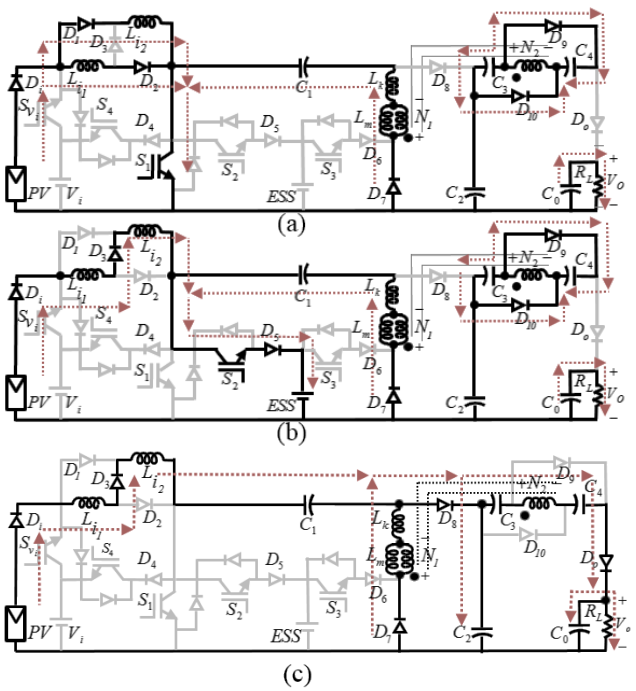

Fig.8. A schematic diagram of the proposed converter in ESS charging sub-mode in the 3rd mode (P_{pv}> P_{out}); (a): the 1st state, S_1 is ON; (b): the 2nd state, S_1 is OFF, but S_2 is ON; (c): the 3rd state, S_1 and S_2 are OFF.

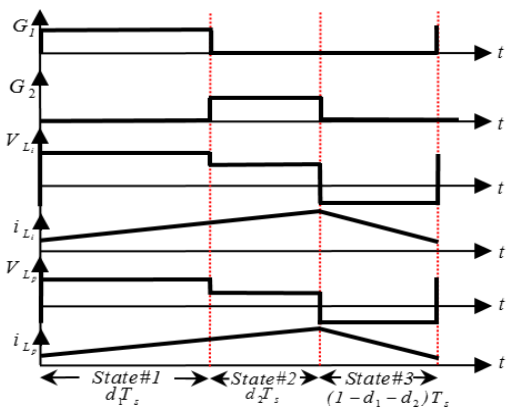

Fig.9. Time characteristic diagrams in the state of P_{PV}> P_{out} in ESS charging states

c. Switching state3 ((d1+d2)Ts <t<Ts)

Fig. 8-(c) depicts current flow. S_1 is turned off, and this state and 2'nd state of 1'st mode are quite similar. Therefore, (2) can be used. By applying the volt-second balance to (1), (13), and (2) respectively, (14) and (15) can be deduced as follows:

$$d_1V_{pv} + d_2(V_{pv} - V_{ESS}) + (1 - d_1 - d_2)(V_{pv} - V_{C_1} - V_{C_2}) = 0;$$
$$V_{C_1} + V_{C_2} = \frac{V_{pv} - d_2V_{ESS}}{1 - d_1 - d_2}; \quad (14)$$
$$d_1V_{C_1} + d_2(V_{C_1} - V_{ESS}) - (1 - d_1 - d_2)V_{C_2} = 0;$$
$$(d_1 + d_2)(V_{C_1} + V_{C_2}) = V_{C_2} + d_2V_{ESS} \Rightarrow V_{C_1} + V_{C_2} = \frac{V_{C_2} + d_2V_{ESS}}{d_1 + d_2};$$
$$V_{C_2} = \frac{(d_1 + d_2)V_{pv} - d_2V_{ESS}}{1 - d_1 - d_2}; V_{C_1} = V_{pv}; \quad (15)$$

Thus, the output voltage can be attained as (16)

$$2d_1KNV_{C_1} + 2d_2KN(V_{C_1} - V_{ESS}) + (1 - d_1 - d_2)\left[V_o - (1+KN)V_{C_2}\right] = 0;$$
$$V_o = \frac{1 - KN}{1 - d_1 - d_2}\left[(d_1+d_2)V_{pv} - d_2V_{ESS}\right]; \quad (16)$$

II. P_{pv}>> P_{out} in ESS charging mode

In this state, the excess power after ESS charging can be used for V_i charging. Fig. 10 depicts three states of operation in the state of P_{pv}>> P_{out} at the time that ESS is fully charged. The excess power is pushed toward V_i for charging by switching on S_4.

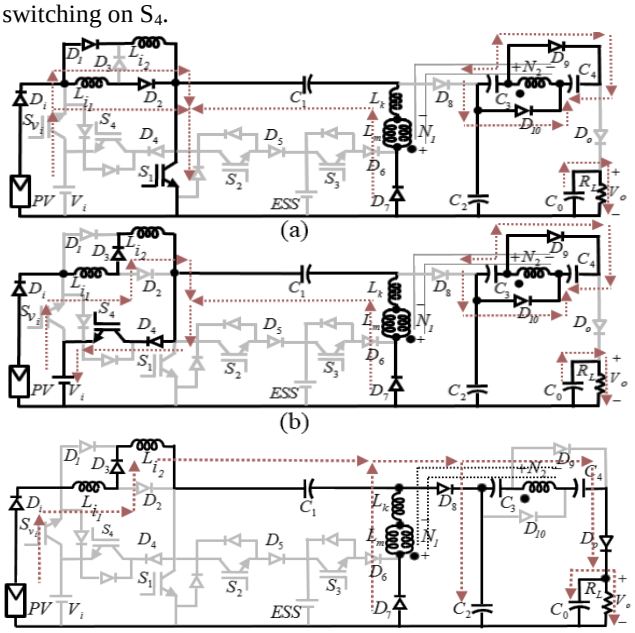

Fig.10. A schematic diagram of the proposed converter in ESS charging sub-mode in the 3rd mode (P_{pv}>> P_{out}); (a): the 1st state, S_1 is ON; (b): the 2nd state, S_1 is OFF, but S_4 is ON; (c): the 3rd state, S_1 and S_4 are OFF.

Hint 3:

In all the above modes, the total input inductor is switched between two quantities. In the first and second steps, two inductors L_{i1} and L_{i2} become parallel and serial with each other, respectively. Therefore, the total input inductor can be calculated as (17).

$$L_i = d_1 \frac{L_{i_1} \times L_{i_2}}{L_{i_1} + L_{i_2}} + (1 - d_1)(L_{i_1} + L_{i_2}); \quad (17)$$

If $L_{i1}=L_{i2}$ is assumed, (17) will be simplified as (18).

$$L_i = 0.5 d_1 \times L_{i_1} + 2(1 - d_1) L_{i_1}; \quad \Rightarrow L_i = L_{i_1}(2 - 1.5 d_1); \quad (18)$$

(18) shows that the total input inductor is related to S_1 duty cycle d_1. Fig.11 depicts L_i amounts by d_1 variations.

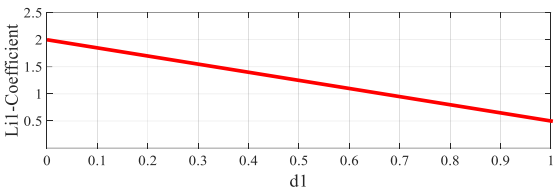

Fig.11. A schematic diagram of the L_{i1} inductor coefficient by d_1 variations (in $L_{i1}=L_{i2}$ assumption)

Hint 4:

As Fig. 11 shows, the first times that d_1 is near one, L_i is on a minimum level which makes a minimum level for the rising time of the input current. As such, the current reaches its desired point in a short time. Then, d_1 approaches the equilibrium point. Therefore, L_i increases and acts as a high quality filter to create minimum ripples for input current.

IV. The converter's power dissipation analysis

The power dissipation of active elements is considered in two groups, the switching and conduction dissipations. The other power dissipation is considered for passive elements as capacitors and inductors [24].

A. Active elements power dissipation

a. Conduction dissipation

This one is the power that dissipates in elements such as transistors and diodes. This type can be calculated as follows:

$$V_{on,sw}(t)=V_T+R_T I; V_{on,diode}(t)=V_d+R_d I;$$

$$P(t)=V_{on}(t).I(t) \Rightarrow P_{cond,sw}(t)=V_T I+R_T I^2; P_{cond,diode}=V_d I+R_d I^2 \quad (19)$$

$$P_{cond,total} = \frac{1}{T}\int_0^T N_{on,sw}.P_{cond,sw} + N_{on,diode}.P_{cond,diode})dt$$

where, $V_{on, sw}$, $V_{on, diode}$ are the ON-state voltage of the switch and diode, respectively. Moreover, R_T and R_d are the resistance of switch and diode, respectively.

b. Switching dissipation

This one is the power that dissipates in switches at the switching times. This type can be calculated as follows:

$$P_{sw} = f_s(N_{on}.E_{on} + N_{off}.E_{off});$$

$$E_{on} = \int_0^{t_{on}} V_{sw}.Idt = \frac{V_{sw}.I.t_{on}}{6}; E_{off} = \int_0^{t_{off}} V_{sw}.Idt = \frac{V_{sw}.I.t_{off}}{6}; \quad (20)$$

$$P_{sw} = \frac{f_s.V_{sw}.I}{6}(N_{on}.t_{on} + N_{off}.t_{off})$$

where, N_{off} and N_{on} are the number of ON-state switches in the current path, respectively. Also, f_s is the fundamental frequency.

Moreover, E_{on} is the energy loss of the switch during the turning-on time and E_{off} is the energy loss during the turning-off time. Moreover, t_{on} and t_{off} are turn-on and turn-off time of the switch, respectively.

Totally, active elements power dissipation can be calculated as follows:

$$P_{active,total} = P_{sw} + P_{cond,total} \quad (21)$$

B. Passive elements power dissipation

For inductors and capacitors, a small internal series resistance is considered. These powers can be calculated as below:

$$P_{c,total} = \sum_{i=1}^{8} ESR_i.I_{C_i}^2; P_{l,total} = \sum_{j=1}^{3} R_{l_j}.I_{l_j}^2$$

$$\Rightarrow P_{passive,total} = P_{c,total} + P_{l,total} \quad (22)$$

where, ESR, I_c, I_l, and R_i are equivalent series resistance of capacitors, the current through capacitors, the current through inductors, and internal resistor of inductors, respectively. In this converter, eight capacitors and three inductors are considered.

Therefore, the dissipated power can be calculated as follows:

$$P_{total,dissipated} = P_{passive,total} + P_{active,total} \quad (23)$$

Therefore, the converter's efficiency can be calculated as follows:

$$P_{in} = P_{total,disipated} + P_{out} \Rightarrow 1 = \frac{P_{total,disipated}}{P_{in}} + \frac{P_{out}}{P_{in}};$$

$$\Rightarrow \%\eta = 100\frac{P_{out}}{P_{in}} = 100(1 - \frac{P_{total,disipated}}{P_{in}}) \quad (24)$$

It is important to mention that the power dissipation of the transformer's core is ignored.

C. Components' design

The design of components is based on [6] and is considered in the 1st mode of operation. These equations can be written as follows:

$$L_i=\frac{V_{L_i}}{f_s\Delta I_i}=\frac{d_1V_{pv}}{f_s\Delta I_i};V_{S_1-stress}=\frac{V_{pv}-V_{F_{D_1}}}{1-d_1};V_{S_3-stress}=\frac{V_{ESS}-V_{F_{D_3}}}{1-d_3};$$
$$C_o=\frac{I_{Load}}{f_s\Delta V_{c_o}}=\frac{V_{out}}{R_L f_s\Delta V_{out}};V_{S_2-stress}=\frac{V_{pv}-V_{F_{D_i}}-V_{ESS}}{1-d_1-d_2}; \quad (25)$$

Moreover, V_{Lm} can be calculated as below:

$$V_{Lm}=N_p\frac{\Delta BA_e}{(1-d_1)T_s} \quad (26)$$

where ΔB, and Ae, are the magnetic flux density variation and the magnetic core equivalent area, respectively. The turn numbers of the primary and secondary windings can be selected based on the appropriate transformer design guidelines. The apparent power of the HF transformer can be calculated by multiplying the root-mean-square (RMS) voltage and current of the primary winding.

D. The coupled-inductor's transferred power

The power transferred through the coupled-inductor is calculated by multiplying the instantaneous transformer's secondary voltage and current. For this purpose in Figure3, this power can be calculated as follows:

$$at: 0\le t\le d_1T_s \Rightarrow I_{Ls_{in.1'st.state}}=i_{Ls,low}+\frac{i_{Ls,high}-i_{Ls,low}}{d_1T_s};$$
$$at: d_1T\le t\le T_s \Rightarrow I_{Ls_{in.2'nd.state}}=i_{Ls,low}-\frac{i_{Ls,high}-i_{Ls,low}}{(1-d_1)T_s};$$
$$I_{Ls}=\frac{I_{Lp}}{N};V_{Ls}=NV_{Lp};P_{transfered.by.CI}=\frac{1}{T_s}\left(\int_0^{d_1T_s}V_{Ls,high}.I_{Ls_{in.1'st.state}}dt\right. \quad (27)$$
$$\left.+\int_{d_1T_s}^{T_s}V_{Ls,low}.I_{Ls_{in.2'nd.state}}dt\right)$$

E. The loss of the elements considerations

For this purpose, a comparison must be done to have an estimation of the dissipation of each group of elements in contrast with the other groups. For this means some assumptions are considered as follows:

1-The power dissipated in each passive element is considered 0.1 watts.

2-The dissipated power of each group of elements is considered approximately the number of element in the converter.

3- The power dissipated in each diode is considered 0.2 watts.

4- The power dissipated in each transistor is considered 1 watt.

Therefore, the portion of each element can be approximately calculated as table1, and its related pie chart is depicted as follows:

TABLE 1
THE POWER DISSIPATED BY EACH ELEMENT

Row	Element	No. of elements presented in a period	Dissipated power of each group (Watts)
1	Inductor	4	0.4
2	Capacitor	4.4	0.44
3	Diode	5.6	1.12
4	Transistor	1	1

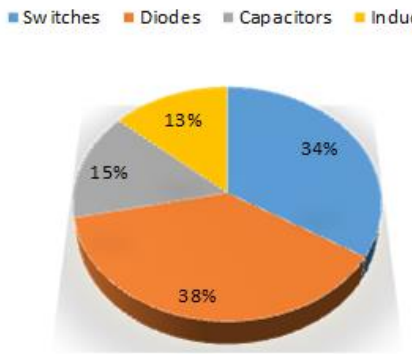

Fig.12. The element's losses pie chart

V. The proposed converter's dynamic behavior

The system's stability around an operating point is described by the system's behaviour in transient state. Primarily, as mentioned in the previous section, the proposed converter operates in four different conditions. In this converter, there will be several inputs and outputs. Therefore, an MIMO control system can be considered for this converter. The state variables are i_{Li}, i_{Lm}, V_{C1}, V_{C2}, and V_{CO}. The state-space average model of the converter can be obtained as follows. In the 1'st operation mode ($P_{pv}=P_{out}$), the average model of the system can be obtained as (28).

$$L_i\frac{di_{L_i}}{dt}=V_{pv}-(1-d_1)(V_{C_1}+V_{C_2});$$
$$L_m\frac{di_{L_m}}{dt}=d_1KV_{C_1}-(1-d_1)KV_{C_2};$$
$$C_1\frac{dV_{C_1}}{dt}=(1-d_1)i_{L_i}-d_1i_{L_m}; \quad (28)$$
$$C_2\frac{dV_{C_2}}{dt}=(1-d_1)\left[i_{L_i}+(1-\frac{1}{N})i_{L_m}\right];$$
$$C_O\frac{dV_{C_o}}{dt}=\frac{(1-d_1)}{N}i_{L_m}-d_1\frac{V_{C_o}}{R_L};$$

In the 1st sub-mode of the 2nd mode (ESS discharging mode ($P_{PV}<P_{out}$, $d_3>d_1$)), the average model of the system can be obtained as (29).

$$
\begin{aligned}
L_i \frac{di_{L_i}}{dt} &= V_{pv} - (1-d_1)(V_{C_1} + V_{C_2});\\
L_m \frac{di_{L_m}}{dt} &= d_1 K(V_{ESS} + V_{C_1}) + (d_3 - d_1)K(V_{ESS} - V_{C_2}) - (1-d_3)KV_{C_2};\\
C_1 \frac{dV_{C_1}}{dt} &= (1-d_1)i_{L_i} - d_1 i_{L_m};\\
C_2 \frac{dV_{C_2}}{dt} &= (1-d_1)\left[i_{L_i} + (1-\frac{1}{N}) i_{L_m} \right];\\
C_o \frac{dV_{C_o}}{dt} &= \frac{(1-d_1)}{N} i_{L_m} - d_1 \frac{V_{C_o}}{R_L};
\end{aligned}
\tag{29}
$$

In the 2nd sub-mode of the 2nd mode (ESS discharging mode ($P_{PV}<P_{out}$, $d_3<d_1$)), the average model of the system can be obtained as (30).

$$
\begin{aligned}
L_i \frac{di_{L_i}}{dt} &= V_{pv} - (1-d_1)(V_{C_1} + V_{C_2});\\
L_m \frac{di_{L_m}}{dt} &= Kd_3(V_{ESS} + V_{C_1}) + K(d_1 - d_3)V_{C_1} - K(1-d_1)V_{C_2};\\
C_1 \frac{dV_{C_1}}{dt} &= (1-d_1)i_{L_i} - d_1 i_{L_m};\\
C_2 \frac{dV_{C_2}}{dt} &= (1-d_1)\left[i_{L_i} + (1-\frac{1}{N}) i_{L_m} \right];\\
C_o \frac{dV_{C_o}}{dt} &= \frac{(1-d_1)}{N} i_{L_m} - d_1 \frac{V_{C_o}}{R_L};
\end{aligned}
\tag{30}
$$

$$
\begin{aligned}
L_i \frac{di_{L_i}}{dt} &= V_{pv} - d_2 V_{ESS} - (1-d_1-d_2)(V_{C_1} + V_{C_2});\\
L_m \frac{di_{L_m}}{dt} &= Kd_2 V_{ESS} + K(d_1+d_2)V_{C_1} - K(1-d_1-d_2)V_{C_2};\\
C_1 \frac{dV_{C_1}}{dt} &= (1-d_1-d_2)i_{L_i} - (d_1+d_2)i_{L_m};\\
C_2 \frac{dV_{C_2}}{dt} &= (1-d_1-d_2)\left[i_{L_i} + (1-\frac{1}{N}) i_{L_m} \right];\\
C_o \frac{dV_{C_o}}{dt} &= \frac{(1-d_1-d_2)}{N} i_{L_m} - (d_1+d_2)\frac{V_{C_o}}{R_L};
\end{aligned}
\tag{31}
$$

In the 1st sub-mode of the 3rd mode (ESS discharging mode ($P_{PV}>P_{out}$), the average model of the system can be obtained as (31). The state variables and duty cycles can be divided into two components so-called equilibrium and the perturbation points can be assumed as (32).

$$
\begin{aligned}
x &= \bar{x} + \tilde{x};\\
d &= \bar{d} + \tilde{d};
\end{aligned}
\tag{32}
$$

where x, $\bar{x}$, $\tilde{x}$, d, $\bar{d}$, and $\tilde{d}$ are state variable, state equilibrium, state perturbation, duty cycle, duty cycle equilibrium, and duty cycle perturbation, respectively. The perturbations are much smaller than the equilibrium points. Based on this assumption and substituting (32) into (28), the system's small signal model can be achieved. This model can also be represented in matrix form as (33).

$$
\begin{aligned}
\dot{\tilde{x}} &= A\,\tilde{x} + B\,\tilde{u};\\
\tilde{y} &= C\,\tilde{x} + D\,\tilde{u};
\end{aligned}
\tag{33}
$$

The system's small signal model in operation modes can be expressed as follows:

In the 1st operation mode ($P_{pv}=P_{out}$). (See (34) and (35)).

$$
A = \begin{pmatrix}
0 & 0 & -(1-\bar{d}_1)/L_i & -(1-\bar{d}_1)/L_i & 0\\
0 & 0 & K\bar{d}_1/L_m & -K(1-\bar{d}_1)/L_m & 0\\
(1-\bar{d}_1)/C_1 & -\bar{d}_1/C_1 & 0 & 0 & 0\\
(1-\bar{d}_1)/C_2 & (1-\bar{d}_1)(N-1)/NC_2 & 0 & 0 & 0\\
0 & (1-\bar{d}_1)/NC_o & 0 & 0 & -\bar{d}_1/R_L C_o
\end{pmatrix};
$$

$$
B = \begin{pmatrix}
(\bar{V}_{C_1} + \bar{V}_{C_2})/L_i\\
K(\bar{V}_{C_1} + \bar{V}_{C_2})/L_m\\
-(\bar{i}_{L_i} + \bar{i}_{L_m})/C_1\\
\left[(1-N)\bar{i}_{L_m} - N\bar{i}_{L_i}\right]/NC_2\\
-(R_L \bar{i}_{L_m} + N\bar{V}_{C_o})/R_L NC_o
\end{pmatrix}
\tag{34}
$$

$$
y = \begin{pmatrix} \tilde{i}_{pv}\\ \tilde{i}_{ESS}\\ V_{ESS}\\ V_{C_o} \end{pmatrix};\ C = \begin{pmatrix} 1&0&0&0&0\\ 1&1&0&0&0\\ 0&0&1&0&0\\ 0&0&0&0&1 \end{pmatrix};\ D = 0;\ \tilde{x} = \begin{pmatrix} \tilde{i}_{L_i}\\ \tilde{i}_{L_m}\\ \tilde{V}_{C_1}\\ \tilde{V}_{C_2}\\ \tilde{V}_{C_o} \end{pmatrix};\ \tilde{u} = \begin{pmatrix} \tilde{d}_1 \end{pmatrix}
\tag{35}
$$

By substituting (32) into (29) and (30), the system's small signal model can be achieved. In the 1st and the 2nd sub-modes of the 2nd mode (ESS discharging mode ($P_{PV}<P_{out}$, $d_3>d_1$ and $d_3<d_1$)), all matrices except B are the same as the 1st operation mode ($P_{pv}=P_{out}$). In all those modes B and $\tilde{u}$ are presented as (36).

$$B=\begin{pmatrix} (\overline{V}_{c_1}+\overline{V}_{c_2})/L_i & 0 \\ (\overline{V}_{c_1}+\overline{V}_{c_2})K/L_m & KV_{ESS}/L_m \\ -(\tilde{i}_{L_i}+\tilde{i}_{L_m})/C_1 & -(\tilde{i}_{L_i}+\tilde{i}_{L_m})/C_1 \\ -\left[N\tilde{i}_{L_i}+(N-1)\tilde{i}_{L_m}\right]/NC_2 & 0 \\ -(R_L\tilde{i}_{L_m}+N\overline{V}_{Co})/R_LNC_o & 0 \end{pmatrix};\tilde{u}=\begin{pmatrix}\tilde{d}_1\\ \tilde{d}_3\end{pmatrix} \quad (36)$$

By substituting (32) into (31), the system's small signal model can be achieved in the 3'rd operation mode ($P_{pv}>P_{out}$ and $P_{pv}>>P_{out}$) as follows:

$$A=\begin{pmatrix} 0 & 0 & -(1-\bar{d}_1-\bar{d}_2)/L_i & -(1-\bar{d}_1-\bar{d}_2)/L_i & 0 \\ 0 & 0 & K(\bar{d}_1+\bar{d}_2)/L_m & -K(1-\bar{d}_1-\bar{d}_2)/L_m & 0 \\ (1-\bar{d}_1-\bar{d}_2)/C_1 & -(\bar{d}_1+\bar{d}_2)/C_1 & 0 & 0 & 0 \\ (1-\bar{d}_1-\bar{d}_2)/C_2 & (1-\bar{d}_1-\bar{d}_2)(N-1)/NC_2 & 0 & 0 & 0 \\ 0 & (1-\bar{d}_1-\bar{d}_2)/NC_o & 0 & 0 & -(\bar{d}_1+\bar{d}_2)/R_LC_o \end{pmatrix} \quad (37)$$

$$B=\begin{pmatrix} (\overline{V}_{c_1}+\overline{V}_{c_2})/L_i & (\overline{V}_{c_1}+\overline{V}_{c_2}-V_{ESS})/L_i \\ (\overline{V}_{c_1}+\overline{V}_{c_2})K/L_m & (\overline{V}_{c_1}+\overline{V}_{c_2}+V_{ESS})K/L_m \\ -(\tilde{i}_{L_i}+\tilde{i}_{L_m})/C_1 & -(\tilde{i}_{L_i}+\tilde{i}_{L_m})/C_1 \\ -\left[N\tilde{i}_{L_i}+(N-1)\tilde{i}_{L_m}\right]/NC_2 & -\left[N\tilde{i}_{L_i}+(N-1)\tilde{i}_{L_m}\right]/NC_2 \\ -(R_L\tilde{i}_{L_m}+N\overline{V}_{Co})/R_LNC_o & -(R_L\tilde{i}_{L_m}+N\overline{V}_{Co})/R_LNC_o \end{pmatrix} \quad 38)$$

$$y=\begin{pmatrix}\tilde{i}_{pv}\\ \tilde{i}_{ESS}\\ V_{ESS}\\ V_{C_o}\end{pmatrix};C=\begin{pmatrix}1&0&0&0&0\\1&1&0&0&0\\0&0&1&0&0\\0&0&0&0&1\end{pmatrix};D=0;\tilde{x}=\begin{pmatrix}\tilde{i}_{L_i}\\ \tilde{i}_{L_m}\\ V_{C_1}\\ V_{C_2}\\ V_{C_o}\end{pmatrix};\tilde{u}=\begin{pmatrix}\tilde{d}_1\\ \tilde{d}_2\end{pmatrix} \quad (39)$$

All elements of the matrix in (34), (36), (37), and (38) are fixed except for L_i which varies with d_1.

By calculating the eigenvalues of each matrix A for all operation modes in accordance with the duty cycles' ranges (0 ~ 1), it can be concluded that the real part of them is negative. Thus, this indicates the stability of the system for all modes of operation. Using the numerical values shown in Table 2, the bode diagrams of the proposed converter are obtained as shown in Figures 13-15. As depicted in all figures, the phase and gain margins of the transfer function indicate the stability of the proposed converter.

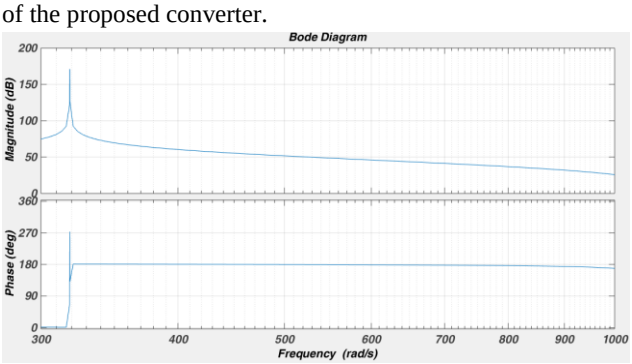

Fig.13. The bode diagram of the transfer function in the 1st mode ($P_{pv}=P_{out}$)

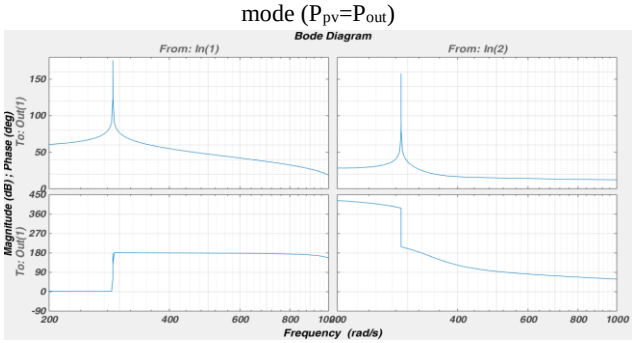

Fig.14. The bode diagram of the transfer function in the 2nd mode ($P_{pv}<P_{out}$)

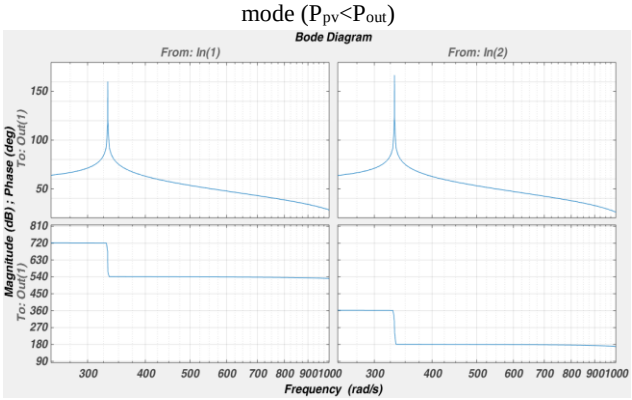

Fig.15. The bode diagram of the transfer function in the 3rd mode ($P_{pv}>P_{out}$)

Fig. 16 depicts the block diagram of a system with its controller. The β and system are the output's feedback coefficient and a controllable plant, respectively.

Fig. 17 depicts the proposed converter with its controller. β is assumed one for all four converters' outputs. This converter has three inputs G_1, G_2, and G_3, which are gate pulses made by the controller for switches S_1, S_2, and S_3, respectively. The outputs i_{pv}, i_{ESS}, V_{ESS}, and V_o are the input current, ESS's charging current, ESS's voltage, and output voltage, respectively.

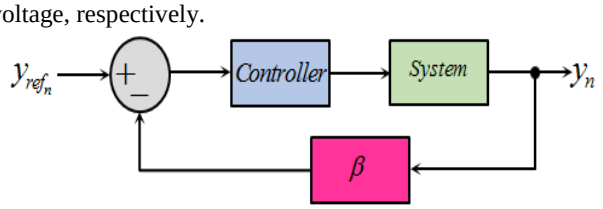

Fig.16. The block diagram of a system with its controller

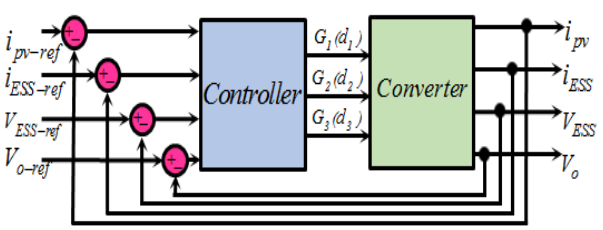

Fig.17. The block diagram of converter with its controller

As Fig. 17 shows, there are four references in accordance

with the outputs. The controller makes appropriate duty cycles d_1, d_2, and d_3 for reaching the outputs to desired points.

Fig. 18 shows the designed MIMO block diagram of the controller for the proposed converter. This block has eight inputs consisting of four measured parameters V_o, V_{ESS}, I_{ESS}, P_{pv} and their references. The P_{out} reference is compared to P_{pv}. This comparison decides to set the desired operational mode. The comparators Comp.4 and Comp.5 are considered for this purpose. Comp.1-3 are designated to compare V_o, V_{ESS}, and I_{ESS} with their references, respectively. This controller consists of a number of logic gates, comparators, adders, and a ramp signal generator to generate PWM signals. Because the output of Comp.1-3 must be analogue signals, when implementing the controller, a low-pass filter is placed in the output of these comparators. As such, the integral of their outputs is taken. Therefore, combining a series comparator with a low-pass filter will act like a PI controller .Thus the controller is Logic-PI-PWM-based. The comparators 6-8 are used to convert level to pulse width compared to a ramp signal generator to generate PWM pulses for the three main switches. In order to explain how this controller works, three modes are assumed as follows:

A. $P_{pv}<P_{out}$

The output of Comp.4 is low, but the outputs of gates OR and strobe are high. This allows the pulses generated by comp.6 to appear at the G3 output. Initially, V_o is less than its reference $V_{o\text{-}ref}$, and due to this difference, the output level of Comp. 1 is non-zero, creating the d_3 duty cycle. Moreover, the output level of Comp. 4 is zero. Therefore, the output of the Min block is zero, and according to the level of difference between V_o and $V_{o\text{-}ref}$, the duty cycle d_1 is generated. A voltage threshold V_t is considered to control the output voltage ripples. When V_o reaches its reference neighborhood, the output of the Max block is zero. This speeds up the controller before it reaches its output reference.

B. $P_{pv}=P_{out}$

All the explanations mentioned in the previous mode apply to this mode except that the strobe output is low. Therefore, G_3 is disabled and G_1 can be triggered.

C. $P_{pv}>P_{out}$

In this case, the output of the strobe is zero. Therefore, the output G_3 is disabled. At first, V_o is lower than its reference value, and the output of Comp. 1 is non-zero. Therefore, the output G_1 is triggered. Whenever, one of or both V_{ESS} and i_{ESS} fall below their (its) reference value(s), the Min will select the minimum value, and the duty cycle d_1 and d_2 are deeply affected by the difference voltage of the output of Comp. 1 and this value. Therefore, the negative result of this subtraction causes outputs G_2 and G_1 to be deactivated and triggered, respectively. Initially, before V_o reaches its reference level, G_1 is the only output that is triggered, after which the G_1 and G_2 will be triggered. The NOT gate is intended to support ESS short circuit.

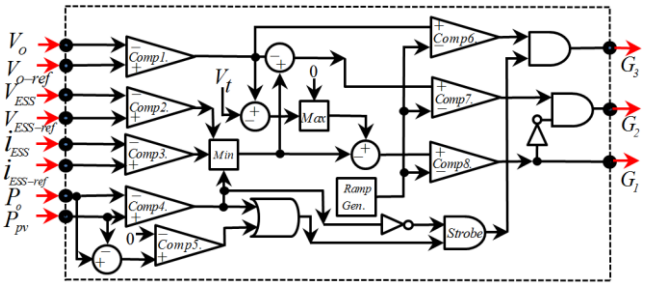

Fig.18. A schematic diagram of the proposed controller

VI. The comparison between the proposed converter and other works

Table 2 presents a comparison between the proposed converter and other works. It shows the three main advantages of this converter over other converters as follows:

1- Regardless of the type of input source used, the proposed converter operates independently and has no dependence on the type of input RES source.

2- The existence of an auxiliary ESS in the proposed converter enables the proposed converter to take over the task of producing power together with the main ESS when it is dark and unable to receive power from the main input. As such, this converter can provide output power 24 hours a day.

3- With the appropriate selection of the winding ratio used in the proposed converter, it is possible to create an increase mode in the output current compared to the input.

4- Due to the increasing property of the output voltages compared to the input in the SEPIC converter and the presence of voltage multipliers in the output of the proposed converter, the voltage gain of the converter reaches a number greater than one. Therefore, according to the third case mentioned above, the proposed converter will have a voltage gain and a current value greater than one at the same time.

5- The presence of the switched inductor in the proposed converter creates a strong filter at the input that reduces the rise time and ripple of the input current.

6- [23], in terms of performance, is the closest converter to the proposed converter. Items 2 to 5 mentioned above are not provided in [23]. The only advantage of [23]'s converter is that it has fewer diodes than our proposed converter (2 fewer). Of course, the proposed converter has 3 more capacitors than [23]'s converter, which is not particularly important due to the lower power losses in the capacitors.

TABLE 2
A PERFORMANCE COMPARISON BETWEEN THE PROPOSED CONVERTER AND THE OTHERS

	Specifications	Structures				
		[6]	[9]	[13]	[23]	Proposed converter
Number of	Coupled Inductor	1	2	1	0	1
	Diode	M+1	4	4	4	6
	Transistor	2	2	1	2	2
	Capacitor	M+2	3	5	2	5
	ESS	0	0	0	1	2
	Bidirectional port	0	0	0	1	2
Stress of	current	Iin1/(1-d2)	IL/d	ILin/d	IL1/d1	ILi/d1
	switch voltage	Vo/n(M+1)	Vo/(2+n)	Vo/(2+n)	(Vpv-VfDi)/(1-d1)	(Vpv-VfDi)/(1-d1)
	Diode voltage	2Vo/n(M+1)	Vo	(n+1)Vo/(n+2)	Vo-VEss	nVLm
RES's Usage		No	No	No	Yes	Yes
RES's type dependence		Yes	Yes	Yes	No	No
Input's expandability		No	No	No	Yes	Yes
Voltage Gain (or Output Voltage)		n(M+1)/(1-d)	(2+n)/(1-d)	(2+n)/(1-2d)	(d1+d3)VEss +d1Vin/(1-d1)	$V_O = \frac{1-KN}{1-d_1}\left[d_1 V_{pv} + d_3(1-d_1)V_{ESS}\right]$

where M, n (N), and V_{fDi} are the number of voltage multipliers used in the converter, turn ratio, and forward voltage of diode D_i, respectively.

VII. Simulation results and power management analysis

In this section, the EMTDC/PSCAD simulation results are performed to confirm theoretical analysis of the proposed converter performed here. Figures 18–22 show the simulation results. The values of different elements are summarised in Table 3.

TABLE 3
THE PARAMETERS VALUES

Parameter	Quantity	Parameter	Quantity
C_1	47 µF	L_m	2 mH
C_2	100 µF	Li_1=Li_2	2 mH
C_3	100 µF	L_k	105 µH
C_4	100 µF	V_{pv}	60 ~ 120 V
N	0.5	$V_{ESS-ref}$	24 V
R_L	500 Ω	V_{o-ref}	200V
C_o	220 µF	F_s	40 KHz
C_{pv}	1000 µF	K	0.95

Each mode is presented separately according to Table 4. In this table, the production and consumption power (charge) are marked with a positive and a negative sign, respectively.

The 1st mode: In this mode, only PV is used to supply the output power.

The 2nd mode: In this mode, the power of PV is sent to the output and the excess power is provided by ESS.

TABLE 4
POWER MANAGEMENT IN ALL MODES

Operational Mode No.	Operational Mode	P_{out} (Watts)	P_{pv} (Watts)	P_{ESS} (Watts)	P_{vi} (Watts)
1	$P_{out}=P_{pv}$	*-80*	*+80*	*Not Used*	*Not Used*
2	$P_{out}>P_{pv}$	*-80*	*+55*	*+25*	*Not Used*
3-1	$P_{out}<P_{pv}$	*-80*	*+105*	*-25(ESS Charging)*	*Not Used*
3-2	$P_{out}<<P_{pv}$	*-80*	*+130*	*-25(ESS Charging)*	*-20(Vi Charging)*

The 3rd mode: In this mode, a part of the power generated by PV, which is requested by the output, is sent to the output, and the excess PV power is spent on ESS charging. To prevent overcharging when ESS is fully charged, the excess PV power will be used to charge. The V_i battery is responsible for supplying power to the input of the converter to generate the output voltage (in the absence of PV at night). The production capacity is marked with a positive sign and the consumption power (charge) is marked with a negative sign.

This converter can be used to supply regional electricity. To change the output load when the household consumption changes, a single-phase inverter is included in the output of this converter in the simulation. The amount of power consumed by the consumer and the power produced by PV can be variable. To consider all the aforementioned situations, the simulation has been done in two states .In the first simulation state, V_{pv} is considered between two levels of 80 and 120 volts. In the second state, these two levels are considered between 60 and 80 volts. In both states, the output load changes between 200 and 400 Ohms (in several moments different from the moments of Vpv changes). Figures 19-21 show the information related to the simulation of the first state and Figures 22-24 also show the information related to the second state.

A. The first state of simulation

As shown in Figure 19, V_{pv} is sometimes changed and at other times, R_o changes between two levels. The output voltage reacts quickly with these changes and reaches the reference level .

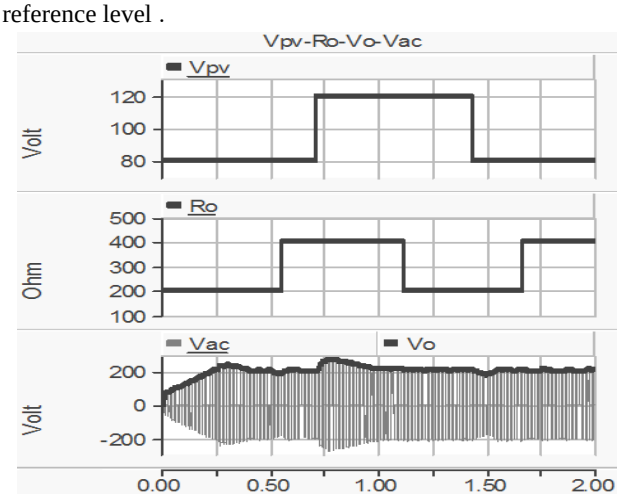

Fig.19 The PSCAD converter simulation results (V_o, V_{ac}, V_{PV}, R_o) in the state of P_{pv}>=P_{out}

As shown in figure 20, in the initial times when PV is able to supply the P_{out}, this task is assumed by itself. At times when the output load is low or the power produced by PV is excess, by activating the S_2 switch, this excess power is stored in the ESS.

As shown in this figure, the G_1 gate is only triggered in this mode, and P_{out} is supplied by the P_{pv} alone.

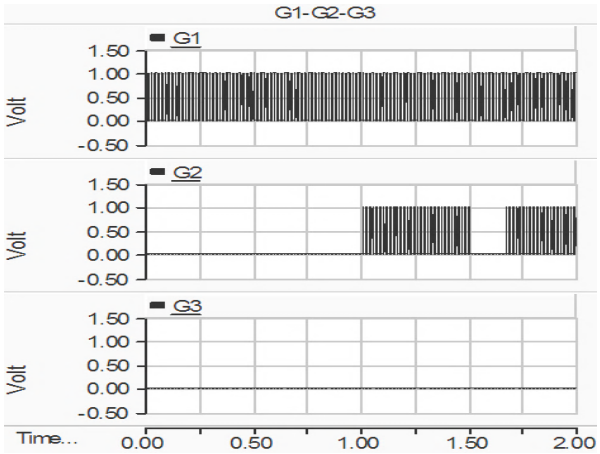

Fig. 20 The PSCAD converter simulation results (G_1, G_2, G_3) in the state of $P_{pv}>=P_{out}$

Figure 21 shows the load current changes according to what is related to V_{ac} in Figure 18. In the same figure, the changes in P_{out} and P_{pv} are shown, which shows that P_{pv} is greater than P_{out}. I_{pv} variations are also specified in this Figure. I_{pv} is associated with a slight overshoot at times when R_o and V_{pv} change, but it appears with a slight ripple in the rest of the times.

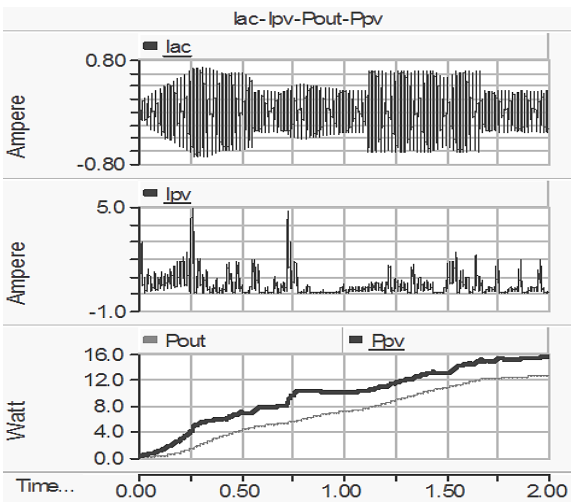

Fig.21 The PSCAD converter simulation results (I_{ac}, I_{pv}, P_{PV}, P_{out}) in the state of $P_{pv}>=P_{out}$

B. Second State of simulation

The output of this state is shown in Figures 22-24. Figure 22 shows the changes in V_{pv} between the levels of 60-80 volts. At different times with these voltage variations, R_o also changes. This figure also shows the outputs of the proposed converter and inverter, which reach the reference level after a short period of time, even with changes in the output load and input voltage. Figure 23 depicts the command pulses of S_1-S_3 switches. When the requested output power exceeds Ppv, switch S_3 is turned on to provide output power with the help of ESS. As it is clear in this figure, S_2 does not work during the entire simulation because there is no excess power for storage.

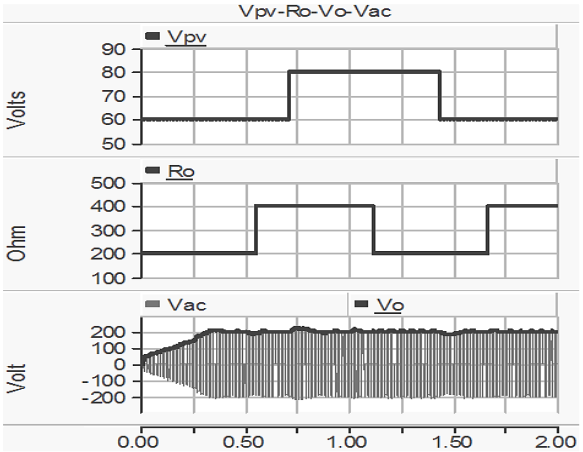

Fig.22 The PSCAD converter simulation results (V_o, V_{ac}, V_{PV}, R_o) in the state of $P_{pv}<=P_{out}$

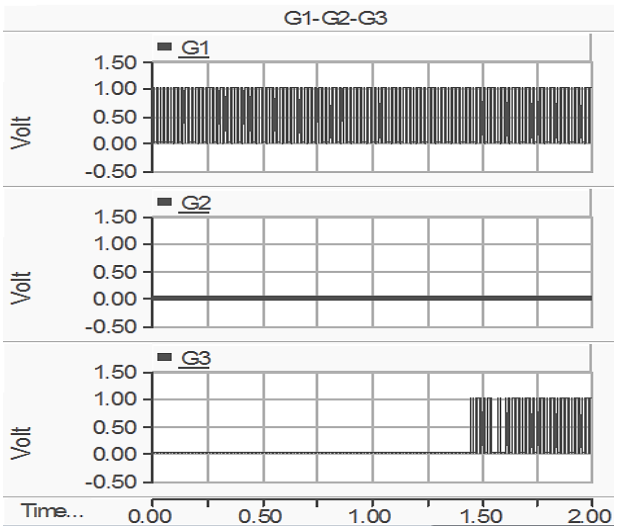

Fig.23 The PSCAD converter simulation results (G_1, G_2, G_3) in the state of $P_{pv}<=P_{out}$

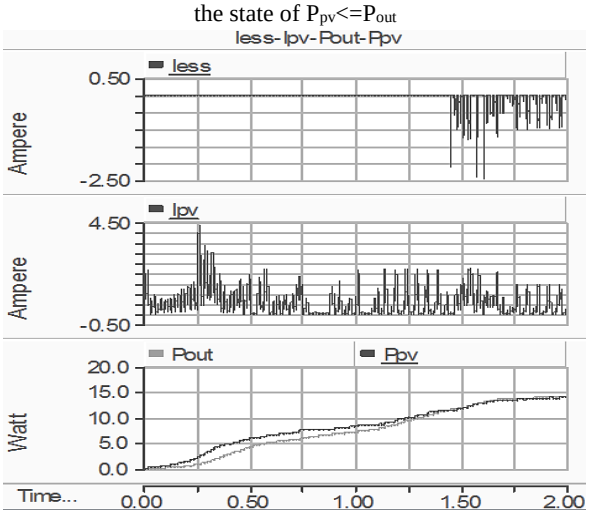

Fig.24 The PSCAD converter simulation results (I_{ess}, I_{pv}, P_{PV}, P_{out}) in the state of $P_{pv}<=P_{out}$

Figure 24 shows the variations in P_{out} and P_{pv} in relation to each other and I_{pv} and I_{ESS} at the time of switching on S_3.

VIII. Conclusions

In this paper, a step-up voltage and current multi-input DC/DC SEPIC-based converter with coupled and switched inductors is proposed. An improved converter has been presented as a novel one by promoting existing structures. The controller strategy based on power management is considered to maximize the use of RES power in this converter. The main advantages of the proposed converter are as follows:

1- The stability of the proposed converter against momentary changes in V_{PV} and R_o. This property is evident according to the simulation results.

2- Considering a secondary ESS as V_i instead of PV allows the converter to be active 24 hours a day.

3- The first priority in providing the power required for the output load is assigned to PV. This means that PV supplies all the load power required; otherwise, it will be done with the help of the main ESS.

4- Due to the use of SI as the input of the converter, the ripple and rise time of the input current is reduced.

5- Due to the use of CI, SEPIC, and VMM, it is possible to simultaneously increase the current and voltage gain.

6- In this converter, it is also possible to use other RES energy sources to supply the input power.

Different modes of operation are discussed and validated via PSCAD simulation results.

REFERENCES

[1] Mohseni, P., Hosseini, S.H., Sabahi, M., and et al.: 'A new high step-up multi-input multi-output DC–DC converter', IEEE Trans. Ind. Electron., 2019, 66, (7), pp. 5197–5208

[2] Maalandish, M., Hosseini, S.H., and Jalilzadeh, T.: 'High step-up DC/DC converter using switch-capacitor techniques and lower losses for renewable energy applications', IET Power Electron., 2018, 11, (10), pp. 1718–1729

[3] Dongsheng, Y., Jie, Y., Ruidong, X., Zhenglong, X., Herbert, H., and Tyrone, F.: 'A Family of Module-Integrated High Step-up Converters with Dual Coupled Inductors', IEEE Trans. Power Electron., 2018, pp. 2169-3536

[4] Rehman, Z., Ibrahim A., and Subhas, M.: 'Multi-input DC/DC converters in renewable energy applications an overview', Elsevier Renewable and Sustainable Energy Reviews, 41, 2015, pp. 521–539

[5] Guipeng, C., Zhufeng, J., Yan, D., Xiangning, H., and Xinlin, Q.: 'Principle and Topology Synthesis of Integrated Single-Input Dual-Output and Dual-Input Single-Output DCDC Converters', IEEE Transactions on Industrial Electronics, 2018, 65, (5), pp. 3815–3825

[6] Mohseni, P., Hosseini, S., Maalandish, M., and Sabahi, M.: 'Ultra-high step-up two-input DC–DC converter with lower switching losses', IET Power Electron., 2019, 12, (9), pp. 2201–2213

[7] Yiyang, L., John, L., and Swamidoss, S.: 'Improved quadratic boost converter using cross coupled-inductor', IEEE 4th Southern Power Electronics Conference (SPEC), 7 February 2019, DOI: 10.1109/SPEC.2018.8635857

[8] Zhe, L., Wei, Q., and Xi, Z.: 'An Optimized Zero Voltage Zero Current Transition Boost Converter Realized by Coupled Inductor', IEEE Trans. Ind. Electron., 2019, 34, (9), pp. 8882–8893

[9] Yining, L., Wei, Q., and Xi, Z.: 'A Novel Isolated SEPIC Based Converter with High Voltage Gain and ZVS Characteristic', 2019 22nd International Conference on Electrical Machines and Systems (ICEMS), 05 December 2019, DOI: 10.1109/ICEMS.2019.8922028

[10] Savakhandeh, V., Chewale, M., Sarwade, R., Chavan, P., and Jagadale, A.: 'Coupled Inductor and Voltage Doubler Based Boost Converter for High Step-up Application', 2018 International Conference on Control, Power, Communication and Computing Technologies (ICCPCCT), March 2018, DOI: 10.1109/ICCPCCT.2018.85742302018

[11] Yao, Z., Zeng, J., and Junfeng, L.: 'High Step-up Low-voltage Stress Boost Converter Based on Coupled Inductor', 2018 IEEE International Power Electronics and Application Conference and Exposition (PEAC), November 2018, DOI:10.1109/PEAC.2018.8590536

[12] Pourjafar, S., Sedaghati, F., Shayeghi, H., and Maalandish, M.: 'A New High Step-Up DC-DC Converter with Coupled Inductor Suitable for renewable Applications', IET Power Electron., October 2018, DOI: 10.1049/ IET-PEL.2018.5414

[13] Samadian, A., Hosseini, S.H., Sabahi, M., and Maalandish, M.: 'A New Coupled Inductor Non-isolated High step up Quasi Z-Source DC-DC Converter', IEEE Transactions on Industrial Electronics, August 2019, DOI: 10.1109/ TIE.2019.2934067, pp. 0278-0046

[14] Alsaleem, A., Bubshait, A., and Godoy, M.: 'A Low Current-Ripple Coupled-Inductor Step-Up DC-DC Converter for Voltage-Multiplier Topology Solar PV Applications', 2018 IEEE Energy Conversion Congress and Exposition (ECCE), DOI: 10.1109/ ECCE.2018.8558463, pp. 2329-3748

[15] Yifeng, W., Fuqiang, H., Liang, Y., Yan, R., and Ruixin, L.: 'A Three-Port Bidirectional Multi-Element Resonant Converter with Decoupled Power Flow Management for Hybrid Energy Storage Systems', IEEE Access, October 2018, DOI: 10.1109/ ACCESS.2018. 2872683, pp. 61331-61341

[16] Varesi, K., Hosseini, S.H., Sabahi, M., Babaei, E., Saeidabadi, S., and Vosoughi, N.: 'Design and Analysis of a Developed Multi-Port High Step-Up DC-DC Converter with Reduced Device Count and Normalized Peak Inverse Voltage on the Switches/Diodes', IEEE Transactions on Power Electronics, June 2019, 34, (6), pp. 5464–5475

[17] Faraji, R., Ding, L., Rahimi, T., Kheshti, M., Matioli, E., and Esteki, M.: 'Soft-Switched Three-Port DC-DC Converter with Simple Auxiliary Circuit', Access (Volume 9), 28 April 2021, DOI: 10.1109/ACCESS.2021.3076183, pp. 2169-3536

[18] Faraji, R., Ding, L., Esteki, M., Mazloum, N., and Ali Khajehoddin, S-.: 'Soft-Switched Single Inductor Single Stage Multi-Port Bidirectional Power Converter for Hybrid Energy Systems', IEEE Transactions on Power Electronics, (Volume:36, Issue:10, Oct. 2021), DOI: 10.1109/TPEL.2021.3074378

[19] Yuanmao, Y., Wei, P., and Bijia, J.: 'High Step-Up DC-DC Converter with Multi Winding CL and Switched Capacitor', IET Power Electronics, November 2018, DOI:10.1049/IET-PEL.2018.5454, pp. 2232-2240

[20] Xianbin, Q., Donglai, Z., and Mingzhu, F.: 'A Coupled Inductor Based High Gain Non-Isolated Three-Port DC-DC Converter', 2018 IEEE International Power Electronics and Application Conference and Exposition

(PEAC), November 2018, DOI: 10.1109/ PEAC.2018.8590286

[21] Eskandarpour Azizkandi, M., Sedaghati, F., Shayeghi, H.: 'A New Boost DC-DC Converter Based on a Coupled Inductor and Voltage Multiplier Cells', October 2019 International Journal of Industrial Electronics, Control and Optimization (IECO), Vol. 2, No. 4, pp. 265-278

[22] Ehsani, M., Saedi, M, Radmanesh, H., Abrishamifar, A.: 'Comparisons between Generalized Predictive Control and Linear Controllers in Multi-Input DC-DC Boost Converter', Jan 2020 International Journal of Industrial Electronics, Control and Optimization (IECO), Vol. 1, No. 3, pp. 27-34

[23] Haghighian, S., Tohidi, S., Feyzi, M.R., and Sabahi, M.: 'Design and analysis of a novel SEPIC-based multi-input DC/DC converter', IET Power Electronics, October 2017, DOI: 10.1049/iet-pel.2016.0654, pp. 1393-1402

[24] Shalchi Alishah, R., Hosseini, S.H., Babaei E, and Sabahi, M.: 'A New General Multilevel Converter Topology Based on Cascaded Connection of Sub-Multilevel Units with Reduced Switching Components, DC Sources and Blocked Voltage by Switches' IEEE Transactions on industrial electronics, June 3 2016, DOI: 10.1109/TIE.2016.2592460

Gholamreza Mohebalizadeh was born in Tehran, Iran, in 1967. He received the B.S. degree in electronic engineering from the University of Shiraz, Shiraz, in 1991, the M.S. degree in nuclear engineering from Tehran Azad University, Tehran, Iran, in 2000, and he is the student of Ph.D. degree in electrical engineering of the Islamic Azad University, Shabestar Branch. His current research interests include power electronic converters and renewable energy systems.

Hasan Alipour received the B.Sc., M.Sc. and Ph. D degrees in power electrical engineering from Iran University of Science and Technology (IUST), Tehran, Iran, in 2008, University of Tehran, Tehran, Iran, in 2011, and University of Tabriz, Tabriz, Iran, in 2015, respectively. Currently, he is an assistant professor in the engineering faculty of Islamic Azad University, Shabestar Branch. His research interest focuses on Electric and Hybrid Electric Vehicles, Electric Machines Drive, Linear Electric Motors, renewable Energies, and Distributed Generation.

Leila Mohammadian was born in Tabriz, Iran in 1984. She received her B.S., M.S. and Ph.D. degrees in Electrical Engineering from the Department of Electrical and Computer Engineering, University of Tabriz, Tabriz, Iran, in 2007, 2011 and 2015, respectively. She is with Shabestar Branch, Islamic Azad University, Shabestar, Iran, since 2011. She has been an Assistant Professor from 2015. Her current research interests include the analysis and control of power electronic converters and their applications.

Mehran Sabahi was born in Tabriz, Iran, in 1968. He received the B.S. degree in electronic engineering from the University of Tabriz, Tabriz, in 1991, the M.S. degree in electrical engineering from Tehran University, Tehran, Iran, in 1994, and the Ph.D. degree in electrical engineering from the University of Tabriz, in 2009. In 2009, he joined the Faculty of Electrical and Computer Engineering, University of Tabriz, where he has been an Associate Professor since 2014. His current research interests include power electronic converters and renewable energy systems.